An analysis of special white dwarfs: from ancient planetary debris to intrinsic phenomena to accurate flux calibrators

by

Abbigail Kathryn Elms

Thesis

Submitted to the University of Warwick

for the degree of

Doctor of Philosophy

Department of Physics: Astronomy and Astrophysics

May 2025

THE UNIVERSITY OF
WARWICK

Contents

List of Tables

List of Figures

Acknowledgments

Personal Acknowledgements

Academia is challenging, therefore it is very much a team effort. I would like to thank all of the people who supported me.

Firstly, I would like to thank my supervisor, Pier-Emmanuel Tremblay, for being a fantastic boss and mentor. I am grateful for the scientific freedom you gave me in my research and for allowing me to travel to so many national and international conferences, collaboration opportunities and telescope observing runs. I am also grateful to all of my collaborators for their patience and wisdom.

I would like to thank three of my colleagues from the Warwick Astronomy & Astrophysics group: Gareth, you have been an invaluable friend over the past 4 years, I am so glad I met you; Andreas, you lit up our office every day with your stories and laughter, I will miss our chats; and Mairi, we have sat next to each other every day in the office, had intertwining research, taught labs together, and gone on almost every work trip together - thank you for everything.

Special thanks go to: my mom, sister and dad, who have supported me throughout my whole academic journey; Alice, Mel, Ollie & Jake, who have shown me nothing but love and kindness since I moved to Coventry; and Simon, thank you for your constant love, understanding and support.

Institutional Acknowledgements

This research received funding from the European Research Council under the European Union's Horizon 2020 research and innovation programme number 101002408 (MOS100PC).

This reseach was supported in part by the European Union's Horizon 2020 research and innovation programme (Grant agreement number 101020057 (WD-PLANETS), the Leverhulme Trust Grant (ID RPG-2020-366), the UK STFC consolidated grant ST/T000406/1. The authors acknowledge financial support from Imperial College London through an Imperial College Research Fellowship grant awarded to CJM.

Parts of this research were based on observations collected at the European Southern Observatory under ESO programme 105.20ET.001.

This work has made use of data from the European Space Agency (ESA) mission *Gaia* (`https://www.cosmos.esa.int/gaia`), processed by the *Gaia* Data Processing and Analysis Consortium (DPAC, `https://www.cosmos.esa.int/web/gaia/dpac/consortium`). Funding for the DPAC has been provided by national institutions, in particular the institutions participating in the *Gaia* Multilateral Agreement.

The Pan-STARRS1 Surveys (PS1) and the PS1 public science archive have been made possible through contributions by the Institute for Astronomy, the University of Hawaii, the Pan-STARRS Project Office, the Max-Planck Society and its participating institutes, the Max Planck Institute for Astronomy, Heidelberg and the Max Planck Institute for Extraterrestrial Physics, Garching, The Johns Hopkins University, Durham University, the University of Edinburgh, the Queen's University Belfast, the Harvard-Smithsonian Center for Astrophysics, the Las Cumbres Observatory Global Telescope Network Incorporated, the National Central University of Taiwan, the Space Telescope Science Institute, the National Aeronautics and Space Administration under Grant No. NNX08AR22G issued through the Planetary Science Division of the NASA Science Mission Directorate, the National Science Foundation Grant No. AST-1238877, the University of Maryland, Eotvos Lorand

University (ELTE), the Los Alamos National Laboratory, and the Gordon and Betty Moore Foundation.

This research includes data collected by the *TESS* mission. Funding for the *TESS* mission is provided by the NASA's Science Mission Directorate. This paper includes data collected by the *TESS* mission that are publicly available from the Mikulski Archive for Space Telescopes (MAST).

Some observations for this research were obtained with the Samuel Oschin Telescope 48-inch and the 60-inch Telescope at the Palomar Observatory as part of the Zwicky Transient Facility project. ZTF is supported by the National Science Foundation under Grants No. AST-1440341 and AST-2034437 and a collaboration including current partners Caltech, IPAC, the Weizmann Institute for Science, the Oskar Klein Center at Stockholm University, the University of Maryland, Deutsches Elektronen-Synchrotron and Humboldt University, the TANGO Consortium of Taiwan, the University of Wisconsin at Milwaukee, Trinity College Dublin, Lawrence Livermore National Laboratories, IN2P3, University of Warwick, Ruhr University Bochum, Northwestern University and former partners the University of Washington, Los Alamos National Laboratories, and Lawrence Berkeley National Laboratories. Operations are conducted by COO, IPAC, and UW.

Some of the data presented in this work were obtained at the W. M. Keck Observatory, which is operated as a scientific partnership among the California Institute of Technology, the University of California and the National Aeronautics and Space Administration. The Observatory was made possible by the generous financial support of the W. M. Keck Foundation. We wish to recognize and acknowledge the very significant cultural role and reverence that the summit of Maunakea has always had within the indigenous Hawaiian community. We are most fortunate to have the opportunity to conduct observations from this mountain.

This work has made use of data from The William Herschel Telescope and Isaac Newton Telescopes, which are operated on the island of La Palma by the Isaac Newton Group of Telescopes in the Spanish Observatorio del Roque de Los Muchachos of the Instituto de Astrofísica de Canarias.

Some observations for this research were obtained at the international Gemini Observatory, a programme of NSF's NOIRLab, which is managed by the Association of Universities for Research in Astronomy (AURA) under a cooperative agreement with the National Science Foundation on behalf of the Gemini Observatory partnership: the National Science Foundation (United States), National Research Council (Canada), Agencia Nacional de Investigación y Desarrollo (Chile), Ministerio de Ciencia, Tecnología e Innovación (Argentina), Ministério da Ciência, Tecnologia, Inovações e Comunicações (Brazil), and Korea Astronomy and Space Science Institute (Republic of Korea).

Research at Lick Observatory is partially supported by a generous gift from Google. A major upgrade of the Kast spectrograph on the Shane 3 m telescope at Lick Observatory was made possible through generous gifts from William and Marina Kast as well as the Heising-Simons Foundation.

This research is based on observations made with the NASA/ESA *Hubble Space Telescope* obtained from the Space Telescope Science Institute, which is operated by the Association of Universities for Research in Astronomy, Inc., under NASA contract NAS 5–26555. Support for Program number (16249) was provided through a grant from the STScI under NASA contract NAS5- 26555. These observations are associated with programs GP-14213, GP-15485, GP-16249.

This publication makes use of data products from the Two Micron All Sky Survey, which is a joint project of the University of Massachusetts and the Infrared Processing and Analysis Center/California Institute of Technology, funded by the National Aeronautics and Space Administration and the National Science Foundation.

This publication makes use of data products from the Wide-field Infrared Survey Explorer, which is a joint project of the University of California, Los Angeles, and the Jet Propulsion Laboratory/California Institute of Technology, funded by the National Aeronautics and Space Administration.

The observations from the FORS2 instrument were collected at the European Southern Observatory under ESO programme(s) 113.26ES.001.

Declarations

This thesis is submitted to the University of Warwick in support of my application for the degree of Doctor of Philosophy. It has been composed by myself and has not been submitted in any previous application for any degree.

The science chapters in this thesis are reproductions of Monthly Notices of the Royal Astronomical Society (MNRAS) peer-reviewed publications written by myself, with the input of co-authors. Details of these publications are below:

- Elms et al. (2022), *Spectral analysis of ultra-cool white dwarfs polluted by planetary debris.* Chapter 3 is composed of material from this publication. Spectroscopic observations with X-Shooter were obtained by Boris Gänsicke. Detlev Koester provided the model atmosphere code and made microphysics improvements to it so I could compute atmospheric parameters, in addition he computed diffusion timescales using his envelope code. Detlev Koester wrote the majority of Section 3.4. Nicola Pietro Gentile Fusillo performed time-series analysis on the *TESS* data, wrote the majority of Section 3.6.2 and created the plots in Figure 3.8. Tim Cunningham computed the minimum parent body mass of the accreted planetesimals and created the plots in Figure 3.11.

- Elms et al. (2023), *An emerging and enigmatic spectral class of isolated DAe white dwarfs.* Chapter 4 is composed of material from this publication. Spectroscopic observations from WHT/ISIS and INT/IDS were obtained by Boris Gänsicke, Keck/HIRES and Shane/KAST were obtained by Carl Melis and Ben Zuckerman, and Gemini/GMOS-N were obtained by Erik Dennihy and Atsuko Nitta. The model atmospheres were provided by Pier-Emmanuel

Tremblay. In Section 4.3.1, the $O - C$ analysis was performed by J. J. Hermes and the F-test was performed by James Munday. The analysis performed and writing of paragraphs 5-8 in Section 4.3.1 were mainly completed by Andrew Swan. The model evolutionary sequences using the STELUM code were computed by Antoine Bédard. The IFMR and substellar companion analysis done in Section 4.4.2 was completed by Pier-Emmanuel Tremblay. Section 4.4.3 was mainly written by Pier-Emmanuel Tremblay.

- Elms et al. (2024), *A network of cooler white dwarfs as infrared standards for flux calibration*. Chapter 5 is composed of material from this publication. *HST* spectrophotometric observations were obtained from the majorative effort of Pier-Emmanuel Tremblay, Ralph Bohlin and Nicola Pietro Gentile Fusillo. The model atmospheres were provided by Pier-Emmanuel Tremblay. The Balmer line fitting code was provided by Nicola Pietro Gentile Fusillo, with small changes implemented by myself. The analysis performed and writing of paragraph 4 in Section 5.3.1 was completed by Mark Hollands. *Gaia*, 2MASS and *WISE* synthetic magnitudes and atmospheric parameters from *Gaia* photometric fits were computed by Mairi O'Brien.

Abstract

Over 97 % of main-sequence stars in the galaxy end their stellar evolution as white dwarfs, offering abundant research opportunities for astrophysical phenomena. Their high densities and surface gravities ($\log g$) create pristine hydrogen and helium atmospheres, enabling accurate determination of parameters such as effective temperatures ($T_{\rm eff}$), $\log g$, mass and age. Deviations in a white dwarf's spectral energy distribution (SED) from these simple atmospheres indicate external or internal influences, such as the accretion of planetary debris or magnetic fields.

First, I analysed spectroscopic and photometric data of WD J2147−4035 and WD J1922+0233, identifying them as the coolest metal-polluted white dwarfs known to date. WD J2147−4035 is over 10 Gyr old therefore hosts the oldest known planetary debris in the Milky Way disc. The abundances found in WD J2147−4035 are lithium- and potassium-rich compared to solar system objects, suggesting the accretion of an exotically composed planetesimal. The atmospheric composition of WD J1922+0233 resembles Earth's continental crust, indicating accretion of crust-like material.

I then analysed new spectroscopic and time-series data of DAe white dwarfs WD J0412+7549 and WD J1653−1001, which have emission in their Hα and Hβ Balmer lines. I measured the upper magnetic field strength limit of both stars, calculated their spin periods, confirmed an anti-phase relationship between spectroscopic and photometric variability for WD J0412+7549, and examined possible non-magnetic and magnetic mechanisms which could explain DAe characteristics and their relation to DAHe stars.

Finally, I presented 17 hydrogen-dominated atmosphere white dwarfs with $T_{\rm eff} < 20\,000$ K as accurate spectrophotometric flux calibrators. These cooler white dwarfs than current primary standards are equally, if not more, accurate at IR wavelengths. Spectrophotometric fits of *HST* STIS and WFC3 data successfully predicted the observed fluxes within 3 % over most of the range $1450 - 16\,000$ Å, with a median standard deviation flux residual of 1.41 %. Independent SED and Balmer line fits agreed within 3σ. These results demonstrated that this network is fully consistent with the *HST* flux scale.

Abbreviations

2MASS	Two Micron All-Sky Survey
3D	Three-dimensional
AGB	Asymptotic Giant Branch
Z	Atomic mass
TDB	Barycentric Dynamical Time
BJD	Barycentric Julian Date
BMJD	Barycentric Modified Julian Date
CNO	Carbon-nitrogen-oxygen
CTIO	Cerro Tololo Inter-American Observatory
CCD	Charge-coupled device
χ^2	Chi-square
CIA	Collision-induced absorption
CVZ	Convection zone
DECam	Dark Energy Camera
DESI	Dark Energy Spectroscopic Instrument
DES	Dark Energy Survey

DR	Data release
$\tau_{\rm z}$	Diffusion time-scales
EDR3	Early data release 3
$T_{\rm eff}$	Effective temperature
EDP	Electron degeneracy pressure
W_λ	Equivalent width
ESA	European Space Agency
ESO	European Southern Observatory
FAP	False alarm probability
FFI	Full frame image
FWHM	Full-Width Half Maximum
GMOS	Gemini Multi-Object Spectrograph
GTC	Gran Telescopio Canarias
$z_{\rm grav}$	Gravitational redshift
HR	Hertzsprung-Russell
HRD	Hertzsprung-Russell diagram
HIRES	High Resolution Echelle Spectrometer
HST	*Hubble Space Telescope*
$M_{\rm z}$	Individual metal masses
IR	Infrared
IFMR	Initial-to-final-mass relation

ISM	Interstellar medium
ISIS	Intermediate-dispersion Spectrograph and Imaging System
IDS	Intermediate Dispersion Spectrograph
IRSA	Infrared Science Archive
INT	Isaac Newton Telescope
JWST	*James Webb Space Telescope*
τ_{MS}	Lifetime of a star
LSF	Line spread function
$v_{\rm line}$	Line velocity
L	Luminosity
MagE	Magellan Echellette
MS	Main-sequence
M-R	Mass-radius
$M_{\rm cvz}$	Mass of the CVZ
$M_{\rm H}$	Mass of hydrogen in the CVZ
$M_{\rm z}$	Mass of individual metals in the CVZ
$\langle B_z \rangle$	Mean longitudinal field
MSX	*Midcourse Space Experiment*
MAST	*Mikulski Archive for Space Telescopes*
$M_{\rm z,tot}$	Minimum accreted parent body mass
MWDD	*Montreal White Dwarf Database*

NICMOS	Near Infrared Camera and Multi-Object Spectrometer
NLTE	Non-local thermal equilibrium
1D	One-dimensional
κ	Opacity
OSIRIS	Optical System for Imaging and low-Intermediate-Resolution Integrated Spectroscopy
Pan-STARRS	Panoramic Survey Telescope and Rapid Response System
ϖ	Parallax
PN	Planetary Nebula
Post-AGB	Post-Asymptotic Giant Branch
PDCSAP	Pre-search Data Conditioning Simple Aperture Photometry
H_p	Pressure scale height
p-p	Proton-proton
v_rad	Radial velocity
RGB	Red Giant Branch
RST	*Nancy Grace Roman Space Telescope*
S/N	Signal-to-noise
SDSS	Sloan Digital Sky Survey
STIS	Space Telescope Imaging Spectrometer
SVO	Spanish Virtual Observatory
SED	Spectral energy distribution
R	Stellar radius

SGB	Sub-Giant Branch
SNe	Supernovae
$\log g$	Surface gravity
TESS	Transiting Exoplanet Survey Satellite
TIC	*TESS* Input Catalog
TP-AGB	Thermal Pulse Asymptotic Giant Branch
$M_{\rm z,tot}$	Total accreted parent body mass
UVES	Ultraviolet and Visual Echelle Spectrograph
vMa2	Van Maanen 2
VLT	Very Large Telescope
VISTA	Visible and Infrared Survey Telescope for Astronomy
WD	White dwarf
τ	White dwarf cooling age
$M_{\rm WD}$	White dwarf mass
$V_{\rm WD}$	White dwarf volume
WFC3	Wide Field Camera three
WISE	Wide-field Infrared Survey Explorer
WHT	William Herschel Telescope
ZAMS	Zero-Age-Main-Sequence
ZTF	Zwicky Transient Facility

Elements

H	Hydrogen
He	Helium
Li	Lithium
C	Carbon
N	Nitrogen
O	Oxygen
Na	Sodium
Mg	Magnesium
Al	Aluminium
Si	Silicon
K	Potassium
Ca	Calcium
Fe	Iron
Co	Cobalt
Ni	Nickel

Wavelength Ranges

FUV	Far-ultraviolet: $912 - 1190\,\text{Å}$
UV	Ultraviolet: $0.119 - 0.3\,\mu m$

Optical	Optical: $0.3 - 1\,\mu m$
NIR	Near-infrared: $1 - 5\,\mu m$
MIR	Mid-infrared: $5 - 32\,\mu m$

Quantities

$\mathrm{R}_\odot$	Solar radius: $6.957 \times 10^{8}\,\mathrm{m}$
$\mathbf{M}_\odot$	Solar mass: $1.988 \times 10^{30}\,\mathrm{kg}$
$\mathbf{M}_{\mathrm{Jup}}$	Jupiter mass: $1.898 \times 10^{27}\,\mathrm{kg}$
$\tau_\odot$	10^{9} years
G	Gravitational constant: $6.674 \times 10^{-11}\,\mathrm{Nm^{2}kg^{-2}}$
c	Speed of light: $2.998 \times 10^{8}\,\mathrm{ms^{-1}}$
σ	Stefan-Boltzmann constant: $5.670 \times 10^{-8}\,\mathrm{Wm^{-2}K^{-4}}$
AU	Astronomical unit: $1.496 \times 10^{8}\,\mathrm{km}$
pc	Parsec: $3.086 \times 10^{13}\,\mathrm{km}$

Chapter 1

Introduction

White dwarfs are the final evolutionary stage for the majority of stars in the Universe. Their combination of physical properties, such as intense surface gravities ($\log g$), slow cooling and pristine hydrogen (H) and/or helium (He) atmospheres, make them invaluable cosmic laboratories for studying stellar and galactic evolution, evolved exoplanetary systems and magnetic fields. Additionally, these characteristics result in white dwarfs being excellent cosmic chronometers and spectrophotometric flux standards. White dwarfs are essential to the development of modern astrophysics, and this work contributes to that endeavour.

1.1 Discovery of white dwarfs

By definition, white dwarfs are small compact objects. Their lack of fuel source means they slowly cool over time, thus getting fainter and fainter. These properties combined pose observational challenges for discovering white dwarfs, especially in the era before space telescopes. The first white dwarf, 40 Eridani (Eri) B, was discovered in the 1780s by William Herschel (Herschel, 1785) as a binary companion to the main-sequence (MS) star 40 Eridani A. Over a century later, Williamina Fleming spectroscopically classified 40 Eri B as type A star (Bond et al., 2017). A Hertzsprung-Russell (HR) diagram confirmed that 40 Eri B is extremely faint for its colour (Hertzsprung, 1915) and five magnitudes fainter than its companion (Russell, 1944), which requires this object to have a much smaller radius and greater density than anything previously discovered (Adams, 1914).

The second white dwarf discovered was Sirius B, the closest white dwarf to Earth at ≈ 8 light years away. Bessel (1844) hypothesised astrometrically that Sirius may have an undetected companion exerting a gravitational influence on the star, due to its systematically altered proper motion. Alvan Graham Clark spectroscopically observed Sirius B (Flammarion, 1877; Holberg and Wesemael, 2007) and confirmed the companion as type A, the same as Sirius. With Sirius B being 10 magnitudes fainter than Sirius, this object must have a similar physical composition to 40 Eri B: small radius and large density.

The white dwarf companion to the MS star Procyon A, Procyon B, was observationally discovered in the late 1890s (Schaeberle, 1896), following its astrometrically hypothesised existence by Bessel (1844). However, its classification as a white dwarf was delayed for almost two decades due to its faint magnitude (≈ 10 mag) and close proximity to its bright host star (≈ 0 mag) causing observational challenges.

The discovery of the first and closest single white dwarf, van Maanen's star (vMa2; van Maanen, 1917), preceded the classification of Procyon B. vMa2 was identified because of its high proper motion (≈ 3 arcseconds per year) and relatively faint apparent magnitude of ≈ 12 mag. Spectroscopic follow-up resulted in the initial classification of an F-type star as a result of the presence of several strong metal (elements heavier than He) absorption lines. However, van Maanen (1920) calculated that the star was only ≈ 4 pc away from Earth which would make it an extremely faint F-type star. A few years later, it was realised that vMa2 belonged to the same class of star as 40 Eri B, Sirius B and Procyon B: white dwarfs (Luyten, 1922).

The discovery of the four 'classical' white dwarfs, 40 Eri B, Sirius B, Procyon B and vMa2, paved the way for the exciting, rich and interesting sector of white dwarf astrophysics. Over the past two decades, the Sloan Digital Sky Survey (SDSS; Kleinman et al., 2004, 2013; Eisenstein et al., 2006; Kepler et al., 2021) has spectroscopically classified $\approx 100,000$ white dwarfs. More recently, the spacecraft *Gaia* (Gaia Collaboration et al., 2016) has observed more than 350,000 white dwarfs in the Milky Way (Gentile Fusillo et al., 2019, 2021), revolutionising white dwarf science with precise astrometry and photometry. These large samples have also been complemented by the Dark Energy Spectroscopic Instrument (DESI; DESI Collaboration et al., 2016a,b, 2024a,b; Manser et al., 2024).

1.2 White dwarf formation

Over 97 % of low- and intermediate-mass MS stars ($M/\mathrm{M}_{\odot} \lesssim 8$) in the Milky Way galaxy will end their stellar evolution as white dwarfs (Carroll and Ostlie, 2006; Althaus et al., 2010a), including our Sun. The stars in this mass range form and evolve through typical channels of stellar evolution, and result in characteristically compact objects known as white dwarfs. This section describes this process.

Space is filled with microscopic dust particles and gas, predominantly H in its neutral (H I), ionized (H II) and molecular (H_2) forms, called the interstellar medium (ISM). A small percentage of the ISM is comprised of He and metals, such as carbon (C) and silicon (Si), but all together constitute the building-blocks of stars. Regions of varying density occur in the ISM due to its natural inhomogeneous distribution or local events perturbing the ISM, such as shock waves created by supernovae (SNe). In relatively dense regions, gravitational attraction between ISM atoms is enhanced causing the creation of molecular clouds. The more massive molecular clouds become, the stronger their gravitational force, which pulls in more and more ISM material, resulting in an ever denser and hotter core. Eventually, molecular clouds will reach a critical mass limit for a given density and temperature where they are able to stay in hydrostatic equilibrium, called the Jeans Mass (Jeans, 1902). If the Jeans Mass is exceeded, the inward gravitational attraction of the core dominates the outward thermal gas pressure of the cloud and the external radiation pressure exerted by the surrounding material in the cloud and ISM. The molecular clouds will then contract and condense into protostars.

The central temperature of protostars must be $> 10^6\,\mathrm{K}$ for the nuclear fusion of H to occur. This means that the mass of the molecular cloud that undergoes gravitational collapse is $\gtrsim 0.02\,\mathrm{M}_\odot$. Between $\approx 0.02 - 0.08\,\mathrm{M}_\odot$, deuterium fusion occurs and a brown dwarf is formed. Brown dwarfs are known as 'failed stars' because they are not massive enough to fuse H into He. Above $\approx 0.08\,\mathrm{M}_\odot$, the temperature and pressure in the core of stars is sufficient to fuse H into He via the proton-proton (p-p) chain:

$$\begin{aligned} {}^{1}\mathrm{H} + {}^{1}\mathrm{H} &\longrightarrow {}^{2}\mathrm{H} + \mathrm{e}^{+} + \nu_e \\ {}^{1}\mathrm{H} + {}^{2}\mathrm{H} &\longrightarrow {}^{3}\mathrm{He} + \gamma \\ {}^{3}\mathrm{He} + {}^{3}\mathrm{He} &\longrightarrow {}^{4}\mathrm{He} + {}^{1}\mathrm{H} + {}^{1}\mathrm{H} \end{aligned}$$

where ${}^{1}\mathrm{H}$ is a hydrogen atom (i.e. a proton), ${}^{2}\mathrm{H}$ is deuterium, e^{+} is a positron, ν_e is an electron neutrino, γ is a gamma ray (i.e. a very high-energy photon), ${}^{3}\mathrm{He}$ is the isotope helium-3 and ${}^{4}\mathrm{He}$ is helium. The gamma ray produced through the p-p chain is the thermal energy that provides the outward pressure in the core, preventing the star from gravitational collapse. At this stage, a star is born.

The carbon-nitrogen-oxygen (CNO) cycle begins in stars once the core temperature is $\gtrsim 10^7\,\mathrm{K}$. The CNO cycle is a six-stage sequence of the fusion of H to He via

$$\begin{aligned} {}^{12}\mathrm{C} + {}^{1}\mathrm{H} &\longrightarrow {}^{13}\mathrm{N} + \gamma \\ {}^{13}\mathrm{N} &\longrightarrow {}^{13}\mathrm{C} + \mathrm{e}^{+} + \nu_e \\ {}^{13}\mathrm{C} + {}^{1}\mathrm{H} &\longrightarrow {}^{14}\mathrm{N} + \gamma \\ {}^{14}\mathrm{N} + {}^{1}\mathrm{H} &\longrightarrow {}^{15}\mathrm{O} + \gamma \\ {}^{15}\mathrm{O} &\longrightarrow {}^{15}\mathrm{N} + \mathrm{e}^{+} + \nu_e \\ {}^{15}\mathrm{N} + {}^{1}\mathrm{H} &\longrightarrow {}^{12}\mathrm{C} + {}^{4}\mathrm{He} \end{aligned}$$

where ${}^{12}\mathrm{C}$ is carbon, ${}^{13}\mathrm{C}$ is the isotope carbon-13, ${}^{14}\mathrm{N}$ is nitrogen, ${}^{13}\mathrm{N}$ and ${}^{15}\mathrm{N}$ are isotopes of nitrogen, and ${}^{15}\mathrm{O}$ is the isotope oxygen-15. In the second and fifth steps of the CNO cycle, the unstable nuclei undergo beta-plus decay where a proton converts into a neutron, resulting in a more stable element while preserving the mass number. Low- and intermediate-mass stars fuse H to He via the p-p chain and CNO cycle, but due to the temperature dependence of the CNO cycle stars of mass $\gtrsim 1.5\,\mathrm{M}_\odot$ have the CNO cycle as the dominant fusion process.

Stars start and live most of their lives ($\gtrsim 90\,\%$) as stable MS stars. Once

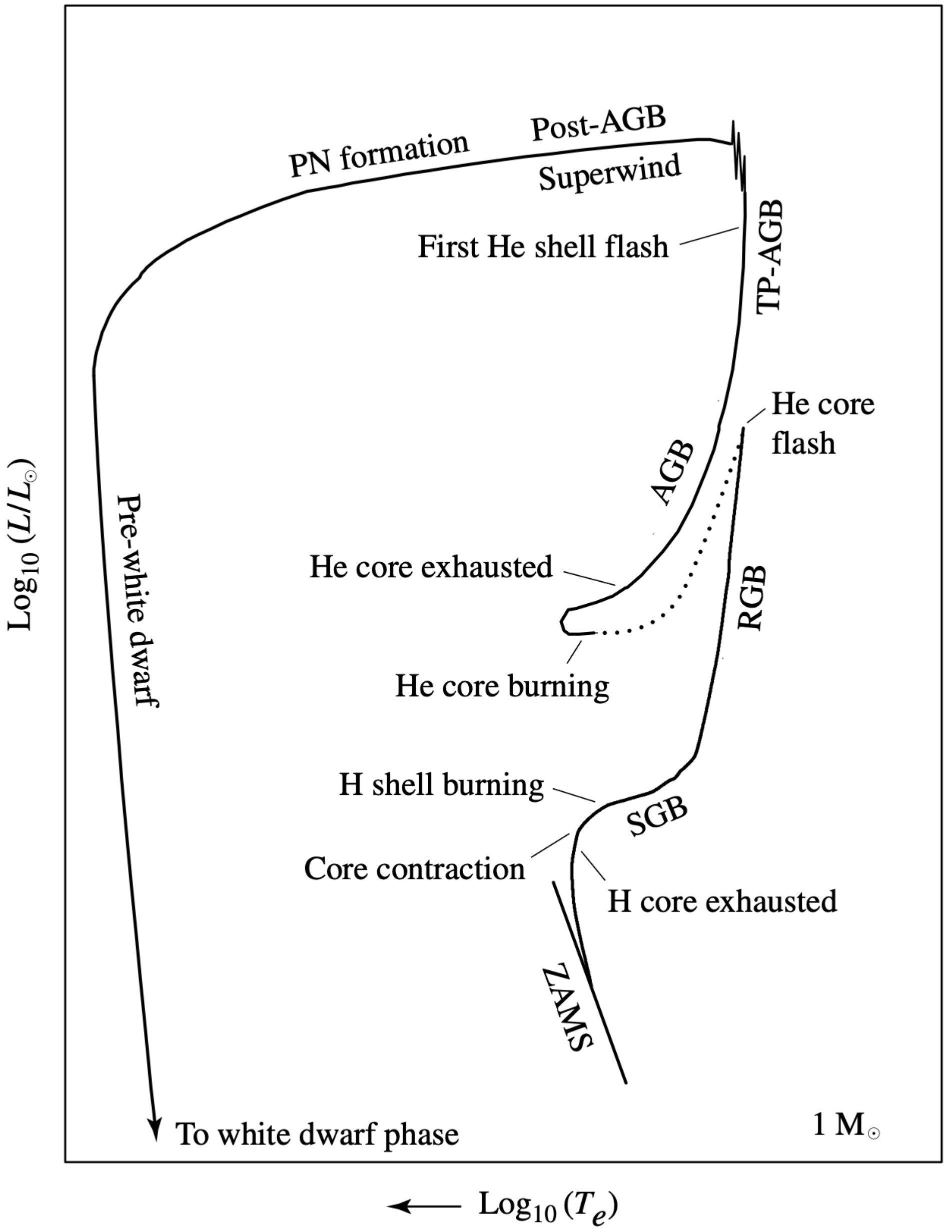

Figure 1.1: A schematic Hertzprung-Russell (HR) diagram of the luminosity and effective temperature evolution of a low-mass star of $1\,\mathrm{M}_\odot$. The dotted phase of evolution represents rapid evolution following the He core flash. The various phases of evolution are labeled as follows: Zero-Age-Main-Sequence (ZAMS), Sub-Giant Branch (SGB), Red Giant Branch (RGB), Asymptotic Giant Branch (AGB), Thermal Pulse Asymptotic Giant Branch (TP-AGB), Post-Asymptotic Giant Branch (Post-AGB), Planetary Nebula formation (PN formation), and Pre-white dwarf phase leading to white dwarf phase. Figure and caption reproduced from Carroll and Ostlie (2006).

core H-burning has ignited, the outward thermal and radiation (i.e. energy) pressure balances the inward gravitational force, resulting in hydrostatic equilibrium. Stars enter the MS at the zero-age main sequence (ZAMS) which is represented by the diagonal line in the schematic HR diagram at relatively low luminosity in Figure 1.1, where luminosity is the energy radiated over the surface area (A) of the star per unit time. HR diagrams show the characteristic stellar evolution of stars as a function of effective temperature ($T_{\rm eff}$) and luminosity (L) using the Stefan-Boltzmann law:

$$L = A\sigma {T_{\rm eff}}^4 = 4\pi R^2 \sigma {T_{\rm eff}}^4, \tag{1.1}$$

where R is the stellar radius and σ is the Stefan-Boltzmann constant. Hence, HR diagrams are a useful diagnostic tool for determining the age and evolutionary stage of a star. $T_{\rm eff}$ is the surface temperature of a star, equivalent to the temperature of a blackbody, i.e. an object with a high enough density to have a definite temperature and to emit radiation, of the same radius as the star that would radiate the same amount of energy. The luminosities of MS stars are related to the stellar mass, M, by

$$L \propto M^{7/2}. \tag{1.2}$$

The lifetime of a star (τ_{MS}) on the MS decreases with increasing mass through the relationship

$$\frac{\tau_{MS}}{\tau_\odot} \approx \left(\frac{M}{M_\odot}\right)^{-5/2}, \tag{1.3}$$

where $\tau_\odot$ is 10^9 years, as more massive stars have higher densities and temperatures hence are able to ignite further nuclear fusion processes after He. For instance, a $1\,\mathrm{M}_\odot$ star like our Sun will have a stellar lifetime of $\approx 10\,$Gyr whereas a $8\,\mathrm{M}_\odot$ star will have a stellar lifetime of $\approx 30\,$Myr. Figure 1.1 shows the stellar evolution of a $1\,\mathrm{M}_\odot$ star from the ZAMS to a white dwarf.

A star will remain on the MS while it is able to generate energy from the fusion of H in its core via the p-p chain and CNO cycle. Once a star has exhausted the H supply in its core, core H-burning ceases and it will evolve off the MS to the Sub-Giant Branch (SGB). At this stage, the star starts to collapse; there is no longer sufficient outward pressure to oppose the inward gravitational force. The SGB is a short transition phase in which the He core temperature increases as a result of its contraction, resulting in a high enough temperature that H-shell burning occurs around the core, fusing the available H from the base of the star's envelope. This shell produces energy, leading to an increase in luminosity, envelope radius and core mass, but a decrease in T_{eff}.

The star enters the Red Giant Branch (RGB) once it has a steady H-burning shell around the core. Radiation is no longer the dominant energy transport mechanism in the photosphere because the opacity (κ), which is the resistance the gas in the envelope produces against radiation passing through it as a function of density and temperature, will have increased enough to allow energy transport to the surface of the star via convection, resulting in a fully convective envelope. As the star ascends the RGB, there is a slow decrease in surface temperature but an increase in the density of the core, outward radiation pressure and envelope radius. At the top of the RGB, the core has contracted enough so that the temperature and density of the core are high enough ($\approx 10^8\,\mathrm{K}$ and $\approx 10^7\,\mathrm{kg\,m^{-3}}$) for fusion of He via the triple-alpha process. This initiates with a high-luminosity, short, explosive release of energy called a He flash. The He flash causes the core to expand and the H-burning shell to be pushed outwards, thus decreasing the luminosity. A C- and O-rich core is created through He-burning, which is surrounded by a He-rich shell, then a H-burning shell, and finally a H-rich outer envelope.

Once the star has exhausted the He in its core, it has reached its hottest point. It then evolves onto the Asymptotic Giant Branch (AGB), where it consists of a carbon-oxygen (C/O) core, a He-burning shell, then a H-burning shell, all surrounded by a non-burning envelope. The core contracts again as gravitational attraction dominates outward pressure. The core is not hot enough to ignite further fusion, but because the core is degenerate, electron-degeneracy pressure (EDP) supports the core from total collapse. The core increases in temperature and instabilities occur in the outer envelope causing pulsations of luminosity, temperature and envelope radius, with an overall increase in luminosity throughout the AGB phase.

At the end of the AGB, H-burning in the shell dominates the energy output, called the Thermal Pulse Asymptotic Giant Branch (TP-AGB) phase. H fuses to He, which gets deposited in the deeper He shell, consequently increasing its mass and temperature. A short, intense period of He fusion called a He shell flash occurs when the temperature gets sufficiently high. This pushes the H-burning shell outwards, causing it to cool and the radius of the envelope to increase. The He-burning shell then decreases in temperature, and the process periodically repeats. The mass of the C/O core steadily increases due to the production of C and O in the He-burning shell, resulting in increased core density. Stellar winds lead to mass loss of the envelope outer layers throughout the AGB phase and at the end the star loses an extensive amount of mass through a superwind (the exact mechanism causing this is not well understood).

The Post-Asymptotic Giant Branch (Post-AGB) occurs once the H- and He-burning shells are depleted and the envelope around the core becomes optically thin (low κ) due to expansion. The expelled envelope is called a planetary nebula (PN), leaving behind the exposed, degenerate stellar core. Gravitational contraction increases the temperature of the core to $\approx 10^5\,\mathrm{K}$, at which it ceases to contract due to the Pauli Exclusion principle (see Section 1.2.1). The remnant C/O core then enters the white dwarf stage, where it slowly cools over time, decreases in luminosity, and is surrounded by a thin envelope of residual H and He.

1.2.1 Mass

The average mass of a white dwarf is $\approx 0.6\,\mathrm{M}_\odot$ (e.g. Kepler et al., 2007; Tremblay et al., 2011; Kepler et al., 2017; Tremblay et al., 2019b; McCleery et al., 2020), which demonstrates the extreme mass loss experienced by stars through stellar evolution (Section 1.2) since MS stars with $M/\mathrm{M}_\odot \lesssim 8$ become white dwarfs. Figure 1.2 shows the mass distribution of the northern white dwarfs within 40 pc, including only objects with $T_\mathrm{eff} > 5000\,\mathrm{K}$, as cool white dwarfs have a low-mass problem where they are systematically modelled to have lower masses than expected (O'Brien et al., 2024). White dwarfs have a radius comparable to that of Earth and mass comparable to that of the Sun (e.g. Joyce et al., 2018), which demonstrates the extreme density of white dwarfs. Approximately $99 - 99.99\,\%$ of the total mass is contained within the degenerate C/O core, with the remaining $0.01 - 1\,\%$ of the total mass contained within the envelope.

There is a theoretical physical upper limit to the mass of white dwarfs governed by quantum physics. White dwarfs are kept in hydrostatic equilibrium due to the EDP exerted by the matter in the core counteracting gravitational collapse (Fowler, 1926). EDP is a consequence of the Pauli Exclusion Principle, which states only one fermion (particles with half-integer spin) can occupy a quantum state (Pauli, 1925). Electrons are fermions and have a quantum property called spin, which is an intrinsic form of angular momentum, and can either be $+1/2$ (spin-up) or $-1/2$ (spin-down). A maximum of two electrons can occupy an orbital within an atom, therefore they must have opposite spins. When matter is condensed into a small volume, like it is in a white dwarf, the density will increase until the electrons populate every possible quantum state. At this point, the matter cannot condense any further resulting in a quantum mechanical pressure: EDP. EDP then stabilises the white dwarf from gravitational collapse and, being independent of temperature,

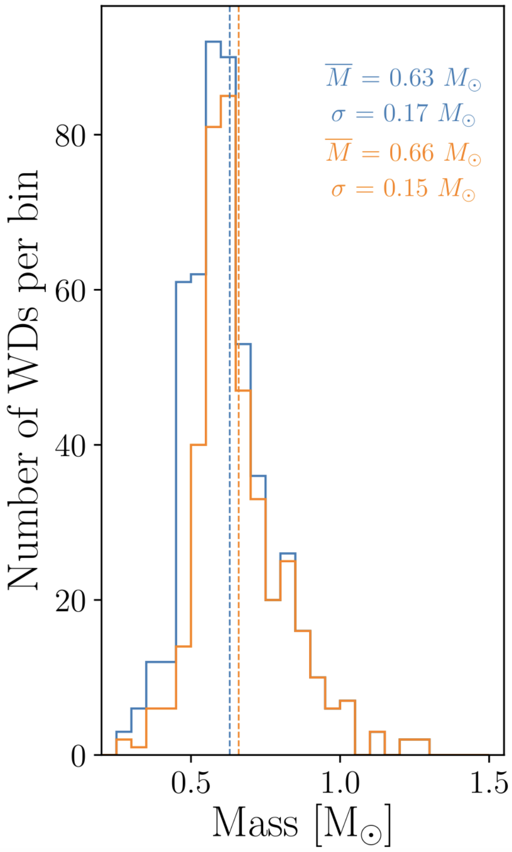

Figure 1.2: Mass distribution of the northern 40 pc sample (blue) with the reduced sample of objects with $T_{\text{eff}} > 5000\,\text{K}$ (orange). Figure and caption reproduced from McCleery et al. (2020).

maintains its stability as the star cools over time.

The mass of a white dwarf is related to its density (ρ) and radius (R_{WD}) by

$$M_{\mathrm{WD}} = \frac{4}{3}\pi\rho R_{\mathrm{WD}}^{3}, \tag{1.4}$$

therefore assuming constant density

$$\frac{M_{\mathrm{WD}}}{V_{\mathrm{WD}}} = \text{constant}, \tag{1.5}$$

where V_{WD} is the white dwarf volume. The mass-volume relation in Eq. 1.5 shows that the volume of a white dwarf is inversely proportional to its mass, thus the more massive a white dwarf (and higher gravitational pressure) the more densely the electrons are packed together resulting in a smaller volume. The Pauli exclusion principle states electrons cannot be infinitely packed together so a finite volume and thus mass must be reached. The maximum mass of a white dwarf allowed by EDP is $\approx 1.44\,\mathrm{M}_{\odot}$, known as the Chandrasekhar mass (Chandrasekhar, 1935).

If a remnant stellar core has mass exceeding $\approx 1.44\,\mathrm{M}_{\odot}$, electrons are forced into ever higher energy states which causes their velocities to near the speed of light. The configuration of electrons becomes unstable and can no longer provide enough pressure to counteract gravitational attraction. As a result, the stellar core collapses to form a Type Ia SNe, neutron star or black hole (depending on mass).

1.2.2 White dwarf evolution and cooling

The process of cooling in white dwarfs is relatively simple and therefore predictable. Accurately modelling this cooling process has been an endeavour for over 50 years because this predictable nature makes white dwarfs reliable cosmic chronometers, or cosmochronometers (Fontaine et al., 2001). These natural ‘clocks’ are important for many areas of astrophysics and cosmology, as they help estimate the age of stars, stellar regions like the Galactic halo, and the Universe itself. With the discovery of over $\approx 350\,000$ high-confidence white dwarf candidates (Gentile Fusillo et al., 2021) using data from the spacecraft *Gaia*, follow-up analysis found that white dwarf surface temperatures range from $3000 \lesssim T_{\mathrm{eff}} \lesssim 140\,000\,\mathrm{K}$.

With the absence of nuclear fusion in their cores, white dwarfs lose their supply of remnant thermal energy from their stellar evolution over timescales of the order of the age of the Universe. Energy is internally transferred through electron conduction, rather than radiation like in MS stars, and is an extremely efficient process due to the very high thermal conductivity of degenerate matter. White dwarf interiors are nearly isothermal, with the only significant temperature gradient occurring in the thin non-degenerate envelope. Energy is lost slowly through the radiative envelope as it inefficiently transfers heat out to space. Consequently, the luminosity of the white dwarf (i.e. energy emitted per unit time) decreases over time. Since luminosity is proportional to the square of the stellar radius (Eq.1.1), the small R_{WD} means their luminosity is intrinsically low, even at relatively high T_{eff}. Thus, white dwarf evolution can be described directly from their luminosity by a relatively simple cooling law (Mestel, 1952),

$$\tau \propto L^{-5/7}, \tag{1.6}$$

where τ is the cooling age of the white dwarf, i.e. time elapsed since the planetary nebula phase when the star became a white dwarf. The τ distinguishes between the total age of the star, which is the sum of the τ and MS lifetime. In this thesis, the MS lifetime of stars was determined using the initial-to-final-mass relation (IFMR) from Cummings et al. (2018).

The work of Mestel (1952) has been expanded over the last 70 years as the advancement of spectroscopy revealed more complicated processes that occur in white dwarfs. Crystallisation of white dwarf cores delays cooling for billions of years (see Section 1.2.3 for details). Convection zones (CVZs) develop in the surface layers of white dwarfs because of the steep temperature gradient between the core and envelope. As the star cools, the temperature gradient increases. When the CVZ grows large enough, it can couple the core to the surface layers, accelerating the cooling process (Fontaine et al., 2001). Additionally, this coupling can dredge-up material from the stellar interior, mixing atoms significantly enough to alter the observed spectral type (e.g. Koester et al., 1982; Pelletier et al., 1986; Cunningham et al., 2020). Work from Cunningham et al. (2019) and Cukanovaite et al. (2021) allowed the accurate 3D modelling of complex convective effects within white dwarfs to be included in computer models. Nowadays, sophisticated cooling sequences (Bédard et al., 2020) generated from detailed calculations of the evolution of the whole white dwarf is the modern way to estimate the white dwarf properties as a function of τ for a given mass.

1.2.3 Crystallisation

The interior degenerate electrons of white dwarfs with sufficiently high density undergo a phase transition where ions form a crystal lattice (Salpeter, 1961). This stage in white dwarf cooling is called crystallisation and effectively slows the rate of cooling for about one billion years by releasing latent heat (van Horn, 1968).

The onset of crystallisation is mass-dependent and occurs in white dwarfs with $6000 \lesssim T_{\mathrm{eff}} \lesssim 15\,000\,\mathrm{K}$. More massive white dwarfs ($\gtrsim 1.0\,\mathrm{M}_{\odot}$) start crystallising earlier (at higher T_{eff}) because their cores reach the required density and temperature sooner. Lower mass white dwarfs ($\lesssim 0.5\,\mathrm{M}_{\odot}$) start crystallising later since their cores are less dense, requiring them to cool to a lower T_{eff} before the core is sufficiently dense for crystallisation to start. Consequently, more massive white dwarfs crystallise for longer than lower mass white dwarfs.

Observational evidence of crystallisation was first seen over half a century after it was theoretically proposed. The HR diagram created from the second data release (DR) of *Gaia* showed a pile-up of cool stars on the cooling sequence (Tremblay et al., 2019a). Over the past few years, efforts have been made to incorporate crystallisation in white dwarf cooling models using updated input physics (Bédard et al., 2022; Venner et al., 2023) to give rise to more accurate models.

1.3 White dwarf spectral types and atmospheres

The interior of white dwarfs emit continuous photons of all wavelengths which resemble a blackbody spectral distribution. As this continuous stream of photons travel outwards from the interior, it encounters the white dwarf atmosphere. The outermost layers of white dwarfs, i.e. the photosphere, are essential in transmitting information about the chemical composition of the atmosphere because the interior photons interact with the atoms in the atmosphere, effectively making the core opaque. Some photons are able to escape from the white dwarf atmosphere entirely, travel through space and become incident on telescopes. Spectrographs are able to disperse the photons into component wavelengths and create a spectrum of flux vs. wavelength of the white dwarf atmosphere (see Section 2.1 for more details).

The photons emanating from white dwarfs are created or modified through various atomic interactions, including: electron transitions between energy states within excited atoms (bound-bound transitions); free electrons accelerated by ions (free-free emission) as any charged particle that accelerates or decelerates must emit radiation; or when free electrons are captured by ions and transition into bound energy levels of the ions, which releases the gained energy as photons (free-bound transitions). Each chemical element has its own unique energy states, therefore photons created from individual elements are analogous to chemical fingerprints at characteristic wavelengths (or frequencies). If a certain element is present in a white dwarf, at the characteristic wavelengths of that element there will either be a flux deficit called an absorption line or a flux excess called an emission line. A flux deficit

Table 1.1: White dwarf spectral types reproduced from Table 1 of McCook and Sion (1999a) and Table 11-1 of Koester (2013).

Spectral Type	Features
DA	Only Balmer lines; no He I or metals
DB	He I lines; no H or metals
DC	Continuous spectrum; no lines deeper than 5 % in any part of the spectrum[a]
DO	He II strong; He I or H
DZ	Metals lines only; no H or He lines
DQ	Carbon features, either atomic or molecular in any part of the spectrum
P	Magnetic with detectable polarisation
H	Magnetic with Zeeman splitting
X	Peculiar or unclassifiable
e	Emission lines
?	Uncertain assigned classification; a colon (:) may also be used
V	Optional symbol to denote variability

[a] In practice, this is no lines deeper than 3σ of the observed S/N.

occurs when atoms absorb photons at the specific wavelengths required to excite its electrons from a lower to a higher energy state, resulting in a reduction of the number of photons at those specific wavelengths that can escape the atmosphere and be detected by telescopes. A flux excess is created in the same way, except the excited electrons drop down energy states and emit photons at the specific wavelengths of the energy transition. Both absorption and emission lines are called spectral lines.

1.3.1 Spectral classification

White dwarfs are separated into spectral types based on their spectral lines. Sion et al. (1983) defined a spectral classification system which is still used in modern white dwarf studies, with a slight embellishment from Koester (2013), and is presented in Table 1.1.

All white dwarf spectral types start with the letter 'D', meaning degenerate object. The most common spectral type, comprising $\approx 75-80\%$ of the white dwarf population, is DA, which display only H absorption lines (e.g. Balmer lines) in the spectra. The next most common white dwarf spectral type is DB, which exhibit He I absorption lines in the spectra. DB white dwarfs comprise $\approx 10-15\%$ of the population. The four other main classes of white dwarfs, which comprise $\approx 5-10\%$

of the population, are: DC, where the continuum is devoid of spectral lines; DO, which have strong He II absorption lines; DZ, where only metal absorption lines are present; and DQ, which have atomic or molecular C absorption lines. It is not fully understood why some white dwarfs are depleted in H, but non-DA white dwarfs likely lost their H in a relatively late-occurring shell flash (see Section 1.2).

If a white dwarf exhibits features from multiple spectral classifications, additional letters can assigned to its spectral type in order of line dominance, e.g. DAB, DBA, DQA, DABZ. The more exotic white dwarfs with magnetic fields (P, H), peculiar or unclassifiable spectra (X), emission lines (e), uncertain assigned classification (?) or variability (V) have their letter classification appended to the main spectral type, e.g. DAe, DAHe, DZQH. Some white dwarfs with C features can display distorted C spectral lines, such as rounded profiles and shifted centroid wavelengths (Hall and Maxwell, 2008), which is conveyed through an appended 'pec'. If a white dwarf has a MS binary companion, then '+MS' is appended to the white dwarf classification. Figure 1.3 exhibits characteristic spectra of eighteen different white dwarf spectral types taken with SDSS.

Classifying white dwarfs may seem trivial, but sometimes it does not tell the whole story. For instance, DC white dwarfs do not exhibit any spectral lines but can still have H or He dominated atmospheres. In DA white dwarfs with $T_{\rm eff} \lesssim 6000\,{\rm K}$, there is insufficient thermal energy to excite the H atoms from the ground state ($n = 1$) to the $n = 2$ level in the optical, or a significant number of H atoms, thus H spectral lines are too weak to be detected and these would appear to have the spectral type DC. Similarly, DB white dwarfs with $T_{\rm eff} \lesssim 12\,000\,{\rm K}$ are unable to excite enough He to the $n = 2$ level in the optical for spectral lines to be apparent, thus they appear as DC white dwarfs. Therefore, cool DC white dwarfs with $6000 \lesssim T_{\rm eff} \lesssim 12\,000\,{\rm K}$ can have He-dominated atmospheres, and those with $T_{\rm eff} \lesssim 6000\,{\rm K}$ can have H- or He-dominated atmospheres. Strong magnetic fields in hot white dwarfs can lead to DC misclassifications, as the spectral lines may become so heavily distorted they merge into the continuum, resulting in an apparently featureless spectrum. Also, variable white dwarfs may only be identified if multiple spectra are taken over different epochs. The spectral classifications of white dwarfs are not fixed and are free to be updated upon inspection of new spectra taken with different or improved instruments.

1.3.2 Radiative and convective atmospheres

Energy is transported through the degenerate core of white dwarfs very easily, due to the extremely dense and almost isothermal conditions allowing electron conduction

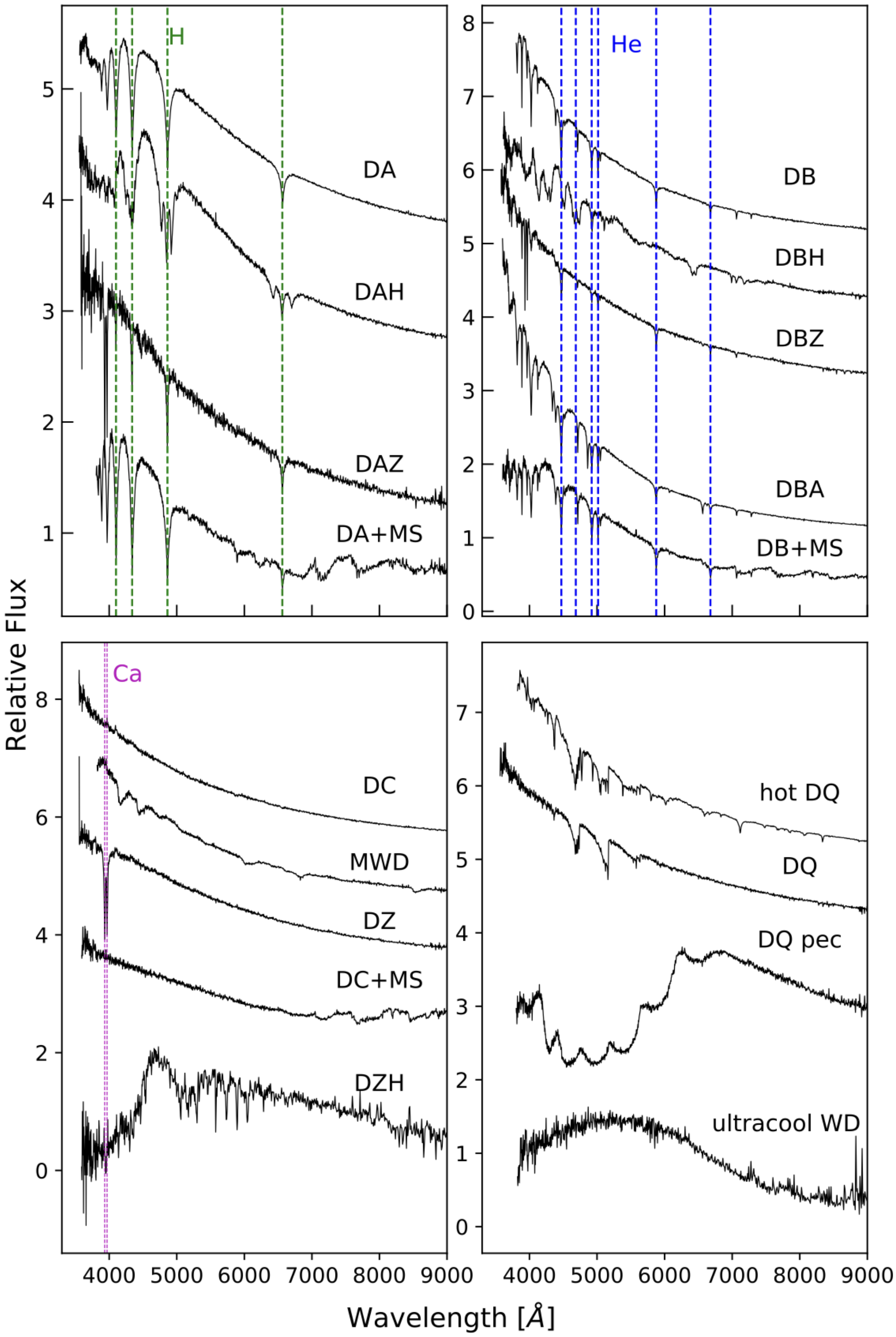

Figure 1.3: Representative SDSS spectral of the different white dwarf spectral types. The spectra have been offset vertically for visualization. Figure and captions have been reproduced from Gentile Fusillo et al. (2019).

to occur. However, the thin, non-degenerate envelope surrounding the core relies on radiative or convective transfer as it is significantly less dense and cooler than the core (Fontaine et al., 2001).

Radiative transfer occurs in the envelope as the photons produced in the core migrate to the outer layers and encounter a lower opacity environment. The mean time it takes for a photon to travel through the low-opacity envelope is much shorter than that of a high-opacity material because they encounter fewer absorption and emission interactions with atoms and ions, meaning they can radiate into space relatively efficiently. Opacity is dominated by four interactions: (i) *bound-free* absorption is when a bound electron in an atom or ion is freed by a sufficiently high energy absorbed photon; (ii) *bound-bound* absorption occurs when a photon is absorbed by an atom or ion but is not of a high enough energy to liberate an electron, only excites it to a higher energy level while still being bound to the nucleus; (iii) *free-free* absorption is when a free electron collides with an ion, absorbs a photon and resumes its free trajectory now at a higher energy; (iv) *scattering* interactions occur when photons collide with free electrons without being absorbed but result in an altered trajectory.

Young and hot white dwarfs have radiative transfer as the dominant energy mechanism, but over time the star cools and convective regions form in the outer layers of the envelope called CVZs. In these zones, convection causes hot material from lower layers - where $T_{\rm eff} \approx 10^5 - 10^6\,{\rm K}$, depending on the atmospheric composition - to rise and be homogeneously mixed with cooler material in the envelope. This warm material then sinks through the CVZ and the cycle starts again. CVZs will continuously grow in mass until the base of the zone extends to the degenerate core, which acts as a physical barrier. Convection cannot occur in degenerate material because it is too dense for the movement and mixing of material so electron conduction dominates as an energy transport mechanism. Since convection is highly efficient, it replaces radiative transfer as the primary transport mechanism whenever it becomes possible (Koester, 2013).

Convection is a relatively simple process, but can rapidly become complex to understand and model in some cases. For instance, magnetic fields may inhibit convective energy transfer in some magnetic white dwarfs, particularly at the surface (Tremblay et al., 2015b). Convection relies on the bulk movement of particles through temperature gradients, however the movement of charged particles in magnetic fields are constrained to magnetic field lines. This limits particle motion and causes suppression of convection, forcing slower radiative energy transfer to occur. DA white dwarfs with magnetic fields larger than $0.002-0.1\,{\rm MG}$ will have suppressed convection, resulting in a largely radiative temperature stratification (Gentile Fusillo et al., 2018; Cunningham et al., 2020). This can lead to white dwarfs with radiative and convective surface regions. In another instance, deep CVZs in cool white dwarfs can reach the C in the core and bring it up into the outer envelope, effectively self-polluting the otherwise pristine H and He atmosphere (Pelletier et al., 1986). This process is called C dredge-up and results in DQ spectral classifications. In white dwarfs with $T_{\text{eff}} \lesssim 6000\,\text{K}$, the dredged-up C can form C_2 molecules which produce molecular swan bands in spectra (Johnson, 1927).

1.3.3 Collision-induced absorption (CIA)

In addition to the interactions contributing to opacity discussed in Section 1.3.2, ultra-cool white dwarfs with $T_{\text{eff}} \lesssim 4000\,\text{K}$ have the dominant opacity source from collision-induced absorption (CIA) in the IR (Fig 1.4, Saumon et al., 2022). CIA is caused by molecular H (H_2) interactions between H, H_2 and He. In the ground state, H_2 molecules are symmetrical and have no electric dipole because they contain two electrons; due to the Pauli Exclusion Principle, one electron must be a spin-up and the other must be a spin-down (see Section 1.2.1 for details). To absorb a photon in the optical or IR, a dipole moment or electron spin quantum state change is required. Neither are satisfied by H_2 molecules therefore they are essentially transparent in the optical and IR. In the UV, which has much higher energies than the optical and IR, electrons can absorb photons and be excited to higher energy states so are not reliant on dipole moments nor spin quantum state changes.

Ultra-cool white dwarfs have extremely dense atmospheres ($\rho \gtrsim 0.1\,\text{g}\,\text{cm}^{-3}$, see Fig 1.5) which must be considered as a dense fluid rather than an ideal gas (Kowalski and Saumon, 2004; Kowalski, 2006, 2014; Blouin et al., 2017, 2018a), so frequent collisions occur between H_2 molecules and atmospheric particles. Collisions can distort the symmetry of H_2 molecules as they form H_2-H, H_2-H_2 and H_2-He pairs causing temporary electric dipole moments, allowing the absorption of optical and IR photons (Lenzuni et al., 1991; Frommhold, 1994; Jørgensen et al., 2000). This results in the suppression of red optical and IR flux, causing shifts in the peak of their spectral energy distributions (SEDs) to bluer wavelengths (Bergeron et al., 1994; Hansen, 1998; Blouin et al., 2017). The strength of CIA increases with decreasing T_{eff} because the atmospheric density increases and hence the frequency of collisions. Regardless of T_{eff}, white dwarfs with strong CIA opacity are designated as IR-faint (Kilic et al., 2020), as CIA suppresses infrared flux through interactions involving H_2. This results in the formation of a characteristic ultra-blue sequence on the HR diagram (See Figs 3.2 and 3.3), as the SEDs of these stars peak at bluer

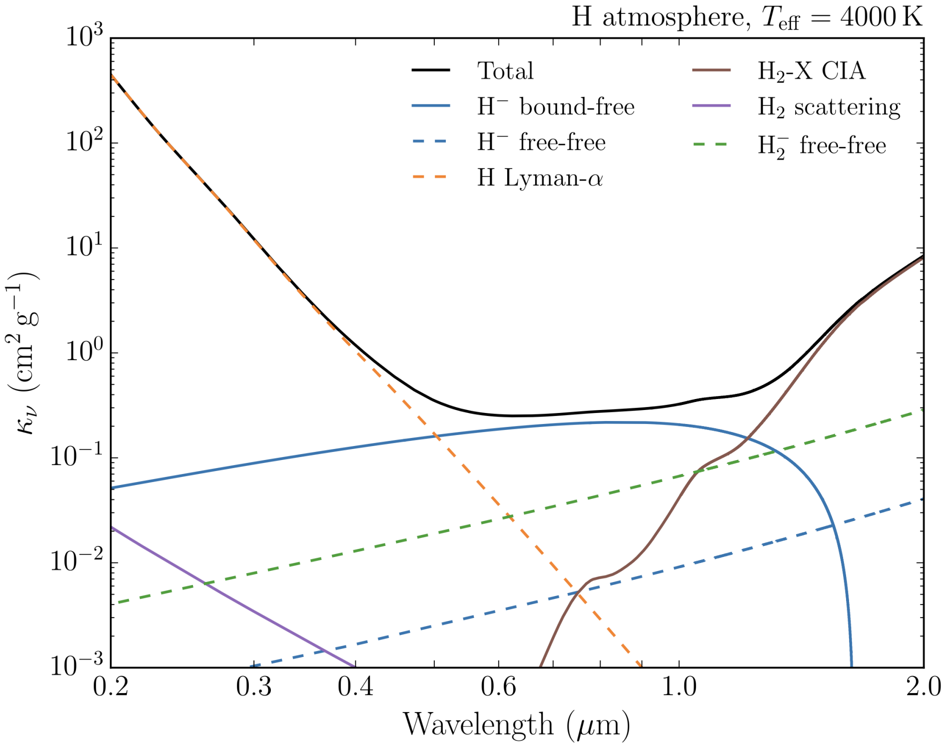

Figure 1.4: Dominant contributions to the radiative opacity of H-atmosphere white dwarfs. Shown is the wavelength-dependent opacity of a cool ($T_{\rm eff} = 4000\,$K) white dwarf, which would be classified as DC due to the absence of spectral lines. A surface gravity of $10^8\,{\rm cm\,s^{-2}}$ is assumed and the opacities are evaluated for the conditions at the photosphere. Figure and captions have been reproduced from Saumon et al. (2022).

wavelengths than expected.

At the extremely high densities of ultra-cool white dwarf atmospheres, CIA opacity undergoes strong pressure distortion which push the limits of well-understood dense fluid physics. Also, the frequent collisions of atmospheric particles causes the broadening of spectral lines. Therefore, it is imperative that CIA opacity must be taken into account in model atmospheres of cool white dwarfs, and its employment in the Koester (2010) model atmosphere code is discussed in Section 3.4. Warmer white dwarfs ($T_{\rm eff} \gtrsim 10\,000\,$K) have less-dense atmospheres therefore less frequent H_2 interactions occur, resulting in insufficient dipole moments and negligible CIA (i.e. red optical and IR absorption). Modelling the atmosphere of warmer white dwarfs is therefore much more simple with fewer uncertainties.

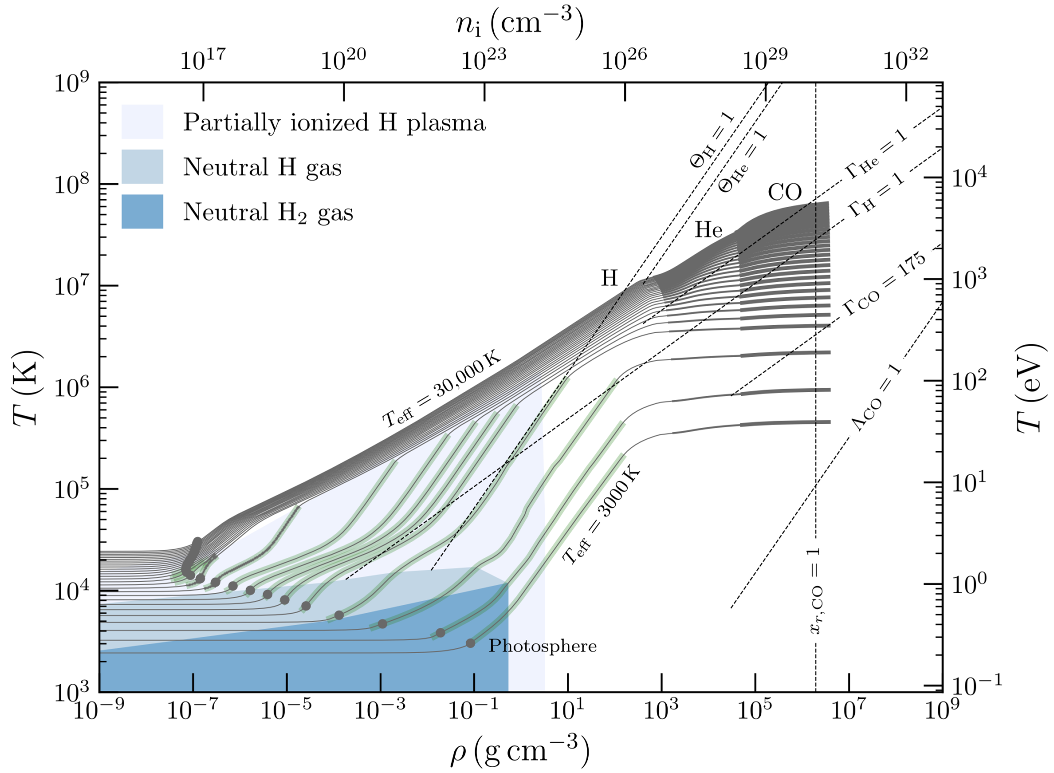

Figure 1.5: Density–temperature profiles of a cooling H-rich white dwarf model. Profiles from $T_\mathrm{eff} = 30\,000\,\mathrm{K}$ to $T_\mathrm{eff} = 3000\,\mathrm{K}$ in steps of $1000\,\mathrm{K}$ are shown. The cooling sequence runs from top to bottom. The thickness of the line indicates the dominant atomic constituent, and regions that are convectively unstable are highlighted in green. The different shadings of blue indicate where the gas is mostly composed of H_2, atomic H gas, or a partially ionized H plasma. The white background indicates a fully ionized plasma of C, O, He or H. Finally, the circles on each profile mark the location of the photosphere, and the dotted lines indicate the values of some important plasma parameters. In this log–log plot, the outer layers of the star are greatly expanded. The surface of the star is toward the left, the center is on the right. Figure and captions have been reproduced from Saumon et al. (2022).

1.3.4 Atmospheric models

White dwarf atmospheric models produce synthetic spectra which can be fit to observed spectra to determine key stellar parameters. This thesis uses a chi-square (χ^2) minimisation to fit models, as it provides a statistically robust way to quantify the difference between the observed data and the model. By minimising the sum of the squared residuals, weighted by the observational uncertainties, χ^2 minimisation identifies the set of model parameters that best reproduces the observed spectrum.

Pure-H models are available for modelling DA white dwarfs (Tremblay et al., 2011, 2013, 2015a) and He-rich models are available for modelling DB/DBA/DC white dwarfs (Cukanovaite et al., 2021). One-dimensional (1D) or three-dimensional (3D) models can be chosen, but 3D models would be the most realistic choice if the white dwarf is likely to have a convective atmosphere (Tremblay et al., 2013). If modelling a hot white dwarf with $T_{\rm eff} \gtrsim 40\,000\,{\rm K}$ then the model should include non-local thermal equilibrium (NLTE) effects (Hubeny and Lanz, 1995). For white dwarfs with $T_{\rm eff} \lesssim 40\,000\,{\rm K}$, LTE models are sufficient because the mean free photon path is much shorter than the distances over which the temperature and pressure in the atmosphere significantly change. This means photons move in a nearly uniform temperature and pressure environment, allowing the atmosphere to be treated as if it were in thermodynamic equilibrium locally at each point despite there being an overall gradient in temperature and pressure across the whole atmosphere. Therefore, local properties are well-approximated by the conditions of the atmosphere in the local vicinity which significantly decreases the complexity of calculating atmospheric models.

Once an appropriate model is chosen, it is fit to the observed data using reduced χ^2 minimisation. This only needs to be applied once for DA and DB white dwarfs, but for DZ white dwarfs an iterative procedure needs to be employed. Metal abundances can have a non-negligible effect on atmospheric parameters because of the additional free electrons, so iterations are required between the computation of synthetic spectra with the best-fitting atmospheric parameters, the fit of the metal spectral lines and the best-fitting photometry. Details of this process are given in Section 3.5.

The synthetic SED created from atmospheric models possess the best-fitting parameters which resemble the physical star to the best of its ability, including: $T_{\rm eff}$, $\log g$, $\log{\rm (H/He)}$, element abundances, magnetic field strength and radial velocity. The remainder of this section details these parameters.

Effective temperature ($T_{\rm eff}$) is the surface temperature of a star, equivalent to the temperature of a blackbody of the same radius as the star that would radiate the same amount of energy. Integrating over the flux density of an observed spectrum yields the total flux (f), which is the total power radiated per unit area of the stellar surface,

$$f = \sigma {T_{\mathrm{eff}}}^4, \tag{1.7}$$

thus allowing T_{eff} to be determined. If the absolute flux level is not known, then T_{eff} can determined from the shape of spectral lines as changes in electron density alters the width and depth of lines. For instance, at low $T_{\mathrm{eff}} \lesssim 9000\,\mathrm{K}$, Balmer lines are weak as most H atoms are in the ground state ($n = 1$); at $10\,000 \lesssim T_{\mathrm{eff}} \lesssim 13\,000\,\mathrm{K}$, Balmer lines reach maximum strength as lots of H atoms are able to reach $n = 2$; then at high $T_{\mathrm{eff}} \gtrsim 13\,000\,\mathrm{K}$, Balmer lines weaken as H atoms become ionised. Equation 1.7 is another form of the Stefan-Boltzmann law shown in Equation 1.1, so once T_{eff} has been determined so can R. Using a mass-radius (M-R) relation created from model evolutionary sequences (Bédard et al., 2020), the M_{WD} and τ can also be found. Work in this thesis employs the M-R relation with C/O cores and either thick ($q_{\mathrm{H}} = M_{\mathrm{H}}/M_{\mathrm{WD}} = 10^{-4}$, where M_{H} is the hydrogen mass) or thin ($q_{\mathrm{H}} = 10^{-10}$) H layers. Thick H layers are normally employed for DA white dwarfs based on theories of post-AGB evolution and the maximum H mass for residual nuclear burning (Iben and Tutukov, 1984; Althaus et al., 2010b). Alternatively, thin H layers are normally employed for He-dominated atmosphere white dwarfs (DB, DC, DQ, DZ). However, exclusively using thick H-layers for DA and thin H-layers for non-DA white dwarfs is not a strict rule - studies have shown evidence for thin H-layers in DA white dwarfs (Fontaine and Wesemael, 1987, 1997; Miller Bertolami et al., 2017; Bond et al., 2017; Cunningham et al., 2020) so it is best to test using both where possible.

Surface gravity ($\log g$) is the logarithm of the white dwarf's gravitational acceleration, expressed in units of cm/s^2. $\log g$ has a subtler impact on observed spectra than T_{eff}, mainly affecting the width of the line profiles. A greater $\log g$ means a denser atmosphere and higher atmospheric pressure, which visually results in wider and shallower spectral lines from an effect called pressure broadening. Similarly to T_{eff}, if $\log g$ is known then the white dwarf R and M_{WD} can be found through a M-R relation (Bédard et al., 2020) and the equation

$$g = \frac{GM_{\mathrm{WD}}}{R^2}, \tag{1.8}$$

where G is the gravitational constant.

Hydrogen to helium abundance $\log(\mathrm{H/He})$ is the logarithm of fractional

H to He abundance in the white dwarf atmosphere. The larger log (H/He), the more H-rich the atmosphere. The smaller log (H/He), the more He-rich the atmosphere.

Element abundances are measured using the depth of spectral lines present in spectra. Individual elements have characteristic wavelengths (frequencies) so are simple to identify and model (see Section 1.3 for more details). The presence of certain spectral lines allows spectral types to be assigned to observed white dwarfs (Section 1.3.1). The atmospheric composition of a white dwarf can be determined by comparing measured elemental abundances with model spectra. If metals are detected, they provide evidence of accreted planetary material.

Magnetic field strength (B) can be measured through the Zeeman splitting of spectral lines or polarisation, provided the spectrum has both a sufficiently high S/N and adequate spectral resolution. More details are provided in Section 1.5.

Radial velocity ($v_{\rm rad}$) is the motion of a white dwarf along the line of sight. This is calculated by first measuring the shift in spectral line wavelengths relative to their known rest (laboratory) values to yield the total line velocity,

$$v_{\rm line} = \frac{\Delta\lambda}{\lambda} c, \tag{1.9}$$

where $\Delta\lambda$ is the difference between observed and rest wavelengths, λ is the rest wavelength and c is the speed of light. In white dwarfs, $v_{\rm line}$ is comprised of $v_{\rm rad}$ and gravitational redshift ($z_{\rm grav}$). The contribution by $z_{\rm grav}$ is a consequence of General Relativity as the strong gravitational field around white dwarfs forces photons to use more energy to escape the heavily warped spacetime than if they were traveling across flat spacetime, thus when the photons reach Earth they are at a lower energy (redder wavelength) than when originally emitted. A photon escaping a white dwarf has

$$z_{\rm grav} = \frac{GM_{\rm WD}}{Rc^2}, \tag{1.10}$$

so if the white dwarf $T_{\rm eff}$ and $\log g$ is known, $M_{\rm WD}$ and R can be derived and thus $z_{\rm grav}$. Both $v_{\rm line}$ and $z_{\rm grav}$ have units of $\rm km\,s^{-1}$ so correcting for $z_{\rm grav}$ yields the radial velocity,

$$v_{\rm rad} = v_{\rm line} - z_{\rm grav}. \tag{1.11}$$

1.3.5 Photometric parameters

White dwarf photometric parameters can be computed by integrating under a model SED for the desired survey bandpass. The appropriate filter transmission function must be used in the calculation, which can be found from e.g. the Spanish Virtual Observatory (SVO) Filter Profile Service (Rodrigo et al., 2012). Details on this process can be found in Section 5.3.2. The computation yields the best-fitting absolute magnitudes, $T_{\rm eff}$, $\log g$ and $M_{\rm WD}$ (Tremblay et al., 2011; Cukanovaite et al., 2021; Bédard et al., 2020). Surveys used in this thesis include: *Gaia* (Vega system); Pan-STARRS (AB system); SDSS (AB system); Two Micron All-Sky Survey (2MASS; Vega system); and Wide-field Infrared Survey Explorer (WISE; Vega system). Descriptions of the different magnitude systems are in Section 2.2.

Grids of photometric models which have been created using the above computations from pure-H, pure-He, or mixed H/He models are publically available from Pier-Emmanuel Tremblay's webpage section 'Derived data: Photometric absolute magnitudes (colours)'.

1.3.6 Diffusion time-scales

Model atmospheres which include metals must account for the different diffusion time-scales ($\tau_{\rm z}$) of individual elements due to gravitational settling. Metals, which have a higher atomic mass ($Z > 2$) than the H and He naturally present in white dwarf atmospheres, diffuse (sink) through the atmosphere depending on Z on short timescales relative to white dwarf cooling ages (Koester, 2009). Thus, a stratification occurs by atomic weight. The type of atmosphere (DA vs. non-DA) and the $T_{\rm eff}$ of the white dwarf also affects $\tau_{\rm z}$ (Paquette et al., 1986; Koester, 2009; Wyatt et al., 2014, see Fig. 1.6). In general, non-DA white dwarfs have longer $\tau_{\rm z}$ due to their denser He-dominated atmospheres. Additionally, $\tau_{\rm z}$ increases with decreasing $T_{\rm eff}$, as cooler white dwarfs have deeper and more massive CVZs that slow the diffusion of heavy elements. Within these CVZs, accreted material is efficiently mixed and remains suspended until it slowly diffuses out through the base of the convective layer into deeper, unobservable regions. This convective mixing significantly prolongs the time metals remain visible in the atmosphere compared to purely radiative white dwarfs.

In general, the higher the atomic mass, the quicker the element diffuses. The $T_{\rm eff}$, $\log g$ and $\log{\rm (H/He)}$ of the white dwarf also impacts the diffusion, therefore envelope codes which input these parameters must be used to compute the actual $\tau_{\rm z}$ of individual elements in each star (Koester et al., 2020). Envelope codes also compute the CVZ mass ($M_{\rm cvz}$), mass of hydrogen in the CVZ ($M_{\rm H}$), and the individual metal masses ($M_{\rm z}$) currently contained in the CVZ which summed together results in a lower limit of the accreted parent body mass ($M_{\rm z,tot}$). More details can be found in Section 3.7.5.

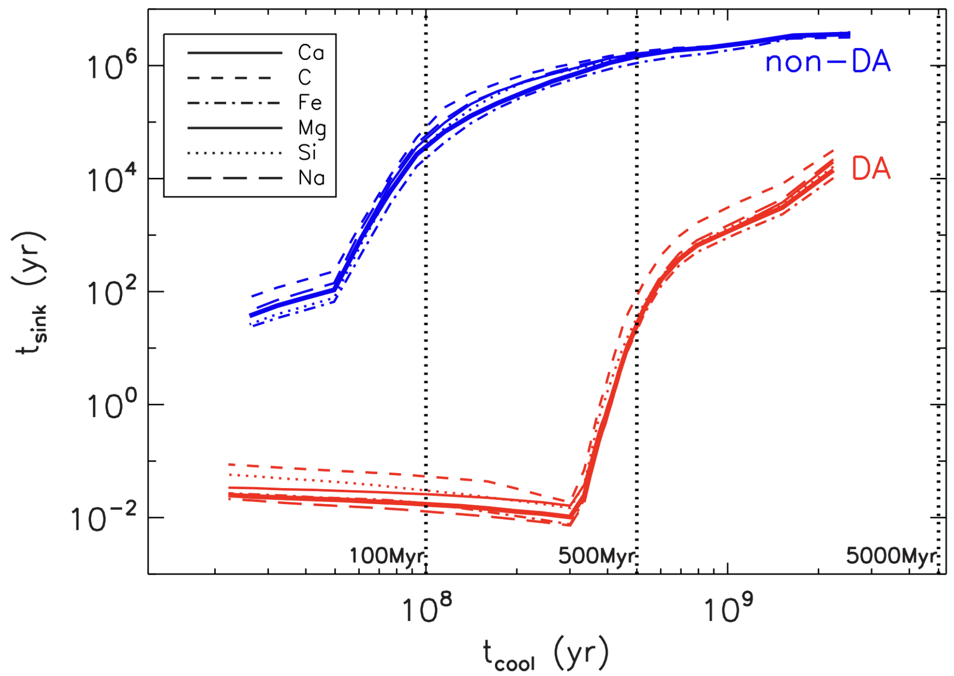

Figure 1.6: Sinking time-scales due to gravitational settling at the base of the convection zone of six different metals (shown with different line-styles as indicated in the legend) as a function of the star's cooling age (from tables 4 – 6 of Koester (2009)) both for DA white dwarfs (i.e., those with H-dominated atmospheres, shown in red) and for non-DA white dwarfs (i.e., those with He-dominated atmospheres, shown in blue). Figure and caption have been reproduced from Wyatt et al. (2014).

1.4 Metal-polluted white dwarfs

1.4.1 Planetary systems around white dwarfs

The DZ spectral class represents white dwarfs that exhibit metal spectral lines. From stellar evolution, white dwarfs should only have H and He present in their atmospheres but observations reveal $25 - 50\,\%$ of white dwarfs are polluted with metals (Zuckerman et al., 2003, 2010; Koester et al., 2014). How did metals end up in the atmospheres of these white dwarfs?

The former question has been pondered for decades, ever since the first evidence of metals was discovered in the spectrum of the white dwarf vMa2 (van Maanen, 1917) and the first spectral analysis was performed on it (Weidemann, 1960). The origin of metal-pollution was not well understood in the 20th century, with vMa2 first classified as an F-type star due to the prominent Ca H+K absorption lines. Nowadays these lines are accepted as the first observational evidence of an extrasolar planetary system (Fig. 1.7, Zuckerman, 2015; Farihi, 2016).

Extensive spectroscopic research into the origin of metals in DZ white dwarfs has been conducted over the past two decades, with the field being revolutionised by high-resolution space- and ground-based spectrographs (e.g. Dickinson et al., 2012). It is now widely accepted that metals in white dwarfs are not left-over from their progenitors nor originate from the interstellar medium, but rather they originate from external planetary bodies and arrived after the white dwarf formed (e.g. Jura, 2003; Zuckerman et al., 2003, 2010; Farihi et al., 2010).

As stars evolve along the RGB, they increase in radius but lose a significant fraction of their mass (Pols et al., 1998; Marigo et al., 2020). For instance, $\approx 1\mathrm{M}_{\odot}$ stars lose $\approx 50\,\%$ of their mass, whereas larger stars of $\approx 2 - 3\mathrm{M}_{\odot}$ may lose a higher fraction of mass. As a result, any planetary system around the star gets significantly disturbed. Any planets relatively close to the star will be engulfed, while further away planets will be pushed out to larger orbits (Burleigh et al., 2002). Sufficiency distant planets will be able to remain intact and orbit the white dwarf, e.g. WD 0806−661 B (Luhman et al., 2011). Planetesimals on orbits close to the Roche radius of the white dwarf can be perturbed onto eccentric orbits from the strong gravitational force exerted by the host star (Veras et al., 2014). However, if a planetesimal enters the Roche radius it will be tidally disrupted and ripped apart into dust, gas and/or even smaller rocky planetesimals. This planetary debris orbits the white dwarf as a dust or gas disc while steadily accreting (e.g. Gänsicke et al., 2016; Veras et al., 2017). Rocky planets which partially survived the final evolutionary stages of their host star can be guilty of polluting white dwarf atmospheres (e.g.

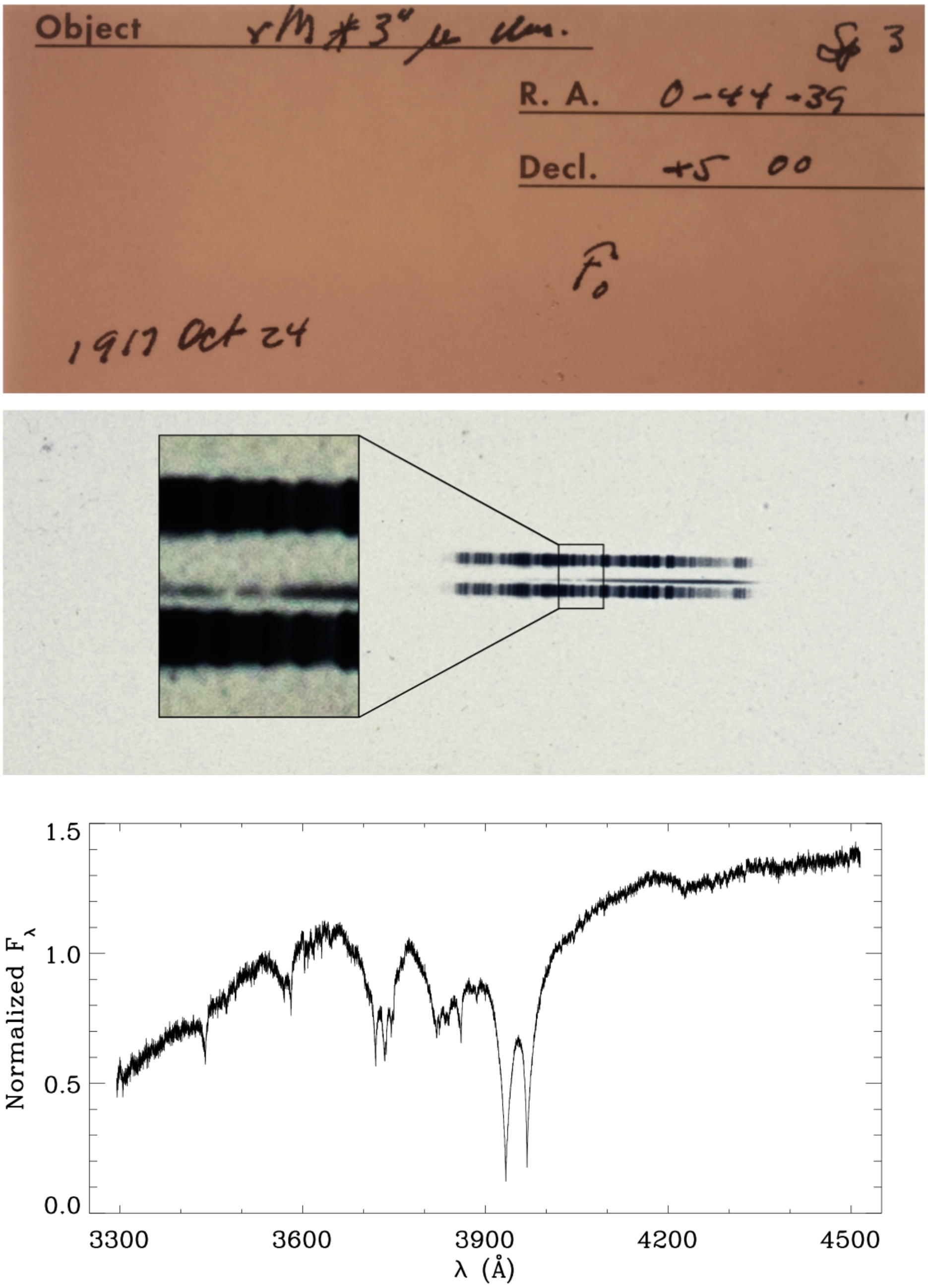

Figure 1.7: The prototype metal-polluted white dwarf vMa2. Upper panels: The 1917 photographic plate spectrum of vMa2, and plate sleeve with handwritten notes by observer W. S. Adams (van Maanen, 1917). Box highlighted are the strong Ca II H+K absorption lines, and are relatively easy to see in the century old spectrum. Lower panel: An optical spectrum of vMa2 taken with the Ultraviolet and Visual Echelle Spectrograph (UVES) on the Very Large Telescope (VLT). All salient features are absorption due to Fe, Mg, or Ca. Figure and caption have been reproduced from Farihi (2016).

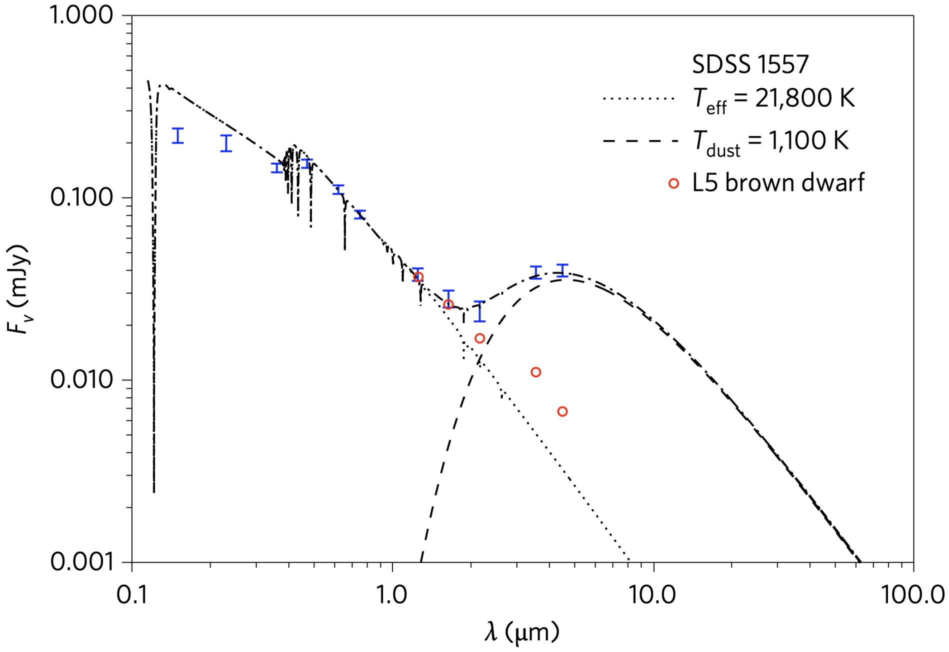

Figure 1.8: Spectral energy distribution. Previously reported multi-wavelength photometric data for SDSS 1557 are plotted as blue error bars, with the stellar flux from a pure hydrogen atmospheric model is shown as a dotted line. Over-plotted as a dashed line is an 1100 K blackbody fitted to the strong, infrared dust emission, and an L5-type brown dwarf is shown as red circles. The dashed-dotted line is the sum of the stellar model and the dust blackbody, modelling the total observed flux. The measured 4.5 μm flux from the system is between 5 and 6 times brighter than any allowed companion, and hence must be due to circumstellar dust. Figure and caption have been reproduced from Farihi et al. (2017).

Graham et al., 1990; Gänsicke et al., 2012; Veras et al., 2014), but tidally captured asteroids or comets are capable of accreting and polluting white dwarf atmospheres too (e.g. Frewen and Hansen, 2014; Mustill et al., 2018; Veras, 2016).

Evidence of accretion comes in the form of metal lines in the spectra of white dwarfs, whereas evidence of dust or gas (circumstellar debris) discs presents itself as an excess of IR emission in the stellar spectrum (Fig. 1.8; e.g. Becklin et al., 2005; Kilic et al., 2005; Farihi et al., 2017). The chemical composition of the accreted rocky body can be deduced by the depth of spectral lines pertaining to metal abundances. However, due to gravitational settling, the heaviest elements diffuse through the CVZ the quickest, resulting in the observed abundances not necessarily being comparable with the originally accreted parent body. Diffusion time-scales allow us to reverse gravitational settling and look back in time to what the atmospheric composition of the white dwarf would have been a certain amount of time ago. Therefore, more accurate estimates of the chemical composition of the parent body can be deduced (see Section 1.4.2).

1.4.2 Composition of accreted planetesimals

The accretion of rocky planetesimals on the pristine H/He atmospheres of white dwarfs provides excellent opportunities to probe the composition of old planetary systems. However, because of the relatively short τ_{z} dependent on Z, composition of the atmosphere and T_{eff} (see Section 1.3.6), the spectroscopically observable metals must have been recently accreted or are still being actively accreted (Vauclair et al., 1979). Actively accreting white dwarfs should have evidence of a circumstellar debris disc (see Section 1.4.1). If evidence of a disc is not found, then it is commonly assumed that the white dwarf stopped accreting relatively recently and we are observing debris retained from the event.

Accretion episodes are typically described as three simplified phases (Koester, 2009). (i) The *increasing state*, where material is actively accreted onto the white dwarf photosphere. The mass of accreted material gradually increases and the atmospheric composition of the white dwarf resembles that of planetary debris. Material starts to diffuse through the atmosphere or is instantaneously mixed throughout the CVZ if present, then the composition diverges as metals diffuse at their individual τ_{z} through to the core. (ii) *Steady-state*, or accretion-diffusion equilibrium, is reached when the rate of accretion balances the rate at which metals diffuse out of the observable atmosphere. This balance occurs when the duration of the accretion event extends over several τ_{z}. (iii) The *decreasing state*, where accretion stops due to all of the planetary debris being accreted. The white dwarf atmospheric abundances exponentially decrease according to the individual τ_{z} of each metal as they diffuse toward the core, resulting in the observable composition not necessarily resembling the exact original parent body chemical composition. The atmospheric chemical abundance analysis in this thesis assumes that DZ white dwarfs are in the decreasing state.

To determine the composition of accreted planetesimals, absolute abundances are measured from the white dwarf spectra then converted into relative abundances using abundance ratios, e.g. log (Ca/Na), log (Li/Na), log (K/Na). The relative abundances of two ratios evolve as

$$\frac{\left(\frac{1}{\tau_{\mathrm{z}_1}} - \frac{1}{\tau_{\mathrm{z}_2}}\right)}{\left(\frac{1}{\tau_{\mathrm{z}_3}} - \frac{1}{\tau_{\mathrm{z}_2}}\right)}, \tag{1.12}$$

which computes the diffusion time-scale slopes in Figure 3.12. The abundance ratios of the white dwarf atmosphere can be compared to other DZ white dwarfs and/or solar system benchmarks such as bulk Earth (McDonough, 2000), the continental crust (Rudnick and Gao, 2003), CI chondrites (Lodders, 2003) and solar abundances (Lodders, 2003). This indicates whether the accreted debris was similar in composition to accreted material on other white dwarfs, known astronomical bodies, or something new and exotic. It also indicates whether the accreted planetesimal was geologically differentiated or not, thus it must have been a relatively large (Earth-sized) planet, minor planet or moon. When a body differentiates, siderophile (Fe-loving) elements (e.g. Fe, Co, Ni) sink into the core because they readily metallically bond with iron, whereas lithophile (silicate-loving) elements (e.g. Li, O, Na, Mg, Al, Si, K, Ca) settle in the crust as they are rock-forming minerals which readily bond with oxygen.

A bulk Earth composition suggests a whole rocky body similar to Earth accreted onto a white dwarf, including a mixture of core-mantle-crust elements dominated by O, Mg, Si and Fe with traces of other metals such as Al, Ca and Ni. It is not possible to establish whether multiple planetesimals from different parent bodies accreted onto a white dwarf or only one large parent body accreted, but an educated assumption can be made that the composition created by many small planetesimals would average out to something similar to bulk Earth. Although, the accretion of one undifferentiated parent body could also have a composition similar to bulk Earth, so caution has to be taken when identifying parent bodies. If a continental crust composition is evidenced by Fe-poor yet Al-, K- and Ca-rich material (Melis and Dufour, 2017) then the accreted debris must have originated from a crust–mantle differentiated body like the Earth. White dwarfs could also accrete a fragment of a planetary continental crust, which could e.g. be relatively Li-rich compared to other elements and therefore present a Li-rich white dwarf atmospheric composition (see Section 3.7.5). Alternatively, a CI chondrite abundance indicates a primitive and undifferentiated accreted body within the carbonaceous chondrite family, which have elements similar to rocky Earth-like material but in slightly different ratios, i.e. Li/Ca and K/Ca are elevated in the crust compared to CI chondrites, in addition to CI chondrites being more Fe-poor. An analysis of the composition of accreted planetesimals in cool DZ white dwarfs compared to solar system benchmarks is done in Section 3.7.5.

1.5 Magnetic white dwarfs

An intriguing subclass of white dwarfs is the magnetic white dwarf (spectral type 'H'). The strengths of magnetic fields in white dwarfs are typically quantified by their surface magnetic field strength, which ranges from tens of kG to hundreds of MG (Schmidt et al., 2003; Bagnulo and Landstreet, 2021). These fields can inhibit surface convective energy transfer, thus influencing the stellar evolution and atmospheric structure of the star (Tremblay et al., 2015b; Cunningham et al., 2020). Furthermore, the analysis of accreted planetary material could lead to erroneous interpretations of parent bodies due to inhibited convective mixing (Cunningham et al., 2021).

More than 20 % of white dwarfs in the local volume-limited 20 pc sample host a detectable magnetic field (Bagnulo and Landstreet, 2021), therefore a comprehensive understanding of them is crucial. Large spectroscopic surveys, such as SDSS and DESI, have the accurate determination of magnetic fields on white dwarf atmospheres and atoms as a key objective. White dwarfs offer unparalleled potential for probing atomic effects under strong magnetic fields, as they can harbor magnetic fields significently stronger than those artificially generated on Earth. Although other astronomical objects, such as neutron stars, exhibit larger magnetic field strengths, white dwarfs are much simpler to study with atmospheric spectroscopy. Furthermore, white dwarfs are much more abundant than neutron stars, enhancing their value as natural laboratories for magnetic phenomena.

1.5.1 Origin of white dwarf magnetism

The origin of magnetic fields in isolated white dwarfs remains a challenging problem in astrophysics (Ferrario et al., 2015). There are four main scenarios to explain magnetic white dwarfs, but none are fully understood nor proven to be conclusive. It is possible that all scenarios contribute to the observed population of magnetic white dwarfs. The four scenarios are as follows:

1. **Fossil fields and MS/giant magnetic fields** are remnant magnetic fields of the white dwarf progenitor (i.e. pre-MS, MS, giant phase). The relatively low (less than tens of kG) magnetic fields in pre-MS or MS stars could have been amplified due to contraction of the core and changes in stellar flux during stellar evolution, then got trapped in the non-convective core regions of the star and released upon the evolution into a white dwarf (Landstreet, 1967; Angel et al., 1981; Braithwaite and Spruit, 2004; Tout et al., 2004; Wickramasinghe

and Ferrario, 2005). This scenario could potentially explain fields up to a few MG, but stronger fields are harder to exclusively explain with this scenario.

2. **Interior dynamo in a binary system** generated within the interior of the white dwarf in the post-common envelope phase with a MS star (Tout et al., 2004, 2008; Briggs et al., 2018; Belloni and Schreiber, 2020) or during a WD-WD merger to become a single star (García-Berro et al., 2012). In this scenario, the white dwarf has interacted in a binary resulting in the rapid movement of charged particles. This scenario could explain magnetic white dwarfs with a mass higher than average mass ($\gtrsim 0.6\,\mathrm{M}_\odot$, see Section 1.2.1).
3. **Crystallisation-induced global dynamo** driven by white dwarf core crystallisation (van Horn, 1968; Isern et al., 2017; Schreiber et al., 2021b,a; Ginzburg et al., 2022; Fuentes et al., 2023). Cool white dwarfs undergo a crystallisation phase (see Section 1.2.3) which combined with the white dwarf's rotation, has been predicted to sustain a global convective magnetic dynamo. As the onset of core crystallisation occurs at a specific evolutionary stage (cooling age), with dependencies on white dwarf mass and core chemical composition, this could be the scenario to explain magnetism in DA(H)e stars (see Chapter 4). Bagnulo and Landstreet (2021) found that in the 20 pc sample the occurrence of magnetism is higher in white dwarfs that have undergone core crystallisation than those with fully liquid cores. This analysis was expanded to the volume-limited 40 pc sample in Bagnulo and Landstreet (2022) where the incidence of magnetism in young (non-crystallized) white dwarfs was found to be $\approx 10\,\%$, whereas it increased to $\approx 30\,\%$ for old (crystallized) white dwarfs.
4. **Unipolar inductor model** which considers the induction of an electric current from the close-in orbit of a rocky planet, or at least a planet core, through the surface of the white dwarf (Goldreich and Lynden-Bell, 1969; Li et al., 1998; Wickramasinghe et al., 2010; Gänsicke et al., 2020; Reding et al., 2020; Walters et al., 2021). In this model, the white dwarf has to already have a magnetic field (though it may be weak), and the rocky body either survived the post-MS evolution and thus be native to the white dwarf system or it could be a product from a metal-rich debris disc left over from a WD-WD merger (García-Berro et al., 2007). The constant periodic motion of the orbiting planet generates an electric current loop between the two bodies, which can amplify the white dwarf's magnetic field to tens or hundreds of MG.

1.5.2 Measurement of white dwarf magnetic fields

Two primary techniques are used to detect and measure magnetic fields in white dwarfs. The first technique is to observe spectral line splitting due to the Zeeman effect (Angel et al., 1974; Jordan et al., 2007; Schmidt et al., 1999; Kawka et al., 2011). We can detect the Zeeman effect in white dwarfs with field strengths $\gtrsim 1\,\mathrm{MG}$, since at these strengths the field interacts strongly enough with the magnetic moments of the electrons to alter their energy levels at an observationally detectable level, depending on instrument resolution and S/N. The emitted photons are therefore at slightly higher and lower energies than expected. The observed spectral line is typically split into three components: one unshifted line at the original atomic wavelength; and two shifted lines, one at a slightly shorter wavelength (higher energy) and one at a slightly longer wavelength (lower energy). The amount of Zeeman splitting depends on the strength of the magnetic field, where stronger fields cause greater splitting, and the particular atom (i.e. electron energy levels) involved.

The second technique is spectropolarimetry. This is employed to detect fields with strengths $\approx 1\,\mathrm{kG} - 1\,\mathrm{MG}$ (Kawka et al., 2007), as these are too weak to observationally detect the Zeeman effect. Spectropolarimetry combines spectroscopy and polarimetry to measure the circular polarisation of light (e.g. Stokes parameters for the circular polarisation (V) and total intensity of light (I)) caused by a weak magnetic field as a function of wavelength (e.g. Landstreet and Angel, 1975; Friedrich et al., 1996; Vornanen et al., 2013). This produces the mean longitudinal field ($\langle B_z \rangle$), which is the average magnetic field strength along the line of sight. The magnetic field strength could differ from the measured $\langle B_z \rangle$ at other points on the white dwarf surface, so time-series spectropolarimetric observations over the white dwarf spin period give a more complete geometry and measure of the field strength. A non-zero $\langle B_z \rangle$ is a positive sign that the observed white dwarf has a magnetic field, even if it is too weak to be observed with Zeeman splitting.

Magnetic fields in white dwarfs can be challenging to detect. Observations need to have sufficiently high S/N so that Zeeman split spectral lines can be distinguished from the noise. The magnetic field must be strong enough to cause the Zeeman effect, otherwise spectropolarimetry must be used to determine the magnetic nature of the star. White dwarfs with dense atmospheres, such as ultra-cool white dwarfs, have significant broadening of spectral lines, which can mask the Zeeman effect and small polarisation signals. The magnetic fields in white dwarfs can have complex geometries, with variations in field strength at different locations causing erroneous conclusions to be drawn about the magnetic nature of white dwarfs depending on their orientation at the time of observation. To get a complete understanding of the white dwarf magnetic field, complete time-series spectropolarimetry needs to be taken over the spin period; however, this is impractical in terms of observational and analysis time. Faint white dwarfs, whether they are cool, old or at large distances from Earth, have weaker observed spectral lines and less photons incident on spectropolarimetric instruments, resulting in no field detections. Next-generation high-resolution instruments and large-scale surveys will help to minimise some of the above challenges.

1.6 Absolute flux calibration

Observational astrophysics relies on flux calibrator (standard) stars for the accurate absolute flux calibration of observed spectra. Absolute flux calibrators are stars whose flux and uncertainties are defined in relation to the International System of Units[1] (SI) so they have SI-traceability (Bohlin, 2014; Gordon et al., 2022), i.e. they are measured in physical units of energy per unit time per unit area per unit wavelength (or frequency). Absolute flux calibration pertains to how close the electron counts per second per pixel off the charge-coupled device (CCD) in the telescope are to the real physical flux value in SI units. Relative flux calibration refers to whether observations of the same star observed on different parts of the sky or with different telescopes/instruments would result in consistent measurements of electron counts per second per pixel as a function of wavelength (Narayan et al., 2019; Axelrod et al., 2023).

There are two categories of absolute flux standards: primary, which any stable star can be; and secondary, whose fluxes are calibrated from the primary standard(s). Secondary standards can be fainter and redder than primary standards resulting in slightly more uncertain fluxes, but they are more numerous and can be observed more frequently across different telescopes and instruments, improving calibration in various conditions. Their increased availability enhances sky coverage and enables broader application across observing programs, facilitating cross-mission calibration as well as inter-calibration between surveys, instruments, and telescopes.

Even though any stable star could be a primary flux calibrator, this does not mean that all are suitable. Primary, and to the best extent possible, secondary flux calibrators must satisfy certain conditions. Good absolute flux calibrator stars should have SEDs as close to a blackbody as possible, thus candidates are carefully chosen based off criteria of which most should be satisfied (Gordon et al., 2022). They must be a single star or in a binary which is wide enough that the two stars'

---

[1] SI base units are the kilogram, meter, second, ampere, kelvin, candela and mole.

spectra do not mix. The star must be of a spectral type which is simple to model, i.e. DA white dwarf or hot MS star such as A- and G-stars, as these have minimal spectral lines and their atmospheric structures are driven by radiative transport. Also, G-stars (like the Sun) can be empirically calibrated with solar analogues and have well-studied properties. F-type stars are less commonly used as calibrators because their spectra are more complex, with significant UV and optical line blanketing and convective layers that are harder to model (Bohlin et al., 2014). The star should not have a circumstellar disc of gas or dust, nor should be significantly photometrically variable ($< 0.25\,\%$) or rapidly rotating. Finally, the star should have low interstellar dust extinction ($E(B-V) \approx 0$) along the line of sight which is well-modelled.

Flux calibrators are employed in the data reduction process once a spectrum of a target has been taken. When a target is observed, the emitted photons are incident on the CCD in the telescope. The photons liberate electrons in the pixels of the CCD which are arranged in a grid. The amount of electrons in each pixel are counted and moved to the readout register, where the charge is converted to a voltage. The voltage passes through an analogue-to-digital converter so the target image can be reconstructed on a computer. Spectrographs utilise telescope CCDs, but first split the photons from the target into individual wavelengths.

A spectrum is a measure of the flux per unit wavelength of an object. Raw spectra, i.e. electron counts per second per pixel straight off a telescope's CCD, are not accurate representations of the observed target because the incident photons will have been influenced by a combination of different effects from the atmosphere, telescope, instrument(s) and detector before being output as a signal. These effects pose challenges in determining the true photons emitted from the target. For instance, telescope and spectrograph optics can affect the efficiency of photon absorption at different wavelengths due to: shutter timing accuracy; contamination from e.g. dust or finger grease; outgassing of instruments or detectors when transitioning to a vacuum environment (Jiao et al., 2019); system non-linearities in e.g. the detector, electronics and analogue-to-digital converter; temporal instabilities in the telescope/instrument coatings; and thermal sensitivities in the quantum efficiency and signal chain. Ground-based observations have additional challenges as variable atmospheric transmissions have to be accounted for, which could be caused by water vapor, aerosols, clouds, satellites and contrails from aircraft. Due to all of the above challenges, raw spectra must be reduced (corrected) using flux calibration.

Galactic extinction from dust poses a challenge for ground- and space-based observations as dust scatters the target's emitted photons along the line of sight, resulting in a distorted spectrum. However, this is not normally possible or desirable to correct for using flux calibration because it is a real astrophysical effect, thus it is usually taken into account in the modelling stage.

Flux calibration requires accurately calibrated spectra of standard stars which are published and freely accessible. An appropriate standard can then be chosen based on location, magnitude, $T_{\rm eff}$ and wavelength coverage, depending on the target, and be observed with the same observing setup as the target. This is to ensure the observation of the standard star and target suffer from similar systematic effects, thus they can be easily identified and removed via flux calibration. The flux (F) of the published spectrum of the standard star is divided by the newly acquired flux, that is electron counts per second per pixel (N), from the observed spectrum of the standard star to produce the instrumental sensitivity,

$$S = F/N, \tag{1.13}$$

of the telescope for that particular time and location. The instrumental sensitivity includes all the features of the spectrum which are not native to the target. Once the target has been observed by the telescope, its flux (n) is multiplied by the instrumental sensitivity to produce a flux calibrated spectrum (Bohlin, 2014) with flux,

$$f = Sn. \tag{1.14}$$

1.6.1 *HST*/CALSPEC flux scale

Historically, Vega was considered the primary absolute flux standard, specifically its flux at 5557.5 Å (vacuum). Vega is relatively bright so its flux is easily measured and recorded, plus it passes close to the zenith for most northern observatories, making the effects of atmospheric absorption easier to mitigate. However since telescopes and instruments have advanced, the brightness of Vega saturates some detectors and southern observatories can only observe it at high airmass which increases the amount of flux lost via atmospheric scattering and absorption. Vega has also been discovered to be a rapid rotator, making it difficult to assign one model SED with a single $T_{\rm eff}$ and $\log g$ across the UV to the IR. Additionally, Vega has an IR excess due to a circumstellar debris disc which makes it an unreliable calibrator in the IR (Gray, 2007). For these reasons, different primary absolute flux standards are used in the present day.

The most internally consistent set of primary flux standards are three hot ($T_{\rm eff} > 30\,000$ K) DA white dwarfs: GD 71, GD 153 and G191-B2B (Bohlin et al., 2014). These stars are the simplest type of white dwarf to model over the UV to IR, are relatively bright ($11.7 < V < 13.4$) and have little reddening ($E(B-V) \lesssim 0.001$; Bohlin et al., 2020). The *Hubble Space Telescope* (*HST*) spectrophotometry, primarily from the Space Telescope Imaging Spectrometer (STIS), the Wide Field Camera three (WFC3) IR grisms, and the Near Infrared Camera and Multi-Object Spectrometer (NICMOS) (Bohlin, 2014; Bohlin et al., 2020), of these three primary standards were modelled with white dwarf atmosphere models to create synthetic SEDs. The absolute flux level is set by a reconciliation of the original Vega flux at 5557.5 Å (Megessier, 1995) with the *Midcourse Space Experiment* (*MSX*) IR absolute flux to define the absolute flux at all wavelengths over the UV, visible and NIR (Bohlin, 2014; Bohlin et al., 2020). These SEDs provide the basis for the *HST* absolute flux scale and are publicly available on CALSPEC[2], which is a database of primary and secondary spectrophotometric absolute flux standard stars on the *HST* flux scale containing measured stellar spectra and modelled SEDs with a goal of subpercent flux precision.

STIS is calibrated using the three primary standards, thus the accuracy of the other standards in CALSPEC which were observed with STIS are tied to the three primary standards. CALSPEC flux standards are used for the calibration of *HST*, the *James Webb Space Telescope* (*JWST*), *Gaia* and other ground- and space-based instrumentation. CALSPEC includes primary and secondary absolute flux standards which are MS stars (O-, B-, A-, F-, G-type), DA white dwarfs (hot, cool, faint) and stars within the globular cluster NGC6681 (Messier 70). 149 standards have complete STIS coverage, although only 116 of these have published model SEDs.

STIS is the *HST*'s oldest active instrument (installed in 1997) and has three primary detectors: FUV-MAMA, NUV-MAMA and CCD. The STIS gratings span $1150 - 10\,300$ Å and have low (L), medium (M) and high (H) dispersion modes. The L dispersion mode has resolving power $R \approx 500 - 1000$ with a wide wavelength coverage captured in a single, relatively short exposure, so is optimal for taking SEDs and identifying spectral lines. The STIS observations in this thesis (Chapter 5; Elms et al., 2024) used the gratings G140L, G230L, G430L and G750L. The G140L is used on the FUV-MAMA, G230L is used on the NUV-MAMA, and G430L and G750L are both on the CCD. The WFC3 grisms G102 and G141 were also used for observations in this thesis, which span the red optical and NIR wavelength range $8000 - 17\,000$ Å. The throughput with respect to wavelength for each filter is shown in Figure 1.9 for

---

[2] https://www.stsci.edu/hst/instrumentation/reference-data-for-calibration-and-tools/astronomical-catalogs/calspec

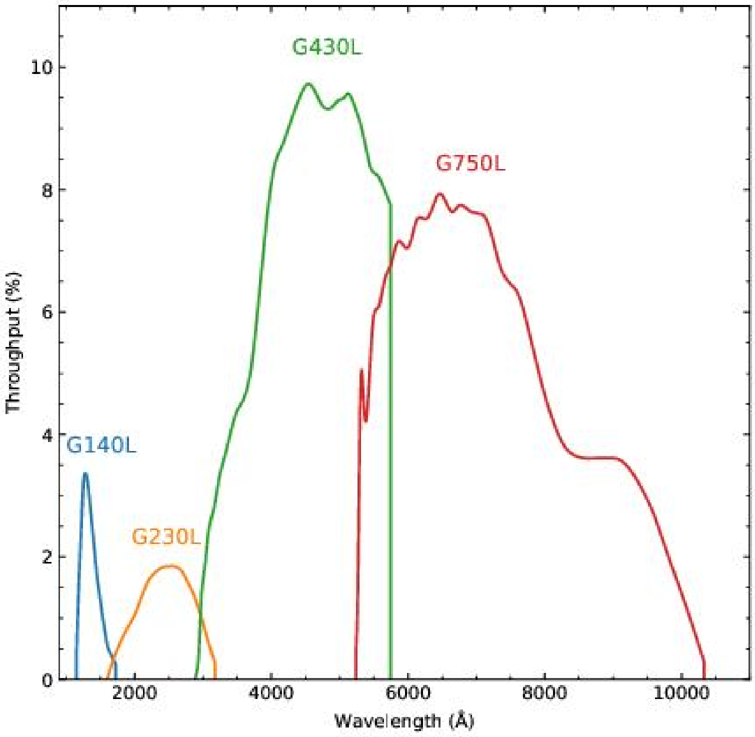

Figure 1.9: The throughput with respect to wavelength for the STIS gratings G140L, G230L, G430L and G750L. Figure has been reproduced from Fig 4.2 of Chapter 4.1 in the STIS Instrument Handbook at https://hst-docs.stsci.edu/stisihb.

STIS and Figure 1.10 for WFC3.

1.6.2 White dwarfs as IR calibrators

The overall goal for flux calibration is to have a complete network of absolute flux calibrators accurate to subpercent precision which cover all wavelengths from the UV to IR, magnitudes and T_{eff}. This is achievable through the amalgamation of individual networks with different stellar properties focusing on certain parameter spaces. Here we focus on white dwarfs.

Hot white dwarfs are relatively bright and have fully radiative atmospheres therefore are simple to model in the optical. The three hot primary standards are consistent within 1% at optical wavelengths ($0.3 - 1\,\mu$m) with *HST* spectrophotometric observations (Bohlin, 2014; Narayan et al., 2019) but discrepancies of >1% are evident outside the optical (Bohlin et al., 2011; Bohlin, 2014; Bohlin et al., 2022). Unfortunately, their magnitudes are close to some *JWST* instrument observational

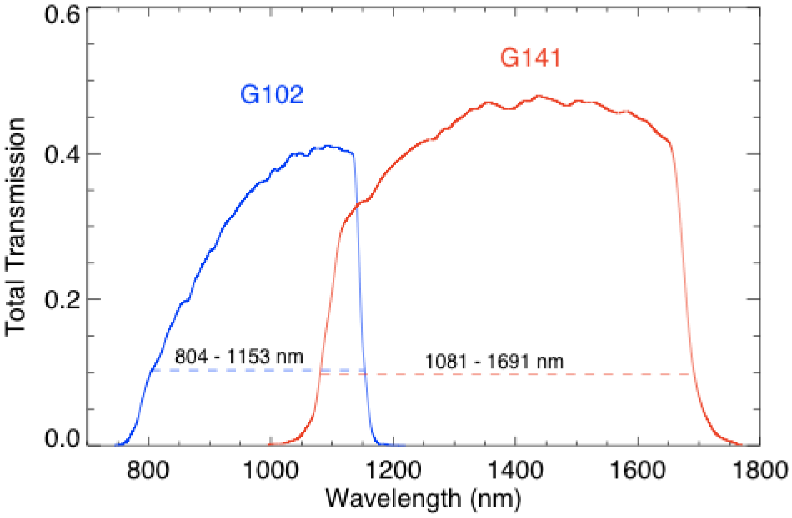

Figure 1.10: The throughput with respect to wavelength for the WFC3 gratings G102 and G141. The spectral ranges with more than 10% throughput are indicated. The figure has been reproduced and caption modified from Fig 8.4 of Chapter 8.3 in the WFC3 Instrument Handbook at https://hst-docs.stsci.edu/wfc3ihb.

limits and exceed the normal observing mode saturation limits of some upcoming surveys, particularly those designed for deep, wide-field observations (e.g. LSST, *Euclid*).

Recent studies have collated a network of 32 hot but faint ($16.5 < V < 19.5$) white dwarfs, which are below the normal observing mode saturation limits of several modern instruments and have all-sky coverage (Narayan et al., 2016, 2019; Calamida et al., 2022; Axelrod et al., 2023; Bohlin et al., 2025). These achieve consistency within 1% of the *HST* flux scale at optical wavelengths and within 3% at UV and IR wavelengths, however all faint standards are several hundred parsecs away so are heavily reliant on being de-reddened which introduces uncertainties.

Cooler ($T_{\rm eff} < 20\,000$ K) white dwarfs than the hot primary standards have a larger sky density, less reddening due to being at distances < 100 pc, are still relatively bright in the IR, suffer much less from NLTE effects or UV metal line blanketing (Werner, 1996; Gianninas et al., 2010; Rauch et al., 2013), and the latest DA model atmospheres can effectively account for convective effects for white dwarfs with $T_{\rm eff} \lesssim 13\,000$ K (Tremblay et al., 2013, 2019b). Cooler white dwarfs achieve consistency within 3% of the *HST* flux scale over most of the wavelength range $1450 - 16\,000$ Å, with residuals of 1.47% and 1.15% when fitting the UV and optical+NIR regions separately, respectively (Elms et al., 2024).

The expanded CALSPEC network of hot, faint and cooler secondary absolute flux calibrators has proven to be consistent with the *HST*/CALSPEC flux scale over the UV, optical and IR regimes. Future observations with high-resolution and extended wavelength coverage instruments on e.g. *JWST* compared to STIS+WFC3 will further improve this consistency as atmospheric models will improve based off better data. Current and future instruments onboard large-aperture telescopes such as the *JWST*, *Euclid* and *Nancy Grace Roman Space Telescope* (*Roman*) will also improve dust extinction maps resulting in a more accurate de-reddening function (Gordon et al., 2023).

Using white dwarfs as absolute flux calibrators in the IR pushes forward the accuracy frontier in observational astronomy. Accurate absolute flux standard stars are crucial for understanding the true nature of astronomical sources, and particularly in the IR it benefits multiple areas of science:

1. **Cosmology** investigations of dark energy will advance, as SNe brightness and redshift measurements become more accurate, thus constraining the equation of state parameters to a smaller parameter space. Photometric redshifts will become more accurate, allowing dark matter studies using weak gravitational lensing to advance.

2. **Stellar astrophysics and exoplanet research** will progress as stellar models will become more accurate. Fundamental stellar parameters and the characterisation of exoplanets will become more certain, in addition to having a greater understanding of the energy balance in stars.

3. **Inter-calibration of surveys, instruments and telescopes** to use the same spectrophotometric flux standards with the same physical flux scale will ensure accurate SEDs are produced regardless of the equipment used, in addition to more reliable observational data. Uncertainties which arise from photometric transformations between magnitude systems (see Section 2.2) will decrease, as zero-point inconsistencies and numerical errors will be eradicated. Combining data from multiple surveys for one research goal will have reduced uncertainty as there will be no need for individual post-observation corrections.

1.7 Thesis layout

This thesis comprises the research I have conducted to improve our understanding and usage of white dwarfs. Chapter 2 discusses the methods used to analyse spectroscopic, photometric and time-series data throughout this thesis. Chapter 3 reviews the analysis of the two most ultra-cool DZ white dwarfs known to date and their evolved planetary systems (Elms et al., 2022). Chapter 4 details the most recent analysis of the only two white dwarfs which belong to the white dwarf spectral class DAe (Elms et al., 2023). Chapter 5 discusses how DA white dwarfs cooler than current primary standards can be used as reliable absolute flux calibrators in the IR, and presents the network of 17 white dwarfs with $T_{\mathrm{eff}} < 20\,000\,\mathrm{K}$ which can be used as secondary absolute flux calibrators (Elms et al., 2024). I conclude my results in Chapter 6 and discuss future prospects for the three studies in this thesis.

Chapter 2

Methodology

2.1 Spectroscopy

Spectroscopy is a technique that disperses observed photons from a target into component wavelengths. It produces a continuous SED of the target, allowing the investigation of wavelength-dependent features such as spectral lines (see Sections 1.3 and 1.3.1 for details). Spectroscopy is a crucial technique in white dwarf science as it allows the determination of: stellar parameters such as $T_{\rm eff}$ and $\log g$; atmospheric composition (i.e. spectral type); the velocity and spin/orbital/pulsation period of the star; whether accretion of planetary debris occurred and what the parent body composition could have been; if there is a circumstellar debris disc; and whether the star hosts a magnetic field and at what strength.

Spectroscopy is performed by spectrographs, which are instruments that attach to telescopes. When photons enter the telescope, they are focused through the slit of the spectrograph. This diverges the photons onto a collimating mirror, which orients the photons into a parallel beam. The beam is then incident of a diffraction grating which disperses the photons into component wavelengths and reflects them at wavelength-dependent angles. The photons are then focused by the camera mirror onto the detector (CCD). Diffraction gratings orientated on the hypotenuse side of a right-angled triangular prism are called grisms, which are useful in practice, as they can be switched in and out of the instrument without moving the detector. The resolving power (R) of a spectrograph is given by

$$R = \frac{\lambda}{\Delta\lambda}, \tag{2.1}$$

where λ is the wavelength at which the resolution needs to be determined and $\Delta\lambda$ is the limiting resolution of the spectrograph, i.e. the difference in wavelength between two spectral lines of the same intensity that can be distinguished. Low- to intermediate-resolution long-slit spectroscopy with grism spectrographs is mainly used in this thesis, however echelle spectrographs are also used for some observations. Echelle spectrographs produce high-resolution spectroscopy because they have very high diffraction orders, i.e. the light is dispersed into lots of different directions as a function of wavelength.

The raw spectrum produced from the spectrograph then needs to be reduced and calibrated before used for precise scientific analysis, which is usually done by automated telescope pipelines or experienced astrophysicists/astronomers for that particular spectroscopic instrument. This process includes telluric correction of absorption lines from the Earth's atmosphere and flux calibration using standard stars (see Section 1.6). All of the spectroscopic data used in this thesis were externally

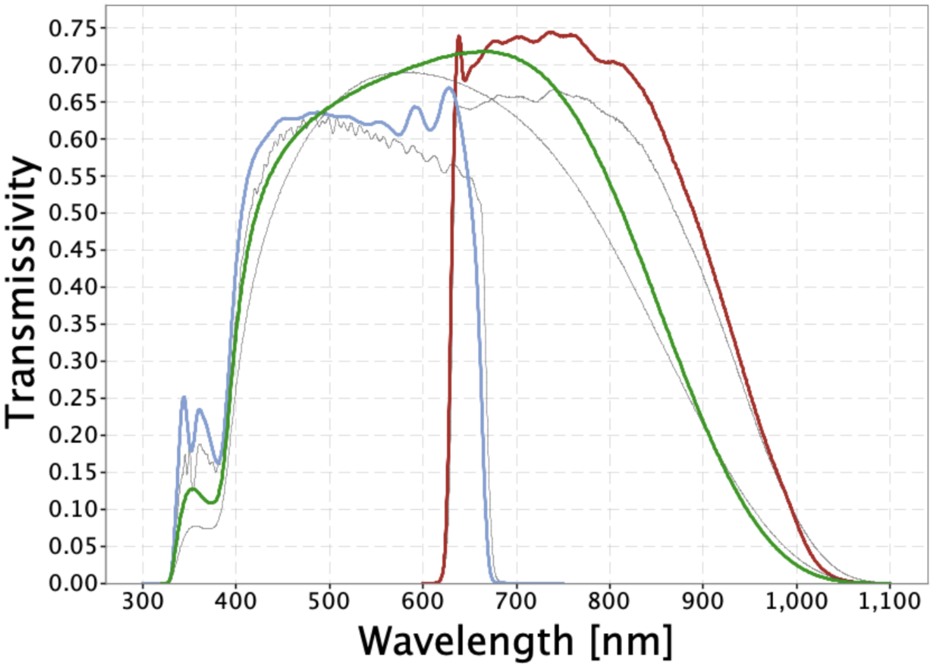

Figure 2.1: G (green), G_{BP} (blue) and G_{RP} (red) passbands for the *Gaia* DR3 photometric system; grey curves represent nominal pre-launch curves. Figure and caption reproduced from Fig 5.26 of Chapter 5.4.1 in the *Gaia* DR3 documentation at https://gea.esac.esa.int/archive/documentation/GDR3/.

reduced and calibrated.

2.2 Photometry

Photometry is a crucial technique in white dwarf science for measuring an astronomical object's brightness in terms of its radiated flux. Brightness is commonly measured in units of magnitudes which is on a logarithmic scale. The higher the magnitude, the dimmer the object. The lower the magnitude, the brighter the object. Telescopes have different photometric filters which only let photons of a specific wavelength range through. The flux measured in each filter provides information about an object's brightness at that wavelength, and comparing magnitudes from different filters defines the object's colors. Photometric magnitudes are always quoted with the corresponding filter to facilitate comparisons between objects and observations from different telescopes. For instance, in the *Gaia* G filter, white dwarfs typically range from magnitudes $\approx 8-22\,\mathrm{mag}$. Figure 2.1 shows the spectral response of the *Gaia* G, G_{BP} and G_{RP} filters as a function of wavelength.

There are two types of magnitudes: apparent magnitude, usually denoted with a lower-case m, is a measure of how bright an object is from Earth; and absolute magnitude, usually denoted with a capital M, which is a measure of how bright an object would be if it were 10 pc away from Earth. The distance modulus is a measure of the distance to an object, given by

$$m - M = 5\log(d) - 5, \tag{2.2}$$

where d is the distance to the object in parcecs. Eq. 2.2 can also be used to calculate m or M.

For two objects, the difference of their magnitudes relate to the ratio of the flux (F) received by the telescope by

$$m_1 - m_2 = -2.5\log_{10}\left(\frac{F_1}{F_2}\right). \tag{2.3}$$

The two comparison objects could have been observed with different detectors which use different magnitude systems. Different magnitude systems use different standard stars as zero points, which are essential for calibrating photometric observations to the same absolute scale. Commonly used magnitude systems are the Vega and AB systems. In the Vega system, the star Vega is used as the standard star and has an apparent magnitude of approximately zero at all wavelengths. A star with flux (F) has a magnitude

$$m = -2.5\log_{10}\left(\frac{F}{F_{\text{Vega}}}\right) \tag{2.4}$$

in the Vega system, where F_{Vega} is the flux spectrum of Vega which is available from CALSPEC. In the AB system, the standard star is a hypothetical flat-spectrum source with constant flux per unit frequency that defines zero magnitude (Oke, 1974). A star with flux density (F_ν) has a magnitude

$$m(AB) = -2.5\log_{10}(F_\nu) - 48.60 \tag{2.5}$$

in the AB system. Therefore, to determine an absolute measurement of brightness between two objects, a common magnitude system must be chosen and observed magnitudes converted as appropriate.

2.3 Time-series analysis

Observing an object over many epochs can be very useful, as measuring the changes in brightness characterises the behaviour of the star over time. Exposures of a

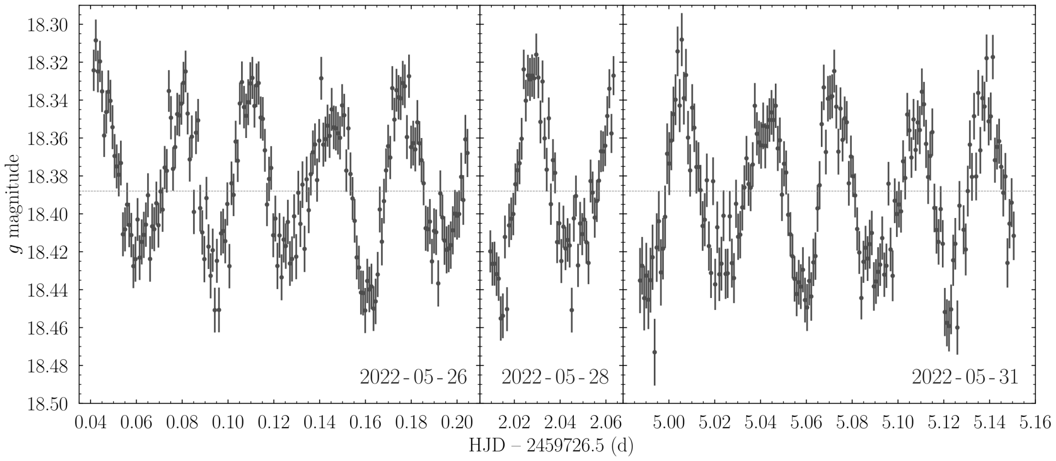

Figure 2.2: Liverpool Telescope (LT) photometry of WD J1616+5410. The horizontal dashed line corresponds to the median value of the LT photometry. Figure and caption reproduced from Manser et al. (2023).

target can be sequential over a single night, or can be taken over multiple nights over weeks, months or years to monitor the star. By combining these observations, a light curve can be constructed that spans the full observing period (Fig 2.2) or the phase of the object (see Figs 2.3 and 4.2). The spin/orbital/pulsation period can then be measured and any transiting exoplanets or debris can be detected. For white dwarfs, if there is no evidence of metals, then binarity or something on the white dwarf surface could be causing the variability (see Chapter 4).

Time-series analysis can be compared with multi-epoch spectroscopic observations to detect spectral line variability, which is a rare occurrence in white dwarfs but nevertheless interesting (see Section 6.2.1). The main classes of white dwarf variability are:

1. **Planetary debris transits and/or debris disk variability**, typically associated with infrared excess and metal pollution.

2. **Magnetic phenomena or surface homogeneity over the rotation period**, characterised by spectral line shape changes without radial velocity shifts, often accompanied by a detected magnetic field.

3. **Pulsations**, which manifest as multi-mode variations with characteristic periods of minutes.

4. **Binarity**, strongly indicated by spectral line radial velocity variations.

Throughout analysis, time-series observations must all have one consistent

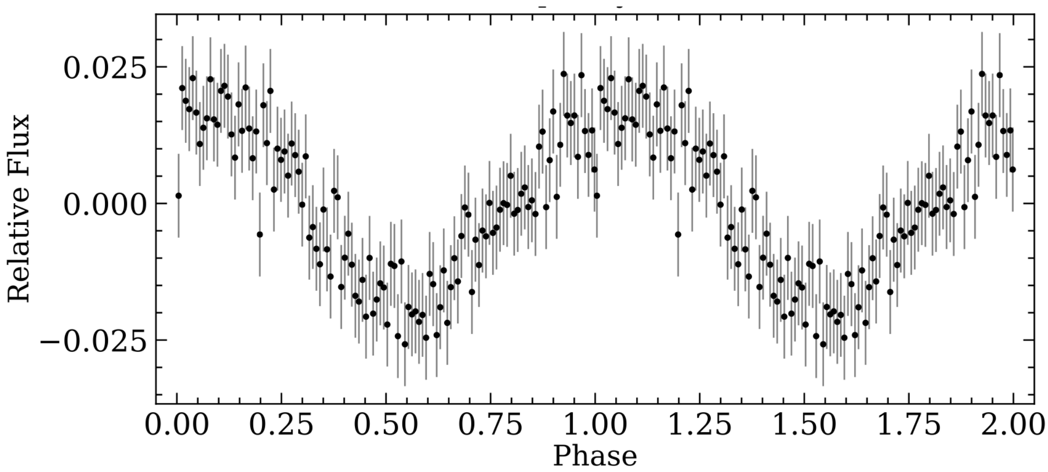

Figure 2.3: *TESS* photometry of WD J0412+7549 folded on the peak period. Each point is an average of 400 recordings. Figure and caption reproduced from Walters et al. (2021).

time frame. This thesis employs the Barycentric Dynamical Time (TDB) frame, which is a relativistic coordinate time scale that takes into account gravitational time dilation effects due to the Sun and other massive solar system bodies and is referenced to the barycenter of the solar system, i.e. the center of mass of all the objects in the solar system.

A consistent time format must also be used throughout analysis, although there are multiple time formats used in the literature and in practice. The `python` package `astropy` has simple functions for converting Coordinated Universal Time (UTC) ISOT times, which are generally given with observational data in the form YYYY-MM-DDThh:mm:ss, to different time formats and frames. Some telescopes and missions give observational time data in other formats, for instance observations from *TESS* are in the *TESS* Barycentric Julian Day (BTJD) format which is the elapsed days since 2015-01-01T00:00:00 and observations from the Magellan Echellette (MagE) are in the Modified Julian Date (MJD) format. MJD is a modern version of the Julian Date (JD) format, as it represents the number of days elapsed since 1858-11-17T00:00:00. MJD starts over 6000 years after day 0 of the JD, resulting in smaller numbers which are easier to incorporate into computational analysis, and it starts at midnight rather than noon.

This thesis uses the Barycentric Julian Date (BJD), which is the Julian Date (JD) corrected for differences in the Earth's position with respect to the barycenter of the solar system, and Barycentric Modified Julian Date (BMJD) formats. Useful conversions for the BJD, BTJD and BMJD are as follows:

$$\mathrm{BJD} = \mathrm{BTJD} + 2\,457\,000.0, \tag{2.6}$$

$$\mathrm{BMJD} = \mathrm{BJD} - 2\,400\,000.5, \tag{2.7}$$

although to make dates easier to work with, I express times in BJD − 2 450 000.5 which is equivalent to BMJD − 50 000.

Chapter 3

Spectral analysis of ultra-cool white dwarfs polluted by planetary debris

3.1 Introduction

Over 97 % of main-sequence stars ($M/\mathrm{M}_\odot \lesssim 8$) in the Milky Way galaxy will end their stellar evolution as white dwarfs, making these the most common type of stellar remnant. Typical white dwarfs consist of a dense C/O degenerate core of comparable radius to the Earth, surrounded by a thin envelope of residual hydrogen and helium left over from the progenitor's post-main-sequence evolution. The degenerate core creates an efficient environment for electron conduction which makes it almost isothermal.

Throughout their lives, white dwarfs slowly cool by radiating their residual internal thermal energy away through their thin non-degenerate envelopes (Mestel, 1952; Althaus et al., 2010a). Thus the coolest white dwarfs, with ultra-cool effective temperatures, $T_{\text{eff}} < 4000\,\text{K}$, tend to have the largest cooling ages depending on their atmospheric composition and radius (mass). Studying white dwarfs within the Milky Way allows us to calibrate stellar ages (Fouesneau et al., 2019; Rebassa-Mansergas et al., 2021) and probe the formation and evolution of the Galactic neighbourhood (Winget et al., 1987; Rowell, 2013; Tremblay et al., 2014; Kilic et al., 2017; Fantin et al., 2019, 2020), with the analysis of cool remnants being particularly important as these provide constraints on its oldest stars (Bergeron et al., 1997; Gianninas et al., 2015; Lam et al., 2020).

Spectroscopy reveals the atmospheric composition of white dwarfs and allows us to separate them into spectral types. White dwarfs should only have hydrogen or helium present in their atmospheres due to high surface gravities ($\log g \approx 8$) and fast diffusion timescales causing heavy elements to sink below the photosphere (Paquette et al., 1986; Koester, 2009), yet metals are found to pollute 25 – 50 % of all white dwarfs (Zuckerman et al., 2003, 2010; Koester et al., 2014). It is now well established that these metals contaminate white dwarfs through the accretion of tidally disrupted rocky bodies which survived the final evolutionary stages of its host star (Graham et al., 1990; Jura, 2003; Farihi et al., 2010; Gänsicke et al., 2012; Veras et al., 2014; Cunningham et al., 2022).

White dwarfs with $T_{\text{eff}} \lesssim 5000\,\text{K}$ generally have featureless spectra as they are too cool to display hydrogen or helium absorption lines (DC spectral type), but can show strong metal lines (DZ spectral type) if polluted by planetary debris (Sion et al., 1983). The metal lines in these cool DZ white dwarfs can provide invaluable information on the physical conditions present in these dense, cool atmospheres in a way that is not possible with their featureless DC counterparts (Blouin et al., 2019a). However, the extreme high density ($\gtrsim 0.1\,\text{g}\,\text{cm}^{-3}$) in the atmosphere of these remnants affects their observed photometry and spectroscopy which complicates assessments of their $T_{\rm eff}$, mass and age.

The atmospheric collision induced absorption (CIA) of H_2-H_2, H_2-He, H-He, H_2-H and He-He-He in cool white dwarfs can greatly alter their spectral energy distributions (SEDs), leading them to display optical and near-infrared (NIR) colours that can be much bluer than a blackbody (Bergeron et al., 1994; Hansen, 1998; Blouin et al., 2017). CIA opacities and the treatment of charged and neutral particle interactions must therefore be carefully considered within cool white dwarf model atmosphere codes. As the physics of these extreme conditions is not yet fully understood, uncertainties remain on mass and age estimates (Bergeron and Leggett, 2002; Gianninas et al., 2015; Kilic et al., 2020; Hollands et al., 2021; Kaiser et al., 2021; Bergeron et al., 2022). Regardless of $T_{\rm eff}$, white dwarfs with strong CIA opacity are designated as infrared-faint (IR-faint; Kilic et al., 2020).

The spacecraft *Gaia* (Gaia Collaboration et al., 2016) measures the precise astrometric and photometric quantities of stars in the Milky Way and has allowed the recent identification of more than 300 000 new white dwarf candidates (Gentile Fusillo et al., 2019, 2021). Spectroscopic follow-ups (Tremblay et al., 2020; Kaiser et al., 2021) have revealed several new cool DZ stars, which led to the first detections of lithium and potassium in the atmosphere of white dwarfs and different propositions to explain the intriguingly high abundances of these elements compared to calcium and sodium, including the accretion of planetary crusts and lithium-enhanced primordial gas (Hollands et al., 2021; Kaiser et al., 2021). Distinguishing between these two scenarios now requires an enlarged sample of cool DZ white dwarfs as well as a more accurate characterisation of their ages.

This work focuses on spectroscopic observations and analysis of two ultra-cool DZ white dwarfs WD J214756.59−403527.79 (hereafter WD J2147−4035) and WD J192206.20+023313.29 (hereafter WD J1922+0233). These were first identified as white dwarf candidates from *Gaia* (Gentile Fusillo et al., 2019, 2021). Apps et al. (2021) re-identified WD J2147−4035 as a nearby star with unusual colours and speculated that it is an extremely cool white dwarf. WD J1922+0233 was previously confirmed as a DZ in Tremblay et al. (2020) while WD J2147−4035 is spectroscopically identified as a DZQH in this work – we broadly refer to this star as a member of the DZ class throughout this chapter.

In Section 3.2, we present spectroscopic and photometric observations of WD J2147−4035 and WD J1922+0233. These are put into the context of a sample of *Gaia* white dwarfs within 100 pc, including a subsample of DZ white dwarfs with $T_{\rm eff} < 5000$ K, in Section 3.3. We describe the microphysics improvements to our model atmospheres which allow us to derive the $T_{\rm eff}$, $\log g$, mass, cooling age and chemical abundances of WD J2147−4035 and WD J1922+0233 in Sections 3.4–3.6. In Section 3.7 we discuss our results and conclude in Section 3.8.

3.2 Observations

The *Gaia* Early Data Release 3 (EDR3; Gaia Collaboration et al., 2021) astrometry of WD J2147−4035 and WD J1922+0233 is given in Table 3.1. We have corrected the parallax values for all objects to account for the zero point offset following Lindegren et al. (2021).

Tremblay et al. (2020) conducted the first spectroscopic observations of WD J1922+0233 with the Gran Telescopio Canarias (GTC) Optical System for Imaging and low-Intermediate-Resolution Integrated Spectroscopy (OSIRIS; Cepa et al., 2000, 2003) spectrograph. Tremblay et al. (2020) speculated that WD J1922+0233 is the first detected ultra-cool DZ white dwarf that exhibits strong optical CIA[1]. Given the limited wavelength coverage of the observations, the sodium D-line was the only line detected. The first spectroscopic observations of WD J2147−4035 are presented in this work. It was selected as a high-confidence white dwarf candidate from Gentile Fusillo et al. (2021) as part of a spectroscopic survey of the southern 40 pc sample (O'Brien et al., 2023).

We observed WD J2147−4035 and WD J1922+0233 on 2021 June 5-7 with X-shooter (Vernet et al., 2011) on the Very Large Telescope (VLT) of the European Southern Observatory. We used slit widths of 1.0, 0.9, and 0.9 arcsec in the blue (UVB, 3000 – 5600 Å, $R = 5400$), visual (VIS, 5500 – 10 200 Å, $R = 8900$) and NIR (10 200 – 24 800 Å, $R = 5600$) arms, respectively. The exposure times in the UVB, VIS, and NIR arms were 2×1800, 2×1750, and 12×300 s. The data were reduced following standard practices and using the `Reflex` pipeline (Freudling et al., 2013). The flux calibration was carried out using observations of the pure-hydrogen white dwarf LTT 7987, obtained with the identical instrument setup as the science spectroscopy, and telluric correction was performed using `molecfit` (Smette et al., 2015; Kausch et al., 2015). The X-Shooter spectra for WD J2147−4035 and WD J1922+0233 are shown in Figure 3.1, where we have highlighted spectral lines of metals detected in one or both spectra (see Section 3.6) with coloured vertical bars: calcium, sodium and potassium are detected in WD J1922+0233; sodium, lithium, potassium, and tentatively carbon, are detected in WD J2147−4035. The spectra

---

[1] Blouin et al. (2018b) have previously identified a cool DZ white dwarf SDSS J0804+2239 with strong near-IR CIA.

Table 3.1: Astrometry for the white dwarfs in our DZ subsample. WD J2147−4035 and WD J1922+0233 are the main focus of this work, while the remaining six stars are used for comparison. The *Gaia* EDR3 parallax (ϖ) values listed have been corrected to account for the zero point offset following Lindegren et al. (2021). Proper motions, μ, are given in the right ascension (α) and declination (δ) directions. We calculated the tangential velocity, $v_\perp$, and Galactic velocity components of all eight stars in this work, where U indicates motion radially away from the Galactic centre, V is in the direction of the Galaxy's rotation and W is perpendicular to the disc. We have assumed zero radial velocity in the calculations of U, V and W. Values are given in the J2016.0 epoch.

	RA	Dec	ϖ (mas)	Distance (pc)	$\mu_\alpha \cos(\delta)$ (mas yr^{-1})	μ_δ (mas yr^{-1})	$v_\perp$ (km s^{-1})	U (km s^{-1})	V (km s^{-1})	W (km s^{-1})
WD J2147−4035	21:47:56.59	−40:35:27.78	35.79 ± 0.49	27.94 ± 0.38	−84.11 ± 0.42	−112.39 ± 0.42	18.59 ± 0.26	−9.80	−13.65	7.96
WD J1922+0233	19:22:06.20	+02:33:13.29	25.36 ± 0.27	39.43 ± 0.41	69.66 ± 0.25	−29.16 ± 0.24	14.11 ± 0.15	1.83	0.07	−14.00
WD J1824+1213	18:24:58.44	+12:13:06.82	25.00 ± 0.18	40.00 ± 0.29	−280.11 ± 0.18	−1078.43 ± 0.17	211.27 ± 1.54	−141.95	−151.35	−39.74
WD J1330+6435	13:30:01.16	+64:35:23.71	11.52 ± 0.78	86.79 ± 5.51	−110.63 ± 1.51	−23.30 ± 1.38	46.51 ± 3.02	30.45	−32.86	12.51
WD J1644−0449	16:44:17.01	−04:49:47.71	12.65 ± 0.87	79.07 ± 5.07	80.58 ± 0.95	−45.40 ± 0.75	34.67 ± 2.25	−13.98	5.44	−31.25
WD J2356−2054	23:56:44.76	−20:54:53.77	15.28 ± 0.58	65.46 ± 2.50	−295.49 ± 0.57	−239.37 ± 0.42	118.01 ± 4.33	−114.85	−24.96	10.58
WD J2317+1830	23:17:26.73	+18:30:52.75	26.40 ± 0.31	37.89 ± 0.44	−33.85 ± 0.32	−452.81 ± 0.26	81.55 ± 0.94	−45.36	−40.84	−54.08
WD J1214−0234	12:14:56.38	−02:34:02.83	26.26 ± 0.12	38.09 ± 0.17	358.65 ± 0.14	−419.28 ± 0.09	99.61 ± 0.44	−92.41	−24.09	−28.33

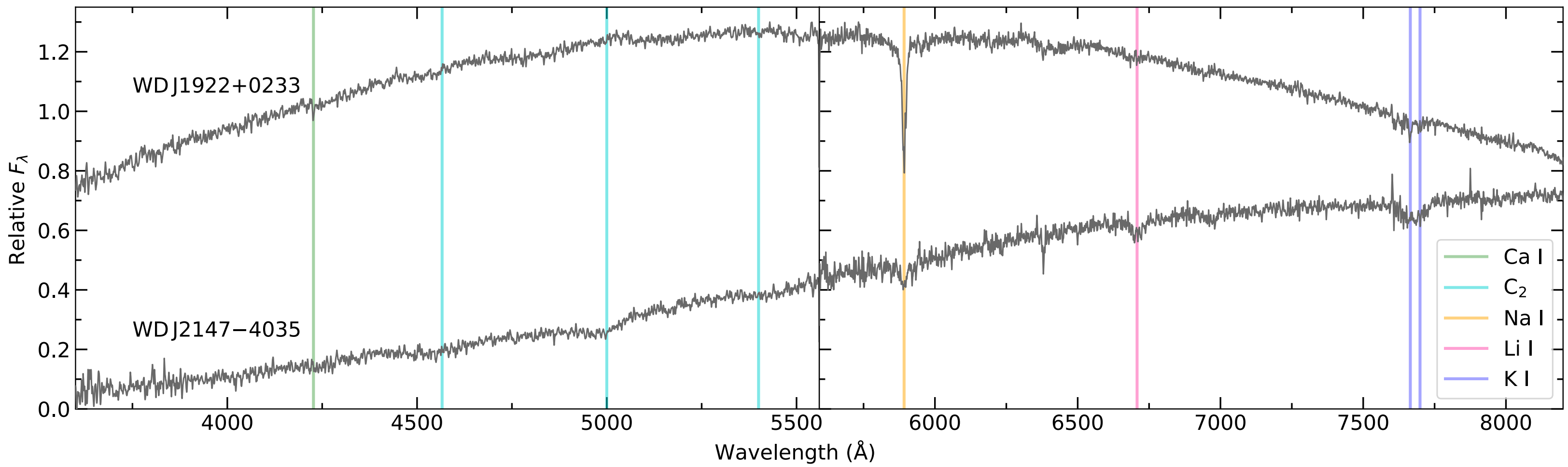

Figure 3.1: Optical spectra (grey) from the VLT X-Shooter spectrograph for WD J2147−4035 and WD J1922+0233, comprised of observations taken with the UVB (left panel) and VIS (right panel) arms. Spectral lines of Ca I (4227 Å), Na I D (5893 Å), Li I (6708 Å) and K I (7665 Å and 7699 Å) are highlighted with coloured vertical bars to show metal detections of Na I D and K I in both white dwarfs, Ca I in WD J1922+0233 and Li I in WD J2147−4035. We made a tentative detection of carbon in WD J2147−4035 as the three strongest C_2 Swan band systems (aqua vertical lines) blueshifted to the centroid wavelengths measured in the DQpecP star LP 351−42 are in excellent agreement to the observed broad, rounded absorption features. F_λ is the flux per unit wavelength. Spectra are convolved by a Gaussian with a FWHM of 2 Å for clarity. Telluric absorption from the Earth's atmosphere are evident in the region ≈ 7600 – 7640 Å in both spectra.

Table 3.2: Optical and IR photometry for WD J2147−4035. The *Gaia* G magnitude has been corrected following the procedure from Lindegren et al. (2021).

Survey	Filter	Magnitude (mag)
Gaia	G	19.959 ± 0.008
	G_{BP}	20.949 ± 0.089
	G_{RP}	19.024 ± 0.046
DES	g	21.400 ± 0.020
	r	19.858 ± 0.007
	i	19.298 ± 0.007
	z	19.106 ± 0.010
	Y	18.901 ± 0.027
VHS	J	17.581 ± 0.015
	K	17.625 ± 0.091
WISE	$W1$	16.965 ± 0.050
	$W2$	16.717 ± 0.095

obtained from the NIR arms of X-shooter for both stars are not used in this chapter as they had insufficient flux for any scientific application.

Tables 3.2 and 3.3 display the available survey photometric data of WD J2147−4035 and WD J1922+0233, respectively. Corrections to the *Gaia* EDR3 G magnitude measurements were applied following the procedure from Lindegren et al. (2021), with the corrected values shown in the tables. WD J1922+0233 has Panoramic Survey Telescope and Rapid Response System (Pan-STARRS; Chambers et al., 2016; Flewelling et al., 2020) DR2 photometry whereas WD J2147−4035 does not; instead, we used $grizY$ photometry from the Dark Energy Camera (DECam; Flaugher et al., 2015) from DR1 of the Dark Energy Survey (DES; Dark Energy Survey Collaboration et al., 2016; Abbott et al., 2018) located at the Cerro Tololo Inter-American Observatory (CTIO), as this has similar bandpasses to Pan-STARRS. WD J2147−4035 also has NIR photometry from DR6 of the Visible and Infrared Survey Telescope for Astronomy (VISTA) Hemisphere Survey (VHS; McMahon et al., 2013) and the Wide-field Infrared Survey Explorer (WISE; Wright et al., 2010) CatWISE2020 catalogue (Marocco et al., 2021).

3.3 Sample of cool DZ white dwarfs

Several other metal-polluted white dwarfs with $T_{\mathrm{eff}} < 5000\,\mathrm{K}$ are found in the literature, from which we selected a subsample to use as a comparison to WD J2147−4035 and WD J1922+0233 in terms of astrometric, photometric and atmospheric param-

Table 3.3: Optical photometry for WD J1922+0233. The *Gaia* G magnitude has been corrected following the procedure from Lindegren et al. (2021).

Survey	Filter	Magnitude (mag)
Gaia	G	19.120 ± 0.004
	$G_{\rm BP}$	19.407 ± 0.036
	$G_{\rm RP}$	18.654 ± 0.032
Pan-STARRS	g	19.588 ± 0.013
	r	19.056 ± 0.011
	i	18.937 ± 0.023
	z	19.099 ± 0.038
	y	19.467 ± 0.020

eters. We limited our subsample to include spectroscopically confirmed DZ stars with: $T_{\rm eff} < 5000$ K and lithium and/or potassium detections; or, $T_{\rm eff} < 4000$ K within error bars. This selection criteria yielded WD J235645.10−205449.94 (hereafter WD J2356−2054[2]) from Blouin et al. (2019a), WD J164417.02−044947.71 (hereafter WD J1644−0449) from Kaiser et al. (2021) and four white dwarfs from Hollands et al. (2021): WD J182458.45+121316.82, WD J133001.17+643523.69, WD J231726.74+183052.75 and WD J121456.38−023402.84 (hereafter WD J1824+1213, WD J1330+6435, WD J2317+1830 and WD J1214−0234, respectively). Together with WD J2147−4035 and WD J1922+0233, these eight white dwarfs comprise our subsample and their astrometry is given in Table 3.1.

3.3.1 *Gaia* white dwarfs within 100 pc

To determine the unique nature of WD J2147−4035 and WD J1922+0233, we employed Hertzsprung–Russell diagrams (HRDs) to compare them to the *Gaia* EDR3 white dwarf sample within 100 pc of the Sun and the SDSS (York et al., 2000) footprint from Gentile Fusillo et al. (2021). We imposed selection criteria to only return objects which have SDSS *ugriz* photometry and are within 100 pc, which resulted in a sample of 5613 objects. We found 2865 (51.0 %)[3] of these 5613 stars have published spectral classifications of white dwarf spectral types (Sion et al., 1983). All binary spectral types are excluded from the sample of 2865 white dwarfs. All spectral classifications were obtained from the Gentile Fusillo et al. (2021) *Gaia*−SDSS

---

[2] Also known as WD J2356−209 in Blouin et al. (2019a).

[3] The total number of objects with a spectrum in the 100 pc sample and SDSS footprint is 2917 (52.0 %). The total number of confirmed white dwarfs (including main white dwarf spectral types, 'Other SpT', all binaries and CVs) in the 100 pc sample and SDSS footprint is 2887 (51.4 %).

Table 3.4: Breakdown of the identified main spectral types of the 2871 white dwarfs in the 100 pc sample. This sample contains 2865 spectroscopically confirmed white dwarfs within 100 pc and the SDSS footprint from Gentile Fusillo et al. (2021), including two DZ subsample stars defined in this work (see text) WD J2317+1830 and WD J1214−0234, and the remaining six DZ subsample stars. All binary spectral types and CVs are excluded. 'Other SpT' are stars that are identified as white dwarfs but cannot be subclassified due to low-quality spectra, magnetic fields or peculiarities; additional observations or modelling are needed to clarify these spectral types.

Spectral Type	Total Number
DA	1861
DB	74
DC	667
DQ	117
DZ	138
Other SpT	8
Subsample DZ	6

spectroscopic catalogue, the literature (Kilic et al., 2006, 2010, 2020) or the Montreal White Dwarf Database (MWDD; Dufour et al., 2017).

Narrow-band *grizy* photometry from Pan-STARRS was subsequently obtained for the white dwarf sample within 100 pc and the SDSS footprint, which complimented the broad bandpass photometry from *Gaia* EDR3 in our analysis. The sample is displayed in the HRDs in Figures 3.2 and 3.3, which is representative of the white dwarf cooling sequence. Absolute magnitudes are computed using *Gaia* EDR3 parallaxes. Pan-STARRS photometry is used in Figure 3.2 whereas *Gaia* photometry is employed in Figure 3.3.

The DZ subsample stars were added to the main sample, except WD J1214−0234 and WD J2317+1830 as they are in the SDSS footprint, which increased our sample to 2871 white dwarfs within 100 pc with spectral classifications; a breakdown of the number of white dwarfs with each spectral type is shown in Table 3.4. The eight subsample DZ white dwarfs are plotted in Figures 3.2 and 3.3 and indicated with red open markers. WD J2147−4035 does not have Pan-STARRS photometry so we used DECam photometry instead.

WD J2147−4035 and WD J1922+0233 occupy relatively isolated positions on the HRDs, suggesting they have unusual parameters and extreme natures (see Section 3.7.2 for further discussion). WD J1922+0233 has an unusually blue colour relative to its dim absolute magnitude and therefore could have strong CIA opacity, as suggested by the unusual spectral shape and red flux deficit in Figure 3.1 (see

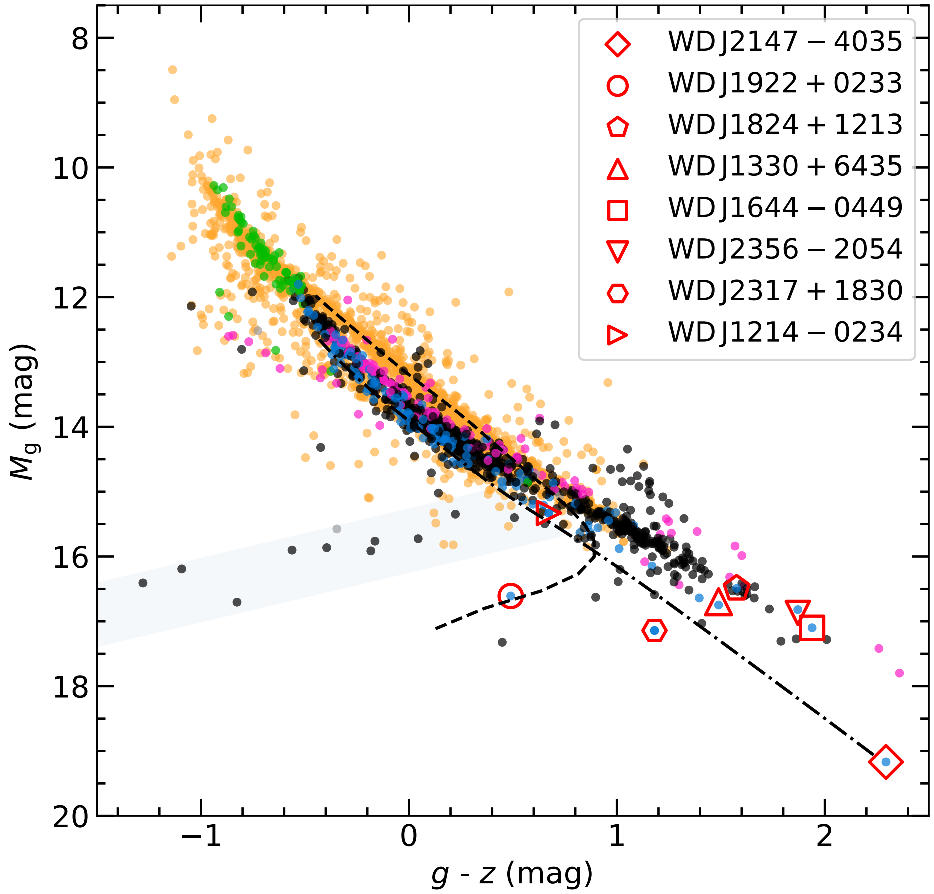

Figure 3.2: Hertzsprung-Russell diagram displaying our spectroscopically confirmed 100 pc white dwarf sample of 2871 stars, including the 2865 white dwarfs from the Gentile Fusillo et al. (2021) *Gaia* EDR3 100 pc SDSS footprint and the DZ subsample stars defined in this work (see text), using photometry from Pan-STARRS. The DZ subsample is indicated by open red markers. DECam photometry is used for WD J2147−4035. The best-fitting indicative model cooling sequences, between $2750 < T_{\text{eff}} < 10\,000$ K, for WD J2147−4035 is with $\log g = 8.25$ and $\log(\text{H/He}) = -5.0$ (dashed-dotted line) and for WD J1922+0233 is with $\log g = 7.75$ and $\log(\text{H/He}) = -2.5$ (dashed line). Objects on the ultra-blue sequence are indicated by the shaded blue region in both panels. The legends in this figure and Figure 3.3 apply to both panels.

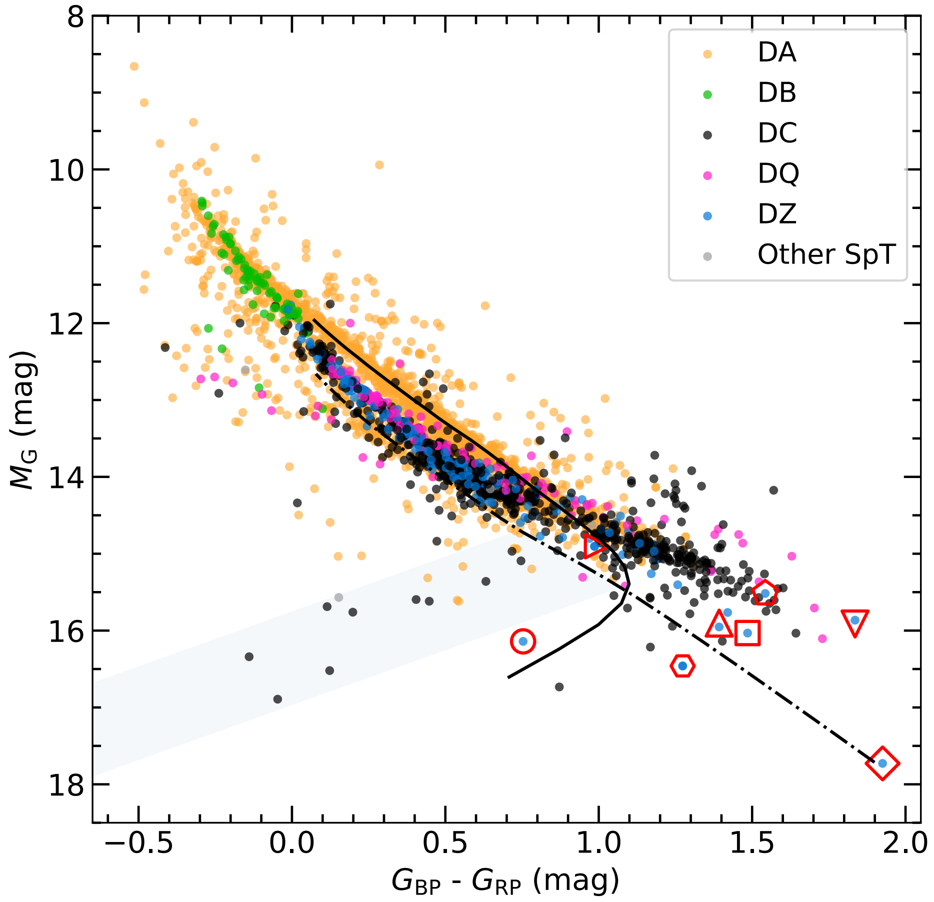

Figure 3.3: Hertzsprung-Russell diagrams displaying our spectroscopically confirmed 100 pc white dwarf sample of 2871 stars, including the 2865 white dwarfs from the Gentile Fusillo et al. (2021) *Gaia* EDR3 100 pc SDSS footprint and the DZ subsample stars defined in this work (see text), using photometry from *Gaia*. The DZ subsample is indicated by open red markers. The best-fitting indicative model cooling sequences, between $2750 < T_{\rm eff} < 10\,000$ K, for WD J2147−4035 is with $\log g = 8.25$ and $\log(\mathrm{H/He}) = -5.0$ (dashed-dotted line) and for WD J1922+0233 is with $\log g = 7.75$ and $\log(\mathrm{H/He}) = -2.0$ (solid line). Objects on the ultra-blue sequence are indicated by the shaded blue region in both panels. The legends in this figure and Figure 3.2 apply to both panels.

also Tremblay et al., 2020). WD J2147$-$4035 is an obvious outlier to the main white dwarf cooling sequence as it is the dimmest and reddest object out of the sample, which suggests it is an old remnant. Comparison with the local 40 pc *Gaia* sample reveals WD J2147$-$4035 as the intrinsically faintest spectroscopically confirmed white dwarf in the optical (O'Brien et al., 2023). Also, the extreme red colour of WD J2147$-$4035 indicates it has more moderate CIA.

WD J1214$-$0234 lies on the main white dwarf cooling sequence. WD J1644$-$0449, WD J1824+1213, WD J1330+6435 and WD J2317+1830 are dimmer and redder than the majority of objects in the sample, thus reside in the tail of the main white dwarf cooling sequence. The cool DZ WD J2356$-$2054 is an outlier in Figure 3.3 as it has an extremely red colour of $G_{\mathrm{BP}} - G_{\mathrm{RP}} = 1.84$ mag; this quantity is only slightly smaller compared to WD J2147$-$4035. A larger photometric difference is measured using Pan-STARRS between the two stars, which have measurements of $g - z = 1.88$ mag for WD J2356$-$2054 and $g - z = 2.29$ mag for WD J2147$-$4035. WD J2356$-$2054 has an absolute magnitude with Pan-STARRS and *Gaia* photometry comparable to the DZ stars in our subsample which cluster at the end of the main white dwarf cooling sequence, and is notably brighter than WD J2147$-$4035 in M_{g} by ≈ 2.3 mag and M_{G} by ≈ 1.9 mag. The combination of its absolute magnitude and slightly bluer $g - z$ colour compared to its $G_{\mathrm{BP}} - G_{\mathrm{RP}}$ colour makes WD J2356$-$2054 occupy a less unusual position in Figure 3.2 than Figure 3.3.

Given the narrow Pan-STARRS bandpasses, metal lines in the DZ subsample and WD J2356$-$2054 could impact their positions in the HRD. However, we note that most warmer DZ white dwarfs sit on the main white dwarf cooling track. This suggests that it is the cool nature of these DZ white dwarfs that make them outliers in the HRD, rather than metal lines. This is confirmed by looking at the HRD of Figure 3.3 using the much broader *Gaia* filters.

Ultra-blue sequence

A clear ultra-blue sequence consisting of mainly DC stars is seen in Figures 3.2 and 3.3 and indicated by the shaded blue region in both panels. This sequence was first extensively studied in Kilic et al. (2020). White dwarfs on the ultra-blue sequence are designated as IR-faint as they have optical and NIR flux deficits and thus present strong CIA opacity, with models suggesting mixed H/He atmospheric compositions (see Section 3.7.3).

The white dwarfs populating the ultra-blue sequence in Figures 3.2 and 3.3 have published $\log(\mathrm{H/He}) \sim -3.0$ and are modelled to be as cool as $T_{\mathrm{eff}} \approx 2700$ K

(Kilic et al., 2020), although a more recent analysis by Bergeron et al. (2022) found a warmer lower limit of $T_{\rm eff} \approx 3900\,\rm K$. WD J003908.38+303539.76 is the bluest DC white dwarf on the ultra-blue sequence with $\log{\rm (H/He)} = -3.4$ and $T_{\rm eff} = 4605 \pm 77\,\rm K$ (Bergeron et al., 2022).

No white dwarf from our DZ subsample reside on the ultra-blue sequence. However, WD J1922+0233 resides parallel to the ultra-blue sequence so it could have turned off the main white dwarf cooling sequence later than the other objects in this population, possibly due to it having a slightly different $\log{\rm (H/He)}$ atmospheric abundance.

3.4 Model atmospheres

The model atmosphere code of Koester (2010), with microphysics improvements explained in this section, was used to determine the parameters of WD J2147−4035 and WD J1922+0233.

The atmospheric density of cool white dwarfs can become so high ($\gtrsim 0.1\,\rm g\,cm^{-3}$) that it must be considered as a dense fluid rather than an ideal gas (Kowalski and Saumon, 2004; Kowalski, 2006, 2014; Blouin et al., 2017, 2018a). Deviations from the simple ideal equation-of-state (EOS) become important at these temperatures, especially for helium-rich models. Since the absorption coefficient of pure neutral helium is very small, these atmosphere models reach very high densities. We therefore utilised a non-ideal EOS taking into account the interaction of charged and neutral particles. For the description of the interaction between charged particles we followed Chabrier and Potekhin (1998); Potekhin and Chabrier (2000), but used only the ion-ion interaction as described by the one-component-Coulomb plasma. The model of neutral interactions is based on the classical excluded volume model with hard spheres (see e.g. Hummer and Mihalas, 1988), but modified arbitrarily to obtain the desired result of total ionisation in the density regime of about $3-8\,\rm g\,cm^{-3}$ (Saumon et al., 1995). Together the charged and neutral particle interactions lead to a lowering of the energy for the ionisation of individual atoms and the dissociation of molecules. The non-ideal effects also have a contribution to the pressure and to other thermodynamic quantities like the adiabatic gradient.

We employed CIA opacities for $\rm H_2$-$\rm H_2$ (Abel et al., 2011; Borysow et al., 2001), $\rm H_2$-He (Abel et al. 2012 with scaling factor from Blouin et al. 2017), H-He (Gustafsson and Frommhold, 2001) and $\rm H_2$-H (Gustafsson and Frommhold, 2003). In principle there should also be a He-He-He CIA contribution (Kowalski, 2014). We implemented the numerical fit given by Kowalski (2014) and find such a strong IR absorption in WD J2147−4035 that it is impossible to fit the photometry. A likely reason for this is that the maximum density Kowalski (2014) used in the derivation of the numerical fit was 0.1 g cm^{-3}, and in the models shown the He-He-He CIA produces only a fairly minor change. However, in the photospheres of our models the densities reach 3 g cm^{-3} ($n_{\mathrm{He}} = 4.5 \times 10^{23}$ cm^{-3}), which is approximately the photospheric density in WD J2147−4035. As the absorption is proportional to the cube of the density, the extrapolation of the He-He-He opacity to the very high densities in our models is very likely not reliable. We have therefore switched off the effect from He-He-He CIA absorption in our models. For WD J1922+0233, the He-He-He contribution is negligible because of the much stronger contributions involving hydrogen.

3.5 Stellar parameters

Representative cooling sequences which indicate approximate $\log g$ and $\log$ (H/He) for WD J2147−4035 and WD J1922+0233 are shown in Figures 3.2 and 3.3 with the dashed, solid or dashed-dotted lines. The best-fitting cooling sequence for WD J2147−4035 is given in both HRDs by $\log g = 8.25$ and $\log$ (H/He) $= -5.0$. The cooling sequences with $\log g = 7.75$ indicate the best-fit to WD J1922+0233 when using mixed atmospheres of $\log$ (H/He) $= -2.5$ with Pan-STARRS photometry and $\log$ (H/He) $= -2.0$ with *Gaia* photometry. These cooling sequences serve as an indicative tool for deriving the atmospheric parameters of WD J2147−4035 and WD J1922+0233 using a model grid, as described in Section 3.4, and the full photometric data sets.

Our model grid was used to predict synthetic photometry for both objects, which depends on the atmospheric parameters T_{eff}, $\log g$ and $\log$ (H/He) abundance. We relied on the mass-radius relation of Bédard et al. (2020) to predict absolute magnitudes. We used an iterative procedure utilising the photometric (Tables 3.2 and 3.3) and spectroscopic data sets to find the best-fitting atmospheric parameters and individual metal abundances of WD J2147−4035 and WD J1922+0233. We initially estimated atmospheric parameters using the photometric technique, where we fit the observed photometry to our grid of synthetic photometry which included metals over all bandpasses to minimise χ^2. Our minimisation technique utilised the non-linear least-squares Levenberg-Marquardt algorithm (Press et al., 1986) and considered T_{eff}, $\log g$ and $\log$ (H/He) as free parameters. We produced synthetic spectra at those fixed atmospheric parameters, then analysed the fit between the metal absorption lines in the synthetic and observed spectra. The metal abundances

Table 3.5: Atmospheric parameters for the white dwarfs in our DZ subsample. Parameters for WD J2147−4035 and WD J1922+0233 are derived in this work. The quoted uncertainties are purely of statistical nature as derived from the fits, and are much smaller than the model-dependent systematic uncertainties. The parameters for WD J1644−0449 are taken from Kaiser et al. (2021), except for radius (R) and cooling age (τ) which are calculated in this work. Similarly, the parameters for WD J2356−2054 are taken from Blouin et al. (2019a), except for radius (R) and white dwarf mass ($M_{\rm WD}$) which are calculated in this work. Parameters for WD J1824+1213, WD J1330+6435, WD J2317+1830 and WD J1214−0234 are from Hollands et al. (2021). Observational upper limits of log (H/He) are given where a tight constraint could not be derived.

	$T_{\rm eff}$ (K)	$\log g$ (cm s^{-2})	log (H/He)	R ($\times 10^{-5}$ R$_\odot$)	$M_{\rm WD}$ (M$_\odot$)	τ (Gyr)
WD J2147−4035	3048 ± 35	8.195 ± 0.042	< -5.66	1100 ± 32	0.69 ± 0.02	10.2 ± 0.2
WD J1922+0233	3343 ± 54	8.000 ± 0.055	-2.69 ± 0.17	1247 ± 26	0.57 ± 0.03	9.0 ± 0.2
WD J1824+1213	3350 ± 50	7.41 ± 0.07	-0.07 ± 0.10	1741 ± 55	0.28 ± 0.03	5.5 ± 0.4
WD J1330+6435[a]	3660 ± 50	7.65 ± 0.14	< -4.0	1524 ± 115	0.38 ± 0.07	6.0 ± 1.0
WD J1644−0449	3830 ± 230	7.77 ± 0.23	< -2.0	1404 ± 174	0.45 ± 0.12	6.8 ± 0.2
WD J2356−2054	4040 ± 110	7.98 ± 0.07	-1.5 ± 0.2	1263 ± 52	0.56 ± 0.04	8.0 ± 0.8
WD J2317+1830	4210 ± 50	8.64 ± 0.03	-0.09 ± 0.09	793 ± 21	1.00 ± 0.02	9.5 ± 0.2
WD J1214−0234	4780 ± 50	7.97 ± 0.04	-3.19 ± 0.18	1269 ± 29	0.55 ± 0.02	5.8 ± 0.2

[a] Note that Blouin et al. (2019a) found a higher $T_{\rm eff}$ of 4310 ± 190 K and $\log g$ of 8.26 ± 0.15, which were used by Kaiser et al. (2021) to derive a white dwarf mass ($M_{\rm WD}$) of $0.74 \pm 0.10\,{\rm M}_\odot$. These studies use different model atmospheres to Hollands et al. (2021).

were adjusted to optimise the fit. Keeping these new metal abundances fixed, we produced a new grid of synthetic photometry and repeated the photometric fitting. This process was iterated until the best-fitting atmospheric parameters and metal abundances were found. The uncertainties of the best-fitting atmospheric parameters are dependent on one another and are computed from the covariance matrix of the model atmosphere fit, therefore they are statistical in nature and do not account for systematic uncertainty.

Our iterative procedure was most important for WD J2147−4035 as the metal abundances had a non-negligible effect on its atmospheric parameters. The reason for this effect is most likely due to the low atmospheric hydrogen content in the star, hence the metals provide additional free electrons and impact the photospheric structure. Alternatively, the inclusion of metals in the fit of WD J1922+0233 changed the synthetic photometry by less than 0.01 mag, which is within 1σ and therefore not significant.

A lower limit of 0.05 mag for photometric uncertainties was imposed in the fit of WD J2147−4035. This treatment prevented it from being dominated by the very small observed photometric uncertainties at optical wavelengths which may be underestimated considering the star's extremely dim magnitude, compared to the moderately large IR photometric uncertainties (see Table 3.2). The best-fitting model atmosphere for WD J2147−4035 included optimised fixed metal abundances (see Section 3.6) with $T_{\mathrm{eff}} = 3048 \pm 35$ K, $\log g = 8.195 \pm 0.042$ and $\log(\mathrm{H/He}) < -5.66$. Since a further decrease in the hydrogen content led only to minimal changes of the models, we would not exclude the possibility that our best-fitting $\log(\mathrm{H/He})$ abundance is an upper limit instead of a real determination.

The *Gaia* EDR3 G magnitude uncertainty is an order of magnitude smaller than all other optical photometric uncertainties for WD J1922+0233 (see Table 3.3), therefore we added a common systematic uncertainty of 0.01 mag to all measured photometric uncertainties for the fit, to prevent it being dominated by very small uncertainties. Despite the WD J1922+0233 *Gaia* EDR3 parallax and uncertainty having a relative precision of 1.05 %, we also included the parallax as a free parameter in the fit to propagate extra freedom into T_{eff}, $\log g$ and $\log(\mathrm{H/He})$, resulting in their uncertainties being more realistic. The best-fitting model atmosphere for WD J1922+0233 has $T_{\mathrm{eff}} = 3343 \pm 54$ K, $\log g = 8.000 \pm 0.055$ and $\log(\mathrm{H/He}) = -2.69 \pm 0.17$. The best-fitting parallax is 25.330 ± 0.265, which has a percentage difference to the measured *Gaia* parallax of only 0.126 %.

After the completion of this work, a paper by Bergeron et al. (2022) found significant differences in the atmospheric parameters of WD J1922+0233, notably

$T_{\mathrm{eff}} = 4436 \pm 53\,\mathrm{K}$, $\log g = 8.766$ and $\log(\mathrm{H/He}) = -1.73$. However, the physics involved in our atmospheric models (see Section 3.4) and the ones used in Bergeron et al. (2022) differ slightly. Our models included the more recent H_2-He CIA calculations by Abel et al. (2012), which should be superior to Jørgensen et al. (2000) used by Bergeron et al. (2022). We also included non-ideal effects in the EOS. With our models, we found a satisfactory fit to the photometry of WD J1922+0233 for parameters significantly different from Bergeron et al. (2022). A more detailed discussion is beyond the scope of this chapter.

The best-fitting atmospheric parameters for our subsample are shown in Table 3.5. Note that the small uncertainties given for our parameters only include the statistical errors from our fits and no systematic errors from e.g. model uncertainties, so the real errors are likely larger.

Monochromatic model fluxes were calculated with the best-fitting models including metals in the atmospheric structure calculations for WD J2147−4035 and WD J1922+0233. The best-fitting monochromatic model fluxes and synthetic photometry for both stars were converted to AB magnitudes and are shown in Figures 3.4 and 3.5 as a comparison to all available optical and NIR observed photometry. A reasonable fit is achieved between the observed and synthetic photometry for both objects. A visual offset is seen between the synthetic *Gaia* EDR3 G, and to a lesser extent G_{BP} and G_{RP}, magnitudes and our best-fitting models due to the very broad *Gaia* bandpasses. We note the CIA opacities included in the model atmosphere code (see Section 3.4) have a strong effect on the quality of fit of the best-fitting model for WD J1922+0233 to observed photometry, where Figure 3.5 shows the best-fitting model (solid red line) compared to the identical model with all CIA opacities removed (dotted red line). The effect from CIA opacities in WD J1922+0233 is also clear from the blueward shifted peak of its SED to optical wavelengths, near $0.7\,\mu$m in this case, compared to when CIA opacities are removed. This shift represents the extreme deficit of IR flux due to CIA in this ultra-cool star, despite us lacking observational data in the IR. The SED peak of WD J2147−4035 is near $1.4\,\mu$m and is comparable to the SED peak of the best-fitting model of WD J1922+0233 when CIA opacities are removed, which suggests there are only mild effects from CIA opacity in this remnant.

The white dwarf mass (M_{WD}) and cooling age (τ) of WD J2147−4035 and WD J1922+0233 were derived using model evolutionary sequences with thin hydrogen layers (small total hydrogen masses of $1 \times 10^{-10}\,M_{\mathrm{H}}/M_{\mathrm{WD}}$, where M_{H} is the hydrogen mass), and C/O cores (Bédard et al., 2020), and are presented in Table 3.5 with the rest of our subsample. WD J2147−4035 is relatively massive

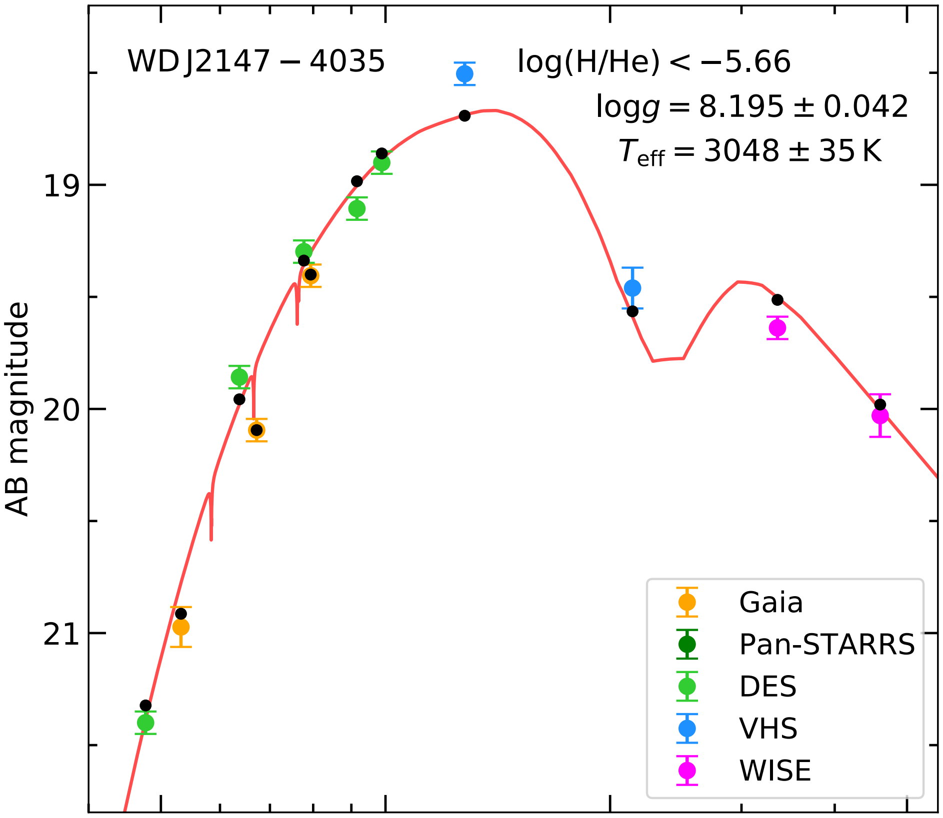

Figure 3.4: Photometric fits between the observed (coloured circles with error bars) and synthetic (black circles) photometry for WD J2147−4035. Monochromatic model fluxes were computed using the best-fitting models including metals (see Section 3.6) and converted to AB magnitudes (red solid line). The predicted *Gaia* EDR3 G, and to a lesser extent $G_{\rm BP}$ and $G_{\rm RP}$, magnitudes are visually offset from the predicted monochromatic magnitudes because of the very broad *Gaia* bandpasses. Error bars correspond to 1σ uncertainties. The legend applies to this figure and Figure 3.5.

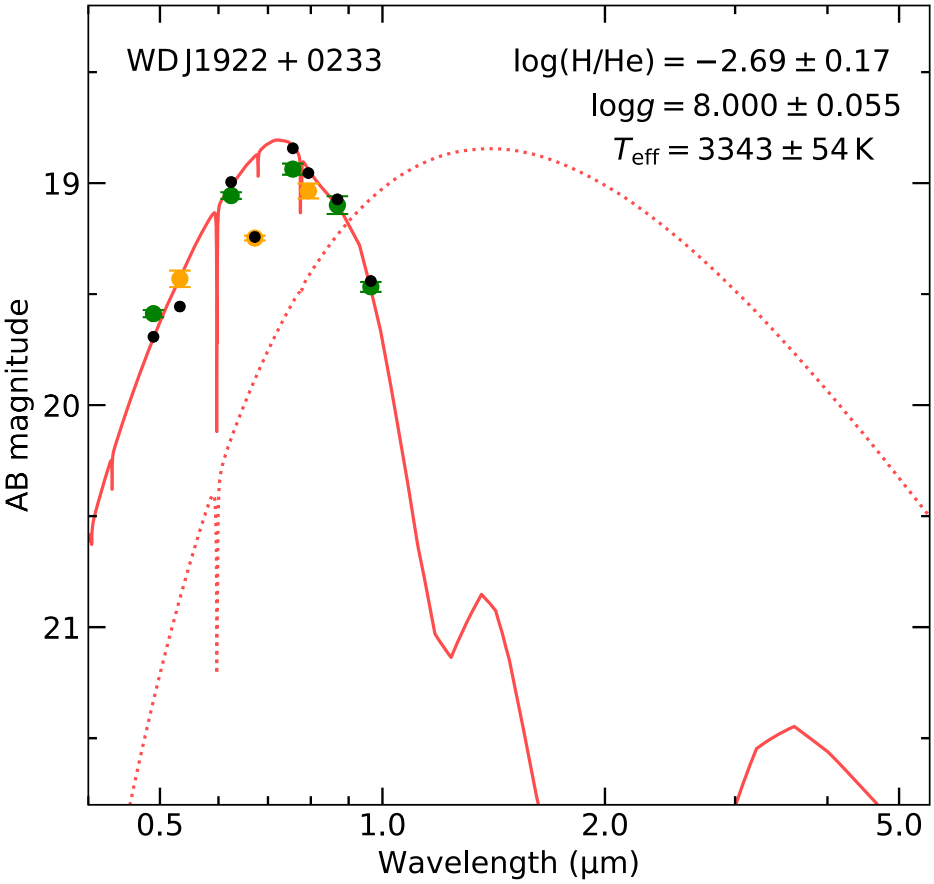

Figure 3.5: Same as Figure 3.4 but for WD J1922+0233. All CIA opacities are removed in the best-fitting model with metals for WD J1922+0233 (red dotted line) to demonstrate the strong effect of CIA opacity on the photometry of this white dwarf.

compared to other cool and ultra-cool remnants with $M_{\rm WD} = 0.69 \pm 0.02\,{\rm M}_{\odot}$ and has the largest cooling age known for a DZ white dwarf of $\tau = 10.21 \pm 0.22$ Gyr. We find $M_{\rm WD} = 0.57 \pm 0.03\,{\rm M}_{\odot}$ for WD J1922+0233 and $\tau = 9.05 \pm 0.22$ Gyr, making it a relatively old white dwarf in terms of cooling age. These white dwarfs have a very low temperature compared to the so-called truncation of the luminosity function at ≈ 4000 K, which is thought to correspond to $\tau \approx 10$ Gyr and thus the oldest white dwarfs in the local Galactic disc (Winget et al., 1987; Kilic et al., 2017). White dwarfs with helium-rich atmospheres are thought to cool more rapidly than ones with hydrogen-rich atmospheres due to the early event of convective coupling (Oppenheimer et al., 2001b; Fontaine et al., 2001), i.e. they will have a lower $T_{\rm eff}$ for the same cooling age. In addition, more massive white dwarfs, and therefore those with smaller radii according to the mass-radius relation of degenerate stars, cool faster than stars of more moderate mass, as they develop a crystallized core earlier so they reach the state of very small specific heat capacity values quicker thus have a rapid final cooling phase (Fontaine et al., 2001). The combination of these effects can help to explain the ultra-cool nature of both stars.

3.6 Metal abundances

The intermediate-resolution optical spectra from our VLT X-Shooter observations of WD J2147−4035 and WD J1922+0233 are shown in Figure 3.1. Strong lines of the Na I D doublet (5893 Å) and K I (7665 Å and 7699 Å) are seen in both spectra. We also detected Ca I (4227 Å) in WD J1922+0233 and Li I (6708 Å) in WD J2147−4035. We made a tentative detection of C_2 in WD J2147−4035 at ≈ 4570 Å, 5000 Å and 5400 Å.

We used an iterative procedure to fit the observed spectra of WD J2147−4035 and WD J1922+0233, using model atmospheres including metals in the atmospheric structure calculations, with the best-fitting atmospheric parameters ($T_{\rm eff}$, $\log g$, $\log$ (H/He); Table 3.5) derived in Section 3.5 to constrain the abundances of detected metals in each star. The individual metal abundances in the models were iterated until a reduced $\chi^2 \approx 1$ was reached. Figures 3.6 and 3.7 show the best-fitting model spectra for WD J2147−4035 and WD J1922+0233 in red, respectively, overlaid on the observed spectra which are zoomed-in on the the metal detections.

The metal abundance measurements of WD J2147−4035 and WD J1922+0233 are presented in Table 3.6 and can be put into the context of metal abundances of other cool DZ white dwarfs found in the literature. The detection and subsequent abundance measurements of K I were possible only after

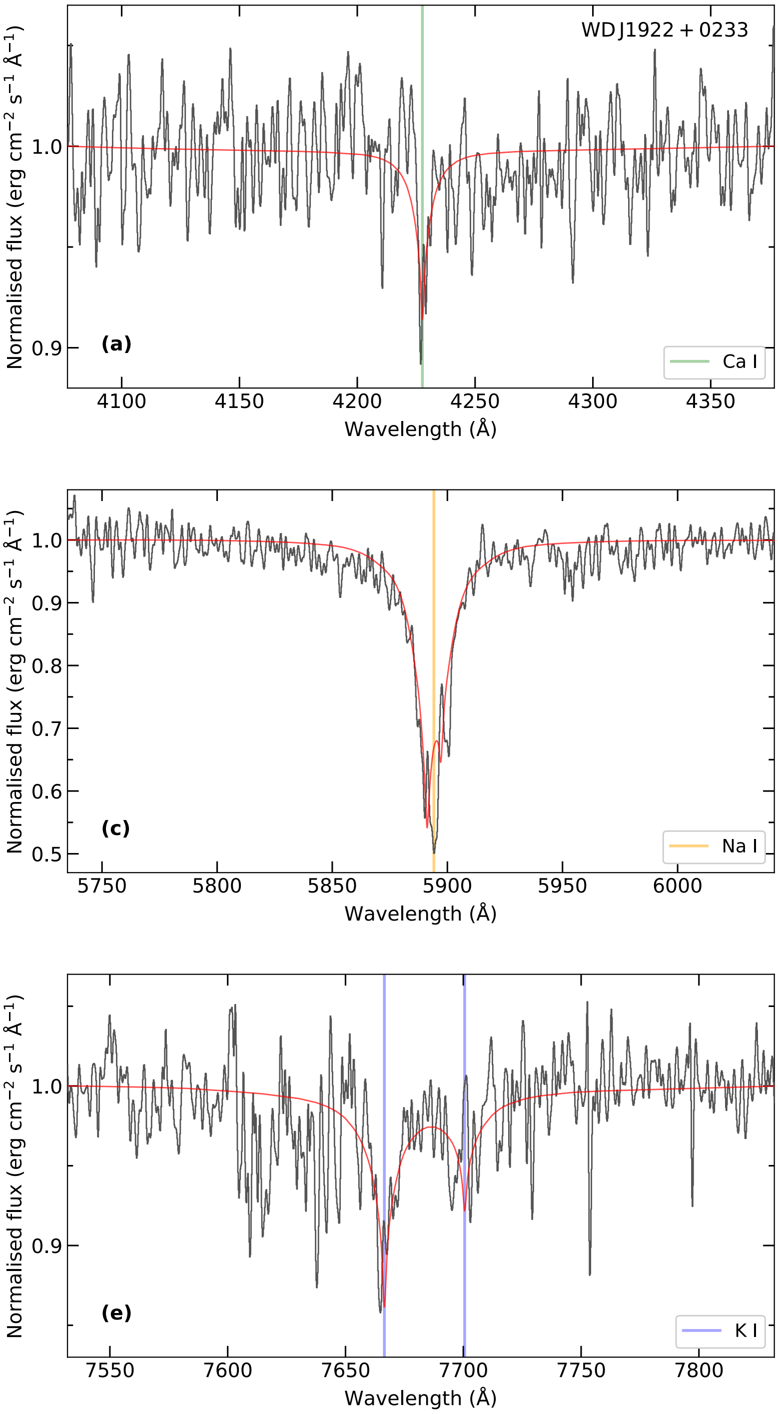

Figure 3.6: VLT X-Shooter normalised spectroscopic observations of WD J1922+0233 zoomed-in on metal detections. The coloured vertical bars indicate the detected metal lines at the appropriate radial velocity of each star (Section 3.7.4). The appropriate radial velocity are applied to the best-fitting models (red). All spectra and models are normalised to a continuum flux of one and convolved with a Gaussian with a FWHM of 1 Å for clarity.

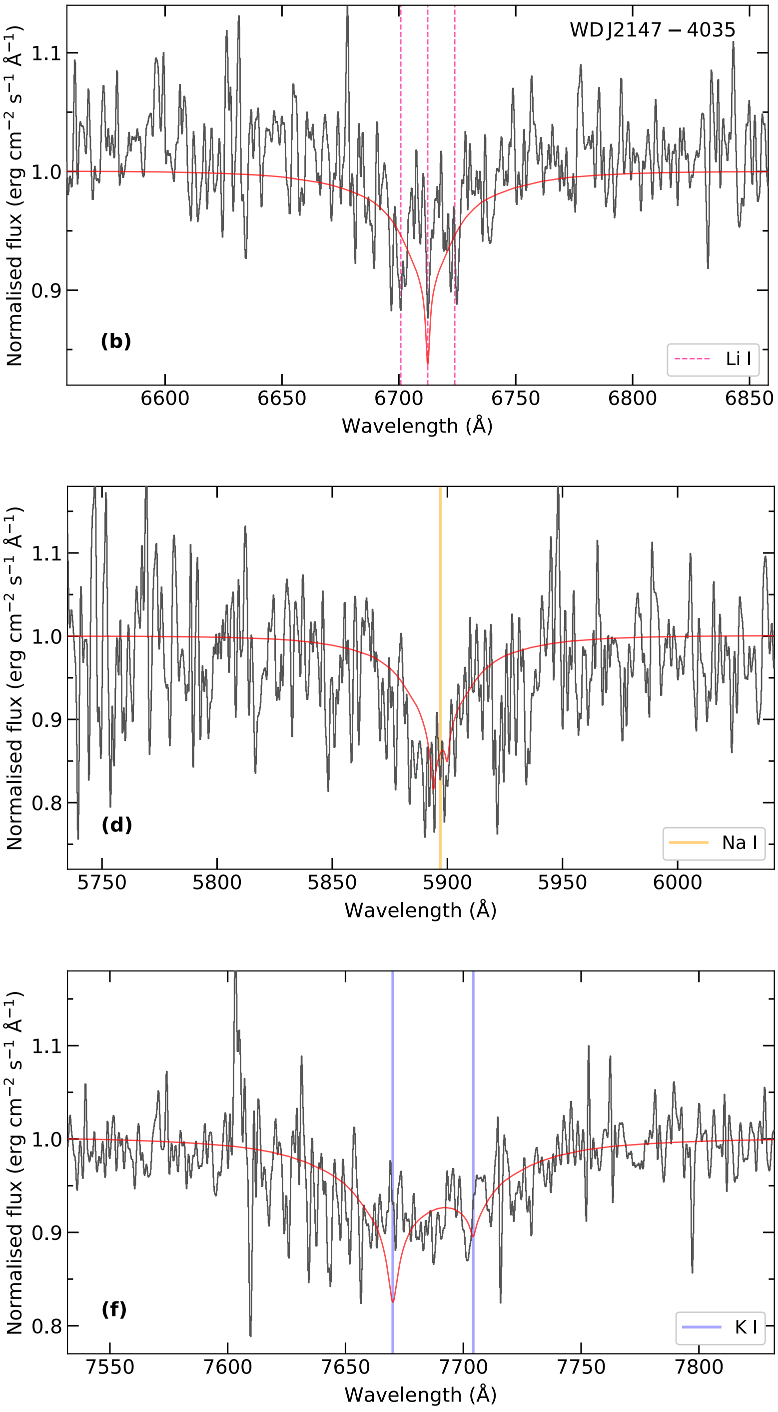

Figure 3.7: Same as Figure 3.6 but for WD J2147−4035. The spectrum in panel (b) shows the Zeeman split Li I (6708 Å) line in WD J2147−4035.

telluric line removal of the atmospheric O_2 absorption band near $\approx 7600\,\text{Å}$ was performed. However, we do not discount the possibility of the K I line shape and strength being affected by the telluric removal as it is an imperfect process. We do not detect Li I in WD J1922+0233 nor Ca I in WD J2147−4035, so we constrained the observational upper limits of these metals by finding the abundance that produced the best-fitting model spectral line just within the noise level of the observed spectra. In Section 3.7.5, we discuss the accretion inferences made from the abundances of the detected metals and observational upper limits for both stars.

C, O, Mg, Si, Al and Fe are not detected in WD J2147−4035 nor WD J1922+0233 but are commonly found in rocky exoplanetesimals and asteroids, and thus in the atmospheres of other DZ white dwarfs (Zuckerman et al., 2007; Klein et al., 2010; Gänsicke et al., 2012; Jura and Young, 2014; Raddi et al., 2015). Therefore, we also included these undetected metals in our model atmospheres and set them to Earth crust (Rudnick and Gao, 2003) abundances relative to sodium (see Section 3.7.5 for further explanation). However, these abundance ratios of Al and Fe for WD J1922+0233 produced absorption lines that were too strong by 0.64 dex and 0.03 dex, respectively, revealing their observational upper limits as $\log(\text{Al}/\text{He}) < -12.65$ and $\log(\text{Fe}/\text{He}) < -12.23$ which we used in the model instead. Table 3.7 displays the values used for all metals included in the model atmospheres of WD J2147−4035 and WD J1922+0233, including the measured abundances of detected metals, observational upper limits and the fixed abundances used for undetected metals.

3.6.1 Magnetic nature of WD J2147−4035

The cool magnetic white dwarf WD J1214−0234 was detected to have the first Zeeman split lithium line in Hollands et al. (2021), where the magnetic field was measured to be 2.1 MG. The Li I spectral line in the X-Shooter spectrum of WD J2147−4035 indicates this star is also magnetic due to it being split into three components from Zeeman splitting. We found a best-fitting magnetic field strength of 0.55 ± 0.03 MG as a result of fitting a constant magnetic field to the Zeeman split Li I line; the three line components produced from this magnetic field are shown in Figure 3.7(a) by the vertical dashed pink lines. We do not analyse sodium or potassium spectral line splitting in WD J2147−4035 because these elements have much larger fine-structure splitting than lithium, hence the pattern is much more complicated than the triplet observed with the lithium line.

Table 3.6: Atmospheric abundance ratios for the white dwarfs in our DZ subsample. Abundances for WD J2147−4035 and WD J1922+0233 were derived in this work. We found the abundances for WD J1644−0449 in Kaiser et al. (2021), WD J2356−2054 in Blouin et al. (2019a), and for WD J1824+1213, WD J1330+6435, WD J2317+1830 and WD J1214−0234 in Hollands et al. (2021). Values for log (H/He) are repeated here for clarity (also found in Table 3.5). Observational upper limits are given for undetected metals. Abundance ratios for solar system benchmarks are calculated from values in McDonough (2000) for bulk Earth, Rudnick and Gao (2003) for the continental crust, and Lodders (2003) for CI chondrites and solar. Fields are left empty where no abundances were given in the literature.

	log (H/He)	log (Ca/He)	log (Na/He)	log (Li/He)	log (K/He)	log (Ca/Na)	log (Li/Na)	log (K/Na)
WD J2147−4035	< −5.66	< −13.20	−13.10 ± 0.20	−13.20 ± 0.20	−12.90 ± 0.20	< −0.10	−0.10 ± 0.28	0.20 ± 0.28
WD J1922+0233	−2.69 ± 0.17	−13.96 ± 0.20	−12.60 ± 0.20	< −13.60	−13.10 ± 0.20	−1.36 ± 0.28	< −1.00	−0.50 ± 0.28
WD J1824+1213	−0.07 ± 0.10	−10.28 ± 0.14	−10.19 ± 0.07	−11.95 ± 0.08	–	−0.21 ± 0.16	−1.76 ± 0.11	–
WD J1330+6435	< −4.00	−10.94 ± 0.36	−10.35 ± 0.12	−11.96 ± 0.29	–	−0.59 ± 0.38	−1.61 ± 0.31	–
WD J1644−0449	< −2.00	−9.5 ± 0.20	−9.5 ± 0.20	−11.2 ± 0.20	−10.9 ± 0.20	0.00 ± 0.28	−1.70 ± 0.28	−1.40 ± 0.28
WD J2356−2054	−1.5 ± 0.2	−9.4 ± 0.1[b]	−8.3 ± 0.2	< −11.7[c]	< −10.4[c]	−1.10 ± 0.22	< −3.40	< −2.10
WD J2317+1830	−0.09 ± 0.09	−10.79 ± 0.12	−9.96 ± 0.07	−11.19 ± 0.08	< −10.50	−0.83 ± 0.14	−1.23 ± 0.11	< −0.54
WD J1214−0234	−3.19 ± 0.18	−10.08 ± 0.11	−9.53 ± 0.06	−11.83 ± 0.08	−10.16 ± 0.08	−0.55 ± 0.13	−2.30 ± 0.10	−0.63 ± 0.10
Bulk Earth	–	–	–	–	–	0.74	−2.69	−1.28
Continental crust	–	–	–	–	–	−0.22	−2.48	−0.25
CI chondrites	6.96 ± 0.05	5.00 ± 0.03	4.98 ± 0.03	1.96 ± 0.06	3.77 ± 0.05	0.02 ± 0.04	−3.02 ± 0.07	−1.21 ± 0.06
Solar	1.10 ± 0.01	−4.54 ± 0.02	−4.60 ± 0.03	−9.80 ± 0.10	−5.78 ± 0.05	0.06 ± 0.04	−5.20 ± 0.10	−1.18 ± 0.06

[b] Updated value from Blouin et al. (2019c).

[c] Updated value from Kaiser et al. (2021).

3.6.2 A 13 h photometric period

Magnetism can result in inhomogeneous brightness distributions across the surface of the white dwarf, which in turn leads to photometric variability on the white dwarf spin period (e.g. Brinkworth et al., 2013). We investigated the photometric variability of WD J2147−4035 by inspecting the full-frame images (FFI) of the Transiting Exoplanet Survey Satellite (*TESS*; Ricker et al., 2014), which observed the star in sectors one and 28. We split the *TESS* full frame image light curves into two segments per sector, before and after the gap occurring during the data downlink. We clipped $\simeq$ three days at the end of each segment of the Cycle 28 data, where the light curves displayed large-amplitude structures that most likely result from the data reduction (given that WD J2147−4035 has a *TESS* magnitude of $T \simeq 18.5$, extracting a light curve is challenging). We then computed discrete Fourier transforms for the four individual light curves using the TSA context within MIDAS (Figure 3.8). All four periodograms contain a strong signal at $\simeq 1.85\,\mathrm{d}^{-1}$, corresponding to a period of $\simeq 13\,\mathrm{h}$. We determined periods of 12.960 ± 0.044, 13.011 ± 0.055, 12.986 ± 0.067, $12.851 \pm 0.064\,\mathrm{h}$ from the four segments by fitting a sine curve to the data, with amplitudes of $1.5 \pm 0.1\,\%$. We suggest that this consistently detected photometric signal represents the spin period of the white dwarf, which is compatible both in amplitude of the modulation and in period with the rotation variability commonly observed in magnetic white dwarfs.

3.6.3 Carbon detection in WD J2147−4035

We made a tentative detection of C_2 in WD J2147−4035 due to the very broad, rounded absorption features centred at $\approx 4570\,\text{Å}$, $5000\,\text{Å}$ and $5400\,\text{Å}$ being consistent with the three strongest C_2 Swan band systems (progressions; Johnson, 1927) when broadened and empirically blueshifted from their nominal wavelengths. These absorption features are similar to those found in cool DQpec white dwarfs, which have distorted carbon features in their optical spectra presenting rounded profiles and centroid wavelengths blueshifted by $\approx 100 - 300\,\text{Å}$ (Hall and Maxwell, 2008). Studies have found that the high atmospheric pressure in cool DQpec stars drives this distortion (Kowalski, 2010), however it is thought that a more complex combination of high atmospheric pressure, chemical composition and magnetic field strength is responsible for the varying distortions observed in individual stars, but the specific mechanisms are currently not fully understood (Liebert et al., 1978; Bergeron et al., 1994; Schmidt et al., 1995, 1999; Hall and Maxwell, 2008; Blouin et al., 2019b).

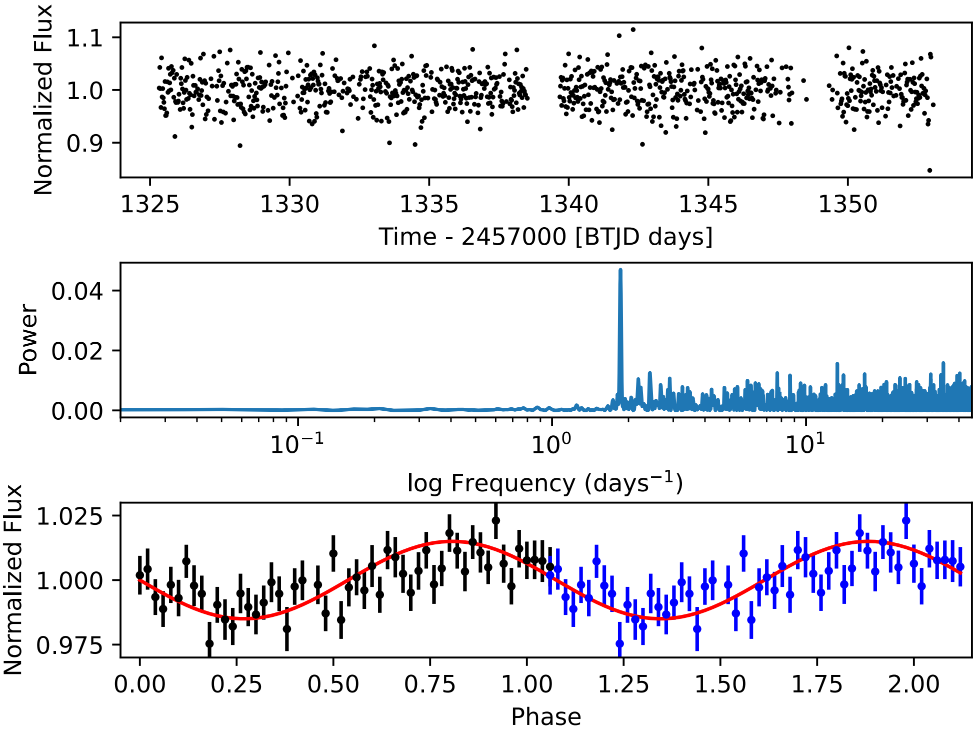

Figure 3.8: FFI *TESS* data from the Sector one observation of WD J2147−4035. The cleaned, de-trended lightcurve is shown in the top panel. The middle panel shows the Lomb-Scargle periodogram, which exhibits a clear signal at $\simeq 0.54$ days. The bottom panel displays the binned phase-folded lightcurve at this nominal period with the data repeated for illustrative purposes (blue points). A sine wave at the same period is shown in red overlay.

One DQpecP and four DQpec stars are found in the MWDD with $T_{\rm eff} < 5000\,{\rm K}$ (in increasing temperature order): LP 351−42, SDSS J1803202.57+232043.3, SDSS J082955.77+183532.6, GJ 3614 and PM J12476+0646. LP 351−42 and GJ 3614 have strong magnetic fields of 100 MG and 50 MG, respectively, in addition to LP 351−42 having detectable polarisation hence its classification of DQpecP (McCook and Sion, 1999a). The other three white dwarfs do not have detected magnetic fields and none of the stars have published log (H/He) atmospheric abundances. The C_2 progressions in all five white dwarfs are blueshifted with respect to the nominal wavelengths, with the largest distortions evident in GJ 3614 and LP 351−42. The C_2 progressions observed in LP 351−42 are in excellent agreement with the broad absorption features in WD J2147−4035 and are shown in Figure 3.1 with aqua vertical lines. LP 351−42 is $\approx 1250\,{\rm K}$ warmer than WD J2147−4035 and has a significantly stronger magnetic field so the reason for this agreement is unclear. An empirical blueshift of $\approx 20\,$Å to the progressions in SDSS J1803202.57+232043.3, which is $\approx 1350\,{\rm K}$ warmer than WD J2147−4035, also provides excellent agreement to the absorption features in WD J2147−4035. The other three DQpec stars require larger blueshifts to their observed progressions to fit the features of WD J2147−4035.

We do not attempt to fit the distorted C_2 progressions in WD J2147−4035 using our model atmospheres as the high atmospheric density, relatively weak bands and low signal-to-noise of the X-Shooter spectrum make a quantitative analysis particularly challenging. However, we still assign the spectral type DZQH to this star. The combination of metals polluting WD J2147−4035, including sodium, lithium, potassium and tentatively carbon, in addition to its ultra-cool temperature and magnetic nature, makes this an extremely rare white dwarf.

3.7 Discussion

3.7.1 Neutral line broadening

Hollands et al. (2021) used an empirically determined factor of ten to reduce the neutral-broadening constant of lithium in their models to extract a good fit to the observations. We found that a reduction factor of 100 gave the best-fitting model to the equivalent width (W_λ) and shapes of observed absorption lines in WD J2147−4035 and WD J1922+0233. Our ad-hoc treatment of the neutral-broadening constant was applied for all observed metals.

The standard neutral-broadening constants for WD J2147−4035 and WD J1922+0233 were calculated using the impact approximation, which is the standard theory of line broadening (Kolb and Griem, 1958; Griem, 1960, 1974). The condition for this application is that the time of effective interaction between two particles, deemed the emitter and perturber, is much shorter than the time between interactions. In our model, the mean distance between emitter and perturber in the photosphere is ≈ 1 Å therefore this is definitely not the case – the emitter is constantly affected by interactions with the perturbers. Alternative approaches include the quasistatic theory (Mozer and Baranger, 1960; Baranger, 1962), which traditionally assumes van der Waals interactions, or the unified theories (Voslamber, 1969; Smith et al., 1969). However, none of these are applicable at ≈ 1 Å distances.

A study performed by Nur et al. (2015) with high density argon corona plasma at very low temperatures found that with increasing hydrostatic pressure the line broadening of gaseous Ar I follows a positive linear relation with particle density, yet when transitioning to a fluid this relation ceases and the line width appears significantly narrower than expected from extrapolation and even decreases at higher densities (see Fig. 5 of Nur et al. 2015). Nur et al. (2015) used a maximum particle density an order of magnitude lower than the density in the photosphere of WD J2147−4035 and WD J1922+0233, so the use of an empirical broadening constant on metal lines within models for ultra-cool DZ white dwarfs may have a plausible justification. Even so, the dense fluid physics involved within the extremely high-pressure photospheres of these stars requires further study so an appropriate theory of line broadening at these densities can be created.

3.7.2 Nature of WD J2147−4035 and WD J1922+0233

The observations of WD J2147−4035 suggest much milder atmospheric CIA compared to WD J1922+0233 because it is very red, with $g - z = 2.29$ mag. There could be two overlapping explanations for the nature of WD J2147−4035: a vastly different log (H/He) ratio to WD J1922+0233, resulting in a much lower H_2 abundance and CIA opacity; or a significant change in non-ideal effects, resulting in the dissociation of H_2 molecules. The presence of metal lines is helpful to break this degeneracy, although the empirical broadening factor needed to fit them in both objects is a significant impairment to extract atmospheric conditions from the metal lines. The main evidence that can be gathered from the metal lines is that hydrogen-dominated atmospheres can be excluded for both objects, making a strong case that cool white dwarfs with unusually strong CIA have mixed log (H/He) atmospheres, as previously accepted from indirect evidence (Kilic et al., 2020). Furthermore, strong non-ideal effects that could ionise more H_2 and therefore force the model fluxes to redder wavelengths, would also ionise alkali metals with low ionisation potentials compared to the H_2 molecule. Therefore, metal line observations also put an upper limit on the strength of non-ideal effects.

The unusual position of WD J1922+0233 on the HRD (Figures 3.2 and 3.3) suggests its nature can be explained by two scenarios: either it is relatively massive which caused it to have a higher (fainter) absolute magnitude than stars of more moderate mass, hence it is placed vertically below the main white dwarf cooling sequence; or, flux suppression in the red optical and IR due to CIA caused the star to have a peak flux emission at bluer wavelengths, resulting in a horizontal placement blueward of the main white dwarf cooling sequence. We conclude the latter is true as we derived a moderate mass for WD J1922+0233 in Section 3.5 and found its SED is indicative of strong CIA opacity due to an extreme IR flux deficit in Section 3.6. Also, cool white dwarfs typically have dense photospheres compared to their warmer counterparts; however, an increasingly higher atmospheric composition of $\log(\mathrm{H/He})$ decreases the density. The complex interplay between photospheric density, non-ideal EOS effects and the abundance of H_2 controls the intensity of CIA (Blouin et al., 2017, 2018a). The maximum intensity of the H_2-He CIA corresponds to an atmospheric abundance of $\log(\mathrm{H/He}) \simeq -3$ (Kilic et al., 2020), which is close to our best-fitting abundance of $\log(\mathrm{H/He}) = -2.69 \pm 0.17$ for WD J1922+0233. This is consistent with observations of strong CIA opacity in the relatively blue WD J1922+0233.

Given available information, the best explanation for the colour differences between WD J2147−4035 and WD J1922+0233 is that the former has a much lower $\log(\mathrm{H/He})$ ratio and only mildly enhanced non-ideal effects compared to WD J1922+0233, resulting in much milder CIA.

3.7.3 Nature of IR-faint white dwarfs

We note that our grid of models is able to provide reasonable solutions for the spectroscopy and photometry of both WD J2147−4035 and WD J1922+0233 with the same microphysics, despite their vastly different positions in the HRD. Yet, tests using our grid of models with $3000\,\mathrm{K} < T_{\mathrm{eff}} < 10\,000\,\mathrm{K}$, $7.0 < \log g < 9.5$ and $-5.0 < \log(\mathrm{H/He}) < 0.0$ proved unable to explain the ultra-blue sequence of DC white dwarfs observed in Figures 3.2 and 3.3 and previously identified in Kilic et al. (2020); Bergeron et al. (2022). The most likely explanation for this behaviour is that the intricate balance between CIA and non-ideal effects is not yet fully accurate in our models for these stars.

Nevertheless, the discovery of WD J1922+0233, the first IR-faint DZ white dwarf with flux suppression in the red optical and IR from strong CIA, and its comparison with other ultra-cool DZ stars, opens a new window to understand the atmospheric composition of IR-faint white dwarfs. These observations suggest that they form a small sub-sample of all cool stellar remnants that have a rather narrow range of $\log(\mathrm{H/He})$ around ≈ -3.0, with the exact value subject to significant modelling uncertainties. This is supported by the finding that all other ultra-cool DZ white dwarfs, with a $\log(\mathrm{H/He})$ ratio that is either small (< -6.0) or large (> -1) according to Table 3.5, reside closer to the main cooling sequence in the various HRDs. WD J1214−0234 has $\log(\mathrm{H/He}) \approx -3.0$ so could be a future member of the ultra-blue sequence, as its current T_{eff} is too high to allow this transition.

The spectral evolution of white dwarfs, i.e. the evolution of the ratio of He- to H-dominated atmospheres, has been extensively studied in recent years (Blouin et al., 2019b; Cunningham et al., 2020; McCleery et al., 2020; Bédard et al., 2020; López-Sanjuan et al., 2022). These studies suggest that the ratio of He- to H-dominated atmospheres is ≈ 0.3 in the range $5000\,\mathrm{K} < T_{\mathrm{eff}} < 6000\,\mathrm{K}$, where it is possible to constrain atmospheric composition from the presence or absence of the Hα line. However, Gentile Fusillo et al. (2020) have demonstrated from optical and IR HRDs that the vast majority of cool ($T_{\mathrm{eff}} < 5000\,\mathrm{K}$) DC white dwarfs, residing near the main cooling sequence, could have either H- or He-rich atmospheres. In other words, there is no clear separation in colour space between these two atmospheric classes, preventing any robust constrain on the spectral evolution of very cool white dwarfs. This is consistent with both He- and H-rich ultra-cool DZ white dwarfs residing at the end of the main white dwarf cooling track in the different HRDs. We disagree with the suggestion of Kilic et al. (2020); Bergeron et al. (2022) that the observations provide evidence of spectral evolution towards strong H-atmosphere dominance for cool DC white dwarfs ($T_{\mathrm{eff}} < 5000\,\mathrm{K}$).

3.7.4 Total age, mass and population membership

Using the M_{WD} we derived (Table 3.5) and the initial-to-final-mass relation (IFMR) from Cummings et al. (2018), we calculated the progenitor mass of WD J2147−4035 to be $2.47 \pm 0.22\ \mathrm{M}_{\odot}$ with a main-sequence lifetime of 0.5 Gyr, with asymmetric 1σ error bars ranging from $0.4 - 0.7$ Gyr. We therefore found the total age to be 10.7 ± 0.3 Gyr which is ≈ 1 Gyr above WD J2317+1830 (Hollands et al., 2021), the most massive object in our DZ subsample (Table 3.5).

Following the same procedure as for WD J2147−4035, we calculated an approximately solar progenitor mass of $1.01 \pm 0.40\,\mathrm{M}_{\odot}$ for WD J1922+0233. The main-sequence lifetime of WD J1922+0233 for solar metallicity therefore has a median of 10.5 Gyr, ranging from 3.8 Gyr to surpassing the age of the Universe (Hurley et al., 2000). Together with the cooling age (Table 3.5), we found the total

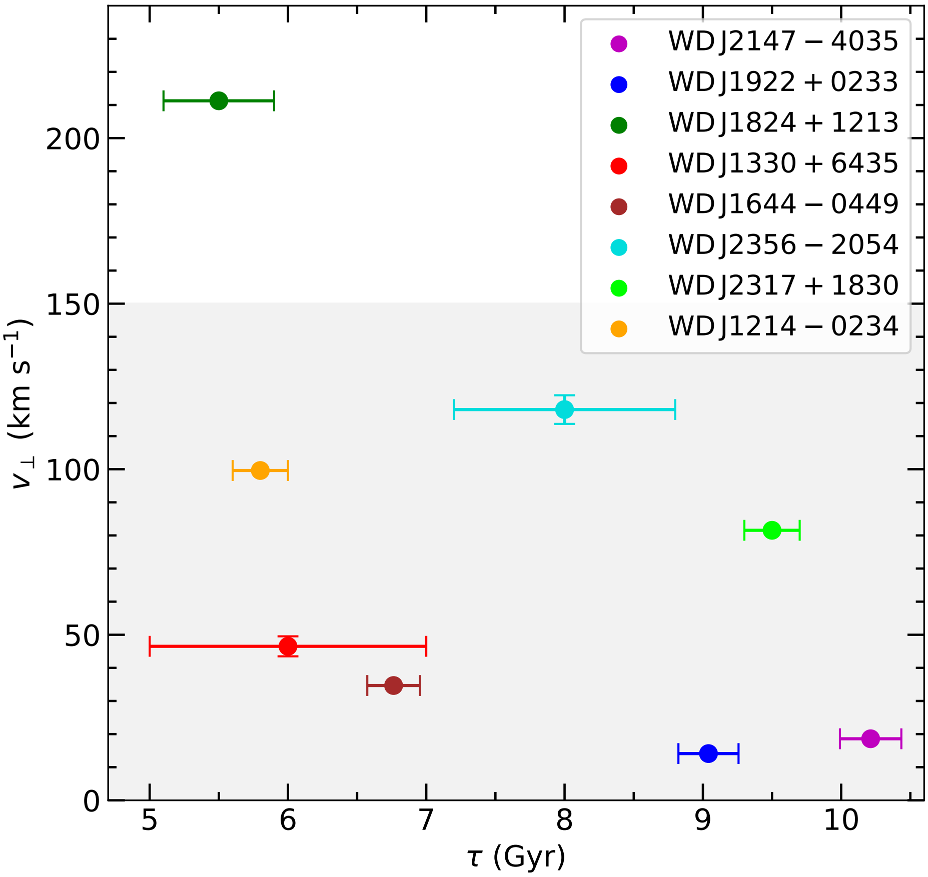

Figure 3.9: Tangential velocity ($v_\perp$) as a function of cooling age (τ) for each DZ white dwarf in our subsample, where error bars represent 1σ uncertainties but are omitted when they lie within the points. The shaded region represents $v_\perp$ consistent with Galactic disc membership. The legends in this figure and Figure 3.10 apply to both panels.

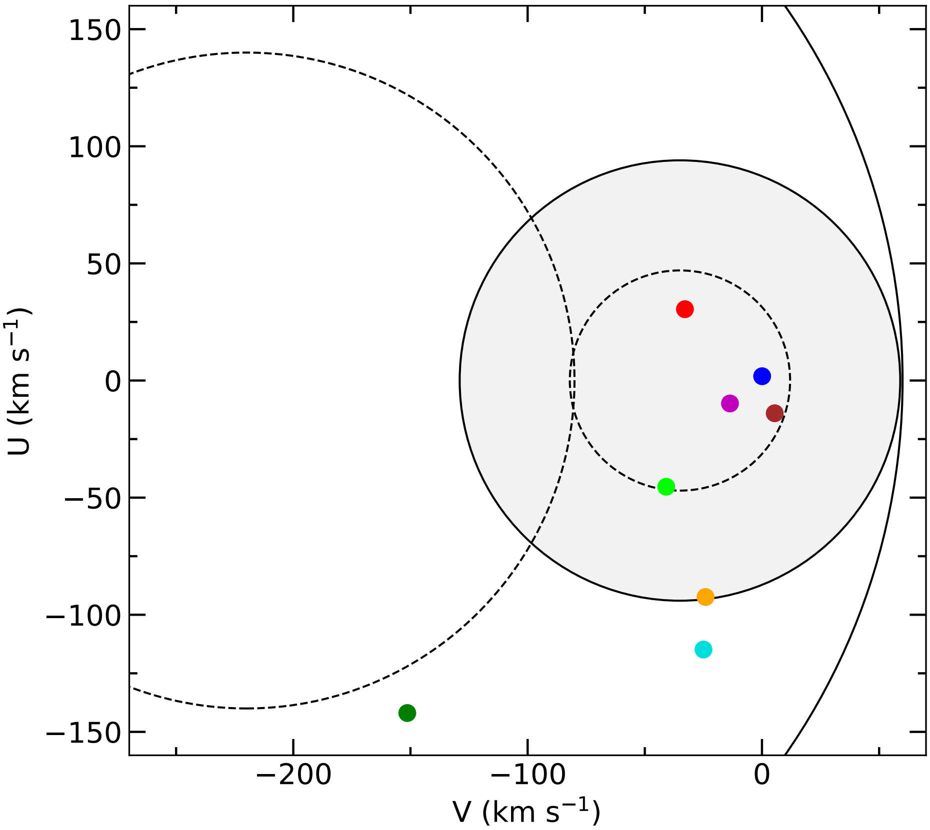

Figure 3.10: Kinematics of each DZ white dwarf in our subsample. The shaded region represents $v_\perp$ consistent with Galactic disc membership. The $v_\perp$ of each subsample DZ star is transformed into Galactic radial (U) and rotational (V) velocity components assuming zero radial velocity. The 1σ and 2σ velocity dispersions of the Galaxy's halo and disc (shaded) are marked by dashed and solid ellipses, respectively. The legends in this figure and Figure 3.9 apply to both panels.

age of WD J1922+0233 to be over 13.8 Gyr which is incompatible with the age of the Milky Way. We conclude that our current model underestimates the mass of WD J1922+0233, likely due to the physics of strong CIA not being fully understood and the uncertainties from our fits only being of a statistical nature, hence its total age remains unknown.

The M_{WD} of remnants with $T_{\mathrm{eff}} < 5000\,\mathrm{K}$ are systematically lower[4] than those of warmer white dwarfs (Bergeron et al., 2019; McCleery et al., 2020; Tremblay et al., 2020), which is inconsistent with the Galactic model prediction of white dwarf cooling at constant mass (Tremblay et al., 2016). This is also the case where strong CIA is present, and likely associated with the physical uncertainties that render their atmospheres notoriously challenging to model (e.g. Gianninas et al., 2015; Bergeron et al., 2022, and see Sections 3.4 and 3.7.1).

The stars in our DZ subsample also suggest M_{WD} underestimations. Three subsample stars have $M_{\mathrm{WD}} \lesssim 0.51\mathrm{M}_{\odot}$ which is not possible from single stellar evolution so these masses must be underestimated (Cummings et al., 2018). Combined with the uncertainties from our fits and existing published ones being of a statistical nature so the real uncertainties are likely larger, it is probable the derived masses of our DZ subsample are low estimates. Although, even if the M_{WD} of WD J2147−4035 was underestimated by $\approx 0.1\,\mathrm{M}_{\odot}$, this would only make the total age smaller by $\approx 0.5\,\mathrm{Gyr}$, given the large cooling age and short main-sequence lifetime. Therefore, WD J2147−4035 is unambiguously one of the oldest known metal-polluted white dwarfs.

To understand the population membership of the DZ subsample, we calculated the tangential velocity ($v_{\perp}$) of each white dwarf using the method described in McCleery et al. (2020) and show the results in Table 3.1 and Figure 3.9 as a function of cooling age (τ). WD J2147−4035 has $v_{\perp} = 18.59 \pm 0.26\,\mathrm{km\,s^{-1}}$ and WD J1922+0233 has $v_{\perp} = 14.11 \pm 0.15\,\mathrm{km\,s^{-1}}$. All but one remnant have $v_{\perp} < 150\,\mathrm{km\,s^{-1}}$ suggesting they are Galactic disc candidates (Gianninas et al., 2015). We do not differentiate between thick and thin disc membership in this work, we instead treat them as one Galactic disc population. WD J1824+1213 has a significantly higher $v_{\perp}$ than the other objects and, together with its relatively small τ of $5.5 \pm 0.4\,\mathrm{Gyr}$, is our only Galactic halo candidate – this conclusion was also drawn by Hollands et al. (2021) and Kilic et al. (2019). Assuming that halo membership makes it the oldest object in the subsample, it requires a large main-sequence lifetime. This is consistent with WD J1824+1213 having the lowest M_{WD}

---

[4] The average M_{WD} for the local 40 pc white dwarf volume sample is $0.66\,\mathrm{M}_{\odot}$ for $T_{\mathrm{eff}} > 5000\,\mathrm{K}$ and $0.52\,\mathrm{M}_{\odot}$ for $T_{\mathrm{eff}} < 5000\,\mathrm{K}$ (Gentile Fusillo et al., 2021).

in Table 3.5.

To further analyse the population membership of our DZ subsample, we transformed their $v_\perp$ into Galactic velocity components U, V and W (Johnson and Soderblom, 1987), which indicate motion radially away from the Galactic center, in the direction of the Galaxy's rotation and perpendicular to the disc, respectively, using *Gaia* EDR3 astrometry and corrected parallaxes from Table 3.1; we present the velocity component values there also. These velocity components are computed in Hollands et al. (2021) for WD J1824+1213, WD J1330+6435, WD J1214−0234 and WD J2317+1830 using *Gaia* DR2 astrometry so updated measurements are reported here. We assumed zero radial velocity in our calculations following standard practices (Hollands et al., 2021; Kaiser et al., 2021) and due to uncertainties in the gravitational redshift corrections from the mass uncertainties. We rely on the previous study of Oppenheimer et al. (2001a) to analyse the velocity dispersions of our subsample and assess their 1σ or 2σ disc or halo membership. We plot our results in Figure 3.10, where the largest dashed and solid ellipses encapsulate the velocity dispersions consistent with the Galaxy's halo up to 1σ and 2σ, respectively. The shaded region represents velocity dispersions consistent with the Galaxy's disc up to 1σ (dashed ellipsis) and 2σ (solid ellipsis). WD J1824+1213 is a likely halo candidate as it has velocity components consistent with 2σ velocity dispersions of the Galaxy's halo. WD J2147−4035, WD J1922+0233, WD J1330+6435, WD J1644−0449 and WD J2317+1830 have velocity components consistent with at least 2σ of the Galaxy's disc hence likely have disc membership. The membership conclusions for the above five subsample objects are consistent with those drawn from their $v_\perp$. WD J2356−2054 and WD J1214−0234 both have an uncertain disc or halo membership allocation in U vs. V space, yet their $v_\perp$ indicates disc membership.

We measured the wavelength shift of the lithium spectral line central component in WD J2147−4035 and the sodium spectral line in WD J1922+0233 compared to rest wavelengths and calculated the line velocities of each star as $120.6 \pm 16.8\,\mathrm{km\,s^{-1}}$ and $-20.1 \pm 10.2\,\mathrm{km\,s^{-1}}$, respectively. Despite uncertainties in the calculations, we corrected for each star's gravitational redshift to determine radial velocities, v_rad, of $80.6 \pm 17.1\,\mathrm{km\,s^{-1}}$ for WD J2147−4035 and $-49.1 \pm 10.6\,\mathrm{km\,s^{-1}}$ for WD J1922+0233. Accounting for v_rad in the calculations of U, V and W for WD J2147−4035 and WD J1922+0233, both stars still indicate Galactic disc membership.

We do not include the total ages of WD J2147−4035 and WD J1922+0233 in our membership assessment because previous estimates of the Galactic disc age from white dwarfs (Winget et al., 1987; Kilic et al., 2017) are thought to be underestimated due to ^{22}Ne dilution cooling delays (Tremblay et al., 2019a; Blouin et al., 2020b; Kilic et al., 2020) being omitted from earlier crystallisation calculations. Nevertheless, both white dwarfs could be utilised in future studies for constraining an upper age limit for the disc of the Milky Way.

3.7.5 Accreted planetary debris

Relative metal abundances measured in the atmospheres of metal-polluted white dwarfs using spectral fitting (Section 3.6) inform us of the bulk compositions of debris accreted from planetary systems. However, atmospheric abundance ratios change over time due to atomic diffusion causing metals to settle from the bottom of the convection zone (CVZ) to the interior. The abundance evolution history of DZ stars can be traced backwards in time by taking into account the diffusion (sinking) timescales ($\tau_{\rm z}$) of individual elements, which each have different rates of diffusion. Cool DZ stars have long $\tau_{\rm z}$ which is the primary mechanism responsible for the long-term evolution of atmospheric abundances, yet the $\tau_{\rm z}$ of all elements are many orders of magnitude shorter than white dwarf cooling ages (Koester, 2009). Therefore, the observation of metal lines in the atmospheres of white dwarfs requires recent or active accretion (Vauclair et al., 1979).

Accretion episodes are typically described as three simplified phases (Koester, 2009): the increasing state, where material is actively accreted into the white dwarf photosphere so its atmospheric composition initially resembles that of the debris as it is instantaneously mixed throughout the CVZ, then the composition diverges as metals diffuse at their individual diffusion velocities through the bottom of the CVZ; steady-state, or accretion-diffusion equilibrium, which is reached if the duration of the accretion event extends over several diffusion timescales; and the decreasing state, where accretion has stopped and the atmospheric abundances exponentially decrease according to the individual diffusion time scales of each metal.

Based on our abundance analysis (see Section 3.7.5), we assume that WD J2147−4035 and WD J1922+0233 are not currently accreting but have instead retained debris from an earlier accretion event. Therefore, we proceed with our analysis on the assumption that both white dwarfs have stopped accreting (i.e. are in the decreasing phase).

A lower limit of the accreted parent body mass ($M_{\rm z,tot}$) can be constrained by the sum over all individual metal masses ($M_{\rm z}$) currently contained in the CVZ, as this measurement is independent of the accretion state (Izquierdo et al., 2021). We used the envelope code described in Koester et al. (2020) to compute $\tau_{\rm z}$, the

Table 3.7: For each metal (Z) included in the model atmospheres for WD J2147−4035 and WD J1922+0233, the first ten rows show the atmospheric abundances (log (Z/He)) we used (observationally detected metals and subsequently measured abundances include uncertainties; observational upper limits are denoted with a less than ($<$) symbol; undetected metals were fixed to the abundances shown and have no associated uncertainties), diffusion timescales (τ_{z}) in Myr and metal masses (M_{z}) in $\times 10^{15}$ g. The subsequent rows show the logarithm of the fractional convection zone mass ($M_{\mathrm{cvz}}/M_{\mathrm{WD}}$) and the minimum mass of the accreted parent body when considering only metals ($M_{\mathrm{z,tot}}$) and hydrogen (M_{H}). Convective overshoot (Cunningham et al., 2019) with a pressure scale height of one is included in the envelope code (Koester et al., 2020) used to calculate parameters.

	WD J2147−4035			**WD J1922+0233**		
Z	log (Z/He)	τ_{z}	M_{z}	log (Z/He)	τ_{z}	M_{z}
Li	-13.20 ± 0.20	4.14	0.699	< -13.60	9.21	0.55
C	-14.69	3.84	0.04	-14.58	8.73	0.10
O	-11.63	2.76	59.94	-11.38	6.38	209.34
Na	-13.10 ± 0.20	1.70	2.92	-12.60 ± 0.20	4.01	18.11
Mg	-12.00	1.68	38.79	-12.73	3.97	14.19
Al	-12.61	1.44	10.59	< -12.65	3.43	18.92
Si	-12.10	1.44	35.63	-11.61	3.44	216.20
K	-12.90 ± 0.20	0.97	7.87	-13.10 ± 0.20	2.35	9.75
Ca	< -13.20	0.97	4.04	-13.96 ± 0.20	2.35	1.38
Fe	-13.14	0.64	6.47	< -12.23	1.57	103.01
$\log(M_{\mathrm{cvz}}/M_{\mathrm{WD}})$	-5.32			-4.95		
$M_{\mathrm{z,tot}}$	1.67×10^{17} g			5.92×10^{17} g		
M_{H}	1.43×10^{21} g			6.50×10^{24} g		

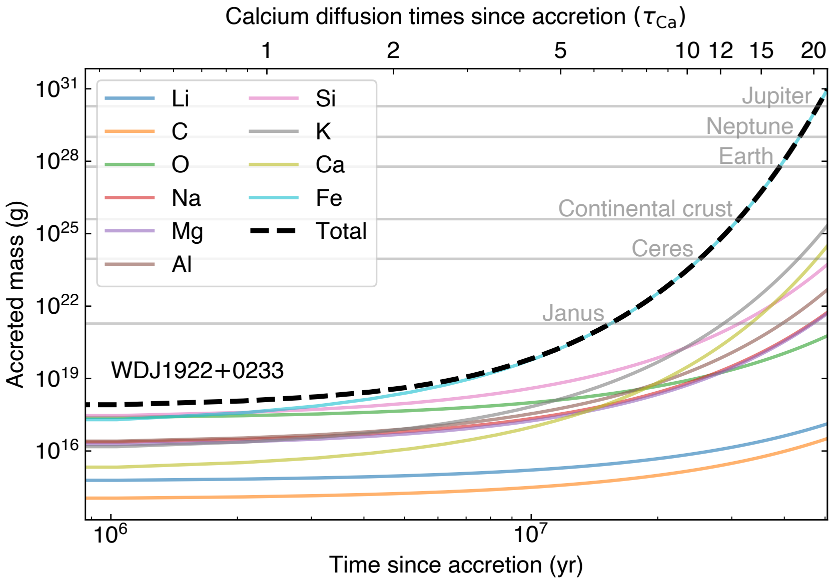

(a)

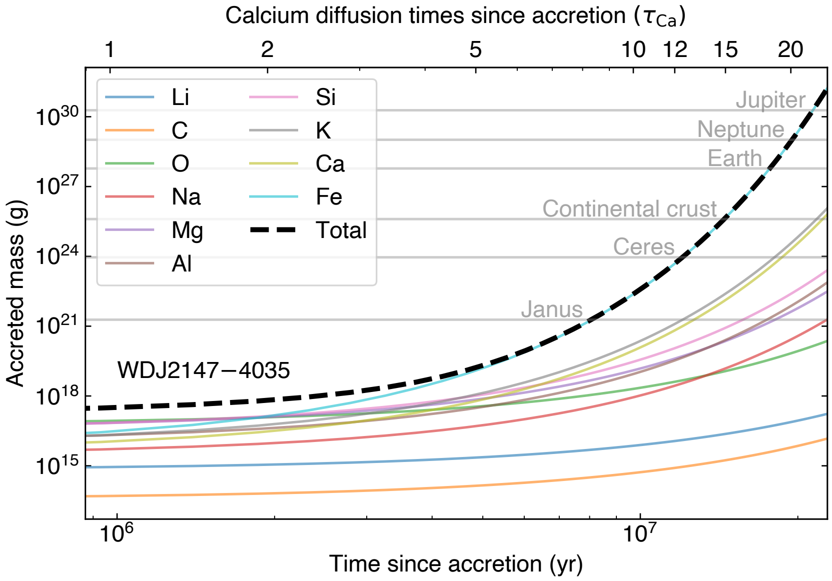

(b)

Figure 3.11: Masses of metals (M_z) in the convection zone of (a) WD J1922+0233 and (b) WD J2147−4035, which are representative of the accreted parent body masses, as a function of time and calcium diffusion times ($\tau_{\rm Ca}$) since accretion ceased. The M_z of metals used in the model atmospheres are shown by coloured solid lines. The black dashed lines represent the minimum accreted parent body mass ($M_{\rm z,tot}$) depending when accretion stopped. We cannot unambiguously determine the fraction of hydrogen mass accreted from planetary debris from the total mass of hydrogen in the CVZ ($M_{\rm H}$), thus the mass of accreted hydrogen is not considered in $M_{\rm z,tot}$. The mass of six solar system objects are shown for comparison.

fractional CVZ mass ($M_{\mathrm{cvz}}/M_{\mathrm{WD}}$) and the mass fraction of each metal included in the model atmospheres of WD J2147−4035 and WD J1922+0233 according to the photospheric abundance, and included convective overshoot (Cunningham et al., 2019) with a pressure scale height (H_{p}) of one. Details on the physics and methods used in the envelope code can be found in Koester et al. (2020), but most important to note for this work is that the boundary conditions for the envelope integration were taken from the atmosphere models at a Rosseland optical depth of ≈ 300. At this depth, the ionisation is significantly higher than in the photosphere ($\tau \approx 2/3$) and CIA opacity is much less important. Therefore the diffusion timescales and fluxes in our final model atmosphere, as well as for our atmosphere model without any CIA absorption, differed very little. Uncertainties in the CIA treatment were hence negligible for these diffusion data.

The resulting parameters computed with our envelope code are listed in Table 3.7. For metals with observationally determined upper limits (see Table 3.7), we computed M_{z} at the abundance of their upper limits. The evolution of M_{z} for each metal is shown by the coloured solid lines in Figure 3.11 as a function of time and calcium diffusion times (τ_{Ca}) since accretion ceased.

$M_{\mathrm{z,tot}}$ is shown by the black dashed line in Figure 3.11 for each white dwarf. Based on the current atmospheric abundances in both stars, we estimated WD J2147−4035 has $M_{\mathrm{z,tot}} \approx 2\times10^{17}$ g and WD J1922+0233 has $M_{\mathrm{z,tot}} \approx 6\times10^{17}$ g at the present time. The mass of the accreted parent body increases exponentially with time elapsed since accretion stopped so this imposes an upper limit on the amount of diffusion times we can go back for each white dwarf; the bigger total mass the parent body has, the less likely it becomes that it could have been accreted. Therefore, it is unlikely that Neptune or Jupiter mass debris accreted onto WD J2147−4035 or WD J1922+0233. Also, the elemental abundances found in the atmospheres of these two stars (Table 3.6) are inconsistent with those of gas planets. We placed upper limits on $M_{\mathrm{z,tot}}$, and therefore τ_{Ca}, on WD J2147−4035 of approximately Earth mass ($\tau_{\mathrm{Ca}} \approx 17$) and WD J1922+0233 of approximately continental crust mass ($\tau_{\mathrm{Ca}} \approx 12$), due to the atmospheric chemical abundance ratios found in this star being most consistent with the Earth crust when considering the cessation of accretion (see Section 3.7.5).

We also determined the mass of hydrogen in the CVZ (M_{H}) for both DZ stars. However, the fraction of hydrogen mass accreted from planetary debris compared to that of a primordial origin from M_{H} cannot be unambiguously assigned. Thus, the mass of accreted hydrogen is not considered in $M_{\mathrm{z,tot}}$. Instead, M_{H} is reported for both DZ stars in Table 3.7, in addition to $M_{\mathrm{z,tot}}$ and $M_{\mathrm{cvz}}/M_{\mathrm{WD}}$.

Atmospheric chemical abundance ratios

To determine the elemental composition of the planetary debris which accreted onto WD J2147−4035 and WD J1922+0233, we calculated the current atmospheric abundance ratios (or observational upper limits) of log (Li/Na), log (Ca/Na) and log (K/Na) (see Section 3.6) and compared them with solar system benchmarks of bulk Earth (McDonough, 2000), the continental crust (Rudnick and Gao, 2003), CI chondrites (Lodders, 2003) and solar abundances (Lodders, 2003) in Figure 3.12. The other DZ stars in our subsample are included for context in Figure 3.12 with their published values shown in Table 3.6.

Our envelope code computed τ_{z} (see Section 3.7.5) for each metal in the CVZ of WD J2147−4035 and WD J1922+0233 (Table 3.7). Using the method outlined in Hollands et al. (2018), we calculated the abundance histories for log (Li/Na), log (Ca/Na) and log (K/Na) of both stars to analyse their past abundance evolutions. These evolutionary tracks are indicated by diagonal grey lines in Figure 3.12 and are marked in intervals of 1 Myr for WD J2147−4035 and 5 Myr for WD J1922+0233, due to its much slower diffusion times. Since the relative metal abundances currently observed in the atmospheres of WD J2147−4035 and WD J1922+0233 are exotic in comparison to solar system benchmarks (see Figure 3.12), and the fact it is not possible to know how long ago accretion ceased, we followed the evolutionary tracks of both stars to determine if their past atmospheric chemical abundance ratios represented parent bodies similar to the abundances of solar system benchmarks after some elapsed diffusion times, while precluding to exceed the upper limits on $M_{\mathrm{z,tot}}$ we imposed on each star in Section 3.7.5. The abundance histories are not plotted for the other five published objects in our subsample (Hollands et al., 2021; Kaiser et al., 2021) but are comparable to the evolutionary tracks for WD J2147−4035 and WD J1922+0233.

Sodium produces the strongest absorption line in WD J2147−4035 and WD J1922+0233, yet these objects have the lowest log (Na/He) abundances out of our DZ subsample (Table 3.6). The log (Ca/Na) abundances for all white dwarfs in the subsample are similar or depleted compared to the solar system benchmarks, with calcium not even being detected in WD J2147−4035. Solar system asteroids tend to have calcium to sodium ratios similar to unity or be slightly calcium-rich (e.g. Schramm et al., 1989; Zuckerman et al., 2007). The atmospheric diffusion of calcium out of the CVZ is more rapid than sodium, therefore to explain these abundances the accretion events must have occurred a long time ago for a large fraction of calcium to have diffused towards the white dwarf core and be currently undetectable. For WD J1922+0233 to have a log (Ca/Na) abundance comparable to the

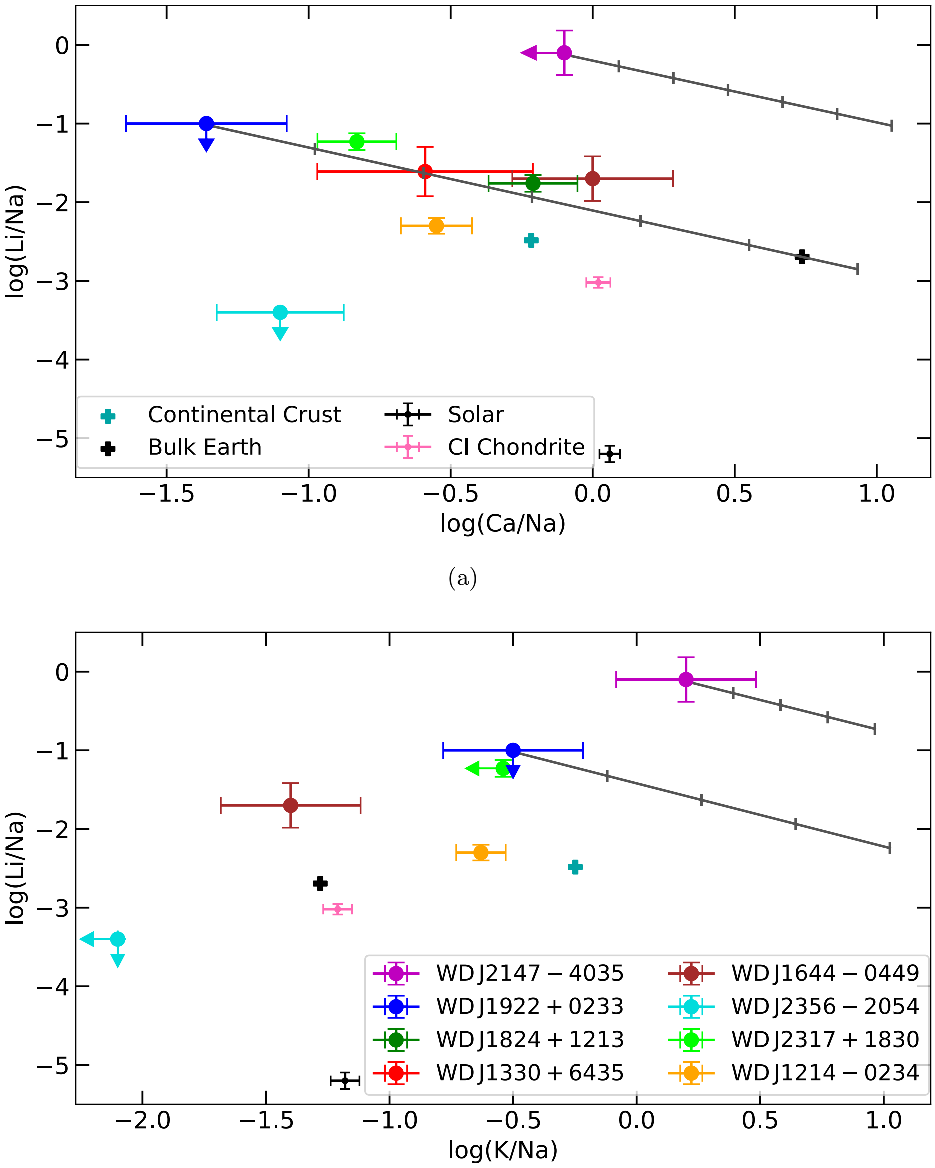

(a)

(b)

Figure 3.12: Abundance ratios for the DZ white dwarfs in our subsample compared to four solar system benchmarks for (a) log (Li/Na) versus log (Ca/Na) and (b) log (Li/Na) versus log (K/Na). Error bars represent 1σ uncertainties and are shown for all subsample objects except when only observational upper limits are derived, which are indicated by arrows. Diffusion timescales for WD J2147−4035 and WD J1922+0233 are shown by grey solid lines which indicate past photospheric abundances. Vertical grey markers on the diffusion timescales are in intervals of 1 Myr for WD J2147−4035 and 5 Myr for WD J1922+0233. The diffusion timescales for the previously published white dwarfs by Kaiser et al. (2021) and Hollands et al. (2021) are omitted but are approximately parallel to the tracks of WD J2147−4035 and WD J1922+0233. The legends apply to both panels.

crust, accretion must have ceased some diffusion times ago due to its significantly depleted current ratio.

Lithium is not detected in WD J1922+0233, though we derived a log (Li/Na) observational upper limit higher than solar system benchmarks; however, its true value could be several 0.1 dex lower which would make the log (Li/Na) and log (Ca/Na) abundances broadly consistent with the continental crust (Rudnick and Gao, 2003) if accretion ceased ≈ 15 Myr ago. Providing the true log (Li/Na) ratio inside the star is similar to our derived upper limit, WD J1922+0233 has an extremely similar composition to bulk Earth if accretion stopped ≈ 28 Myr ago (Figure 3.12(a)). If debris with bulk Earth composition polluted WD J1922+0233 then its $M_{\mathrm{z,tot}}$ would have a comparable mass to the dwarf planet Ceres (Figure 3.11(a); McCord and Sotin, 2005). On the other hand, if a parent body with crust composition accreted ≈ 15 Myr ago, it would have $M_{\mathrm{z,tot}}$ comparable to Saturn's natural satellite Janus (Jacobson et al., 2008), which is ≈ 3 orders of magnitude less massive than Ceres (Figure 3.11(a)). The latter scenario is more likely as the recent accretion of smaller parent bodies is more probable than those of more massive bodies further in the past (Hollands et al., 2021). The accretion of a very small fraction of crust from an Earth-like planet is also probable as Earth's continental crust has a mass $\approx 4 \times 10^{25}$ g (Rudnick and Gao, 2003). WD J1922+0233 has a much higher log (K/Na) abundance than bulk Earth which only enhances with diffusion timescales, yet approaches the region of continental crust abundance ≈ 4 Myr ago, especially if the true lithium abundance is lower than the upper limit we derived. This decreases $M_{\mathrm{z,tot}}$ to ≈ 3 orders of magnitude less massive than Janus and corresponds to an extremely small fraction of crust from an Earth-like planet. From the detected metals and corresponding past abundances in WD J1922+0233, we conclude it is probable that planetary bodies with crust-like compositions and $M_{\mathrm{z,tot}}$ consistent with, or ≈ 3 orders of magnitude less than, Janus accreted $\approx 4 - 15$ Myr ($\approx 1 - 7\,\tau_{\mathrm{Ca}}$) ago onto WD J1922+0233. This conclusion motivated us to set the undetected metals in our model atmospheres to Earth crust (Rudnick and Gao, 2003) abundances relative to sodium (see Section 3.6). We note that this star has a log (Al/He) observational upper limit 0.64 dex lower than the abundance found in the continental crust however this ratio increases to the continental crust value with elapsed diffusion timescales when considering accretion ceased in the past. Our atmospheric abundance assessment of WD J1922+0233 is based on current observations, yet additional follow-up spectroscopy could allow the calculation of more accurate observational upper limits and hence lead to a more conclusive debris analysis.

We also calculated the diffusion timescales of WD J1922+0233 using the T_{eff}, $\log g$, and $\log(\mathrm{H/He})$ parameters computed by Bergeron et al. (2022) (see Section 3.5) to quantify the impact of this change on our accreted planetary debris conclusion. The interpretation of the abundance histories remains very similar, i.e. that planetary debris with a composition similar to the continental crust likely accreted onto WD J1922+0233 in the past. However, τ_{z} of each metal significantly decreased when using the Bergeron et al. (2022) atmospheric parameters, resulting in a much more recent accretion event by $\approx 1-2$ orders of magnitude.

Calcium is not detected in WD J2147−4035, yet the observational upper limit of $\log(\mathrm{Ca/Na})$ we derived is slightly higher than continental crust (Rudnick and Gao, 2003) and could reduce to very similar values to the crust considering the true calcium abundance could be lower by several 0.1 dex. The current $\log(\mathrm{Li/Na})$ and $\log(\mathrm{K/Na})$ abundances in WD J2147−4035 are significantly larger than the ratios found in solar system benchmarks but are closest to continental crust composition. Accretion needed to have ceased ≈ 15 Myr ago to deplete the lithium abundance in WD J2147−4035 to the approximate continental crust $\log(\mathrm{Li/Na})$ value, which would require a $M_{\mathrm{z,tot}}$ consistent with Earth's continental crust (Figure 3.11(b)). However, this would enhance $\log(\mathrm{K/Na})$ to 3.31 dex higher than the ratio found in the crust. We also consider pollution via planetary debris enriched by primordial lithium, as in the Kaiser et al. (2021) scenario, in Section 3.7.5 to explain the high lithium abundance in WD J2147−4035, but we are not convinced this explains the high potassium abundance. The origin of carbon in this DZQH star is difficult to distinguish between accretion from external debris and convective dredge-up of core-carbon within the white dwarf, thus we omit carbon from our debris abundance analysis. We conclude the nature of planetary debris accreted by WD J2147−4035 remains elusive and more observations may be needed, including better limits on $\log(\mathrm{Ca/Na})$, to provide more clarity on how long ago the accretion event occurred. However, we do not discount the possibility of multiple accretion events with parent bodies of varying calcium, lithium and potassium abundances at different times in its history.

Primordial lithium enhancement in WDJ 2147−4035?

High abundances of lithium are predicted to have been produced during Big Bang Nucleosynthesis (BBN), which occurred $\approx 3 - 30$ minutes after the Big Bang (Hou et al., 2017). According to the Kaiser et al. (2021) scenario, the oldest stars and exoplanets would therefore be enriched by primordial lithium, which is then evident in the planetary debris observed in the atmospheres of the oldest white dwarfs.

WD J2147−4035 has a large total age of 10.7 ± 0.3 Gyr and we measured an extremely enhanced current atmospheric lithium abundance in this star, with a log (Li/Na) ratio 2.38 dex higher than the continental crust. However, WD J1824+1213 is a Galactic halo candidate with a likely large total age yet has a log (Li/Na) ratio 1.66 dex lower than WD J2147−4035. It is also unclear how this scenario could explain the extremely large log (K/Na) ratio observed in WD J2147−4035 as potassium is not predicted to have been produced during BBN, but instead created in the cores of stars through stellar nucleosynthesis and dispersed throughout the Universe by supernovae (Audouze and Silk, 1995; Tominaga et al., 2007; Iliadis et al., 2016).

Observational detection limits and telluric lines from O_2 absorption by the Earth's atmosphere causes challenges and false-positives in the potassium detection of metal-poor stars with stellar spectroscopy (Takeda et al., 2002, 2009; Abohalima and Frebel, 2018). Stellar model predictions of log (K/Fe) in metal-poor stars thus tend to under-predict this ratio compared to stellar observations (e.g. Takeda et al., 2009), though studies have found relations between metallicity (log (Fe/H)) and potassium abundance relative to the solar abundance (Gratton and Sneden, 1987a,b; Chen et al., 2000; Takeda et al., 2002; Cayrel et al., 2004; Beers and Christlieb, 2005; Tominaga et al., 2007; Takeda et al., 2009): an enhancement between $0 \lesssim \log(\mathrm{K/Fe}) \lesssim 0.3$ dex from $\log(\mathrm{Fe/H}) \approx 0$ dex to $\log(\mathrm{Fe/H}) \approx -1$ dex for Galactic disc stars; then an approximately constant log (K/Fe) ratio at lower metallicities between $-2.5 \lesssim \log(\mathrm{Fe/H}) \lesssim -1$ dex consistent with halo stars; and a slight decrease in log (K/Fe) for the oldest, hence extremely metal-poor (EMP; $-4 \lesssim \log(\mathrm{Fe/H}) \lesssim -2.5$ dex) stars. Tominaga et al. (2007) report similar trends in the log (Na/Fe) abundance relative to the solar abundance, but with an approximately constant abundance of $\log(\mathrm{Na/Fe}) \approx 0$ dex for metallicities consistent with disc stars, a slight enhancement of $\log(\mathrm{Na/Fe}) \approx 0.5$ dex for metallicities consistent with halo stars, then a decrease to $\log(\mathrm{Na/Fe}) \approx -0.8$ dex in EMP stars.

Therefore, the largest enhancement of log (K/Na) compared to the solar abundance is observed in EMP stars, although there are uncertainties in these studies. The enhancement of log (K/Na) for EMP stars is still not high enough to explain the extreme log (K/Na) ratio currently seen in WD J2147−4035, plus the kinematics of WD J2147−4035 are inconsistent with EMP stars. The only other stellar population with a log (K/Na) abundance enhancement relative to the solar abundance is old disc stars ($\log(\mathrm{Fe/H}) \approx -1$ dex), although this enhancement is ≈ 1.1 dex too small to explain the abundance currently observed in WD J2147−4035.

3.8 Conclusions

We have presented new spectroscopic observations of the ultra-cool DZ white dwarfs WD J2147−4035 and WD J1922+0233. These two stars occupy unusual positions on HRDs compared to objects in the *Gaia* EDR3 white dwarf sample within 100 pc of the Sun and the SDSS footprint (Gentile Fusillo et al., 2021) and the cool DZ subsample. WD J2147−4035 presents very red photometry as it has a depleted atmospheric hydrogen content compared to WD J1922+0233 and therefore has much milder CIA. Conversely, WD J1922+0233 exhibits unusually blue colours relative to its magnitude in Pan-STARRS and *Gaia* EDR3 photometry for an ultra-cool star, due to strong atmospheric CIA causing the suppression of flux in the red optical and IR.

Our model atmosphere code used to fit WD J2147−4035 and WD J1922+0233 includes microphysics improvements in the non-ideal effects and treatment of CIA opacities, in addition to incorporating a reduction of the neutral line broadening of visible metals by an empirical factor of 100, compared to that of Koester (2010). This produced models that gave reasonable solutions for the observed spectroscopy and photometry of WD J2147−4035 and WD J1922+0233. Additional work still needs to be done to address uncertainties in the model atmospheres, such as understanding the behaviour of atoms and molecules at extreme atmospheric densities of $\approx 3\,\mathrm{g\,cm^{-3}}$ to improve understanding of neutral line broadening and He-He-He CIA opacity, which would therefore improve future model atmospheres of ultra-cool DZ white dwarfs.

We found $T_{\mathrm{eff}} = 3048 \pm 35\,\mathrm{K}$ for WD J2147−4035 and $T_{\mathrm{eff}} = 3343 \pm 54\,\mathrm{K}$ for WD J1922+0233, revealing them as the coolest and second coolest DZ white dwarfs known to date, respectively. WD J2147−4035 is also the intrinsically faintest confirmed white dwarf in the optical within the 40 pc *Gaia* sample (O'Brien et al., 2023). The best-fitting log (H/He) abundance ratio of WD J1922+0233 is close to the maximum intensity of H_2-He CIA which is consistent with observations of strong atmospheric CIA opacity in this white dwarf. The cooling age of WD J1922+0233 is 9.05 ± 0.22 Gyr however its total age remains unknown because our model likely underestimated its mass, resulting in an unrealistically large main-sequence lifetime. WD J2147−4035 has a cooling age of 10.21 ± 0.22 Gyr which is the largest known for a metal-polluted white dwarf. As this star does not show evidence of strong CIA, we were able to derive a total age for WD J2147−4035 of 10.7 ± 0.3 Gyr. The kinematics of WD J2147−4035 and WD J1922+0233 suggest they are both Galactic disc candidates.

Strong sodium absorption lines are detected in WD J2147−4035 and WD J1922+0233, similar to the other white dwarfs in our DZ subsample. We also have firm detections of calcium in WD J1922+0233, lithium in WD J2147−4035 and potassium in both objects. We found WD J2147−4035 is magnetic due to the observed lithium spectral line being Zeeman split into three components and found a best-fitting magnetic field strength of 0.55 ± 0.03 MG. Furthermore, we detected a photometric period of $\simeq 13$ h in the *TESS* FFI light curves of this star. Carbon is tentatively detected in WD J2147−4035 due to an excellent fit of the three strongest C_2 Swan band systems when distorted to the centroid wavelengths measured in the DQpecP star LP 351−42, but further observations are needed to constrain the atmospheric carbon abundance. We assigned the spectral type DZQH to WD J2147−4035.

The current log (Ca/Na) abundance in WD J1922+0233 is extremely low compared to solar system benchmarks of continental crust, bulk Earth, solar and CI chondrites. However, considering the possibility that the accretion of debris onto this star has ceased, the past log (Ca/Na) and log (Li/Na) compositions approach similar values to Earth's continental crust ≈ 15 Myr ago – especially if the true abundance of log (Li/Na) is lower than the relatively high observational upper limit we derived. This is also true for the log (Li/Na) and log (K/Na) abundances in WD J1922+0233 from the accretion of a planetary body ≈ 4 Myr ago. The cessation of accretion $\approx 4 - 15$ Myr ago corresponds to an accreted minimum parent body mass consistent with, or ≈ 3 orders of magnitude less than, Janus, or an extremely small mass fraction of continental crust from an Earth-like planet. The detected metals and minimum parent body mass suggest this star was likely polluted by the accretion of planetary debris with a crust-like composition $\approx 4 - 15$ Myr ago.

We find WD J2147−4035 has extremely enhanced log (K/Na) and log (Li/Na) abundances compared to solar system benchmarks. Tracing the abundance evolution history of this star reveals many diffusion times are required to deplete the abundance of log (Li/Na) to broadly approach the continental crust ratio, however log (K/Na) would consequently increase to currently inexplicable values. Follow-up spectroscopy of WD J2147−4035 is required to further constrain the accretion history of this old, ultra-cool, magnetic, metal- and carbon-polluted white dwarf.

Chapter 4

An emerging and enigmatic spectral class of isolated DAe white dwarfs

4.1 Introduction

Almost four decades ago, the isolated white dwarf GD 356 (WD 1639+537) was discovered and found to be magnetic with a hydrogen-dominated atmosphere and Zeeman-split Hα and Hβ Balmer line emission triplets (Greenstein and McCarthy, 1985). It was assigned the spectral class DAHe, a degenerate star with Balmer lines (A), Zeeman-splitting (H) and emission (e). GD 356 was later found to be phometrically variable over a period of 115 minutes (Brinkworth et al., 2004; Wickramasinghe et al., 2010). GD 356 remained the only member of its class until a few years ago, when Gänsicke et al. (2020) and Reding et al. (2020) discovered two new DAHe stars. These new stars evidenced spectroscopic variability in the Hα and Hβ emission features in addition to photometric variability. Walters et al. (2021) conducted recent work on GD 356 with new time-resolved data and also confirmed spectroscopic and photometric variability in this white dwarf. Survey data and targeted spectroscopic follow-up of DAHe candidates, selected due to their photometric variability from hundreds of thousands of white dwarf candidates identified from the spacecraft *Gaia* (Gaia Collaboration et al., 2022), have led to the discovery of 26 DAHe stars to date (Manser et al., 2023; Reding et al., 2023).

Two interesting white dwarfs, WD J041246.84+754942.26 (hereafter WD J0412+7549; Tremblay et al., 2020) and WD J165335.21−100116.33 (hereafter WD J1653−1001; O'Brien et al., 2023), have emerged over the past few years and been classified as DAe - they have hydrogen-dominated atmospheres and exhibit weaker Hα and Hβ line emission than DAHe stars, but intriguingly lack an observable magnetic field i.e. do not show Zeeman-split emission line triplets. These two stars, in addition to two of the 26 DAHe white dwarfs, lie within 40 pc of the Sun. There are 1066 white dwarfs in the 40 pc volume-limited sample of white dwarfs (McCleery et al., 2020; O'Brien et al., 2023) of which 655 are classified as DA, so the identification of four DA white dwarfs with Balmer emission lines to date within this volume attests to a fraction of 0.61 %. The two DAe and 26 DAHe stars closely cluster in one region on the *Gaia* Hertzsprung–Russell diagram (HRD; Walters et al., 2021; Manser et al., 2023) and have a remarkable homogeneity in atmospheric parameters, with effective temperatures $7400\,\mathrm{K} \lesssim T_{\mathrm{eff}} \lesssim 8500\,\mathrm{K}$ and white dwarf masses $0.5\,\mathrm{M}_{\odot} \lesssim \mathrm{M}_{\mathrm{WD}} \lesssim 0.8\,\mathrm{M}_{\odot}$. The DAe and DAHe stars with reliable time-resolved data have measured variability periods of $\simeq 0.08 - 36\,\mathrm{h}$, which is plausibly linked to the rotation period.

DAe and DAHe white dwarfs are encapsulated into one DA(H)e class in this work based on our initial hypothesis that these objects have a similar origin but differ in terms of magnetic field strength and possibly other properties. The magnetic field strengths observed at the surface of DAHe stars range from $\simeq 5 - 147$ MG (Greenstein and McCarthy, 1985; Gänsicke et al., 2020; Reding et al., 2020; Walters et al., 2021; Manser et al., 2023; Reding et al., 2023), resulting in a range of physical effects acting upon the white dwarfs including altered or suppressed surface convection and possibly altered hydrostatic structure of atmospheric layers (Landstreet, 1987; Tremblay et al., 2015b; Ferrario et al., 2015; Fuller and Mathis, 2023). However, $86\pm^{7}_{10}$ % of magnetic white dwarfs within the same region of the *Gaia* HRD do not show Balmer line emission (Manser et al., 2023), suggesting that magnetic field strength is not the only physical parameter defining the DA(H)e class. Recent analyses of DA(H)e stars show no evidence of binarity or ongoing accretion of planetary debris (e.g. see Tremblay et al., 2020, for the DAe WD J0412+7549). Note that there are instances of DAe+dM systems in the literature where the Balmer emission is related to binarity (e.g. Silvestri et al., 2006, 2007; Gianninas et al., 2011), but these systems are not discussed in this work.

Previous studies have explored intrinsic (e.g. stellar structure and internal dynamics) and extrinsic (e.g. planetary mass companions and binary interactions) mechanisms to explain the observations of DA(H)e white dwarfs (Gänsicke et al., 2020; Reding et al., 2020; Schreiber et al., 2021a; Walters et al., 2021; Ginzburg et al., 2022; Reding et al., 2023). An active chromosphere which is hosted by a (magnetic) dark surface spot/region is one explanation for Balmer emission lines. The close clustering of DA(H)e objects on the *Gaia* HRD could be explained by a convective dynamo driven by white dwarf core crystallisation occurring at a specific time in the cooling sequence (Gänsicke et al., 2020; Ginzburg et al., 2022), although this scenario has recently been questioned (Fuentes et al., 2023). While no DA(H)e star to date has been found in a binary system, it has been suggested that Balmer line emission could be caused by a planetary mass companion, possibly from magnetic induction in a close-in orbit (Goldreich and Lynden-Bell, 1969; Li et al., 1998; Wickramasinghe et al., 2010). However, no study has been able to unambiguously conclude on a suitable scenario, therefore the mechanism(s) causing emission in DA(H)e white dwarfs remains a mystery.

In this work, we present new time-domain spectroscopic observations of the two DAe stars, WD J0412+7549 and WD J1653−1001, and analyse their time-series observations from *TESS* (Ricker et al., 2014) and the Zwicky Transient Facility (ZTF; Bellm et al., 2019; Masci et al., 2019). In Section 4.2, we present photometric and spectroscopic time-domain observations of WD J0412+7549 and WD J1653−1001. We analyse the data of both white dwarfs in Section 4.3 to obtain

Table 4.1: Optical and IR photometry, including magnitudes from different filters, for WD J0412+7549 and WD J1653−1001.

Survey	Filter	WD J0412+7549 [mag]	WD J1653−1001 [mag]
Gaia	G	15.815 ± 0.003	15.708 ± 0.003
	$G_{\rm BP}$	15.922 ± 0.004	15.851 ± 0.005
	$G_{\rm RP}$	15.626 ± 0.005	15.385 ± 0.007
Pan-STARRS	g	15.916 ± 0.008	15.872 ± 0.005
	r	15.900 ± 0.004	15.736 ± 0.004
	i	15.948 ± 0.003	15.766 ± 0.001
	z	16.047 ± 0.004	15.817 ± 0.002
	y	16.124 ± 0.005	15.886 ± 0.008
2MASS	J	15.544 ± 0.064	15.122 ± 0.057
	H	15.412 ± 0.133	15.064 ± 0.086
	K	15.519 ± 0.235	15.076 ± 0.138

atmospheric parameters, investigate photometric and spectroscopic line variability and determine limits on radial velocity shifts. In Section 4.4, we discuss our results and conclude in Section 4.5.

4.2 Observations and data

4.2.1 Broad-band photometry

WD J0412+7549 and WD J1653−1001 have photometry in the optical from *Gaia* DR3 and Pan-STARRS (Chambers et al., 2016; Flewelling et al., 2020) DR2, in addition to near-IR photometry from 2MASS (Skrutskie et al., 2006). Table 4.1 displays the available photometric data. We do not include photometry from the *WISE* (Wright et al., 2010) CatWISE2020 catalogue (Marocco et al., 2021) in photometric fits for either object performed in this work as the close proximity of background sources results in the contamination of *WISE* measurements. WD J0412+7549 is ≈ 15 arcsec away from the edge-on dusty galaxy LEDA 2769388 (Paturel et al., 2003) which has an estimated redshift of $z = 0.07$ (Dálya et al., 2018). WD J1653−1001 is ≈ 1 arcsec away from a background main-sequence star (Gaia DR3 4334641562479650816).

Stellar parameters – including spectral type, astrometry and atmospheric parameters – for WD J0412+7549 and WD J1653−1001 are shown in Table 4.2. Details on the photometric and spectroscopic fits performed to calculate the atmospheric parameters are given in Section 4.3.2.

Table 4.2: Observed and derived parameters of WD J0412+7549 and WD J1653−1001. Atmospheric parameters were calculated by performing photometric (Phot) and weighted 3D spectroscopic (3D spec; see text for details) fits. Values are given in the J2016.0 epoch.

Parameter		WD J0412+7549	WD J1653−1001	
Designation		*Gaia* DR3 551153263105246208	*Gaia* DR3 4334641562477923712	
Spectral type		DAe	DAe	
RA		04:12:46.23	16:53:35.21	
Dec		+75:49:42.68	−10:01:16.33	
Parallax	ϖ [mas]	28.53 ± 0.03	30.65 ± 0.04	
Distance	d [pc]	35.05 ± 0.04	32.63 ± 0.04	
Proper motion	μ_α [mas yr^{-1}]	-140.90 ± 0.03	159.38 ± 0.05	
	μ_δ [mas yr^{-1}]	26.11 ± 0.03	-211.01 ± 0.03	
Absolute magnitude	M_G [mag]	13.092 ± 0.003	13.140 ± 0.003	
Effective temperature	T_eff [K]	8546 ± 87	7388 ± 71	(Phot)
		8578 ± 106	7613 ± 95	(3D spec)
Surface gravity	$\log g$ [cm s^{-2}]	8.260 ± 0.030	7.930 ± 0.030	(Phot)
		8.316 ± 0.025	7.893 ± 0.030	(3D spec)
Mass	$\mathrm{M_{WD}}$ [$\mathrm{M_\odot}$]	0.76 ± 0.02	0.55 ± 0.02	(Phot)
		0.80 ± 0.02	0.53 ± 0.02	(3D spec)
Radius	R [$\times 10^{-5}$ $\mathrm{R_\odot}$]	1072 ± 19	1331 ± 23	(Phot)
		1027 ± 19	1366 ± 26	(3D spec)
Cooling age	τ [Gyr]	1.290 ± 0.057	1.154 ± 0.048	(Phot)
		1.419 ± 0.086	1.019 ± 0.050	(3D spec)
Magnetic field strength	B [MG]	< 0.05	< 0.05	
Spin period	P [h]	2.2891144 ± 0.0000016	80.534 ± 0.087	

4.2.2 Time-domain spectroscopy

Spectroscopic observations of WD J0412+7549 were made using four different ground-based telescopes spanning 27 months. The long time-frame between observations allows for a dedicated search for variability in the Balmer emission lines. Observational details are listed in Table 4.3 for WD J0412+7549 and WD J1653−1001, including the exposure times ($t_{\rm exp}$), number of exposures ($n_{\rm exp}$) and the total duration of each observing run. Sections 4.2.2 – 4.2.2 discuss the observations of WD J0412+7549 made with each telescope in detail. Section 4.2.2 presents the spectroscopic observations of WD J1653−1001.

WHT/ISIS

Intermediate-resolution spectroscopy of WD J0412+7549 was obtained with the double-arm Intermediate-dispersion Spectrograph and Imaging System (ISIS) on the Cassegrain focus of the 4.2-m William Herschel Telescope (WHT) at the Observatorio del Roque de los Muchachos on La Palma, Spain. We used the default CCD detectors EEV12 $2048 \times 4096\,\mathrm{pixel}^2$ in the blue (R600B grating, resolving power $R \approx 2000$) arm and RED+ $2048 \times 4096\,\mathrm{pixel}^2$ in the red (R600R grating, $R \approx 2700$) arm. The approximate wavelength ranges covered by the blue and red arms in our observations are 3100 – 5400 Å and 5700 – 9000 Å, respectively, thus all Balmer line (Hα to Hζ) regions were observed. We used a slit width of 1.2 arcsec and dispersions of 0.49 Å/pixel in the blue arm and 0.45 Å/pixel in the red arm. We imposed a binning of 2×2, resulting in an average resolution of ≈ 2 Å.

Observations were taken on 2018 October 14-16 with 600 s exposures. Three exposures were taken on 2018 October 14 while one exposure was taken on each of the subsequent nights.

Keck/HIRES

High-resolution optical spectra of WD J0412+7549 were obtained on 2019 December 9 from the High Resolution Echelle Spectrometer (HIRES; Vogt et al., 1994) instrument on the Keck-1 10-m telescope at the W. M. Keck Observatory, Hawaii. Observations were taken using the mosaic of three MIT-Lincoln Lab (MIT/LL) $2000 \times 4000\,\mathrm{pixel}^2$ CCDs with the red collimator (HIRESr) and C5 decker ($R \approx 40\,000$), with slit width 1.148 arcsec and 1×2 binning. The wavelength coverage of our HIRES observations is approximately 4800 – 6700 Å, with small gaps between echelle orders. The Hα and Hβ line regions were covered with this setup with an average resolution of ≈ 0.15 Å.

Table 4.3: Time-domain spectroscopic observations for WD J0412+7549 and WD J1653−1001 obtained from ground-based telescopes, detailing the exposure time (t_{exp}), number of exposures (n_{exp}) for each observing run and the duration of the observing run. Numbers separated by a colon represent exposures taken in the blue:red arms.

Object	Date	Telescope/Instrument	t_{exp} (s)	n_{exp}	Duration (h)
WD J0412+7549	2018-10-14	WHT/ISIS	600	3	0.56
	2018-10-15	WHT/ISIS	600	1	0.17
	2018-10-16	WHT/ISIS	600	1	0.17
	2019-12-09	Keck/HIRES	1800	2	4.29
	2020-08-17	INT/IDS	1200	2	0.67
	2020-08-18	INT/IDS	900	12	3.14
	2020-10-04	Gemini/GMOS-N	300	8	0.73
	2020-10-05	Gemini/GMOS-N	300	8	0.73
	2021-01-12	Gemini/GMOS-N	300	20	2.08
WD J1653−1001	2018-05-22	Shane/KAST	3000:1000	1:3	0.83
	2023-05-15	Shane/KAST	2000:1000	2:4	1.11

Two 1800 s exposures were taken of WD J0412+7549 with 3.79 h separation (time between exposure start times) as a check for emission line variability. The spectra were reduced and extracted using the HIRES software package MAKEE[1]. Keck observed the standard star Feige 110 on the same night as WD J0412+7549 so we used this spectrum to correct for the instrumental response function (IRF) of the telescope. Although Feige 110 has Hα and Hβ lines, the rest of the spectrum is featureless and an accurate representation of the IRF. Therefore, we used $1-3$ orders before/after the Balmer line regions in Feige 110 to correct the spectra of WD J0412+7549.

INT/IDS

We collected intermediate-resolution spectroscopic observations of WD J0412+7549 on two consecutive nights using the Intermediate Dispersion Spectrograph (IDS) on the Cassegrain focus of the 2.5-m Isaac Newton Telescope (INT), located at the Observatorio del Roque de los Muchachos on La Palma, Spain. Our setup utilised the EEV10 $4096 \times 2048\,\mathrm{pixel}^2$ CCD detector in the blue arm with a slit width of 1.2 arcsec. We used the R632V grating centred at 5720 Å, resulting in a dispersion of 0.90 Å/pixel over the approximate wavelength range $4200-7000$ Å with a spectral resolution of $R=2400$. We employed 1×1 binning and have an average resolution of ≈ 2 Å.

Two 1200 s exposures were taken on 2020 August 17 and twelve 900 s exposures were taken on 2020 August 18. Spectroscopic coverage was achieved for Balmer lines from Hα to Hγ.

Gemini/GMOS-N

We used the Gemini Multi-Object Spectrograph (GMOS; Hook et al., 2004) instrument on the 8-m Gemini-North Telescope (Gemini-N/GMOS-N) to search for variability in the Balmer line emission of WD J0412+7549 over multiple epochs as part of programme GN-2020B-Q-304. Long-slit spectroscopic observations were performed using the three GMOS-N $2048 \times 4176\,\mathrm{pixel}^2$ Hamamatsu CCD (Scharwächter et al., 2018) chips. The B600+G5307 grating ($R \approx 1700$) was used with a central wavelength of 5300 Å and 2×2 binning. The approximate wavelength range covered by our observations is $3900-6700$ Å. Our setup resulted in a dispersion of 0.45 Å/pixel and an average resolution of ≈ 3 Å.

Eight consecutive 300 s exposures were taken on 2020 October 4 and 5, with

---

[1] https://sites.astro.caltech.edu/ tb/makee/

an additional observation taken on 2021 January 12 that consisted of 20 consecutive 300 s exposures. The spectra were flux calibrated and cover Balmer lines from Hα to Hδ. The additional Hϵ Balmer line is also covered by the 2021 January 12 observing run.

Shane/KAST

We observed WD J1653−1001 using the KAST Double Spectrograph on the Shane 3-m Telescope at the Lick Observatory in California, USA. We utilised the default set-up of the KAST spectrograph, using a Fairchild $2000 \times 2000\,\mathrm{pixel}^2$ CCD in the blue arm and a Hamamatsu $2000 \times 4000\,\mathrm{pixel}^2$ CCD in the red arm. We observed with a D57 dichroic and a 600/4310 grism for the blue side and a 830/8460 grating for the red side, with respective dispersions of 0.43 Å/pixel and 1.02 Å/pixel. The approximate wavelength range covered by the blue arm was 3600 – 5300 Å and by the red arm was 5700 – 7800 Å. We used a slit width of 1 arcsec, which achieved a resolution of ≈ 1 Å in the blue arm and ≈ 2 Å in the red arm.

The first observation took place on 2018 May 22, with one 3000 s exposure taken in the blue arm and three consecutive 1000 s exposures taken in the red arm. The second observation was taken on 2023 May 15, with two consecutive 2000 s exposures taken in the blue arm and four consecutive 1000 s exposures taken in the red arm. Spectroscopic coverage was achieved for all Balmer lines from Hα to Hζ.

4.2.3 *TESS* observations of WD J0412+7549

The *TESS* spacecraft observed WD J0412+7549 under designation TIC 103222871 in Sectors 19, 25 and 26 during Cycle 2, Sectors 52 and 53 in Cycle 4, and Sector 59 in Cycle 5. Observations were taken between 2019 November 28 and 2022 December 23 (see Table 4.4). Exposure times of 120 s were taken in all six sectors. WD J0412+7549 has a *TESS* magnitude of $T \simeq 15.7$.

Pre-search Data Conditioning Simple Aperture Photometry (PDCSAP) light curves were used for our analysis in Section 4.3.1 as these have systematic errors removed, including error sources from the telescope and the spacecraft (Stumpe et al., 2012; Smith et al., 2012). The PDCSAP light curves for WD J0412+7549 were retrieved from the Mikulski Archive for Space Telescopes (MAST) public data portal. We used the `tsa` context within MIDAS[2] to carry out the time-series analysis of the *TESS* data.

---

[2] MIDAS is available from the European Southern Observatory

4.2.4 ZTF observations of WD J1653$-$1001

ZTF is a robotic time-domain survey which uses the 48-inch Schmidt Telescope at the Palomar Observatory in California, USA (Masci et al., 2019). In this work, we use DR15 observations of WD J1653$-$1001 which were taken in the green- (g) and red- (r) bands of ZTF between 2018 March 17 and 2022 November 09. The light curves were retrieved from the public NASA/IPAC Infrared Science Archive (IRSA). Exposure times of 30 s were taken in all observations.

4.3 Analysis

4.3.1 Photometric and spectroscopic variability

All spectroscopic analysis of WD J0412+7549 in this work was performed on the IRF corrected Keck data and flux calibrated Gemini, INT and WHT data. All observation time-stamps for WD J0412+7549 and WD J1653$-$1001 were converted to a Barycentric Julian Date (BJD) Barycentric Dynamical Time (TDB). The time format used for all data is Barycentric Modified Julian Date (BMJD) minus 50 000 which is BJD(TDB) $-$ 2 450 000.5.

Photometric variability of WD J0412+7549

We computed discrete Fourier transforms for each *TESS* sector (see Section 4.2.3) individually. All power spectra contained a single, strong signal at a period of $\simeq 2.29$ h. We determined the spin period and its uncertainty by performing a sine-fit to the data using $\Delta\text{flux} = A\sin(2\pi t/P - \phi) + c$ in each sector, where A is the amplitude, t is the observation time of each measurement, P is the period, ϕ is the phase-shift and c is an offset. The results are reported in Table 4.4. The *TESS* ephemeris closest to the center of the entire dataset which corresponds to the photometric maximum is $\text{BMJD} - 50\,000 = 9368.75658(31) + 0.095379756(93)\,E$, so we chose this as an epoch T_0 to phase all *TESS* light curves to the same baseline.

Next, we computed a discrete Fourier transform of the entire *TESS* observations (Figure 4.1). No other strong peaks were detected across the periodogram and the period at $\simeq 2.29$ h is detected above a false alarm probability (FAP) of 1 %. The inset of Figure 4.1 shows the power spectrum around the confirmed period, and displays a complex alias pattern which is consistent with the window function due to the sparse sampling across the full baseline spanned by the *TESS* data.

A magnetic field can result in inhomogeneous brightness distributions across the white dwarf surface, which in turn leads to photometric variability on the

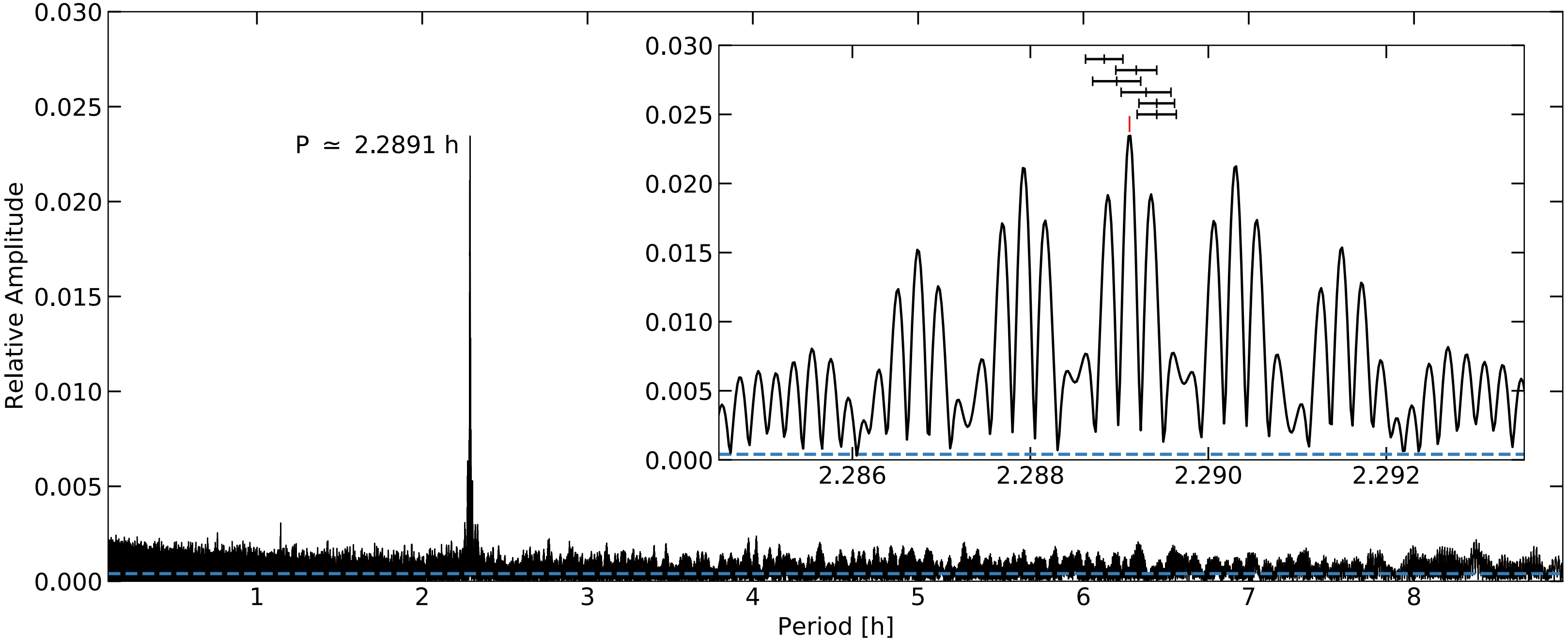

Figure 4.1: Power spectrum computed from the combined *TESS* observations of WD J0412+7549. The strongest periodic signal is at $P \simeq 2.2891\,\mathrm{h}$ and is detected above a FAP of one % (blue dashed line). Inset is a zoom-in on the strongest signal, where the red tick above the central signal represents the uncertainty of the period determined from a sine fit to the combined *TESS* data and the six black error bars illustrate the periods and uncertainties derived from the six individual *TESS* sectors (see Table 4.4).

Table 4.4: Dates of the six *TESS* observations of WD J0412+7549 and white dwarf spin periods measured from sine-fits to each sector independently. A combined period was measured from combining all sectors and fitting a sine function. Amplitudes from the sine-fits are reported here.

Sector	Dates	Period [h]	Amplitude [%]
19	2019 Nov 28 – Dec 23	2.28942(22)	2.69 ± 0.13
25	2020 May 13 – Jun 08	2.28942(20)	2.68 ± 0.12
26	2020 Jun 08 – Jul 04	2.28930(28)	2.23 ± 0.13
52	2022 May 18 – Jun 13	2.28897(27)	2.05 ± 0.12
53	2022 Jun 13 – Jul 09	2.28919(23)	2.16 ± 0.11
59	2022 Nov 26 – Dec 23	2.28883(21)	2.22 ± 0.10
Combined		2.2891144(16)	2.29 ± 0.05

white dwarf spin period (e.g. Brinkworth et al., 2013). The combined data from the six *TESS* sector observations clearly show the photometric variability of WD J0412+7549 (Figure 4.2). The top panel of Figure 4.2 shows the light curve consisting of all data points folded upon the best-fitting period, in addition to the same data binned into 400 phase bins. A sinusoidal shape is visible when the light curve is extended over two phases. The bottom panel of Figure 4.2 shows the zoomed-in light curve on the 400 phase bins with a fitted sinusoid overlaid in red. The period obtained from a sine fit to the combined *TESS* data is 2.2891144(16) h. The period uncertainty is much smaller than the separation between the three central aliases in the power spectrum, and we hence conclude that this is an unambiguous measurement of the spin period of the white dwarf throughout the *TESS* observations – under the assumption that the period is constant.

We investigated the possibility that the period measured for WD J0412+7549 is actually half the period of variability, due to there being potentially two poles or emission spots (Manser et al., 2023; Reding et al., 2023). We inspected the phase-folded light curves on both $P = 2.2891144(16)$ h and $2P$, but no additional structures were evident on twice the period. Therefore, we assume the periodic signal detected is likely the spin-period of the white dwarf assuming a single emission spot.

Inspecting the *TESS* spin measurements (Table 4.4) may suggest a trend of a decrease with time. The reduced χ^2 of the periods measured from the six *TESS* sectors against the assumption of a constant period is ≈ 1.5, which hints that the period may not be constant. However, an observed minus calculated $(O - C)$ analysis does not evidence a significant period change, as the line of best-fit gradient is -0.007 ± 0.061 with a reduced $\chi^2 \approx 1.03$. We also performed an F-test to

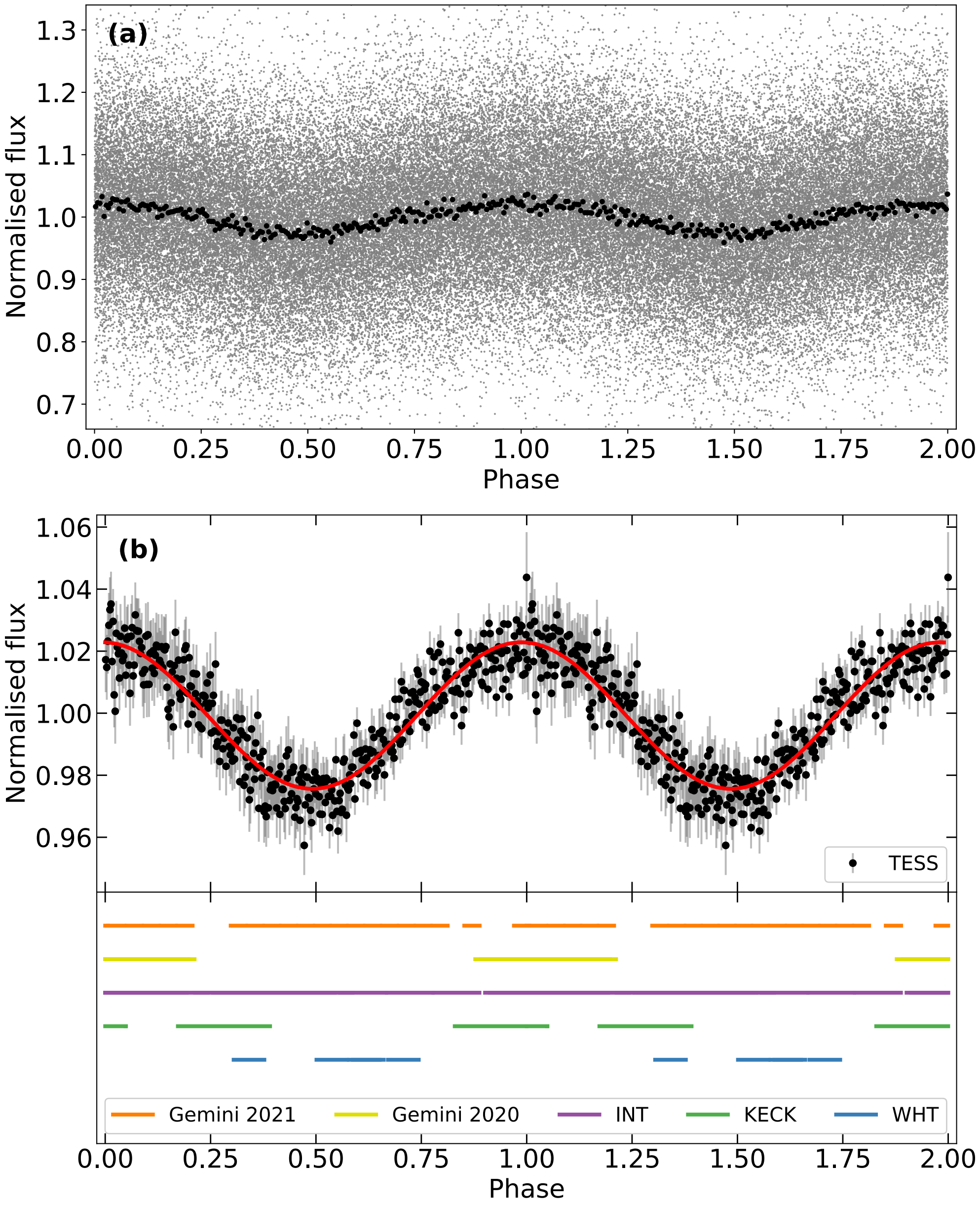

Figure 4.2: The combined *TESS* data from the individual 120 s cadence observations of WD J0412+7549 showing (a) all data points (grey) folded at the best-fitting period and the same data binned into 400 data points (black), and (b) the binned data points (black) fitted with a sine wave (red overlay) at the same period as the light curve and the phase of the spectroscopic observations. Full spectroscopic phase coverage by the WHT (blue), Keck (green), INT (purple) and Gemini telescopes is achieved. Gemini observations taken in 2020 (yellow) and 2021 (orange) are distinguished. The data in all panels are repeated over two phases for illustrative purposes. Phase = 0 corresponds to the photometric maximum at $T_{\mathrm{BMJD}-50\,000} = 9368.75658(31)$ d. Error bars are not shown in (a) for clarity but are shown in (b) to represent the 1σ scatter in each bin.

determine the significance of a linear trend to the full set of data, testing the null-hypothesis that a linear trend is not reflective of the data presented. Following the methodology described in Munday et al. (2023), we find an F-ratio of 20.53 which, under the $F(1, n-2)$ distribution for our $n = 6$ measurements, indicates that there is a 98.94 % (2.6σ) significance of a linear trend in the data. We note that the apparent decreasing trend in the individual periods may be related to small phase or period drifts, or simply be an artifact of the instrument. For now, we caution against over-interpreting the apparent trend and recommend that the spin period of WD J0412+7549 should keep being monitored.

In the bottom panel of Figure 4.2, the phase coverage of each exposure taken with the WHT, Keck, INT and Gemini telescopes are represented with horizontal coloured bars. WD J0412+7549 was observed on three consecutive nights with the WHT, which covered $\approx 31\,\%$ of the periodic signal identified. The two 30-minute exposures taken by Keck resulted in $\approx 44\,\%$ of the spin period being spectroscopically covered. The INT exposures taken over two consecutive nights covered $\approx 98\,\%$ of the spin period. The Gemini exposures taken in 2021 covered $\approx 79\,\%$ of the spin period, but together with the 2020 exposures $\approx 87\,\%$ was covered. Considering all of the above observations, we have achieved full spectroscopic phase coverage of WD J0412+7549 with short-cadence observations which allowed us to analyse the emission line variability over the entire spin period (Section 4.3.1).

Photometric variability of WD J1653−1001

The g-band and r-band flux of WD J1653−1001 was calculated from the ZTF magnitude data, relative to the median magnitude in each band. We combined the g-band and r-band datasets and weighted the contribution of the individual band points equally. Then, we computed Lomb-Scargle periodograms (Lomb, 1976; Scargle, 1982) using the `python` package `astropy.timeseries` (Astropy Collaboration et al., 2013, 2018, 2022) for the individual g-band and r-band light curves in addition to the combined g- and r-band light curve (Figure 4.3).

The strongest signals in all three power spectra occur at periods $\gtrsim 11.5$ h. ZTF is sensitive to shorter periods than *TESS* due to shorter exposure times, so if WD J1653−1001 had a similar period with similar amplitude to that found for WD J0412+7549 then it would be detected. The strongest signal in the g-band power spectrum is at a period of $\simeq 29.4729644$ h which we attribute to the moon and not as a true measurement of the white dwarf spin period.

Out of the five strongest signals in all three power spectra, only the periodic

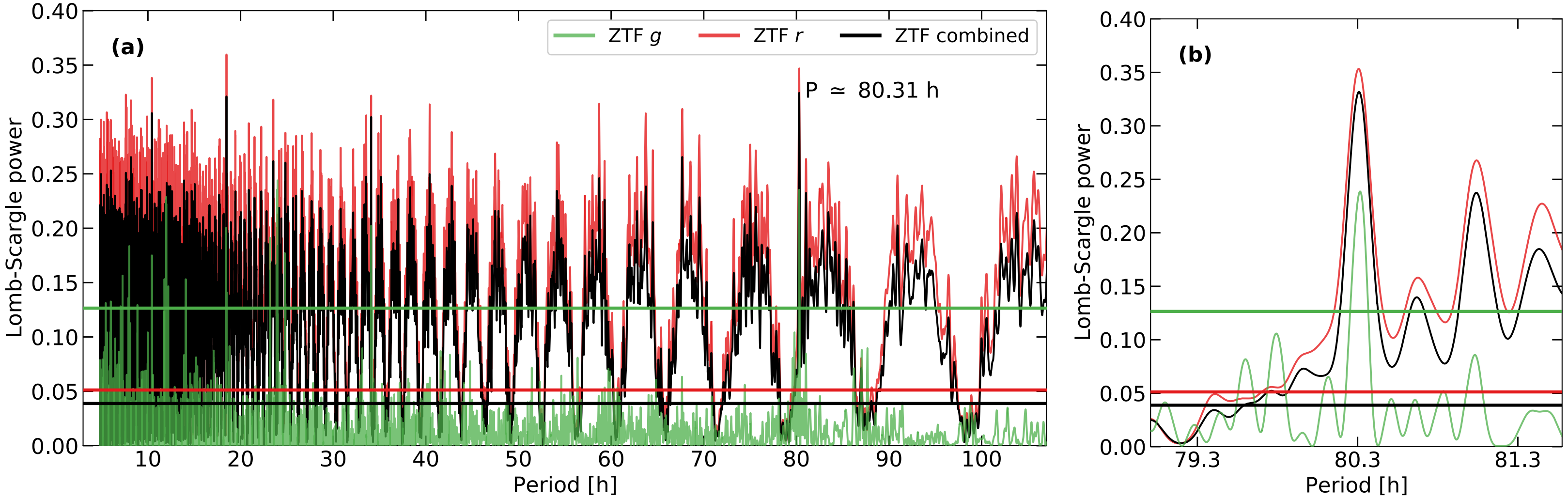

Figure 4.3: Power spectra computed from the g-band, r-band and combined g- and r-band DR15 ZTF data of WD J1653−1001. The signal common to all power spectra out of the five strongest signals in the individual power spectra corresponds to a period of $\simeq 80.31$ h, which is detected above a FAP of one % (green, red and black solid lines). Panel (b) shows the power spectra zoomed in on the periodic signal at $\simeq 80.31$ h. The legend applies to both panels.

signal at $\simeq 80.31$ h is common to all three and is detected above a FAP of 1 %[3]. The period of $\simeq 80.31$ h is the strongest signal in the combined g- and r-band power spectrum, the second strongest signal in the r-band power spectrum and the third strongest signal in the g-band power spectrum. However, with the current ZTF data it is not possible to unambiguously determine whether the peaks at $\simeq 80.31$ h are aliases related to the sampling rate or are indeed the intrinsic periodic signal. We note that the periodic signal at $\simeq 18.48$ h is the strongest signal in the r-band and second strongest signal in the combined g- and r-band power spectra, however it is the 23rd strongest signal in the g-band power spectrum, so is not considered the dominant periodic signal at this time.

Despite the uncertainty related to the period, we created phase-folded light curves on a 80.31 h period with the g-band, r-band and combined g- and r-band data and fit them with a sinusoidal function. There is very little variation between the g-band and r-band light curves (Figure 4.4), with the amplitudes of both differing by $< 1\sigma$. Therefore, we used the combined g- and r-band light curve to measure the period of WD J1653−1001 from the sine fit, which resulted in 80.534 ± 0.087 h and an amplitude 2.3 ± 0.2 %. The period uncertainty is within 1σ of the strongest detected periodic signal and is much smaller than the separation between adjacent aliases in the power spectrum. Previous studies from Reding et al. (2020) and Manser et al. (2023) found a colour dependence on the strength of variability in DAHe stars, so WD J1653−1001 differs from DAHe stars in this way as no colour dependence is evident.

We performed further analysis to determine the likelihood that the measured periodic signal of 80.534 ± 0.087 h is intrinsic to WD J1653−1001, due there being a background main-sequence star ≈ 1 arcsec away from this white dwarf. The proper motion of WD J1653−1001 reveals that over the span of ZTF observations included in DR15, the white dwarf moved from one side of the main-sequence star to the other while almost directly passing in-front of it. There is no indication that WD J1653−1001 and the contaminant were resolved into separate sources by ZTF so we cannot exclusively determine with ZTF whether the period of variability is sourced from WD J1653−1001 or the contaminant.

To help determine whether the periodic signal is coming from WD J1653−1001 or the contaminant, we created a variability metric to investigate the likelihood of the objects being variable. Our variability metric takes a similar approach to Guidry et al. (2021), which was used by Reding et al. (2023) to identify the

---

[3] The modulation in the g- and r-band are near identical so the FAP of the combined datasets is a very good approximation.

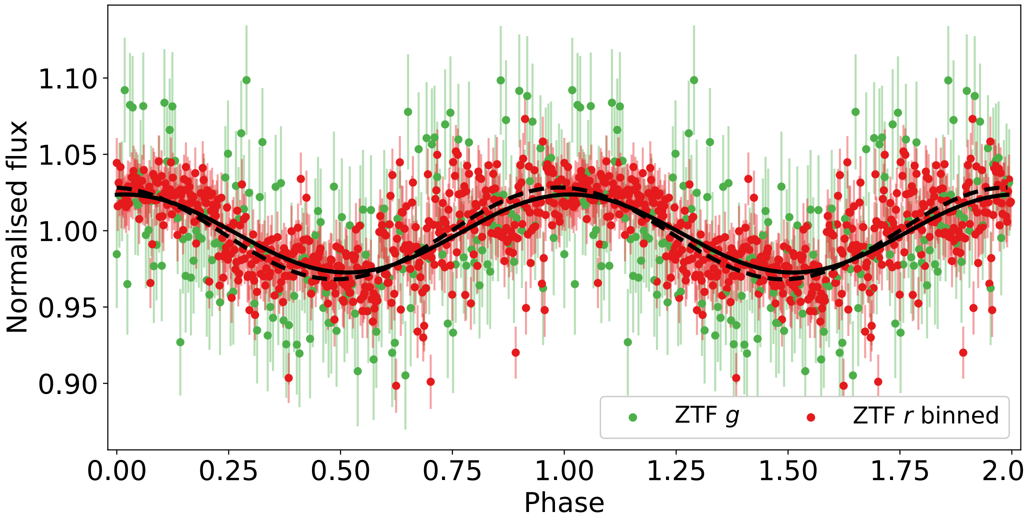

Figure 4.4: ZTF DR15 g- (green) and r- (red) band light curves of WD J1653−1001, phase-folded onto a period of 80.31 h. Sine waves were fitted on the g- and r-band light curves, shown by the black dashed and solid curves, respectively. The g-band raw data is shown, whereas the r-band data has been binned into 400 data points. The data is repeated over two phases for illustrative purposes. Phase = 0 corresponds to the photometric maximum at $T_{\mathrm{BMJD}-50\,000} = 9701.44(5)$ d for the g-band light curve and $T_{\mathrm{BMJD}-50\,000} = 9702.07(5)$ d for the r-band light curve. Error bars are shown to represent the 1σ scatter in each measurement bin.

DAHe stars LP 705−64 and WD J143019.29−562358.33. Our metric compensates for some systematic effects and is easy to interpret: it returns a sigma value relative to the median photometric scatter of sources of similar brightness and sky position. For example, the two stars just mentioned return 3.9σ and 5.5σ, respectively, i.e. they show significantly more photometric scatter than similar sources.

The variability metric is calculated using the scatter in individual *Gaia* G-band observations. That quantity is not directly available, so it is estimated for every source in the catalogue as $S = \sqrt{\text{PHOT\_G\_N\_OBS}/\text{PHOT\_G\_MEAN\_FLUX\_OVER\_ERROR}}$. The distribution of S for sources of the same brightness should be approximately Gaussian, with a long tail of high values for variable sources. To model that distribution across the catalogue, the 16th, 50th, and 84th quantiles of S (denoted e.g. S_{50}) are determined within many magnitude bins. The local distribution of S for any given source can then be estimated by interpolation. The variability of that source is then calculated as $\sigma_S = (S - S_{50})/S_{16}$ where $S < S_{50}$, or $\sigma_S = (S - S_{50})/S_{84}$ where $S > S_{50}$. However, inspection of σ_S values across the sky of such values reveals the clear imprint of the *Gaia* scanning law. Fractional residuals S/S_{50} are calculated for every source in the catalogue, and the median of those residuals calculated within every level-7 HEALpix pixel. Those positional medians provide a correctional scaling factor, as the median residual within each HEALpix pixel should be unity in the absence of systematics. The scaling factor is interpolated between HEALpix pixel centres and used to correct S across the entire catalogue. Quantiles of S are then recalculated within each magnitude bin, and the whole procedure iterated until the positional corrections converge on unity.

We assessed photometric variability S for both objects compared to a random sample of 10 000 main-sequence stars from the same region of the *Gaia* HRD as the background object. Both WD J1653−1001 and the contaminant are 5σ outliers, meaning either both or one of them is photometrically variable but *Gaia* cannot fully resolve the two objects. Of the 10 000 main-sequence stars, 2.5 % are variable at or above 5σ. Using the same variability metric on the sample of DA(H)e stars revealed that the two DAe stars and one DAHe star are variable at or above 5σ. The DAHe stars have a median variability of 0.6σ, with the maximum being 5.5σ. Therefore, 10.7 % of DA(H)e stars and 100 % of DAe stars are variable above 5σ which are both larger than the probability that the variability is coming from the contaminant main-sequence star.

As a last check, we looked in *Gaia* DR3 which has entries for WD J1653−1001 and the contaminant and found the `phot_variable_flag` parameter (Eyer et al., 2017, 2022) identified variability in the photometric data for WD J1653−1001, but unfortunately the photometric data of the main-sequence star was not processed or exported to the catalogue. The four DA(H)e stars which have a median photometric error above 3.9σ are classified as variable in *Gaia* DR3 which provides validation to our own variability metric.

The possibility of WD J1653−1001 having surface features more complex than a single spot/region beneath the chromosphere cannot be ruled out with the current ZTF data. The phase-folded light curve on $2P = 161.068$ h has two maxima and minima per cycle which could suggest the presence of two emission spots/regions (Manser et al., 2023; Reding et al., 2023). If this is the case, then the period of variability would be $2P$, with the measured period of 80.534 ± 0.087 h being an alias. However, we cannot confidently conclude either way due to the uncertainty surrounding the ZTF periodic signal analysis.

The combination of the ZTF power spectra, phase-folded light curve, *Gaia* DR3 variability flag and our own variability check makes us confident that WD J1653−1001 is photometrically variable, with a dominant periodic signal of 80.534 ± 0.087 h. However, only by obtaining full phase coverage of this star with dedicated follow-up time-domain observations – which has ideally been resolved for WD J1653−1001 and the contaminant main-sequence star – will it be possible to unambiguously confirm whether the measured periodic signal is the true spin period for WD J1653−1001, if it is an alias, or if it is indeed the period of variability for the contaminant.

Spectroscopic variability

Spectra taken of WD J0412+7549 using the WHT (Figure 4.5), Keck (Figure 4.6), INT (Figure 4.7) and Gemini (Figure 4.8) telescopes all evidence Hα and Hβ line emission. The emission line strength clearly changes between exposures taken over the spin period, which is strong evidence of emission line variability.

WD J0412+7549 was observed by the WHT on three consecutive nights. Multiple observations were made on the first night so the stacked spectrum is presented in Figure 4.5, in addition to the single spectra taken on the subsequent two nights. Erroneous wavelength shifts were apparent in the original spectra suggesting that improper wavelength calibration had been performed. A reliable wavelength calibration could not be performed on these spectra, hence we do not pursue this avenue further.

Two 30-minute exposures covering the Hα and Hβ line regions were taken with Keck of WD J0412+7549 and are shown in Figure 4.6. It is clear that both

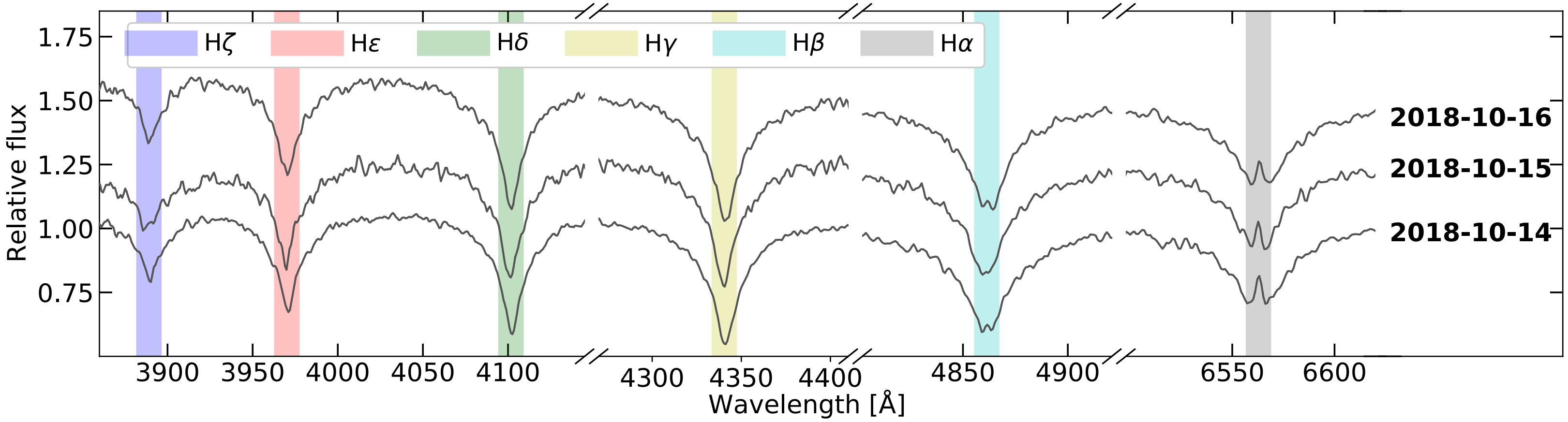

Figure 4.5: WHT spectra from three consecutive nights of observations of WD J0412+7549, taken around the Hα to Hζ line regions. Three exposures were taken on 2018 October 14, however we show the stacked spectrum here. The observation UT dates are shown on the right of the plot. Spectra are convolved with a Gaussian with a FWHM of 2 Å and offset vertically for clarity.

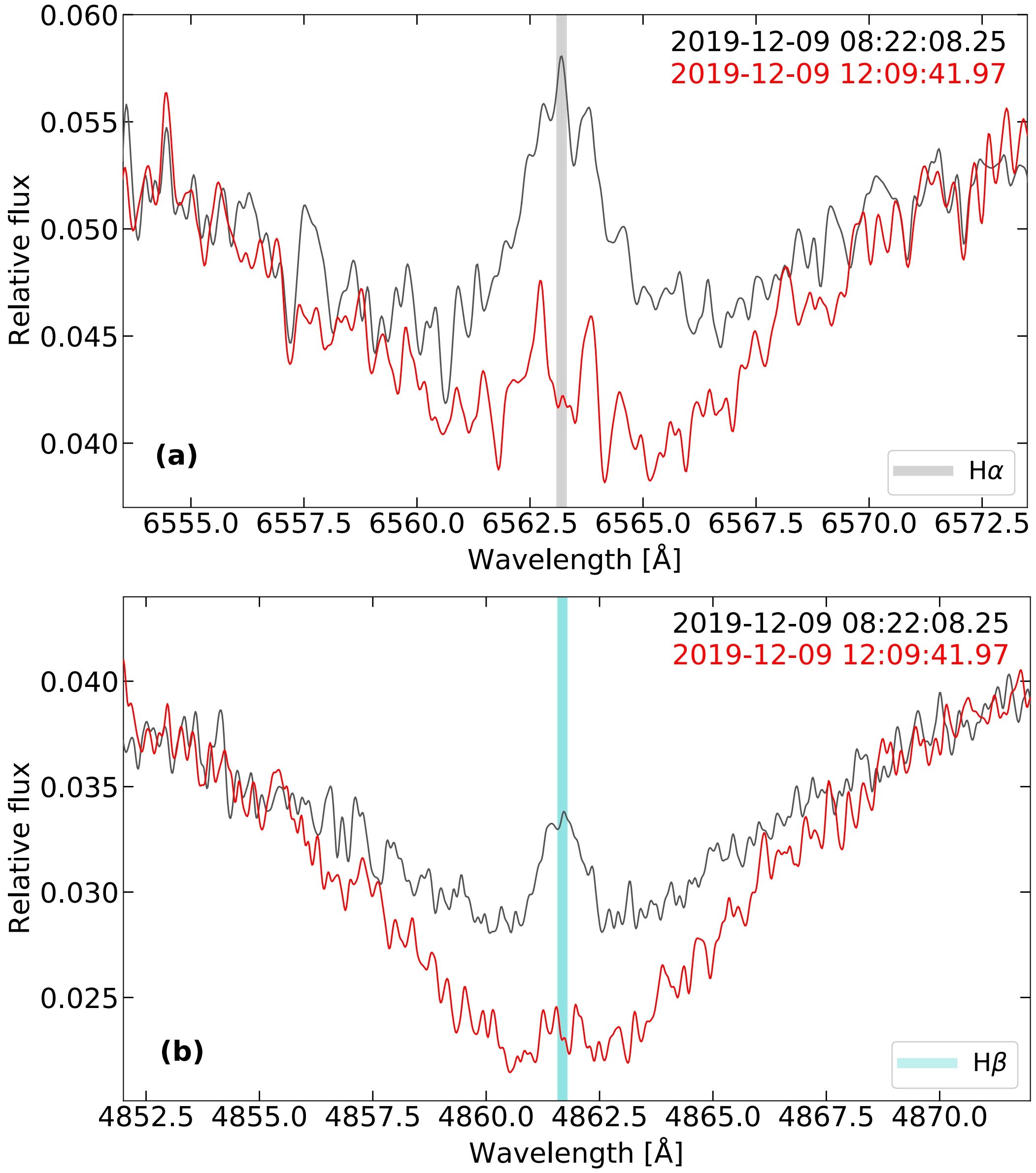

Figure 4.6: Two 30-minute exposures of WD J0412+7549 taken with the Keck HIRES instrument. Spectra were taken 3.79 h apart around the emission core of (a) Hα and (b) Hβ. The coloured vertical bars indicate the rest wavelengths of Hα (grey) and Hβ (aqua) corrected for radial velocity (Section 4.3.3). All spectra have had the instrumental response function removed (see text for details) and are smoothed with a 5-pixel boxcar for clarity. The observation UT date and start times are shown in the top right corner of the plots.

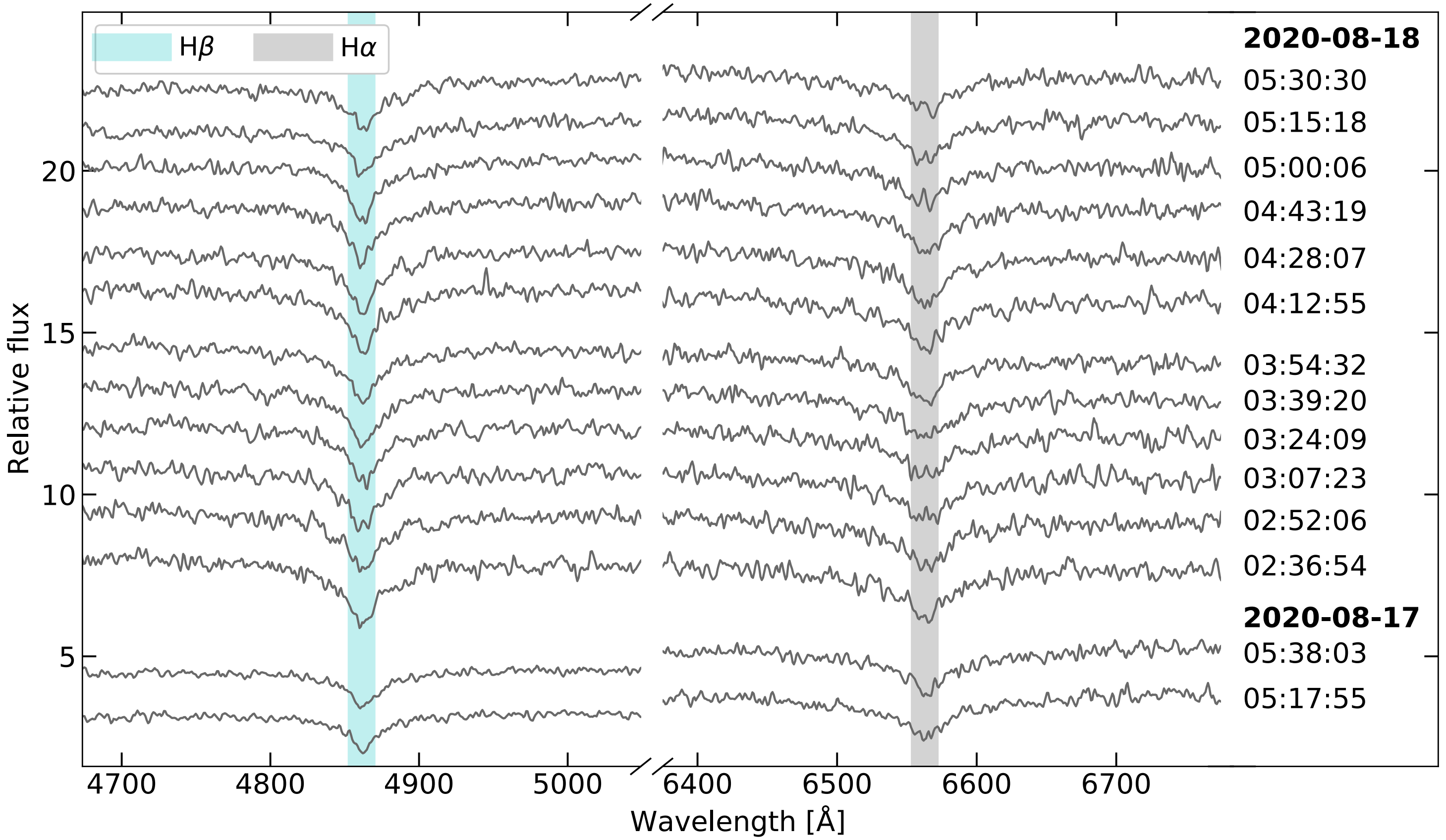

Figure 4.7: 14 exposures of INT IDS spectroscopy taken around the emission core of Hα and Hβ. The observation UT date and start times are shown on the right of the plot. Spectra are convolved with a Gaussian with a FWHM of 2 Å and offset vertically for clarity.

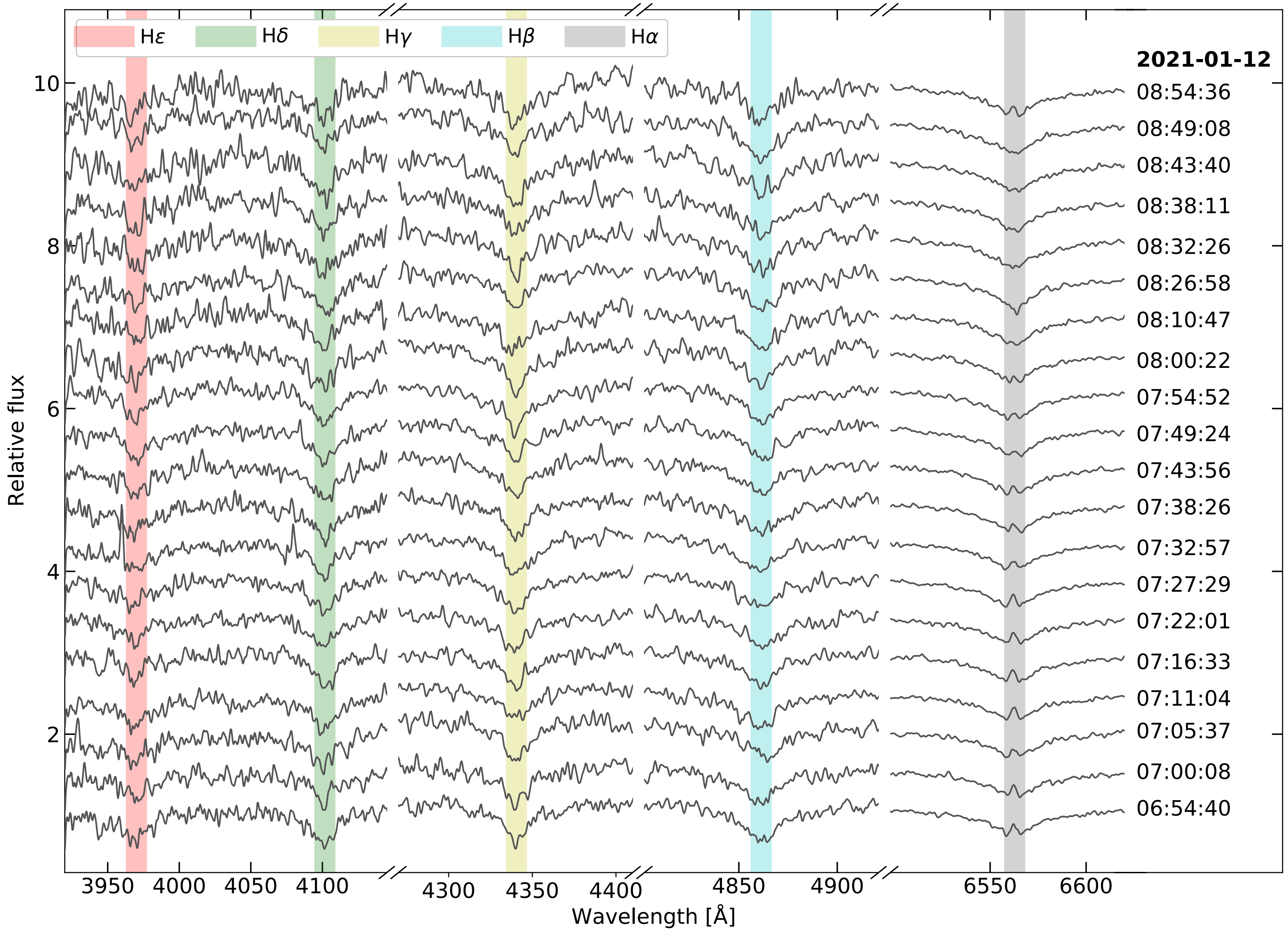

Figure 4.8: Gemini spectra of the 20 exposures taken on 2021 January 12 of WD J0412+7549 around the Hα to Hδ line regions. The observation UT date and start times are shown on the right of the plot. Spectra are convolved with a Gaussian with a FWHM of 3 Å and offset vertically for clarity.

Balmer emission lines change in strength between exposures, which were taken 227.56 min apart. Broad emission wings are evident in both exposures, and likely result from the different temperature and pressure stratifications of the atmosphere and chromosphere in (possibly magnetic) spots. However, further investigation is required to confirm this.

The Hα and Hβ emission line variability is seen in all exposures of the INT (Figure 4.7) and Gemini (Figure 4.8) observations, where the line strength variation is observed more gradually due to shorter exposures taken almost over the entire spin period (Figure 4.2). Only the Hα and Hβ line regions are shown in Figure 4.7 as the Hγ line region is cut off by the INT flux calibration and is therefore not reliable. Out of the observations performed with the Gemini telescope, the Hα and Hβ emission line variability is most clearly seen in the exposures taken on 2021 January 12 therefore we only show these spectra in Figure 4.8. Almost pure atmospheric Hα emission and absorption features are visible in the exposures taken at 07:27:29 and 08:26:58, respectively, which occur nearly half a spin period apart (0.433 phase difference).

The spectra of WD J1653$-$1001 taken with the KAST instrument on 2018 May 22 and 2023 May 15 are shown in Figure 4.9, which consists of the individual exposure taken in the blue arm on 2018 May 22 and the stacked spectra from the other exposures. Coverage of the Hα to Hζ line regions was achieved, where the emission cores of Hα to Hβ are clearly visible.

None of the Balmer emission lines in WD J0412+7549 nor WD J1653$-$1001 spectra exhibit Zeeman-splitting therefore no magnetic field detection or strength measurements could be made. Instead, we measured the upper limit of the magnetic field strength using the first Keck exposure of WD J0412+7549, as it has the highest resolution out of all the observations, and the first KAST spectrum of WD J1653$-$1001. We constructed a delta function and convolved it with the spectral resolution of the instrument. We then Zeeman-split the delta function, overlaid it on the Hα emission core and altered the magnetic field strength until the delta function was wide enough that we would visually see Zeeman-splitting and be able to distinguish it from the noise. This technique yielded upper limits on the magnetic field strength $B < 0.05\,\mathrm{MG}$ for both DAe stars. The magnetic field limit obtained from Keck is limited by the intrinsic widths of emission features and the length of the exposures (0.219 of the phase). We cannot exclude the possibility of spin-related magnetic smearing in the emission core over the exposure, or intrinsic broadening from a high temperature chromosphere. Hence, we obtain a similar magnetic field limit from Keck and KAST for both white dwarfs, despite the difference in instrumental resolution.

To investigate the emission activity of WD J0412+7549, we measured the W_λ of the Hα and Hβ emission cores in all exposures, where the smaller the value of W_λ corresponds to stronger emission. The W_λ were normalized using the `python` package `scikit-learn` (Pedregosa et al., 2011) with an L2 normalization, then compared against the phase of each exposure. On average, the W_λ uncertainties are larger for Hβ emission cores which are noisier and shallower than the Hα emission cores. Figure 4.10 displays the W_λ of the Hα and Hβ emission line cores as a function of phase, where $\phi = 0$ corresponds to the photometric maximum at $T_{\mathrm{BMJD}-50\,000} = 9368.75658(31)\,\mathrm{d}$. The data is repeated over two phases for clarity. We fitted a sinusoid to the data to clearly show that the weakest emission (i.e. largest W_λ) occurs at $\phi = 0$. In contrast, Figure 4.2 shows that the photometric flux maximum occurs at $\phi = 0$. Hence, there is an anti-phase relationship between the photometric and emission line variability of WD J0412+7549.

The same analysis of W_λ against phase could not be performed for WD J1653−1001 as there is not enough time-resolved spectroscopic data for this star. However, we measured the W_λ of the Hα emission feature in the three KAST exposures taken in the red arm on 2018 May 22, and found that all three have an identical W_λ. The lack of spectral variability over the 3000 s baseline would be consistent with a large period, possibly with the one found by ZTF (Section 4.3.1), and the spectra taken on 2023 May 15 (Figure 4.9) confirms variability over a longer baseline.

4.3.2 Photometric and spectroscopic parameters

Photometric and spectroscopic fits were performed to calculate the atmospheric parameters of WD J0412+7549 and WD J1653−1001. The best-fitting model for DAe stars was ascertained by testing three DA model atmospheres: 1D radiative, 1D convective and 3D convective (Tremblay et al., 2013, 2015b).

The photometric fits of WD J0412+7549 and WD J1653−1001 were performed using photometry from *Gaia* DR3, Pan-STARRS and 2MASS (Table 4.1). Both DAe stars have ≈ 2.3 % flux variability (see Section 4.3.1) so, based on Eq.16 from Gentile Fusillo et al. (2019), we imposed a lower limit of 0.025 mag on the photometric uncertainties from Pan-STARRS and 2MASS. There are 395 and 599 repeat observations of WD J0412+7549 and WD J1653−1001 in *Gaia* DR3, respectively, thus the G, G_{BP} and G_{RP} measurements stated in *Gaia* DR3 are likely averages over each star's full rotation period which are suitable to use to calculate their photometric parameters. The *Gaia* DR3 measured uncertainties are likely more pre-

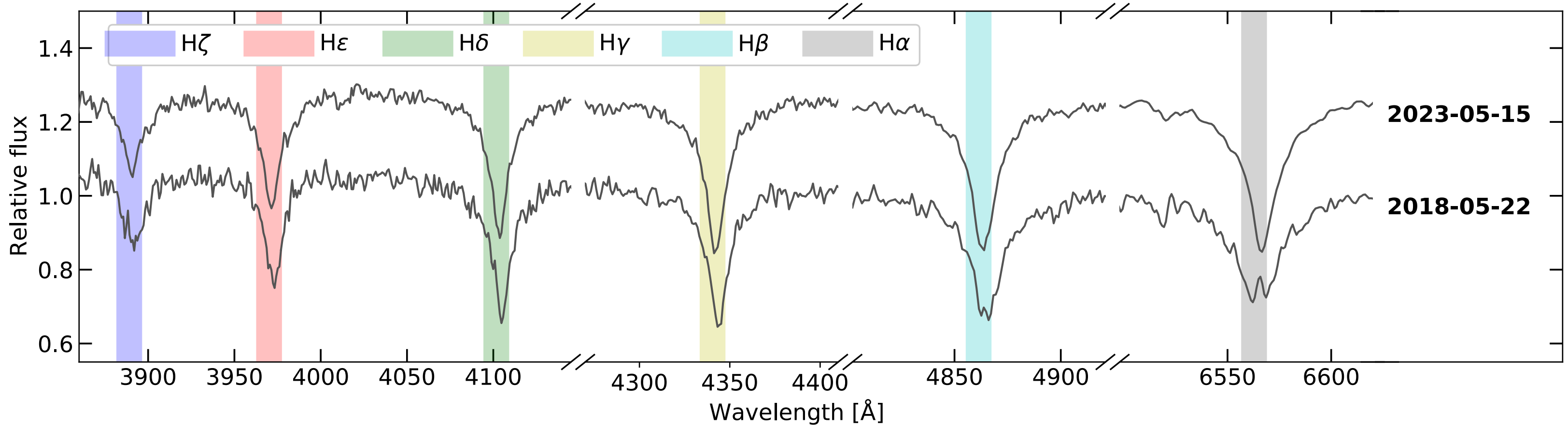

Figure 4.9: Spectra of WD J1653−1001 taken with the KAST spectrograph on 2018 May 22 and 2023 May 15 around the Hα to Hζ Balmer line regions. Shown is the individual spectrum taken in the blue arm on 2018 May 22 and the stacked spectra from the other exposures. The observation UT dates are shown on the right of the plot. Spectra are convolved with a Gaussian with a FWHM of 2 Å and offset vertically for clarity.

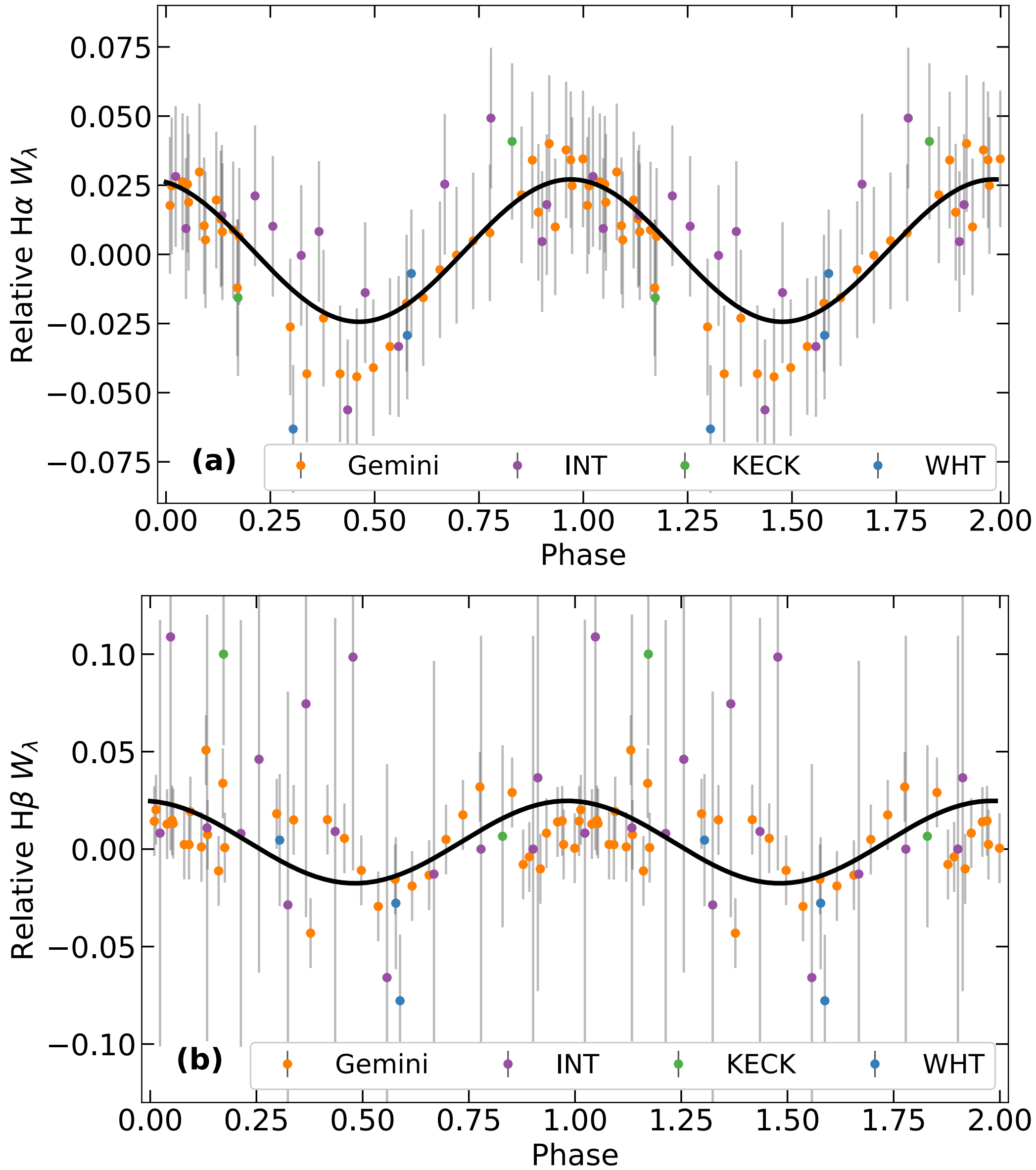

Figure 4.10: The phase of WD J0412+7549 as a function of the relative W_λ of its spectroscopically observed (a) Hα and (b) Hβ Balmer lines by the WHT (blue), Keck (green), INT (purple) and Gemini (orange) telescopes. The data is fitted with a sine wave (black overlay) and repeated over two phases for illustrative purposes. Weakest emission corresponds to the largest W_λ, which occurs at $\phi = 0$ (i.e. photometric maximum). Error bars are correspond to 1σ uncertainties.

cise than our imposed lower limit on the Pan-STARRS and 2MASS measurements, therefore we did not modify these uncertainties.

We tested the photometric fits using the three DA model atmospheres however the differences between atmospheric parameters were negligible. The best-fitting atmospheric parameters were found to be $T_{\rm eff} = 8546 \pm 87\,{\rm K}$ and $\log g = 8.260 \pm 0.030\,{\rm dex}$ for WD J0412+7549 and $T_{\rm eff} = 7388 \pm 71\,{\rm K}$ and $\log g = 7.930 \pm 0.030\,{\rm dex}$ for WD J1653−1001 (Table 4.2).

Figure 4.11 shows the spectral energy distribution (SED) created from the photometric fits of WD J0412+7549 and WD J1653−1001 with observed and synthetic photometry. Reasonable fits were achieved between the observed and synthetic photometry for both DAe stars. The bandpasses of the *Gaia* filters are broad therefore arbitrary nominal wavelengths were used for the SED. There is no near-IR excess seen in the SED of either DAe star.

We conducted spectroscopic fits using the three DA model atmospheres (like in our photometric fits) on the WHT spectra of WD J0412+7549 and on the KAST spectra of WD J1653−1001. The continuum was initially fit on each spectrum with free parameters to extract the Balmer lines. The normalised Balmer lines were then re-fit to give the best-fitting model. We removed Hα lines as the emission core made it challenging to accurately fit the spectra. The central regions around the line cores of the other Balmer lines were also removed to achieve the most accurate fit. The WHT observations for WD J0412+7549 and KAST observations for WD J1653−1001 have approximately equivalent S/N so the weighted mean of the corresponding sets of $T_{\rm eff}$ and $\log g$ were taken as the spectroscopic atmospheric parameters for each model. Similar to our photometric fits, we added the corresponding uncertainty from the $\approx 2.3\,\%$ flux variability of each DAe star to the $T_{\rm eff}$ spectroscopic weighted mean uncertainty. Estimating the uncertainty on the spectroscopic weighted mean of $\log g$ from flux variation is not trivial, so we did not modify those uncertainties.

The 1D convective model provided a worse agreement between photometry and spectroscopy than the more realistic 3D convective model (Tremblay et al., 2013), so it was discarded. It has been argued that magnetic fields suppress convective energy transfer in white dwarfs (Tremblay et al., 2015b; Bédard et al., 2017; Gentile Fusillo et al., 2018; Gänsicke et al., 2020; Cunningham et al., 2021) in the regime $\gtrsim 0.01\,{\rm MG}$ at $T_{\rm eff} \approx 8500\,{\rm K}$, which results in an altered atmospheric temperature structure. Therefore, radiative models are appropriate for stars with $B \gtrsim 0.01\,{\rm MG}$ whereas convective models are best suited for stars with lower magnetic field strengths. We measured the maximum magnetic field strength limit of

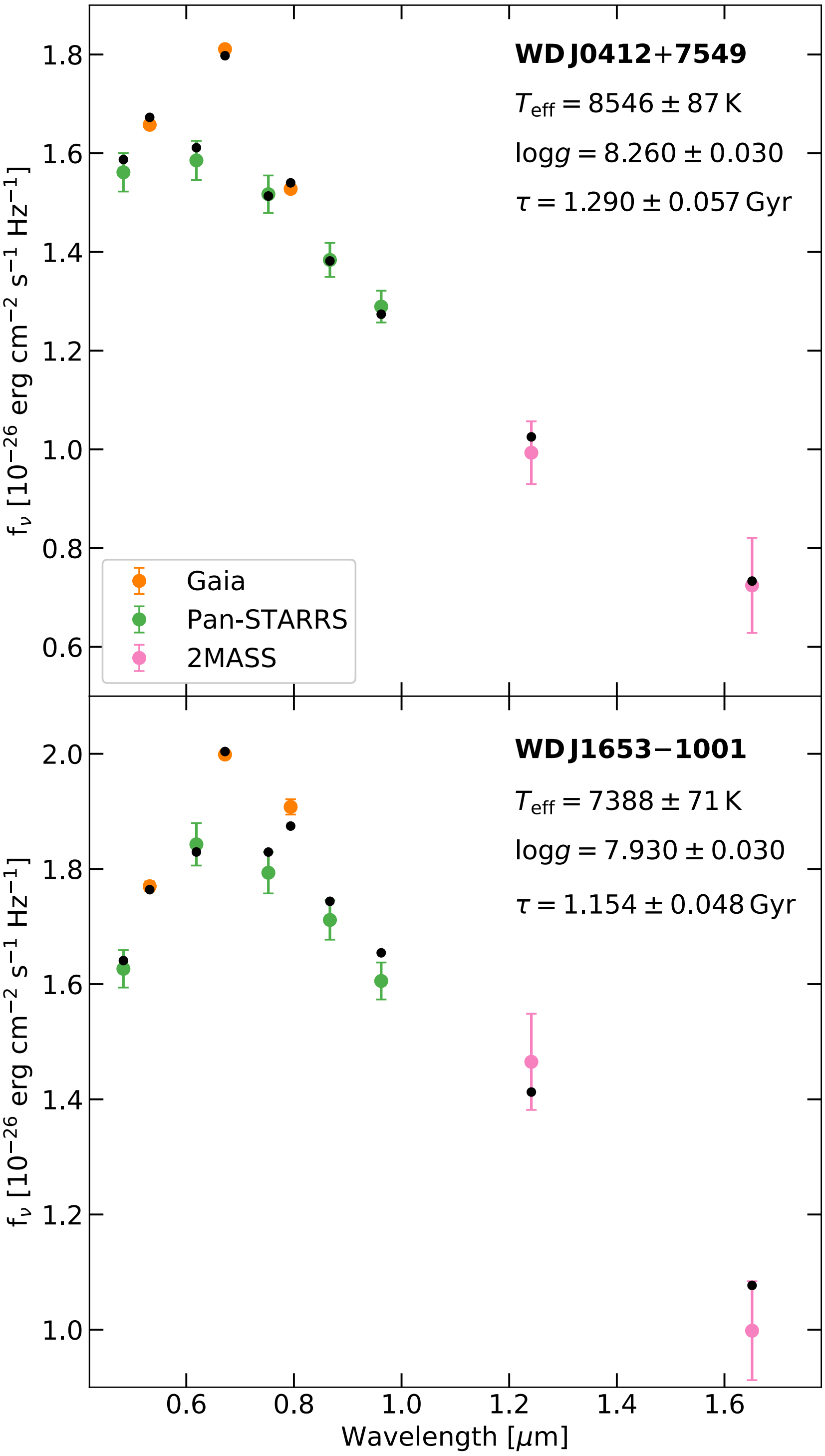

Figure 4.11: Photometric fits between the observed (coloured) and synthetic (black) photometry for WD J0412+7549 and WD J1653−1001. Uncertainties of the Pan-STARRS and 2MASS measurements have an imposed lower limit of 0.025 mag. Error bars correspond to 1σ uncertainties.

WD J0412+7549 and WD J1653−1001 as $B < 0.05$ MG therefore either the 1D radiative or 3D convective model could be valid for these stars.

The 1D radiative spectroscopic fit yielded $T_{\rm eff} = 8015 \pm 100$ K and $\log g = 8.305 \pm 0.023$ dex for WD J0412+7549 and $T_{\rm eff} = 6951 \pm 88$ K and $\log g = 7.622 \pm 0.035$ dex for WD J1653−1001. These results are 4σ and 2σ away from the photometric $T_{\rm eff}$ and $\log g$ calculated for WD J0412+7549, and 4σ and 7σ away from the photometric $T_{\rm eff}$ and $\log g$ calculated for WD J1653−1001, respectively.

The 3D convective spectroscopic fit yielded $T_{\rm eff} = 8578 \pm 106$ K and $\log g = 8.316 \pm 0.025$ dex for WD J0412+7549 and $T_{\rm eff} = 7613 \pm 95$ K and $\log g = 7.893 \pm 0.030$ dex for WD J1653−1001. These results are 1σ and 2σ away from the photometric $T_{\rm eff}$ and $\log g$ calculated for WD J0412+7549, and 2σ and 1σ away from the photometric $T_{\rm eff}$ and $\log g$ calculated for WD J1653−1001, respectively.

The atmospheric parameters obtained using the 3D convective model are in better agreement with the photometric parameters for each star, thus we use 3D convective models for our spectroscopic fits and parameters (Table 4.2). The spectroscopic fits using the 3D convective model for the WHT observations of WD J0412+7549 and KAST observations of WD J1653−1001 are shown in Figures 4.12 and 4.13, respectively, and Figure 4.14 shows the corresponding $T_{\rm eff}$ and $\log g$ parameters obtained from these fits in addition to the weighted mean of the 3D spectroscopic fit parameters and the parameters obtained from the photometric fits.

The photometric parameters for both DAe stars are likely more accurate than the spectroscopic parameters as they are less sensitive to the convection model or emission core removal procedure. Therefore, we use the atmospheric parameters obtained from the photometric fit as our adopted parameters for WD J0412+7549 and WD J1653−1001.

4.3.3 Radial velocity of WD J0412+7549

The Balmer emission observed in DAe stars could have intrinsic or extrinsic origins. To test for an extrinsic origin, we searched for evidence of a companion using the radial velocity ($v_{\rm rad}$) of the Hα emission line core from multiple spectroscopic exposures. We measured the wavelength shift of the Hα emission line central components in WD J0412+7549 compared to rest wavelengths in all Keck, INT and Gemini spectroscopic data. The spectra observed using Keck are of the highest spectral resolution compared to the other observations so are the most reliable to calculate the radial velocity of WD J0412+7549. A reliable radial velocity variation of WD J1653−1001 cannot be calculated with the available KAST spectra.

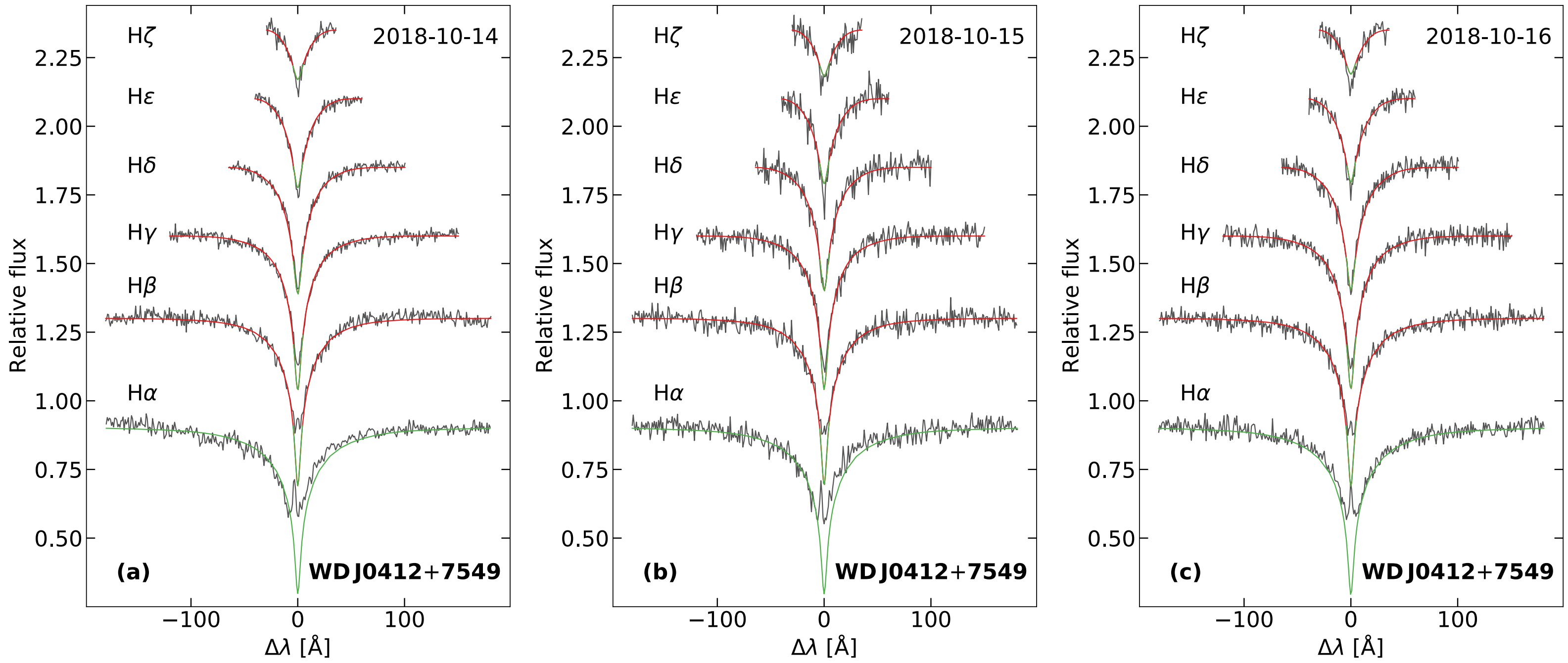

Figure 4.12: Spectroscopic fits of the normalized observed Balmer line profiles (black) with a 3D convective DA model atmosphere for (a-c) the WHT spectra of WD J0412+7549 and (d-e) the KAST spectra of WD J1653−1001, where the UT date of the observation is in the top right corner of the plots. The best-fitting model is overlaid in red and the green lines are the regions which were removed from the fit. Lines are offset vertically for clarity.

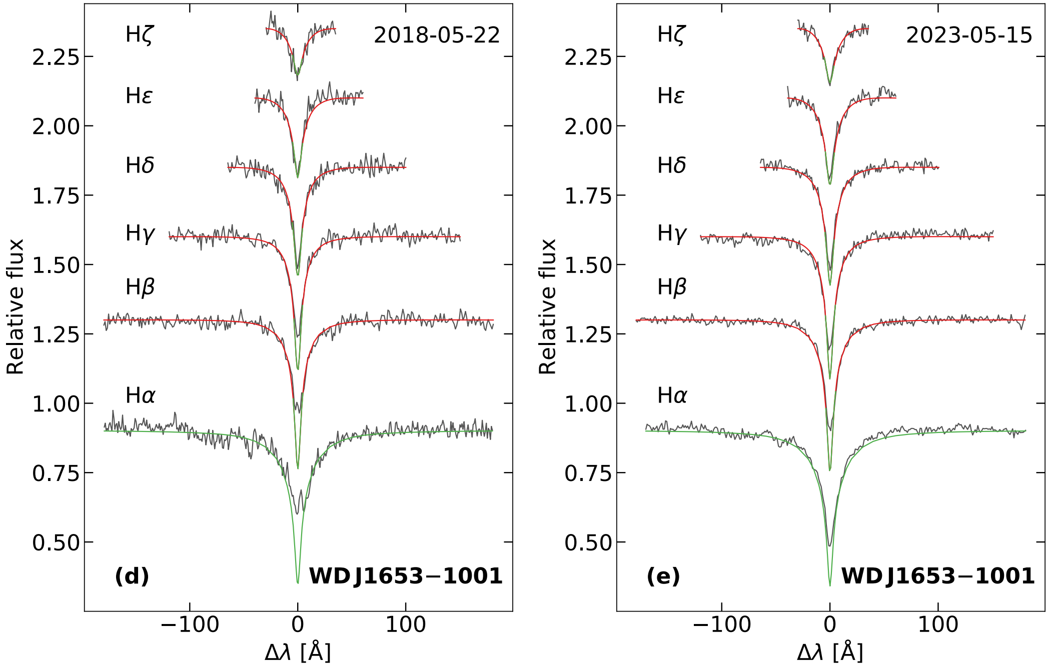

Figure 4.13: Same as Figure 4.12 but for the KAST spectra of WD J1653−1001 (d-e).

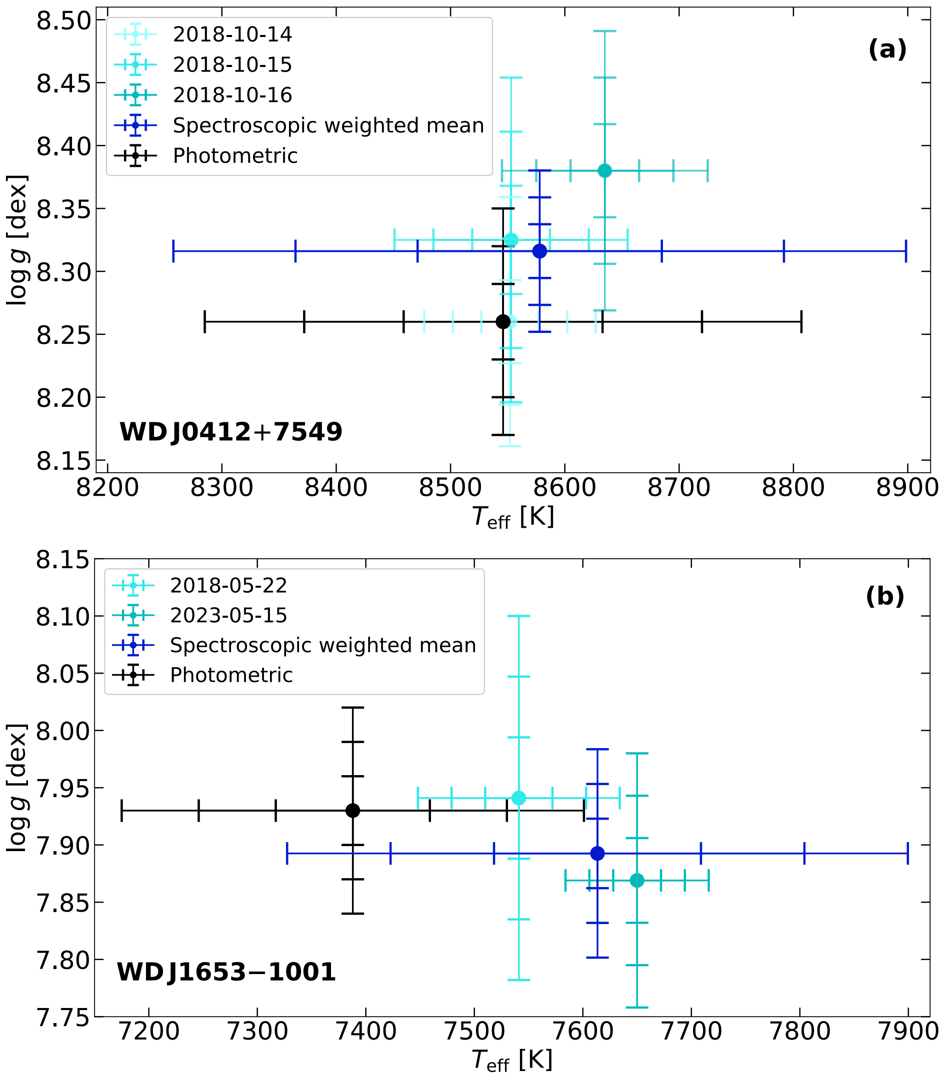

Figure 4.14: Atmospheric parameters obtained from photometric and 3D spectroscopic fits of (a) WD J0412+7549 and (b) WD J1653−1001. 3D spectroscopic fits were performed on each WHT observation of WD J0412+7549 and KAST observation of WD J1653−1001, with their corresponding $T_{\rm eff}$ and $\log g$ shown in varying shades of light blue. The 3D spectroscopic weighted mean (dark blue) of the parameters calculated from the individual 3D spectroscopic fits are shown, along with the parameters calculated from the photometric fits (black). Error bars correspond to 1σ, 2σ and 3σ uncertainties.

Our procedure consisted of creating a Gaussian of a fixed-width and convolving it by the spectral resolution of the instrument at the Hα line. We then fitted the Gaussian to the emission line 10 000 times while moving it horizontally within the noise of the core emission wings. The peak of the fitted Gaussian which corresponded to the minimum convolution between the Gaussian and emission line was the best-estimate of the central wavelength of the emission line. The Keck spectroscopic data were reduced with MAKEE and output with vacuum wavelengths corrected to the heliocentric reference frame, but as no further corrections were made we imposed a lower limit of $5\,\mathrm{km\,s^{-1}}$ for radial velocity uncertainties. For consistency, we applied the same lower limit for all radial velocity uncertainties.

The line velocity obtained by the first Keck observation taken at 08:22:08.25 UT was $21.2 \pm 6.5\,\mathrm{km\,s^{-1}}$. The second Keck observation was taken at 12:09:41:97 UT, which is at a 0.438 phase shift from the end of the first exposure. The Hα core emission line variability between exposures is significant, with the second Keck exposure evidencing a much shallower emission core (Figure 4.6). The Hα emission line in the first Keck exposure has an approximate Gaussian structure thus our fitting procedure to measure the line velocities was successful. Accurately measuring the Hα line velocity in the second Keck exposure proved challenging because the emission drastically decreases and the S/N ratio does not allow us to confidently say if there is sub-structure within the emission lines. Since the earlier Keck exposure clearly showed the emission line cores to have a Gaussian structure, we assumed the core in the second exposure does too. We therefore performed the same fitting procedure on the second Keck exposure to yield the Hα emission line velocity of $14.3 \pm 7.2\,\mathrm{km\,s^{-1}}$.

The gravitational redshift of WD J0412+7549 was calculated to be $45.1 \pm 1.5\,\mathrm{km\,s^{-1}}$. Correcting the emission line velocities for the gravitational redshift yielded v_{rad} of $-23.9 \pm 6.6\,\mathrm{km\,s^{-1}}$ and $-30.7 \pm 7.4\,\mathrm{km\,s^{-1}}$ for the first and second Keck exposures, respectively. The direction of movement of WD J0412+7549 is unknown so we only consider the radial velocity variation. Therefore, the radial velocity variation of WD J0412+7549 is $6.9 \pm 9.9\,\mathrm{km\,s^{-1}}$ for a phase difference of 0.438, which is consistent with zero. Using the same fitting procedure on all Gemini spectra, we get an upper limit on the radial velocity variation of $\lesssim 40\,\mathrm{km\,s^{-1}}$.

4.3.4 Core crystallisation

The onset of crystallisation has been suggested as a potential scenario for the close clustering of DA(H)e stars on the *Gaia* HRD (see Section 4.4.1) and for the production of their magnetic fields through a crystallisation-driven convective dynamo

(Isern et al., 2017; Schreiber et al., 2021b,a).

We investigated whether the two DAe stars have started crystallising and, if so, what percentage of their interior is crystallised. To this end, we computed new model evolutionary sequences using the STELUM code (Bédard et al., 2022). Our white dwarf models consist of a C/O/^{22}Ne core, surrounded by a standard helium mantle ($\mathrm{M_{He}/M_{WD}} = 10^{-2}$) and a "thick" outermost hydrogen layer ($\mathrm{M_{H}/M_{WD}} = 10^{-4}$). The core composition is initially uniform, with a standard ^{22}Ne mass fraction of 1.4 %. As for the oxygen mass fraction, the appropriate value is still quite uncertain, which is unfortunate given that this parameter significantly affects the crystallisation process (i.e. a more oxygen-rich white dwarf starts to crystallise earlier; Fontaine et al. 2001; Bauer et al. 2020). On one hand, current pre-white dwarf evolutionary models typically predict central oxygen abundances between 60 % and 70 % (Renedo et al., 2010; Salaris et al., 2022; Bauer, 2023). However, these predictions are notoriously uncertain due to our poor knowledge of nuclear reaction rates and convective boundary mixing in the core helium burning phase (Straniero et al., 2003; Salaris et al., 2010; De Gerónimo et al., 2019; Giammichele et al., 2022). On the other hand, recent asteroseismological analyses of pulsating white dwarfs hint that the central oxygen abundance may be closer to (and perhaps even higher than) 80 % (Giammichele et al., 2018, 2022). To account for this uncertainty, we computed two sets of sequences assuming core oxygen mass fractions of 60 % and 80 %, respectively.

Our new sequences also incorporate several notable improvements at the level of the input physics with respect to the sequences published in Bédard et al. (2020). We included the energy released by ^{22}Ne diffusion in the liquid phase and by carbon/oxygen phase separation upon crystallisation, as outlined in Bédard et al. (2022) and with minor updates discussed in Venner et al. (2023). We also made use of the improved carbon/oxygen phase diagram of Blouin and Daligault (2021), which is a critical ingredient to accurately model the crystallisation process. Finally, we employed the envelope conductive opacities of Blouin et al. (2020a), which result in a faster cooling and thus a slightly earlier onset of crystallisation with respect to the previous conductive opacities of Cassisi et al. (2007).

Figure 4.15 shows the predicted crystallised fraction (by mass) for WD J0412+7549 and WD J1653−1001 according to our model evolutionary sequences. Assuming a core oxygen abundance of 60 %, crystallisation has not started for WD J0412+7549 below 1σ. At 3σ, the crystallised fraction could reach ≈ 15 %. However, if we assume a core oxygen abundance of 80 % for WD J0412+7549, then the predicted crystallised fraction is ≈ 15 %. At 1σ the crystallised fraction could

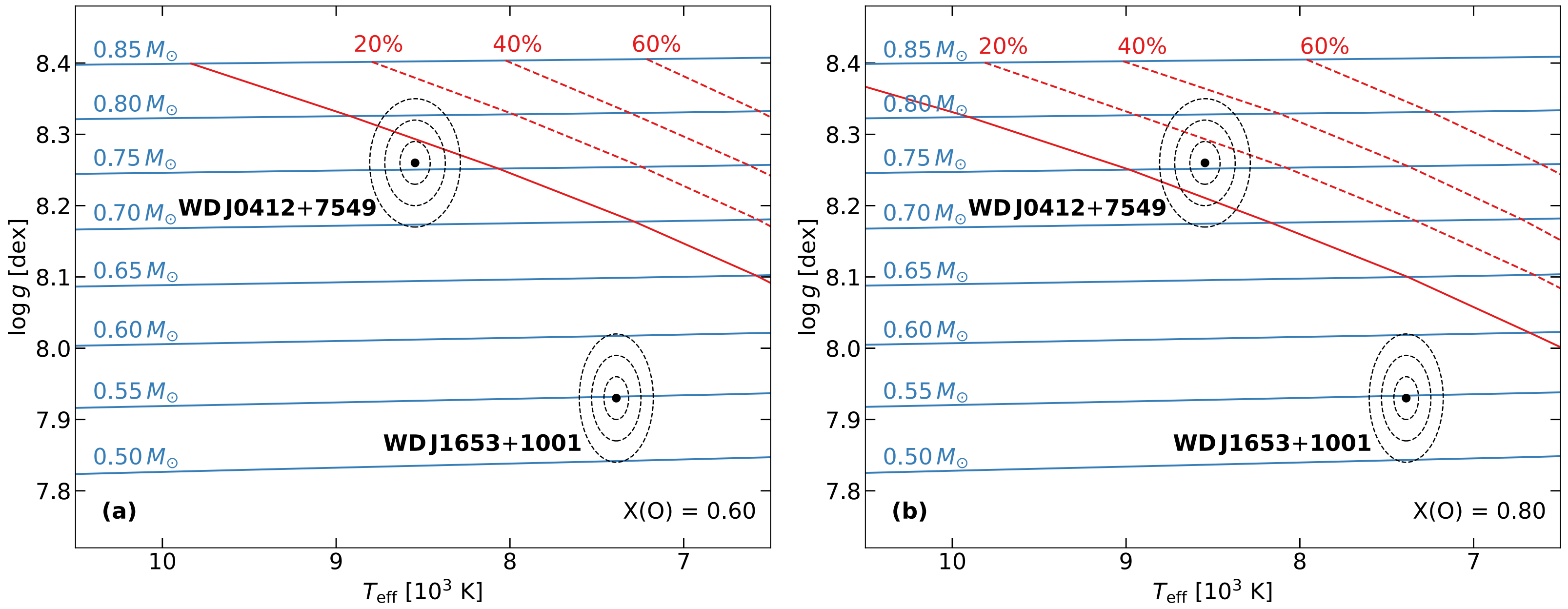

Figure 4.15: Evolutionary models showing the crystallised fraction (by mass) for WD J0412+7549 and WD J1653−1001 assuming core oxygen mass fractions of (a) 60 % and (b) 80 %. The photometric parameters of the two DAe stars are represented by black dots, with the dotted ellipses showing the 1σ, 2σ and 3σ uncertainties. Shown are the model sequences for white dwarf masses $0.50 - 0.85\,\mathrm{M}_\odot$ (blue tracks), the onset of crystallisation (solid red line) and the evolutionary stages where the star is 20 %, 40 % or 60 % crystallised (dotted red lines).

increase to 20 %, and further increase to almost 40 % at 3σ. Crystallisation has not started for WD J1653−1001 up to 3σ when assuming either core oxygen abundances.

4.4 Discussion

4.4.1 Physical characteristics of DA(H)e stars

WD J0412+7549 and WD J1653−1001 lack observable Zeeman-split Balmer lines in their emission cores upon inspection of their spectra (see Secion 4.3.1), hence have no detectable magnetic field and are classified as DAe. This is an important difference with the larger DAHe class as these stars have Zeeman-split Balmer lines with measured field strengths in the range $\simeq 5-147$ MG (Greenstein and McCarthy, 1985; Gänsicke et al., 2020; Reding et al., 2020; Walters et al., 2021; Manser et al., 2023; Reding et al., 2023), which are $2-3$ orders of magnitude higher than the upper limit determined for DAe white dwarfs. There are known magnetic white dwarfs with field strengths between $0.05-5$ MG, e.g. in the 40 pc sample (Bagnulo and Landstreet, 2021, 2022; O'Brien et al., 2023) so possible reasons for the apparent absence of DA(H)e stars in this field range are: poor spectroscopic phase-coverage of magnetic DA stars resulting in the misclassification of DA(H)e stars as DAH or DA due to phase-dependent emission (Manser et al., 2023); the emission strength may correlate with magnetic field strength, making the identification of Zeeman-split Balmer emission lines more difficult at low magnetic field strengths and in spectra which are not of high S/N or resolution (Bagnulo and Landstreet, 2018; Ferrario et al., 2020). Dedicated and high-resolution spectroscopic follow-up of all white dwarfs in the relevant portion of the *Gaia* HRD is required to understand whether this gap of field strengths in DA(H)e white dwarfs is real or a selection effect.

However, DAe stars have undeniable similarities to the larger DAHe class. None of the known DA(H)e stars exhibit metal absorption features in their spectra which suggests they are not actively accreting nor have recently accreted planetary material (Koester et al., 1997; Jura, 2003; Gänsicke et al., 2019). Also, all DA(H)e stars closely cluster in one region of the *Gaia* HRD in $G_{\rm BP}-G_{\rm RP}$ vs $G_{\rm abs}$ compared to the parameter space occupied by white dwarf candidates within 100 pc of the Sun (Figure 4.16; Gentile Fusillo et al., 2019). Manser et al. (2023) explored the close clustering of DA(H)e stars and found that within the cluster region ≈ 3 % of white dwarfs are classified as DA(H)e and $\approx 10-30$ % of DAH stars exhibit Balmer line emission. The close clustering could suggest that Balmer line emission is a consequence of a short-lived evolutionary stage of DAH or DA white dwarfs which have cooling ages of > 1 Gyr (Manser et al., 2023). The cause of the trigger

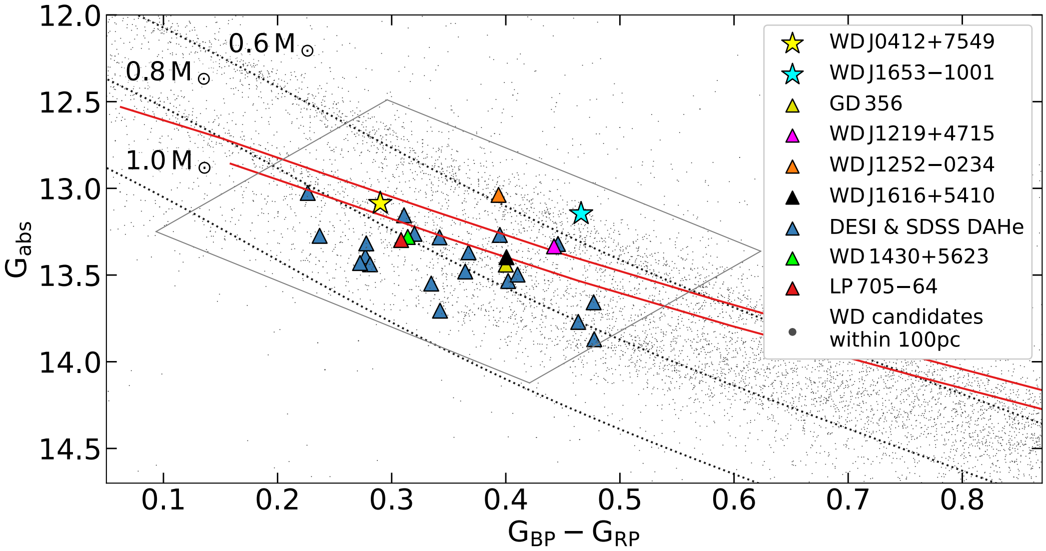

Figure 4.16: *Gaia* HRD zoomed-in on the white dwarf cooling sequence where DA(H)e reside, which is based off fig. 8 in Manser et al. (2023). The two DAe stars WD J0412+7549 and WD J1653−1001 (stars) are shown, in addition to the DAHe white dwarfs from the literature (triangles), compared to white dwarf candidates within 100 pc of the Sun (grey dots; Gentile Fusillo et al., 2019). The gray box shows the region defined in Manser et al. (2023) which bounds the DA(H)e stars. The black dotted lines show the cooling tracks of 0.6 $M_\odot$, 0.8 $M_\odot$ and 1.0 $M_\odot$ DA white dwarfs calculated with new model evolutionary sequences (discussed in Section 4.3.4) and a core oxygen mass fraction of 60 %. The red solid lines show the predicted onset of crystallisation assuming core oxygen mass fractions of 60% (lower) and 80% (upper).

of Balmer line emission in this niche evolutionary stage is still unknown.

There is a homogeneity in atmospheric parameters of the DA(H)e stars as they have $7400\,\mathrm{K} \lesssim T_{\mathrm{eff}} \lesssim 8500\,\mathrm{K}$ and white dwarf masses $0.5\mathrm{M}_{\odot} \lesssim \mathrm{M}_{\mathrm{WD}} \lesssim 0.8\,\mathrm{M}_{\odot}$. The spin period of WD J0412+7549 is consistent with those of DAHe stars which fall in the range $\simeq 0.08 - 36\,\mathrm{h}$. We derived a tentative spin period of $\simeq 80.5\,\mathrm{h}$ for WD J1653−1001 (Section 4.3.1) which is slower than the spin periods of other DA(H)e stars. We confirm spectral variability for WD J1653−1001, as we find evidence of Balmer line cores filled with emission in all observed phases (Figures 4.9 and 4.13), but additional time-domain observations and analysis is required to unambiguously determine the variability nature of WD J1653−1001. Out of the 28 DA(H)e stars, 57 % are photometrically variable and 29 % are spectroscopically variable. Note that these variability fractions are likely lower limits since not all DA(H)e have time-domain data.

It is clear that for WD J0412+7549 the photometric flux maximum corresponds to the minimum strength of emission lines, i.e. the photometric and spectroscopic variability are in anti-phase (Section 4.3.1). The same phase relationship was found in the DAHe stars SDSS J125230.93−023417.72 (Reding et al., 2020), GD 356 (Walters et al., 2021), WD J1616+5410 (Manser et al., 2023), suspected in SDSS J121929.45+471522.8 (Gänsicke et al., 2020) and visually identified in LP 705−64 and WD J143019.29−562358.33 (Reding et al., 2023). Thus, the seven DA(H)e stars that have adequate phase coverage in spectroscopic observations and exhibit spectroscopic variability have a confirmed or suspected anti-phase relationship with photometric variability. An anti-phase relationship is indicative of a dark spot/region beneath an optically thin chromosphere, whereas we would expect an in-phase relationship if there is a closely orbiting companion.

WD J0412+7549 has radial velocity variation of $\lesssim 40\,\mathrm{km\,s^{-1}}$ and both DAe stars have no evidence of near-IR excess, suggesting that neither star has a stellar companion (see Section 4.4.2). This is consistent with the DA(H)e class in general, where none of the class members have confirmed stellar or planet mass companions.

4.4.2 What is causing the Hα and Hβ emission lines?

Both non-magnetic and magnetic mechanisms have been put forward as possible reasons for Balmer emission lines in cool white dwarfs ($T_{\mathrm{eff}} \leq 8500\,\mathrm{K}$). In the following subsections, we will discuss the feasibility of each of these mechanisms being present in the DAe stars WD J0412+7549 and WD J1653−1001.

Unseen companions

We now explore the possibility of a stellar or substellar companion, such as a brown dwarf or planet, orbiting the DAe stars and causing the Balmer emission lines. It is feasible that a white dwarf can have a planetary mass companion as it is well established that planets can survive the stellar evolution of their host star into a white dwarf (Villaver and Livio, 2007; Mustill and Villaver, 2012; Rao et al., 2018; Ronco et al., 2020). Recent observations have suggested planet candidates orbiting white dwarfs (Thorsett et al., 1993; Sigurdsson et al., 2003; Luhman et al., 2011; Gänsicke et al., 2019; Vanderburg et al., 2020; Blackman et al., 2021; Mullally et al., 2024), but no substellar companions have been confirmed around DA(H)e stars at this time.

We are able to place upper mass limits on potential companions of WD J0412+7549 and WD J1653−1001 by comparing infrared photometry of these stars from 2MASS, JHK and *WISE* reported in the CatWISE2020 catalog (Marocco et al., 2021) to brown dwarf flux models (Phillips et al., 2020). Despite neglecting background contaminated *WISE* photometry from all photometic fits performed in this work, we include it here as the peak wavelengths of late-spectral-type objects fall in the far-IR thus *WISE* measurements are optimal for placing limits on potential brown dwarf companions. The $W1$ band places the strongest constraints on companion spectral type due to a flux dip in brown dwarf models in $W2$. Using the $\mathrm{M_{WD}}$ we derived from photometry (Table 4.2) and the initial-to-final-mass relation (IFMR) from Cummings et al. (2018), we calculated the progenitor mass of WD J0412+7549 to be $3.1 \pm 0.2\,\mathrm{M_{\odot}}$ and the total age of the system to be 1.54 ± 0.13 Gyr. The photometry in the $W1$ filter is 15.226 ± 0.023 mag which, with the total age of the system, places a mass constraint on a substellar brown dwarf companion of $< 60\,\mathrm{M_{Jup}}$. Doing the same analysis for WD J1653−1001 reveals a progenitor mass of $0.8 - 0.9\,\mathrm{M_{\odot}}$ and the total age of the system to be > 10 Gyr. The $W1$ measurement for this system is 14.347 ± 0.015 mag but there is no evidence that the white dwarf and close-proximity background main-sequence star have been resolved. Using the $W1$ measurement and total age of the system, we can place a mass constraint of $< 80\,\mathrm{M_{Jup}}$ on a companion. Even though the $W1$ measurement is contaminated, we reach a similar result when using 2MASS photometry from the JHK filters.

If the Balmer line emission in these DAe stars originates from a companion, then we expect the orbital period to be the same as the photometric variability period. Kepler's laws can be used to predict the radial velocity of the emission feature if it was emitted by a companion in WD J0412+7549. We do not entertain an inclination of 0° (face-on orbit) as we would not observe photometric variations in this case. Assuming an inclination of 90° (edge-on orbit), the companion would require a radial velocity variation with a lower limit of $\gtrsim 400\,\mathrm{km\,s^{-1}}$ compared to an observed radial velocity variation upper limit of $\approx 10\,\mathrm{km\,s^{-1}}$ for WD J0412+7549. Even an inclination of 45° would require the companion to have a radial velocity of $\approx 280\,\mathrm{km\,s^{-1}}$ which is still infeasibly large. Therefore, we can largely rule out that the emission is from a companion and instead it must originate from the stellar surface.

If DAe stars have a companion but the Balmer emission lines are assumed to originate from the white dwarf surface and the orbital period corresponds to the photometric period, then the radial velocity of the star will be dependent on the companion mass. During the companion's orbit, the force exerted onto the star would cause the Balmer line emission cores and wings to radially shift with a consistent amplitude. With the current observations of WD J0412+7549, it is only possible to measure the radial velocity of the Balmer line emission cores but this is sufficient for our analysis. We can constrain a companion upper mass limit of $115\,\mathrm{M}_\oplus$ for a favourable edge-on inclination.

Magnetic mechanisms

It is possible that the same magnetic mechanism which causes the detectable magnetic field in DAHe stars is present in DAe stars and causes all objects in the DA(H)e class to have Balmer emission lines, yet the magnetic field in DAe stars is not strong enough to cause these lines to be Zeeman-split into triplets. Magnetic field lines could emerge for a certain T_eff and $\mathrm{M_{WD}}$, resulting in an intrinsically-activated chromosphere for a limited amount of time, before the white dwarf continues to evolve along the cooling track as a DA or DAH. The undetectable magnetic field in DAe stars could therefore be due to them being at slightly different stages of the DA(H)e evolutionary phase which could cause the magnetic field to be smaller or buried below the photosphere as the field lines simply have not had time to emerge from the surface yet.

The origin of magnetic fields in isolated degenerate stars is not well understood, although several theories have been developed to explain their presence, such as: fields remnant from the progenitor pre-main sequence (fossil fields) or main sequence stars that got trapped and retained in the non-convective core regions of the star and released upon the evolution into a white dwarf (Landstreet, 1967; Angel et al., 1981; Braithwaite and Spruit, 2004; Tout et al., 2004; Wickramasinghe and Ferrario, 2005); a dynamo acting in the common envelope phase (Tout et al., 2004;

Briggs et al., 2018; Belloni and Schreiber, 2020) or during a merger (García-Berro et al., 2012); or a convective dynamo driven by white dwarf core crystallisation (van Horn, 1968; Isern et al., 2017; Schreiber et al., 2021b,a; Ginzburg et al., 2022).

The unipolar inductor model has been explored in the literature (Goldreich and Lynden-Bell, 1969; Li et al., 1998; Wickramasinghe et al., 2010) as a potential mechanism for magnetism and the emission feature in DAHe stars (Gänsicke et al., 2020; Reding et al., 2020; Walters et al., 2021). This model involves the induction of an electric current from the close-in orbit of a rocky planet through the host star's magnetosphere, which consequently heats up the host's atmosphere at the magnetic poles causing emission. An in-phase relationship between photometric and spectroscopic variability is expected from the unipolar model. However, DA(H)e stars have been found to have an anti-phase relationship (Section 4.3.1), suggesting they host a photospheric dark spot below an optically thin emission region, i.e. with a temperature inversion above the photosphere, which is inconsistent with the unipolar model (Walters et al., 2021).

Observational evidence and the similar physical characteristics of DA(H)e stars suggest that the Balmer emission lines are caused by a mechanism internal to the white dwarf, such as magnetic emergence or an intrinsically-activated chromosphere. An active and hot chromosphere (above the photosphere) in polar magnetic regions would cause the change in intensity of Balmer emission lines which we observe as spectroscopic variability over the spin period, in addition to flux variations from underlying cooler/warmer photospheric regions which we observe as photometric variability as the white dwarf rotates. Note that photometric variability could also be caused by other magnetic effects (opacities, polarisation) and more observations (e.g. multi-wavelengths) are needed to conclude whether the photometric temperature is variable over the surface (Fuller and Mathis, 2023).

A local surface dynamo (or chromospheric activity itself) to explain magnetic field generation is ruled out as the amount of energy stored in the convection zone and upper layers is unable to explain magnetic fields larger than about 1 kG (Fontaine et al., 1973; Tremblay et al., 2015b).

A crystallisation-induced global dynamo has been theorised to cause the production and emergence of magnetic fields in isolated white dwarfs thus could be the reason for magnetism in DA(H)e stars (Isern et al., 2017; Schreiber et al., 2021b,a). The Balmer line emission could then result from the emergence at the stellar surface of these newly generated magnetic field lines. But, more recently, doubts have been raised on the efficiency of this mechanism due to the small convective velocities[4] and kinetic energy flux reservoir (Fuentes et al., 2023). The onset of core crystallisation depends on white dwarf mass and core chemical composition but otherwise occurs at a specific evolutionary stage, resulting in it being a possible explanation for the close clustering of DA(H)e stars on the *Gaia* HRD (Schreiber et al., 2021a).

Core crystallisation combined with the white dwarf's rotation has been predicted to sustain a global magnetic dynamo (Ginzburg et al., 2022). The dependence of these factors results in a relationship between the fraction of the core which is crystallised, the spin period and magnetic field strength (Schreiber et al., 2021b,a; Ginzburg et al., 2022; Fuentes et al., 2023). We used evolutionary model sequences to calculate the fraction of the DAe stars which are crystallised based on their photometric parameters (see Section 4.3.4). The core oxygen abundance in white dwarfs is poorly understood, thus uncertainty is introduced in our evolutionary model sequences as this parameter influences the onset of crystallisation. To acknowledge this uncertainty, we calculated two sets of models: one with a standard core composition of 60 % oxygen (left panel of Figure 4.15); and one with a heavier core composition of 80 % oxygen (right panel of Figure 4.15). It is apparent that the onset of crystallisation occurs earlier when a higher core oxygen abundance is assumed, as the increased mean molecular weight raises the core density and enhances Coulomb coupling between ions, allowing the core to reach the crystallisation threshold at higher T_{eff}.

From our evolutionary model sequences, we cannot determine whether WD J0412+7549 has started to crystallise or not as it depends on its core composition (which is uncertain) and the precision of its T_{eff} and $\log g$ photometric parameters. If WD J0412+7549 has an 80 % core oxygen abundance, the crystallised fraction could be as high as 40 % at 3σ. We can exclude that WD J1653−1001 has started to crystallise considering up to 3σ of its photometric parameters and both 60 % and 80 % core oxygen abundances.

The position of DA(H)e stars on the *Gaia* HRD is compared to the onset of crystallisation in Figure 4.16. In this work, we have improved the modelling in different ways and therefore we can now be relatively confident that the atmospheric parameters are robust. First, the photometric parameters ($T_{\mathrm{eff}}/\log g$) of DA(H)e white dwarfs with 3D convective or 1D radiative models (accounting for magnetic effects) were shown to be similar (see Section 4.3.2). It has also recently been shown that photometric atmospheric parameters for cool ≈ 8000 K magnetic white dwarfs

---

[4] This refers to slow compositionally-driven internal convection and it is unrelated to the surface dynamo discussed earlier.

using non-magnetic models are likely to be accurate (McCleery et al., 2020; Hardy et al., 2023).

In addition, the crystallisation sequences we used include up-to-date physics (see Section 4.3.4). When an oxygen mass fraction of 80 % is assumed, two out of 28 DA(H)e stars have not started to crystallise within 3σ. When an oxygen mass fraction of 60 % is assumed, out of the 28 DA(H)e white dwarfs seven have not started to crystallise within 1σ nor five within 3σ. Uncertainties still remain in crystallisation models (e.g. Blouin et al., 2021), but at present the predicted onset of crystallisation does not fully match with the emergence of DA(H)e stars, and even then it is expected that the emergence of surface magnetic fields from a crystallisation dynamo will be delayed from the onset of crystallisation (Ginzburg et al., 2022).

An anti-correlation between the magnetic field strength and the white dwarf spin period is expected for a crystallisation-driven dynamo (Ginzburg et al., 2022). The tentative positive correlation found by Manser et al. (2023) in the nine DAHe stars with ZTF-determined spin periods and the three previously published DAHe stars is not in agreement with the relationship $B \propto P^{-1/2}$ found by Ginzburg et al. (2022) for a magnetic field generated by a crystallisation-driven convective dynamo in single white dwarfs. This observation, coupled with the fact that some DAe stars have likely not started to crystallise, makes it challenging to unequivocally attribute crystallisation as the universal origin mechanism for their magnetic fields. However, emergence of magnetic fields from another mechanism such as magnetic diffusion of pre-white dwarf fields over Gyr timescales, can still be an explanation for DA(H)e stars (Cantiello et al., 2016; Bagnulo and Landstreet, 2021, 2022), even though it needs fine tuning for the emergence to almost coincide with the onset of crystallisation.

From studies of volume limited samples, magnetism has been found to be rare and generally weak in young canonical mass ($\approx 0.6\,\mathrm{M}_\odot$) white dwarfs, yet the magnetic incidence appears to increase for cooling ages larger than $2 - 3$ Gyr (Bagnulo and Landstreet, 2022). This is likely evidence that magnetic fields emerge from the interior to the stellar surface within this age range. The delayed magnetic field emergence could explain the existence of DA(H)e stars and their close clustering on the *Gaia* HRD, rather than scenarios where the magnetic field has always been at the white dwarf surface. Field emergence is not unique to any magnetic generation scenario so we cannot narrow down the origin of the fields. It is yet to be determined whether DA(H)e stars were originally DA where a mechanism caused the emergence of both the magnetic field and spectral emission features together, or if they were

DAH stars which were incident to a mechanism which produces Balmer line emission. However, the discovery of delayed magnetic field emergence – independent of DA(H)e observations – gives support to the scenario that DA are the progenitors of DA(H)e stars, suggesting Balmer line emission is connected to the magnetic field generation mechanism(s).

It is interesting to note that the DA(H)e variability strip in the *Gaia* HRD coincides with the maximum strength of the hydrogen opacity in the non-degenerate envelope (see fig. 6 of Saumon et al., 2022), and this opacity bump is even more sharply peaked in stellar radius for radiative magnetic structures (Tremblay et al., 2015b). We speculate that it could result in instabilities and waves responsible for activity at the surface, but it would not explain a change in the incidence of magnetic white dwarfs with temperature (Bagnulo and Landstreet, 2022).

4.4.3 An explanation for photometric variability in WD J0412+7549

In order to explain the causes of photometric variability, we used the *TESS* bandpass and integrated different white dwarf model fluxes to perform two tests. In the first test, we computed the flux using our best-fitting 3D convective DA model atmosphere without line emission, and then with added artificial line emission based on the observed Keck spectrum at peak emission. The flux variation was 0.04 %, which rules out that Balmer line emission is causing the observed photometric variation of $\approx 2.29 \pm 0.05\,\%$.

In the second test, we used our 1D radiative and 1D convective DA model atmospheres[5] on opposing sides of the star to model convective and radiative magnetic regions, respectively (Figure 4.17). We assumed a constant effective temperature across the surface. The impact of magnetic fields on a stellar structure can be estimated from the plasma-β parameter ($\beta = 8\pi P/B^2$, where P is the thermal pressure and B the magnetic field strength). It was found from 3D magneto-hydrodynamic (MHD) simulations (Tremblay et al., 2015b) that a value of $\beta \sim 1$ will inhibit convective energy transfer in the white dwarf atmosphere. Magnetic fields larger than this critical value, corresponding to $0.002 - 0.1$ MG in DA white dwarfs (Cunningham et al., 2020), will therefore result in a largely radiative temperature stratification (Gentile Fusillo et al., 2018). For WD J0412+7549, the critical field to inhibit convection is $B \approx 0.01$ MG, so a plausible scenario to explain photometric variability is that one side of the star harbours a small magnetic field (above $B \approx 0.01$ MG

---

[5] The use of 1D convective models is to allow for a better differential comparison using the same atmosphere code.

but below the detection limit of 0.05 MG) resulting in a radiative structure, while other regions are able to remain convective (Tremblay et al., 2015b, see also Section 4.3.2).

The different atmospheric temperature stratifications in convective and magnetic regions result in different SEDs. We find that flux peaks on the convective side of the star in the *TESS* bandpass, with a flux deficit on the radiative side. A flux variation of ≈ 5 % is predicted between the two regions, which suggests that even subtle effects on the atmospheric structure from small magnetic fields ($\approx 10-50$ kG) could be responsible for the photometric *TESS* flux variation. Under this scenario, the photometric minimum corresonds to the radiative (magnetic) side, in line with the expectation of an active chromosphere and line emission in magnetic regions. While the effective temperature remains constant, the smaller flux in the *TESS* bandpass for the radiative region implies that light is emitted from a slightly cooler region of the atmosphere. This is analogous to the previously suggested scenario where DA(H)e stars have cool magnetic regions (Walters et al., 2021), but does not require a yet unexplained mechanism to change the effective temperature across the surface.

We note that the above prediction could be tested with multi-wavelength photometric studies and spectropolarimetry, to confirm that one or more phases have a radiative structure and magnetic field strength $\approx 10-50$ kG. We also note that this scenario is unlikely to apply for DAHe white dwarfs, in particular for GD 356 where spectropolarimetric observations suggest that in all rotation phases the surface is highly magnetic (Walters et al., 2021), hence likely radiative.

4.5 Conclusions

Two DAe white dwarfs, WD J0412+7549 and WD J1653−1001, have been discovered in the past three years. They have hydrogen-dominated atmospheres and exhibit Hα and Hβ line emission. These characteristics are the same as DAHe stars, yet DAHe stars have Zeeman-split Balmer emission lines indicating magnetism. The class DA(H)e incorporates DAe and DAHe stars due to the hypothesis that they have a similar origin, as their uncoincidental close clustering on the *Gaia* HRD indicates these stars may be experiencing a short evolutionary phase where magnetic fields with vastly different strengths trigger Balmer line emission. The physical mechanism(s) causing DA(H)e stars is still unknown.

This work provides detailed follow-up of the two known DAe stars by presenting new time-domain spectroscopic observations and analysis of the latest photo-

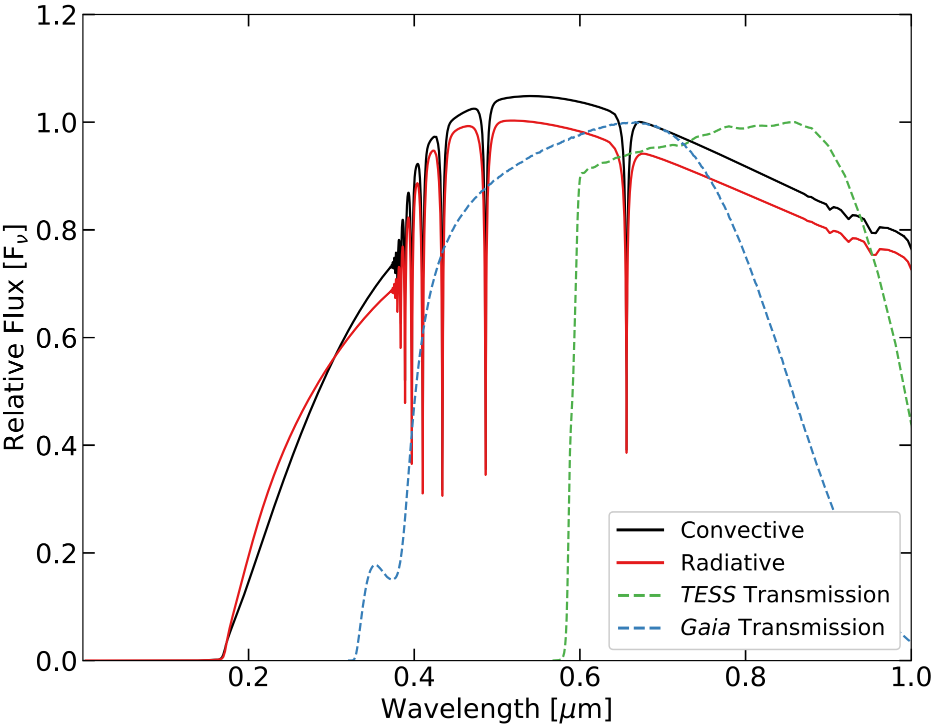

Figure 4.17: Model spectra created from the same 1D model atmosphere code with a pure-hydrogen equation-of-state, showing radiative (red curve) and convective (ML2/$\alpha = 0.8$; black curve) structures corresponding to opposing sides of the star. A constant effective temperature across the white dwarf surface is assumed. The normalised *TESS* (green) and *Gaia* (blue) bandpasses are shown.

metric time-series data. Both DAe stars do not have detectable magnetic fields, with upper limits on magnetic field strength of $B < 0.05\,\mathrm{MG}$. We confirm that both DAe stars exhibit photometric and spectroscopic variability, which we interpret as the white dwarf spin period. WD J0412+7549 has a period of $2.2891144 \pm 0.0000016\,\mathrm{h}$ and WD J1653−1001 has a tentative period of $80.534 \pm 0.087\,\mathrm{h}$. Additional photometric follow-up with larger phase coverage is needed to confidently determine the period of WD J1653−1001 as the current ZTF data is contaminated by an unresolved background main-sequence star.

WD J0412+7549 has spectroscopic data spanning its entire phase, including two high-resolution Keck spectra. We calculated the radial velocity of this star using its Hα emission line and found an absence of significant radial velocity variation, which indicates it is originating from the white dwarf surface or chromosphere. The similar physical characteristics of DAe and DAHe stars (Section 4.4.1) suggests that the mechanism causing the Balmer line emission and photometric variability is in common, and likely intrinsic to the white dwarf, rather than a substellar companion body closely orbiting the stars as has been suggested in previous studies (Walters et al., 2021). Furthermore, WD J0412+7549 has an anti-phase relationship between photometric (flux) and spectroscopic (emission) variability which is the same phase relationship found in DAHe stars. An anti-phase relationship is the expectation of a photospheric dark spot/region with a temperature-inverted and optically thin chromospheric emission region, and not of a closely orbiting companion.

We have shown that the photometric flux variation in WD J0412+7549 could be readily explained by radiative (magnetic) and convective hemispheres having different SEDs, with a threshold of $B \approx 10\,\mathrm{kG}$ between the two faces. Testing this scenario would require better phase resolved limits on magnetic fields down to $1-10\,\mathrm{kG}$, a measurement that could be made difficult by the short rotation period.

It is possible that magnetic emergence has not occurred yet or has just started to occur in DAe stars, which explains their lack of a detectable magnetic field but similarities with DAHe stars. Therefore, the physical origin of their characteristics could be the same as DAHe stars. We explored magnetic mechanisms that could drive a magnetic field in isolated white dwarfs, including global and local surface dynamos. A global dynamo is created from the combination of core crystallisation and the white dwarf rotation. Our modelling could not determine if WD J0412+7549 has started to crystallise but we conclude that WD J1653−1001 has not started to crystallise. Spectroscopic and multi-wavelength photometric follow-up of DAe stars is required to further understand their behaviours and to determine the origin of this class.

Chapter 5

A network of cooler white dwarfs as infrared standards for flux calibration

5.1 Introduction

Now, more than ever, the creation and use of a reliable and self-consistent flux scale is of paramount importance. We have entered a pioneering era of space telescopes and instruments, which are providing previously unattainable data for objects in our Galaxy and beyond, especially in the near-IR (NIR; $0.8 - 5\,\mu$m) and mid-IR (MIR; $5 - 32\,\mu$m).

HST provides high-resolution imaging and broad wavelength coverage from the far-ultraviolet (FUV; $0.0912 - 0.2\,\mu$m) to NIR. New generation observatories will compliment and further the scientific reach of *HST*, for instance *JWST*, the *Euclid* spacecraft and *Roman* have an array of high-resolution and high-sensitivity instruments which facilitate photometric and spectroscopic observations from the FUV to MIR regimes. Similar capabilities will be achieved with first generation high-resolution instrumentation on ground-based telescopes, such as the Multi-AO Imaging Camera for Deep Observations (MICADO) on the Extremely Large Telescope (ELT). Data from these instruments will revolutionise fields in cosmology, such as dark energy and dark matter, and astrophysics, such as stellar evolution and exoplanet studies. However, observational data calibration is a major source of uncertainty for many instruments and scientific fields (Hounsell et al., 2018; Tayar et al., 2022; Wilson et al., 2023). For example, the accurate comparison between the fluxes of distant redshifted and nearby SNe in the rest frame has a crucial impact on our understanding of the nature of the dark energy that is driving the observed accelerating cosmic expansion (Stubbs and Brown, 2015; Scolnic et al., 2015, 2022; Brout et al., 2022). To reach this full scientific potential, photometric and spectroscopic instruments must be accurately calibrated on a single consistent flux scale, as uncertainties from flux standards propagate into scientific results (Hounsell et al., 2018).

To date, the most internally consistent set of primary flux standards are three hot ($T_{\rm eff} > 30\,000\,$K) H-dominated atmosphere (DA) white dwarfs: GD 71, GD 153 and G191-B2B (Bohlin et al., 2014). The SEDs, which are flux as a function of wavelength, of these primary standards provide the basis for calibration of the *HST* spectrophotometry, primarily from STIS, the WFC3 IR grisms, and NICMOS (Bohlin, 2014; Bohlin et al., 2020). While fits to Balmer lines determine $T_{\rm eff}$ and $\log g$, i.e. the shape of the SEDs, the absolute flux level is set by a reconciliation of the original Vega flux at 5557.5 Å (vacuum; Megessier, 1995) with the *MSX* IR absolute flux to define the absolute flux at all wavelengths over the UV, visible and NIR (Bohlin, 2014; Bohlin et al., 2020). These SEDs provide the basis for the *HST* absolute flux scale and are publicly available on CALSPEC[1], which is a database of primary and secondary spectrophotometric absolute flux standard stars on the *HST* flux scale containing measured stellar spectra and modelled SEDs. CALSPEC standards are used for the calibration of *HST*, *JWST*, *Gaia* and other ground- and space-based instrumentation. Therefore, the precision and accuracy of observational astrophysical and cosmological studies which use CALSPEC standards are entirely dependent on the CALSPEC precision of measured and modelled SEDs.

Hot DA white dwarfs have fully radiative atmospheres, therefore, their optical spectra are relatively simple to model. Their $T_{\rm eff}$ and $\log g$ determine accurate model SEDs (Holberg et al., 1985). SED models of the current three hot standards are consistent within 1 % at optical wavelengths ($0.3 - 1\,\mu$m) with *HST* spectrophotometric observations (Bohlin, 2014; Narayan et al., 2019). However, outside the optical, discrepancies of > 1 % are evident (Bohlin et al., 2011; Bohlin, 2014; Bohlin et al., 2022), because uncertainties arise in hot white dwarf model atmospheres from complex NLTE effects, trace metal contamination and UV metal line blanketing (Werner, 1996; Gianninas et al., 2010; Rauch et al., 2013). Hot white dwarfs have a lower sky density ($\simeq 0.75\,\rm deg^{-2}$ at $G < 20$) than cooler white dwarfs, forcing the selection of more distant hot stars with larger reddening effects and more uncertain *Gaia* parallaxes. Also, hot white dwarf SEDs drop rapidly in flux at longer wavelengths. These sources of uncertainty are non-negligible and propagate into the results of scientific studies.

The need for faint standards, e.g. below the saturation limits of several instruments, has motivated the expansion of hot white dwarf standards in recent years using *HST* spectrophotometry from faint ($16.5 < V < 19.5$) and photometrically stable DA white dwarfs spanning the whole sky (Narayan et al., 2016, 2019; Calamida et al., 2022; Axelrod et al., 2023). These studies have achieved consistency within 1 % of the *HST* flux scale at optical wavelengths, thus establishing all-sky spectrophotometric secondary standards for wide-field optical surveys. Good agreement was also found in the NIR regime with WFC3 observations.

We propose to add a network of 17 cooler DA white dwarfs with $T_{\rm eff} <$ 20 000 K as secondary spectrophotometric flux standards on the *HST* flux scale. Our network has *HST*/STIS flux calibrated spectra, with 16/17 supplemented by *HST*/WFC3 spectrophotometry, thus they are tied to the three CALSPEC primary standards. Cooler white dwarfs than the current primary hot standards have been proposed in recent years to have a comparable, or even higher, accuracy at IR

---

[1] https://www.stsci.edu/hst/instrumentation/reference-data-for-calibration-and-tools/astronomical-catalogs/calspec

wavelengths compared to hot white dwarfs (Tremblay et al., 2017; Gentile Fusillo et al., 2020). DA white dwarfs with $T_{\rm eff} < 20\,000\,{\rm K}$ suffer much less from NLTE effects or UV metal line blanketing, have a larger sky density than hot white dwarfs, their energy distributions peak in the optical/NIR, and are still relatively bright in the IR compared to their hotter counterparts. Cooler white dwarfs at distances $\lesssim 100\,{\rm pc}$ have the advantage of having less reddening than further away hot white dwarfs, while still being reliable calibrators for IR observing modes. The latest DA model atmospheres can effectively account for convective effects which are important for white dwarfs with $T_{\rm eff} \lesssim 13\,000\,{\rm K}$ (Tremblay et al., 2013, 2019b) so there are no reservations about modelling cooler white dwarfs which might have arisen decades ago, even though dense atmospheres below 6000 K are still subject to a low-mass problem (O'Brien et al., 2024).

The exclusive use of hot white dwarfs as flux calibrators may not be the optimal choice for achieving the highest accuracy possible, in particular with the dawn of next-generation IR missions. Our proposed network of 17 cooler calibrators can be used in parallel with hot white dwarf calibrators depending on the science case. This network will provide an independent estimate for secondary SEDs compared to the current primary SEDs; and the difference between SEDs based on cool or hot white dwarfs sets limits on the precision of flux calibrations. We split our network into 13 warm ($13\,000\,{\rm K} < T_{\rm eff} < 20\,000\,{\rm K}$) flux standard candidates and four extra flux standard candidates, which consist of the three coolest ($T_{\rm eff} < 13\,000\,{\rm K}$) white dwarfs in the network and one which has no *HST*/WFC3 spectrophotometry. There is an on-sky separation of < 4 h between the white dwarfs across the whole sky, which ensures adequate sky coverage for the vast majority of science cases.

Section 5.2 presents *HST* spectrophotometric observations of the 17 white dwarfs in our network, in addition to their *Gaia* Data Release 3 (DR3) astrometry and optical and IR photometry. We describe the fitting procedures implemented on the observed *HST* data with our model atmospheres in Section 5.3 which allow us to derive two sets of independent $T_{\rm eff}$ and $\log g$ best-fitting parameters, in addition to synthetic photometry and *Gaia* atmospheric parameters. In Section 5.4 we discuss our results and conclude in Section 5.5.

5.2 Observations

5.2.1 Hubble Space Telescope spectrophotometry

Our network of 17 flux standard candidates was built using spectrophotometric observations from three *HST* programmes that made use of the STIS and WFC3 instruments. WD 1327−083 and WD 2341+322 were observed in a Cycle 23 (GP-14213) pilot programme on using cooler white dwarfs than the current hot primary standards as near-IR and IR flux calibrators. WD 0352+096 has been observed intermittently over the past few decades, with the latest observations being from a Cycle 25 (GP-15485) programme for CALSPEC and *JWST* standard stars. The remaining 14 white dwarfs were observed in a Cycle 28 (GP-16249) programme specifically targeting candidates for our flux standard network. All 17 stars were selected because they do not have unresolved stellar companions in *HST* and *Gaia*, have H-dominated atmospheres (spectral type DA), have $T_{\rm eff} < 20\,000$ K, and no observed photometric or spectroscopic variability due to pulsations or magnetic phenomena - see Section 5.4.4 for flags from the literature on variability, metal traces, observed magnetism and binarity for the individual white dwarfs in our network.

The STIS low dispersion (L) spectra were obtained with a 52” × 2.0” long slit on the G140L, G230L, G430L and G750L gratings which cover 1140 – 10 200 Å and the WFC3 spectra were obtained with the G102 and G141 grisms which cover 8000 – 17 000 Å. STIS and WFC3 spectrophotometry were merged at 10 115 Å to form complete *HST* SEDs spanning 1140 – 17 000 Å for all 17 candidates except WD 0352+096 which does not have WFC3 data. A log of the *HST* spectrophotometric observations are given in Table 5.1.

5.2.2 *Gaia* DR3 astrometry

The *Gaia* DR3 astrometry for the 17 DA white dwarfs proposed as flux standards is displayed in Table 5.2 and the spatial distribution in Galactic coordinates of the network is shown in Fig. 5.1. The stars are all within 40 pc and have absolute *Gaia* G magnitudes ($M_{\rm G}$) of < 12.7 mag so they are relatively bright compared to white dwarfs in the same volume, which peak at absolute magnitudes of approximately 14.5 mag (O’Brien et al., 2024).

Data for two of the current hot primary standard white dwarfs, GD 153 and GD 71, are also given in Table 5.2 for comparison to the 17 flux standard candidates. The third hot primary standard, G191-B2B, is not included in this chapter (see Section 5.3.1 for more details).

5.2.3 Photometry

Most white dwarfs in our network have optical photometry from *Gaia* DR3 G, $G_{\rm BP}$ and $G_{\rm RP}$ bands (Gaia Collaboration et al., 2023), in addition to IR photometry from

Table 5.1: Log of *HST* STIS and WFC3 spectrophotometric observations for the 17 DA white dwarfs proposed as flux standards. The exposure time ($t_{\rm exp}$), number of exposures ($n_{\rm exp}$) and the duration of the observing run is given. Where observations were taken over multiple dates with multiple exposure times, numbers are separated by a forward slash (/).

Object	Telescope/Instrument	Date [yyyy-mm-dd]	Grating	$t_{\rm exp}$ [s]	$n_{\rm exp}$	Duration [s]
Warm flux standard candidates						
WD 0148+467	HST/STIS	2021-08-07	G140L	1355.0	1	1355.0
		2021-08-07	G230L	718.0	1	718.0
		2021-08-07	G430L	410.0	1	410.0
		2021-08-07	G750L	2000.0	1	2000.0
	HST/WFC3	2021-07-30	G102	138.4	3	415.1
		2021-07-30	G141	115.5	3	346.4
WD 0227+050	HST/STIS	2021-12-19	G140L	953.0	1	953.0
		2021-12-19	G230L	980.0	1	980.0
		2021-12-19	G430L	306.0	1	306.0
		2021-12-19	G750L	1920.0	1	1920.0
	HST/WFC3	2021-09-22	G102	253.0	3	759.0
		2021-07-30	G141	207.1	3	621.4
WD 0809+177	HST/STIS	2022-02-21	G140L	1074.0	1	1074.0
		2022-02-21	G230L	870.0	1	870.0
		2022-02-21	G430L	300.0	1	300.0
		2022-02-21	G750L	1980.0	1	1980.0
	HST/WFC3	2021-09-18	G102	432.1	3	1296.4
		2021-09-18	G141	336.3	3	1008.9

Object	Telescope/Instrument	Date [yyyy-mm-dd]	Grating	t_{exp} [s]	n_{exp}	Duration [s]
WD 1105−340	HST/STIS	2022-01-27	G140L	1368.0	1	1368.0
		2022-01-27	G230L	600.0	1	600.0
		2022-01-27	G430L	324.0	1	324.0
		2022-01-27	G750L	1980.0	1	1980.0
	HST/WFC3	2021-08-03	G102	432.1	3	1296.4
		2021-08-03	G141	384.2	3	1152.7
WD 1105−048	HST/STIS	2022-04-02	G140L	1143.0	1	1143.0
		2022-04-02	G230L	780.0	1	780.0
		2022-04-02	G430L	340.0	1	340.0
		2022-04-02	G750L	1928.0	1	1928.0
	HST/WFC3	2021-12-15	G102	275.9	3	827.7
		2021-12-15	G141	230.1	3	690.2
WD 1327−083	HST/STIS	2016-04-15	G140L	1244.0	1	1244.0
		2016-04-15	G230L	605.0	1	605.0
		2016-04-15	G430L	200.0	1	200.0
		2016-04-15	G750L	936.0	1	936.0
	HST/WFC3	2016-04-15	G102	83.5	1	83.5
		2016-04-15	G141	60.1	3	60.1
WD 1713+695	HST/STIS	2022-07-07	G140L	1364.0	1	1364.0
		2022-07-07	G230L	910.0	1	910.0
		2022-07-07	G430L	342.0	1	342.0
		2022-08-29	G750L	2475.0	1	2475.0
	HST/WFC3	2021-09-20	G102	321.8	3	965.3
		2021-09-20	G141	275.9	3	827.7

Object	Telescope/Instrument	Date [yyyy-mm-dd]	Grating	t_{exp} [s]	n_{exp}	Duration [s]
WD 1911+536	HST/STIS	2021-10-01	G140L	1112.0	1	1112.0
		2021-10-01	G230L	1000.0	1	1000.0
		2021-10-01	G430L	330.0	1	330.0
		2021-10-01	G750L	2080.0	1	2080.0
	HST/WFC3	2021-07-24	G102	336.3	3	1008.9
		2021-07-24	G141	298.8	3	896.5
WD 1919+145	HST/STIS	2022-08-23	G140L	1237.0	1	1237.0
		2022-08-23	G230L	700.0	1	700.0
		2021/2022-10/08-06/23	G430L	330.0	2	660.0
		2022-08-23	G750L	1944.0	2	1944.0
	HST/WFC3	2021-07/09-21/14	G102	253.0	6	1517.9
		2021-07/09-21/14	G141	207.1	6	1242.9
WD 2039−682	HST/STIS	2022-08-01	G140L	1220.0	1	1220.0
		2022-08-01	G230L	1054.0	1	1054.0
		2022-08-01	G430L	342.0	1	342.0
		2022-08-01	G750L	2225.0	1	2225.0
	HST/WFC3	2021-07-27	G102	336.3	3	1008.9
		2021-07-27	G141	298.8	3	896.5
WD 2117+539	HST/STIS	2022-08-27	G140L	1437.0	1	1437.0
		2022-08-27	G230L	700.0	1	700.0
		2022-08-27	G430L	354.0	1	354.0
		2022-08-27	G750L	2060.0	1	2060.0
	HST/WFC3	2021-07/09-31/15	G102	230.1	6	1380.4
		2021-07/09-31/15	G141	184.2	6	1105.3

Object	Telescope/Instrument	Date [yyyy-mm-dd]	Grating	t_{exp} [s]	n_{exp}	Duration [s]
WD 2126+734	HST/STIS	2021-10-02	G140L	1400.0	1	1400.0
		2021-10-02	G230L	913.0	1	913.0
		2021-10-02	G430L	406.0	1	406.0
		2021-10-02	G750L	2200.0	1	2200.0
	HST/WFC3	2021-08-03	G102	253.0	3	759.0
		2021-08-03	G141	207.1	3	621.4
WD 2149+021	HST/STIS	2021-10-02	G140L	965.0	1	965.0
		2021-10-02	G230L	965.0	1	965.0
		2021-10-02	G430L	302.0	1	302.0
		2021-10-02	G750L	1920.0	1	1920.0
	HST/WFC3	2021-07-26	G102	207.1	3	621.4
		2021-07-26	G141	161.3/184.2	3	506.8
Extra flux standard candidates						
WD 0352+096	HST/STIS	2019-02-09	G140L	2379.0	1	2379.0
		2019-02-09	G230L	1101.0	1	1101.0
		2019-02-09	G430L	1200.0	1	1200.0
		1998-02/03-19	G750L	1980.0	2	3960.0
WD 1202−232	HST/STIS	2021-08-05	G140L	749.0/761.0	2	1510.0
		2016-06-15	G230L	2302.2	1	2302.2
		2021-08-05	G430L	1200.0	1	1200.0
		2021-08-05	G750L	1600.0	1	1600.0
	HST/WFC3	2021-07-25	G102	138.4	3	415.1
		2021-07-25	G141	88.0	3	264.0

Object	Telescope/Instrument	Date [yyyy-mm-dd]	Grating	t_{exp} [s]	n_{exp}	Duration [s]
WD 1544−377	HST/STIS	2021-10-03	G140L	1047.0	1	1047.0
		2021-10-03	G230L	1790.0	1	1790.0
		2021-10-03	G430L	300.0	1	300.0
		2021-10-03	G750L	1401.0	1	1401.0
	HST/WFC3	2021-07/09-29/27	G102	161.3/177.9	3/3	1017.7
		2021-07/09-29/27	G141	115.2/127.9	3/3	730.2
WD 2341+322	HST/STIS	2016-05-27	G140L	1370.0	1	1370.0
		2016-05-27	G230L	650.0	1	650.0
		2016-05-27	G430L	240.0	1	240.0
		2016-05-27	G750L	939.0	1	939.0
	HST/WFC3	2016-05-27	G102	176.0	1	176.0
		2016-05-27	G141	128.5	1	128.5

Table 5.2: *Gaia* DR3 astrometry for the 17 DA white dwarfs proposed as flux standards, in addition to two of the current hot primary standards. Proper motions, μ, are given in the right ascension (α) and declination (δ) directions. Absolute magnitudes, M_{G}, are computed using the *Gaia* G magnitude and the *Gaia* parallax. Values are given in the J2016.0 epoch.

Object	*Gaia* DR3 Designation	RA [deg]	Dec [deg]	$\mu_\alpha \cos(\delta)$ [mas yr^{-1}]	μ_δ [mas yr^{-1}]	Parallax [mas]	Distance [pc]	M_{G} [mag]
Hot primary standards								
GD 153	3944400490365194368	194.259	22.030	−38.402 ± 0.045	−202.990 ± 0.051	14.593 ± 0.038	68.526 ± 0.177	9.132 ± 0.003
GD 71	3348071631670500736	88.115	15.886	76.728 ± 0.053	−172.960 ± 0.038	19.564 ± 0.055	51.115 ± 0.144	9.457 ± 0.003
Warm flux standard candidates								
WD 0148+467	356922880493142016	28.012	47.002	4.645 ± 0.031	122.025 ± 0.027	60.564 ± 0.031	16.511 ± 0.008	11.407 ± 0.003
WD 0227+050	2516322146457318144	37.570	5.264	76.958 ± 0.049	−24.502 ± 0.039	37.711 ± 0.051	26.517 ± 0.036	10.703 ± 0.003
WD 0809+177	657056745624156416	123.158	17.617	73.482 ± 0.026	−87.171 ± 0.020	36.977 ± 0.025	27.044 ± 0.018	11.269 ± 0.003
WD 1105−340	5401688425816913920	166.950	−34.349	39.894 ± 0.021	−263.429 ± 0.019	38.195 ± 0.021	26.181 ± 0.014	11.610 ± 0.003
WD 1105−048	3788194488314248832	167.000	−5.160	−55.547 ± 0.031	−442.634 ± 0.028	40.293 ± 0.032	24.818 ± 0.020	11.117 ± 0.003
WD 1327−083	3630035787972473600	202.552	−8.577	−1111.205 ± 0.048	−472.540 ± 0.028	62.148 ± 0.044	16.091 ± 0.011	11.322 ± 0.003
WD 1713+695	1638563322306634368	258.275	69.522	−55.513 ± 0.020	−343.042 ± 0.025	38.094 ± 0.018	26.251 ± 0.012	11.232 ± 0.003
WD 1911+536	2140481412496465152	288.203	53.721	144.450 ± 0.022	136.061 ± 0.019	45.109 ± 0.018	22.169 ± 0.009	11.518 ± 0.003
WD 1919+145	4319908862597055232	290.418	14.678	−33.016 ± 0.027	−75.933 ± 0.023	50.308 ± 0.030	19.878 ± 0.012	11.527 ± 0.003
WD 2039−682	6424566979354709248	311.092	−68.090	182.095 ± 0.018	−228.167 ± 0.023	51.099 ± 0.025	19.570 ± 0.010	11.882 ± 0.003
WD 2117+539	2176116580055936512	319.734	54.212	−85.450 ± 0.026	193.193 ± 0.026	57.764 ± 0.022	17.312 ± 0.006	11.201 ± 0.003
WD 2126+734	2274076297221555968	321.741	73.644	55.338 ± 0.030	−314.200 ± 0.030	44.992 ± 0.026	22.226 ± 0.013	11.153 ± 0.003
WD 2149+021	2693940725141960192	328.106	2.387	15.323 ± 0.042	−300.533 ± 0.044	44.326 ± 0.043	22.560 ± 0.022	11.010 ± 0.003
Extra flux standard candidates								
WD 0352+096	3302846072717868416	58.842	9.788	173.274 ± 0.035	−5.569 ± 0.025	28.587 ± 0.037	34.981 ± 0.045	11.829 ± 0.003
WD 1202−232	3489719481290397696	181.361	−23.552	41.819 ± 0.021	226.558 ± 0.020	95.902 ± 0.018	10.427 ± 0.002	12.647 ± 0.003
WD 1544−377	6009537829925128064	236.873	−37.920	−423.692 ± 0.031	−209.108 ± 0.025	65.689 ± 0.026	15.223 ± 0.006	12.088 ± 0.003
WD 2341+322	2871730307948650368	355.960	32.546	−215.905 ± 0.033	−59.871 ± 0.021	53.762 ± 0.027	18.601 ± 0.009	11.619 ± 0.003

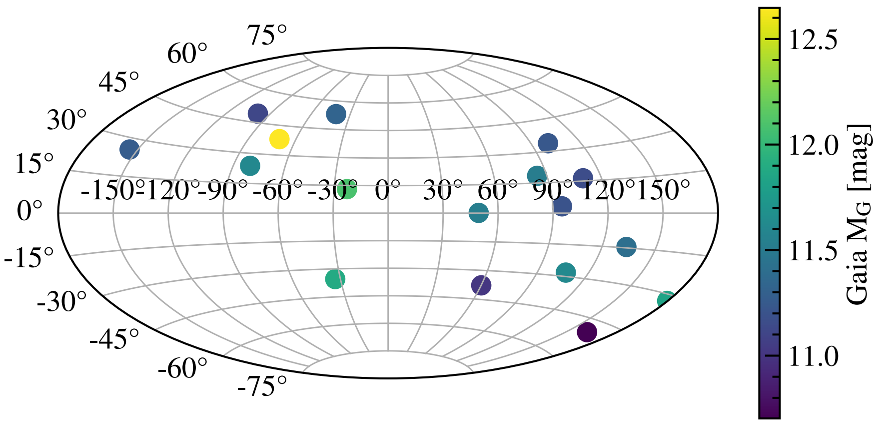

Figure 5.1: Galactic coordinates (latitude and longitude in the J2016.0 epoch) of the 17 white dwarf flux standard candidates from *Gaia* DR3, with their colour representing their absolute magnitudes, M_G, computed using the *Gaia* G magnitude and the *Gaia* parallax (Table 5.2).

2MASS J, H and K_S bands (Skrutskie et al., 2006) and the WISE (Wright et al., 2010) $W1$ and $W2$ bands from the AllWISE source catalogue. Observed photometry is displayed in Table 5.5.

5.3 Analysis

5.3.1 Spectrophotometric fitting

The latest (March 2024) grid of 3D DA local thermal equilibrium (LTE) atmosphere models were used to fit the *HST* spectrophotometry of the 17 DA white dwarfs proposed as flux standards. The grid is an updated version of the work in Tremblay et al. (2013) and Tremblay et al. (2015a), which now has an extended resolution and wavelength coverage ($40 - 600\,000$ Å), is in vacuum wavelengths, and can be used with or without H_2 molecular lines in the UV. This work does not use high-resolution UV data so we employ the grid without H_2 molecular lines. The grid includes models for $7.0 \leq \log g \leq 9.0$ in steps of 0.5 dex (cgs units) and $1500\,\mathrm{K} \leq T_{\mathrm{eff}} \leq 40\,000\,\mathrm{K}$. We have used LTE models because NLTE effects at $< 40\,000$ K are only noticeable on the central, high spectral resolution cores of Balmer lines (Napiwotzki et al., 2020; Munday et al., 2024), which is inconsequential for continuum flux calibration. At $T_{\mathrm{eff}} \lesssim 13\,000$ K atmospheric convection becomes important to predict continuum fluxes from UV to IR, hence we use 3D models which have no free parameters unlike the previous 1D grids based on the mixing-length theory of convection (Tremblay et al., 2013).

Ideally, atmospheric models should correctly predict the SED flux and Balmer line profiles of white dwarf flux standards independently to sub-percent precision. Therefore, we fit the network in two different ways: 1) SED fit of the continuum and *Gaia* DR3 parallax, omitting the Balmer line regions; 2) Balmer line fit of Hβ - Hη. This method allows us to determine two independent $T_{\rm eff}$ and $\log g$ values for each star, thus defining model absolute fluxes with the help of a M-R relation (see e.g. Bédard et al., 2020).

The same fitting methods were conducted on the current hot standards GD 153 and GD 71, except that we used a 1D DA NLTE grid of models due to these stars having $T_{\rm eff} \approx 40\,000$ K and being outside of the range of convection (Tremblay et al., 2011). This grid is in air wavelengths and ranges from $6.5 \leq \log g \leq 9.5$ in steps of 0.5 dex and $1500\,{\rm K} \leq T_{\rm eff} \leq 140\,000\,{\rm K}$. We did not include the current hot standard G191-B2B in our analysis because it has trace metals that strongly influence NLTE effects, thus a different model grid would have to be used to accurately fit its SED (Barstow et al., 1999; Gianninas et al., 2010; Preval et al., 2013; Bohlin et al., 2020).

The input physics prescription and numerical methods for both DA 3D LTE and 1D NLTE model grids can be found on P.-E. Tremblay's Source Model Data webpage[2].

STIS and WFC3 SED fitting

Each observed STIS and WFC3 *HST* spectra were fit with model atmospheres by minimising the reduced χ^2 using the `scipy optimize` trust region reflective (`trf`) algorithm, which is a non-linear least-squares method (Byrd et al., 1987). The fits neglect regions bluer than 1450 Å to avoid the broad Lyman-α H_2^+ satellite region at 1380 − 1410 Å, which appears for stars $T_{\rm eff} < 20\,000$ K (Koester et al., 1985) and increases in strength (i.e. extends to redder wavelengths) for decreasing temperatures - thus, the fits were started at 1700 Å for the two coolest stars in the network WD 1202−232 and WD 1544−377. WD 2341+322 is the third coolest star in the network and has a Lyman-α satellite from H-H collisions at ≈ 1600 Å, however our models fit this feature well and has been proven to be a good indicator of atmospheric parameters (Greenstein and Oke, 1979; Wegner, 1982; Koester et al., 1985; Nelan and Wegner, 1985; Xu et al., 2013) so we kept it in the fit by starting at 1450 Å like the warmer objects in the network. The reddest WFC3 grism extends to 17 000 Å so to avoid the end of the grism where measurements can get unreliable we neglected all wavelengths redder than 16 000 Å, except WD 0352+096 which does not

---

[2] https://warwick.ac.uk/fac/sci/physics/research/astro/people/tremblay/modelgrids/

have WFC3 data so we end the fit at 10 000 Å to avoid the edge of the STIS G750L grating (at 10 238 Å). The Balmer line regions 3815 – 4490 Å, 4681 – 5041 Å and 6385 – 6745 Å were masked in all fits to ensure independent atmospheric parameters were obtained to the separate Balmer line fit parameters.

The DA model Eddington fluxes, H_ν, were converted to $H_\lambda(\lambda)$ for the fits, then compared to the observed fluxes, $f_\lambda(\lambda)$, using

$$f_\lambda(\lambda) = 4\pi \left(\frac{R}{D}\right)^2 H_\lambda(\lambda), \tag{5.1}$$

where R is the white dwarf radius and D is the distance to the white dwarf from Earth, constrained from the *Gaia* DR3 parallax. The model fluxes were reddened (extinguished) using the G23 model from Gordon et al. (2023), which is the latest extinction curve in the `python` package `dust_extinction`[3] for 912 Å to 32 μm and $R(V) = A(V)/E(B-V)$. We used $R(V) = 3.1$ as this is the often used Milky Way average value (Johnson, 1965; Schultz and Wiemer, 1975; Whittet and van Breda, 1980; Fitzpatrick and Massa, 1999). The T_eff, $\log g$, parallax and $E(B-V)$ were free parameters in the fits. The bounds for T_eff and $\log g$ were determined by the model grid limits, parallax was bounded by $\pm 3\sigma$ of the *Gaia* DR3 parallax errors, and $E(B-V)$ had arbitrary bounds of 0.00 – 0.05 mag due to all white dwarfs in the network being < 40 pc thus having minimal reddening effects. We used the DA M-R relation with thick hydrogen layers and carbon-oxygen cores from Bédard et al. (2020)[4] to determine R (and white dwarf mass) using the best-fitting T_eff, $\log g$ and parallax.

Statistical uncertainties were computed from the covariance matrix of the model atmosphere fit scaled by reduced χ^2 to account for the goodness of fit. The systematic error on SED fits were computed by fitting the UV (1450 – 3065 Å) and combined optical+NIR (3065 – 16 000 Å) regions separately to obtain two sets of T_eff and $\log g$ best-fitting parameters.

These pairs of T_eff and $\log g$ disagreed by far more than the statistical errors, indicating some unmodelled systematic uncertainty. To quantify these, we assumed that each white dwarf required some additional variance in $\ln T_\mathrm{eff}$ and $\log g$ that is the same for all objects. We then sought to determine these systematic uncertainties via a maximum-likelihood approach. For a quantity x (where x is either $\ln T_\mathrm{eff}$ or $\log g$) observed for a single system N times (in our case $N = 2$), the ith observation, x_i, can be considered to be drawn from a normal distribution with unknown mean

---

[3] https://github.com/karllark/dust_extinction

[4] https://www.astro.umontreal.ca/~bergeron/CoolingModels/

μ and variance σ^2, with additional measurement uncertainty, e_i. The likelihood of all N observations is therefore

$$L(\mathbf{x}|\mu, \sigma, \mathbf{e}) = \prod_i^N \frac{1}{\sqrt{2\pi v_i}} \exp\left(-\frac{(x_i - \mu)^2}{2v_i}\right), \tag{5.2}$$

where $v_i = \sigma^2 + e_i^2$. Since we are not specifically interested in μ, only σ, we can integrate over μ, reducing the dimensionality to a marginal likelihood that depends only σ. This integral has an analytic solution which can be written as

$$\ln L(\mathbf{x}|\sigma, \mathbf{e}) = k - \frac{1}{2}\left(\ln a - b^2/a + c + d\right), \tag{5.3}$$

where k is a normalising constant, and a–d are sums over the observations given by

$$a = \sum_i^N \frac{1}{v_i}, \quad b = \sum_i^N \frac{x_i}{v_i}, \quad c = \sum_i^N \frac{x_i^2}{v_i}, \quad d = \sum_i^N \ln v_i, \tag{5.4}$$

and are themselves functions of σ. Finally, for M systems with index j, the log-likelihood (dropping proportionality constants)

$$\ln L(\mathbf{x}_1, \ldots, \mathbf{x}_M|\sigma, \mathbf{e}_1, \ldots, \mathbf{e}_M) = \sum_j^M \ln L(\mathbf{x}_j|\sigma, \mathbf{e}_j). \tag{5.5}$$

Because of the marginalisation step, the final likelihood depends only on σ. Therefore determining the maximum-likelihood is a simple case of plotting as a function of σ and visually determining the location of the maximum to whatever precision is desired.

For our 13 warm flux standard candidate white dwarfs, each with two observations, we determined systematic uncertainties of 1.1 % in T_{eff} (i.e. 0.011 in $\ln T_{\text{eff}}$), and 0.01 dex in $\log g$. Data from the extra flux standard candidates is not included in the systematic uncertainty determination due to their SED fits spanning different wavelength ranges to the other 13 candidates. We apply the systematic uncertainties in T_{eff} and $\log g$ to all 17 flux standard candidates and the two primary standards. The combined statistical and systematic uncertainties are displayed in Table 5.3 with the best-fitting T_{eff} and $\log g$ parameters for our network and the two primary standards. The best-fitting extinction value is also quoted in Table 5.3 from each SED fit to three decimal places.

The SED fits between the observed spectrophotometry and best-fitting models for the 13 warm and four extra flux standard candidates are shown in the top left panels of Figures 5.2(a)-(m) and 5.3(a)-(d), respectively. The SED flux residuals are shown in the bottom left panels of the same figures. The best-fitting SED models for the flux standard candidates include the parameters $T_{\rm eff}$, $\log g$, $E(B-V)$, radius and mass. The best-fitting SED models and parameters are available with the electronic distribution of Elms et al. (2024) and on CALSPEC, except the models for WD 1202−232 and WD 1544−377 which are not included in CALSPEC due to potential modelling issues and/or contamination in the IR (see Section 5.4.1). The models for WD 1202−232 and WD 1544−377 included in the electronic distribution of Elms et al. (2024) are cropped at 2300 − 12 700 Å and 2400 − 12 500 Å, respectively, as the flux residuals are majoritively within 5 per cent in these regions.

We calculated the standard deviation of the flux residuals for all 17 candidates and the two hot primary standards over the entire wavelength range of each SED fit, in addition to the UV and combined optical+NIR ranges. The percentages are given in Table 5.4.

Balmer line fitting

For each of our 17 flux standard candidates, an independent set of $T_{\rm eff}$ and $\log g$ values can be obtained by directly comparing the Balmer line profiles with our sets of models. We do this by first continuum normalising both the models and the STIS spectra by fitting a spline, and then cropping out each Balmer line (e.g. Figure 5.2 right panels). We then fit the cropped Hβ to Hη absorption features with our DA model atmospheres using the same `scipy optimize trf` reduced χ^2 minimisation technique as our SED fits. $T_{\rm eff}$, $\log g$ and radial velocity were free parameters in the fits. The bounds for $T_{\rm eff}$ and $\log g$ were determined by the model grid limits, whereas radial velocity was bounded by the range $-300 - 300\,{\rm km\,s^{-1}}$. The same DA M-R relation as in our SED fits (Section 5.3.1) was used to determine R (and white dwarf mass) using the best-fitting $T_{\rm eff}$ and $\log g$. The Hη Balmer line was excluded from the fits for GD 153 and GD 71 because it has negligible W_λ for these hot stars.

Unlike the SED fits, for Balmer line modelling the arbitrarily high natural resolution of our DA models needs to be degraded to match that of STIS. This can be achieved by convolving the models with the appropriate STIS grating Line Spread Function (LSF) at the slit width matching that of our observations. Tabulated LSFs are available at the *HST* STIS web pages[5], which specifies the shape of a monochromatic line feature as observed with the specified instrumental resolution and provides an empirical description of the light distribution along the primary dispersion axis. Hβ to Hη are covered by the G430L grating and Hα is covered by

---

[5] https://www.stsci.edu/hst/instrumentation/stis/performance/spectral-resolution

Table 5.3: Atmospheric parameters of the 17 DA white dwarfs proposed as flux standards, in addition to two of the current hot primary standards, from two fitting methods: 1) SED fit of the continuum and *Gaia* DR3 parallax, omitting the Balmer regions; 2) Balmer line fit of Hβ - Hη. The uncertainties on the SED fits correspond to 1σ and are a combination of the statistical errors from the fits and the systematic errors (1.1 % in T_{eff} and 0.01 dex in $\log g$) obtained in Section 5.3.1. The quoted uncertainties on the Balmer line fits correspond to 1σ and are purely of statistical nature as derived from the fits. These Balmer line fit uncertainties are found to be underestimated in Section 5.4.2 hence we recommend the reader to apply a scale factor of ×3 for further analysis. $\sigma_{T_{\mathrm{eff}}}$ and $\sigma_{\log g}$ correspond to how many σ apart the best-fitting T_{eff} and $\log g$ parameters are from the SED and Balmer line fits. $E(B-V)$ values which are quoted as 0.000 may be non-zero (< 0.0005 mag) in the fit and analysis.

Object	SED fit		Balmer line fit		$E(B-V)$	$\sigma_{T_{\mathrm{eff}}}$	$\sigma_{\log g}$
	T_{eff} [K]	$\log g$ [dex]	T_{eff} [K]	$\log g$ [dex]	$(R_V = 3.1)$ [mag]	[K]	[dex]
Hot primary standards							
GD 153	40120 ± 443	7.818 ± 0.021	39240 ± 251	7.750 ± 0.026	0.000	1.007	0.843
GD 71	33379 ± 367	7.822 ± 0.017	33054 ± 107	7.780 ± 0.020	0.000	0.666	0.673
Warm flux standard candidates							
WD 0148+467	14483 ± 160	8.025 ± 0.012	13784 ± 81	8.032 ± 0.014	0.000	2.403	0.182
WD 0227+050	19190 ± 213	7.903 ± 0.017	19093 ± 55	7.894 ± 0.013	0.000	0.362	0.200
WD 0809+177	16371 ± 181	8.078 ± 0.015	16152 ± 73	8.102 ± 0.015	0.000	0.767	0.509
WD 1105−340	14099 ± 156	8.102 ± 0.014	13618 ± 190	8.120 ± 0.029	0.000	0.815	0.198
WD 1105−048	15826 ± 175	7.940 ± 0.015	15602 ± 74	7.949 ± 0.014	0.000	2.795	0.199
WD 1327−083	15100 ± 167	8.007 ± 0.015	14368 ± 103	7.984 ± 0.019	0.004	2.091	0.356
WD 1713+695	16063 ± 178	8.026 ± 0.015	15629 ± 71	7.979 ± 0.014	0.000	1.563	1.072
WD 1911+536	17424 ± 192	8.316 ± 0.016	17198 ± 71	8.335 ± 0.012	0.000	0.784	0.481
WD 1919+145	15364 ± 171	8.174 ± 0.017	14750 ± 67	8.173 ± 0.015	0.000	2.335	0.003
WD 2039−682	17076 ± 188	8.497 ± 0.016	16726 ± 76	8.502 ± 0.016	0.002	1.182	0.088
WD 2117+539	15583 ± 172	7.949 ± 0.016	14541 ± 72	7.921 ± 0.013	0.002	3.768	0.647
WD 2126+734	16050 ± 177	7.967 ± 0.015	15535 ± 65	7.967 ± 0.013	0.003	1.953	0.005
WD 2149+021	17692 ± 196	8.009 ± 0.016	17695 ± 72	8.019 ± 0.015	0.000	0.011	0.221
Extra flux standard candidates							
WD 0352+096	14810 ± 164	8.320 ± 0.015	14000 ± 260	8.341 ± 0.023	0.000	1.017	0.308
WD 1202−232	8854 ± 100	8.024 ± 0.023	8736 ± 21	7.980 ± 0.019	0.008	0.999	0.716
WD 1544−377	10303 ± 121	7.999 ± 0.033	10581 ± 46	8.012 ± 0.025	0.003	1.517	0.154
WD 2341+322	12852 ± 142	8.027 ± 0.013	12775 ± 128	8.036 ± 0.021	0.000	0.190	0.143

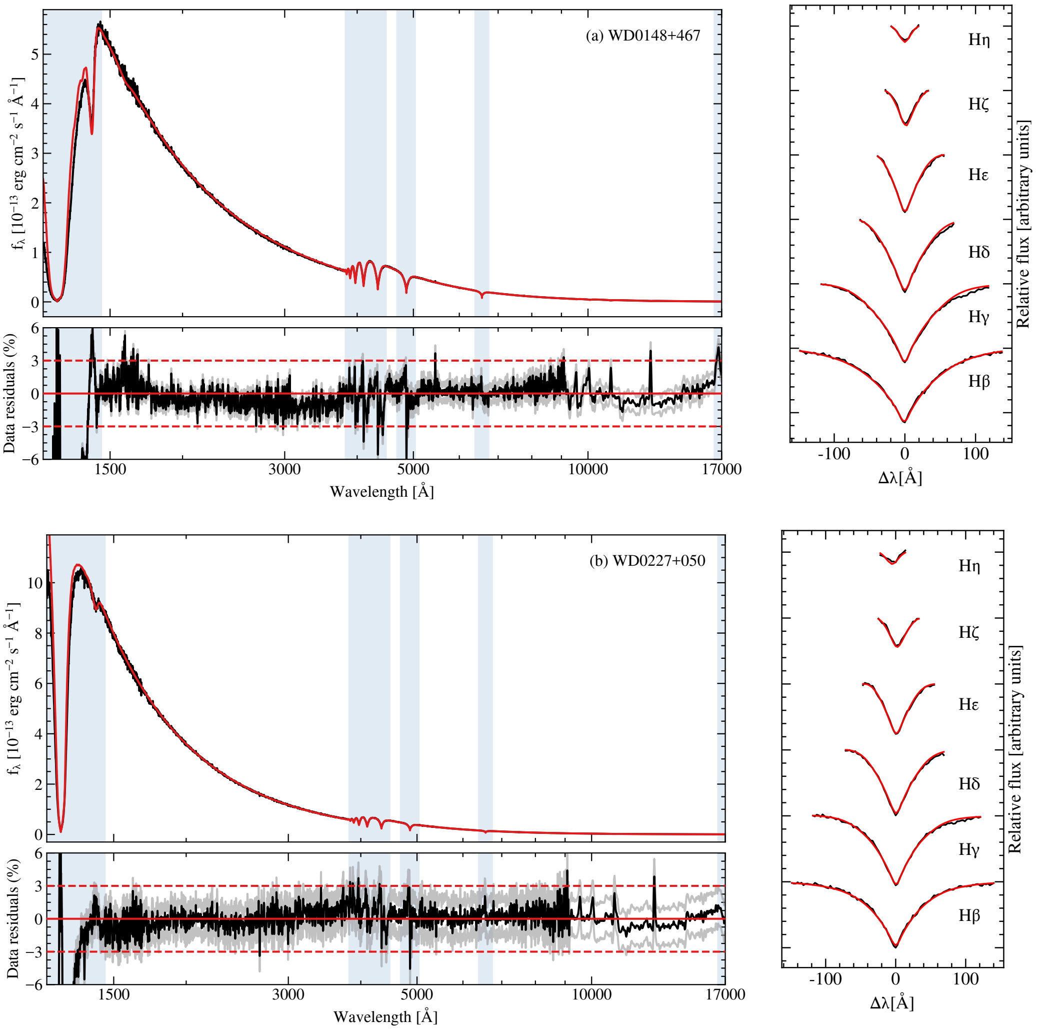

Figure 5.2: Spectrophotometric fits of the STIS and WFC3 data for two of the 13 warm white dwarfs proposed as flux standard candidates, with the WD name of each star given in the corner of the top left panels. *Top left*: SED fit between the observed spectrophotometry (black) and best-fitting model (red). *Bottom left*: Flux residuals from the corresponding SED fit, where the black line is the calculated residual, grey lines indicate residuals $\pm1\sigma$ using only the statistical errors from the fits, and red lines show residuals of 0 and $\pm3\,\%$ as a guide. The shaded blue regions in the left panels indicate wavelength ranges excluded from the fits. *Right*: Balmer line fits for Hβ to Hη between the observed spectrophotometry (black) and best-fitting model (red). The line profiles are vertically offset for clarity. The best-fitting parameters for the SED and Balmer line fits are found in Table 5.3.

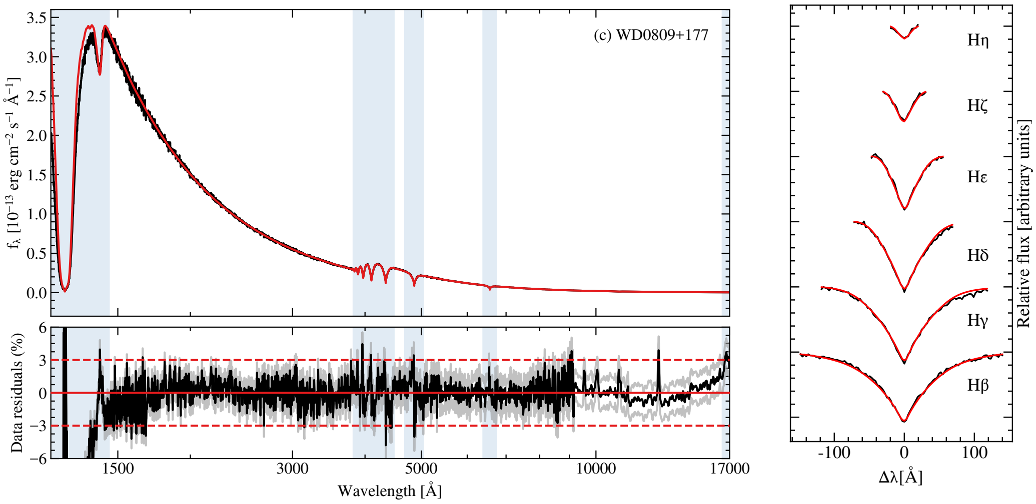
(c) WD0809+177
f$_\lambda$ [10^{-13} erg cm^{-2} s^{-1} Å^{-1}]
3.5
3.0
2.5
2.0
1.5
1.0
0.5
0.0
Data residuals (%)
6
3
0
-3
-6
1500
3000
5000
10000
17000
Wavelength [Å]
Hη
Hζ
Hε
Hδ
Hγ
Hβ
Relative flux [arbitrary units]
-100
0
100
Δλ[Å]

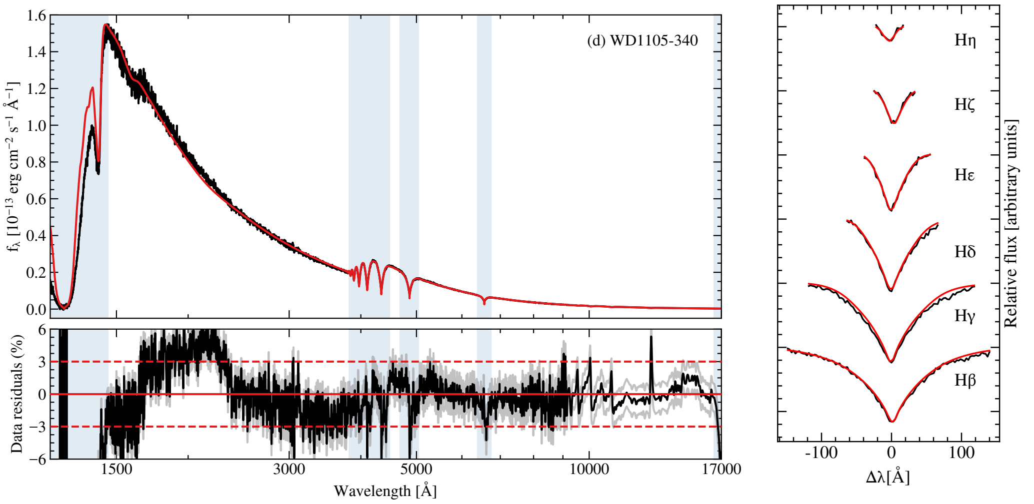
(d) WD1105-340
f$_\lambda$ [10^{-13} erg cm^{-2} s^{-1} Å^{-1}]
1.6
1.4
1.2
1.0
0.8
0.6
0.4
0.2
0.0
Data residuals (%)
6
3
0
-3
-6
1500
3000
5000
10000
17000
Wavelength [Å]
Hη
Hζ
Hε
Hδ
Hγ
Hβ
Relative flux [arbitrary units]
-100
0
100
Δλ[Å]

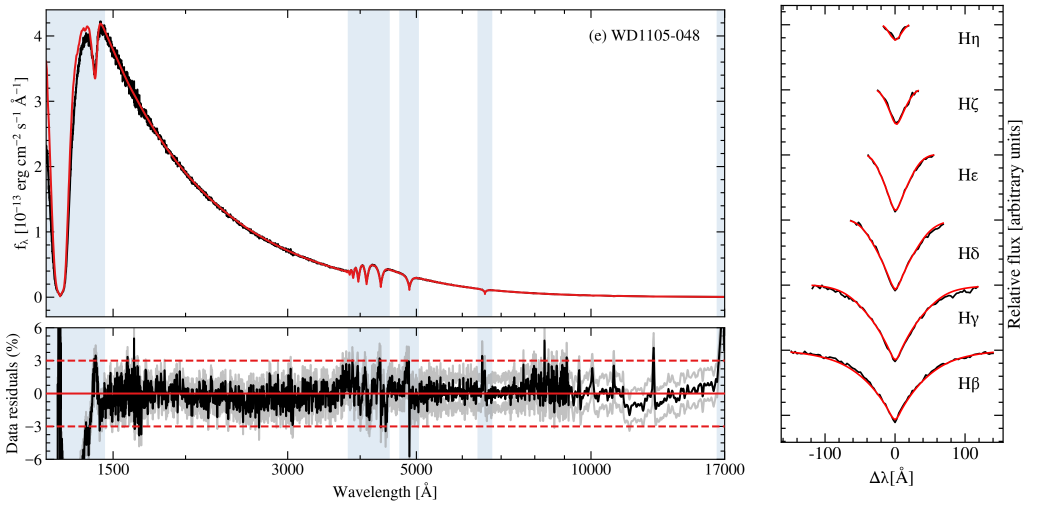
(e) WD1105-048
f$_\lambda$ [10^{-13} erg cm^{-2} s^{-1} Å^{-1}]
4
3
2
1
0
Data residuals (%)
6
3
0
-3
-6
1500
3000
5000
10000
17000
Wavelength [Å]
Hη
Hζ
Hε
Hδ
Hγ
Hβ
Relative flux [arbitrary units]
-100
0
100
Δλ[Å]

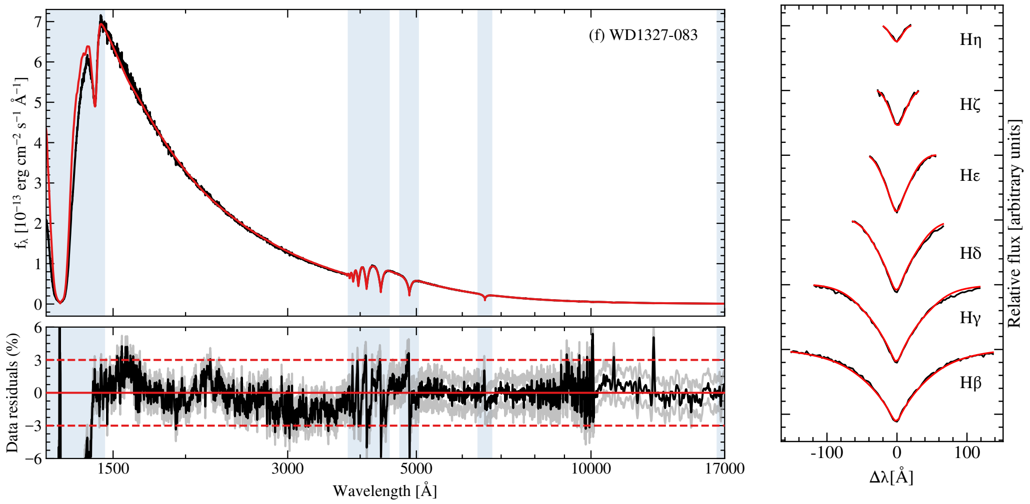
(f) WD1327-083
f_λ [10^{-13} erg cm^{-2} s^{-1} Å^{-1}]
0
1
2
3
4
5
6
7
Data residuals (%)
6
3
0
−3
−6
1500
3000
5000
10000
17000
Wavelength [Å]
Hη
Hζ
Hε
Hδ
Hγ
Hβ
Relative flux [arbitrary units]
-100
0
100
Δλ[Å]

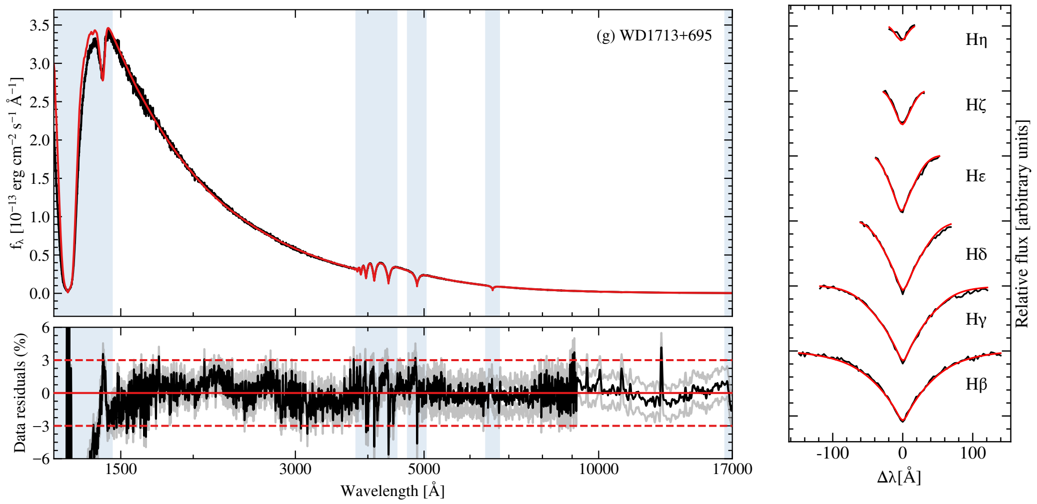
(g) WD1713+695
f_λ [10^{-13} erg cm^{-2} s^{-1} Å^{-1}]
0.0
0.5
1.0
1.5
2.0
2.5
3.0
3.5
Data residuals (%)
6
3
0
−3
−6
1500
3000
5000
10000
17000
Wavelength [Å]
Hη
Hζ
Hε
Hδ
Hγ
Hβ
Relative flux [arbitrary units]
-100
0
100
Δλ[Å]

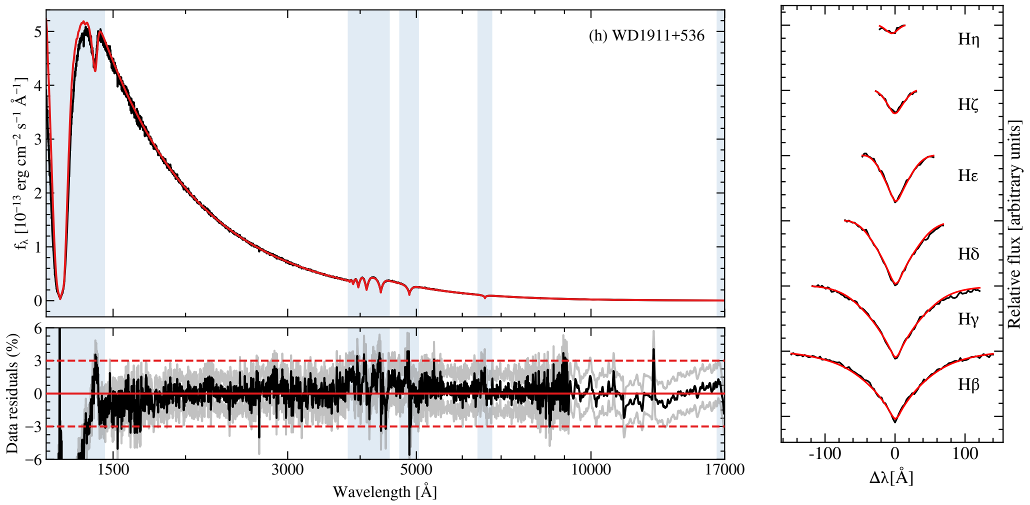
(h) WD1911+536
f_λ [10^{-13} erg cm^{-2} s^{-1} Å^{-1}]
0
1
2
3
4
5
Data residuals (%)
6
3
0
−3
−6
1500
3000
5000
10000
17000
Wavelength [Å]
Hη
Hζ
Hε
Hδ
Hγ
Hβ
Relative flux [arbitrary units]
-100
0
100
Δλ[Å]

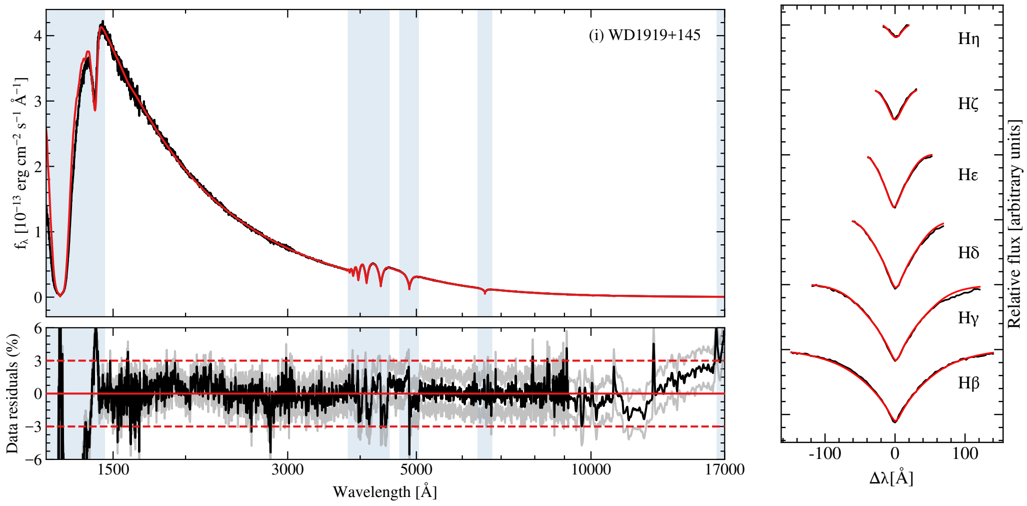
(i) WD1919+145
f_λ [10^{-13} erg cm^{-2} s^{-1} Å^{-1}]
0
1
2
3
4
Data residuals (%)
6
3
0
−3
−6
1500
3000
5000
10000
17000
Wavelength [Å]
Hη
Hζ
Hε
Hδ
Hγ
Hβ
Relative flux [arbitrary units]
-100
0
100
Δλ[Å]

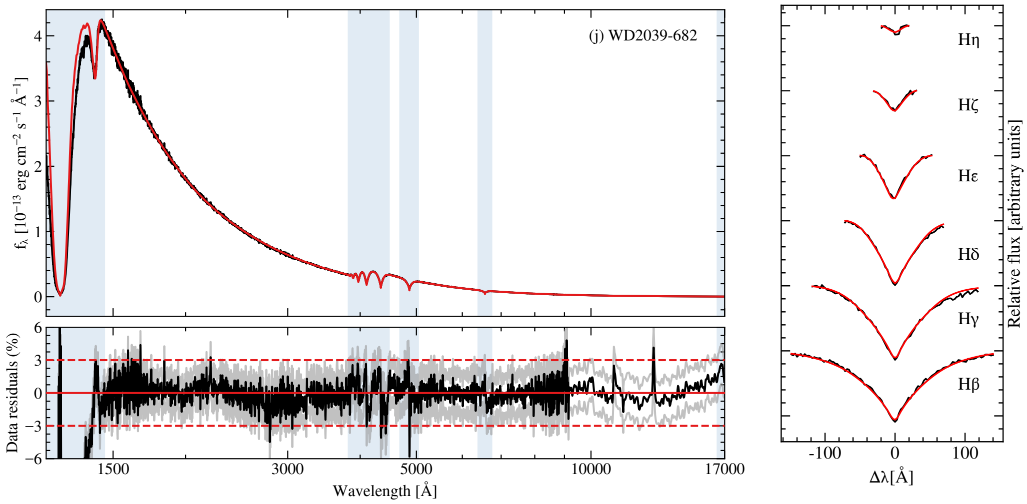
(j) WD2039-682
f_λ [10^{-13} erg cm^{-2} s^{-1} Å^{-1}]
0
1
2
3
4
Data residuals (%)
6
3
0
−3
−6
1500
3000
5000
10000
17000
Wavelength [Å]
Hη
Hζ
Hε
Hδ
Hγ
Hβ
Relative flux [arbitrary units]
-100
0
100
Δλ[Å]

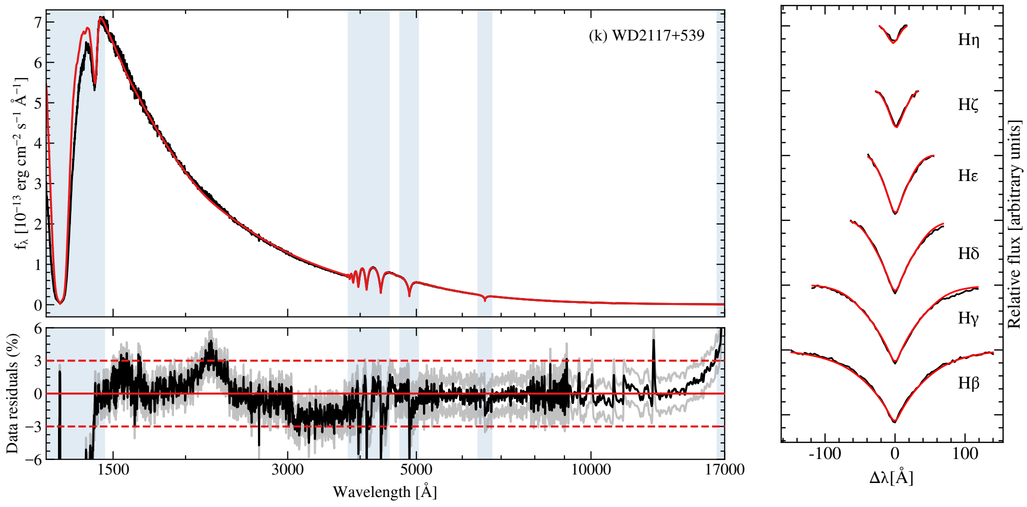
(k) WD2117+539
f_λ [10^{-13} erg cm^{-2} s^{-1} Å^{-1}]
0
1
2
3
4
5
6
7
Data residuals (%)
6
3
0
−3
−6
1500
3000
5000
10000
17000
Wavelength [Å]
Hη
Hζ
Hε
Hδ
Hγ
Hβ
Relative flux [arbitrary units]
-100
0
100
Δλ[Å]

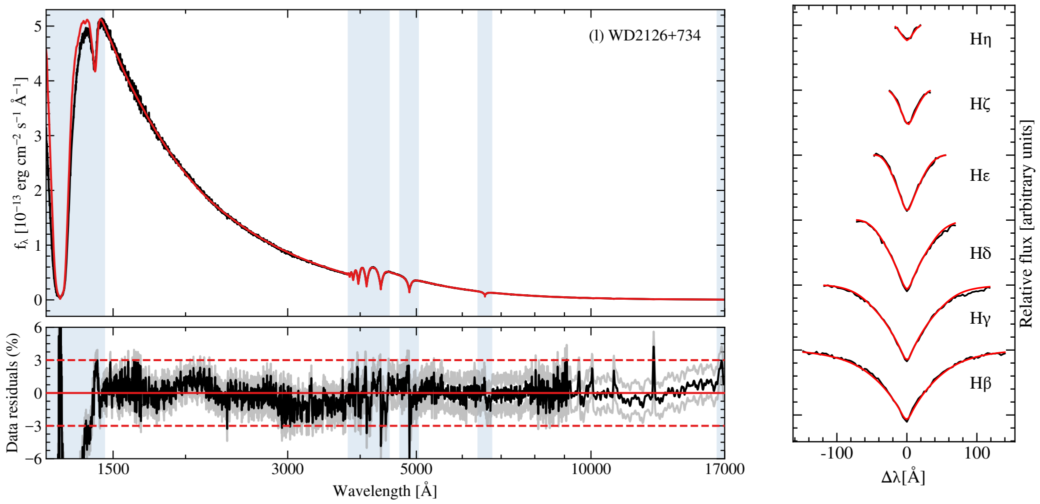
(l) WD2126+734
f$_\lambda$ [10^{-13} erg cm^{-2} s^{-1} Å^{-1}]
Data residuals (%)
Wavelength [Å]
1500
3000
5000
10000
17000
Hη
Hζ
Hε
Hδ
Hγ
Hβ
Relative flux [arbitrary units]
Δλ[Å]
-100
0
100

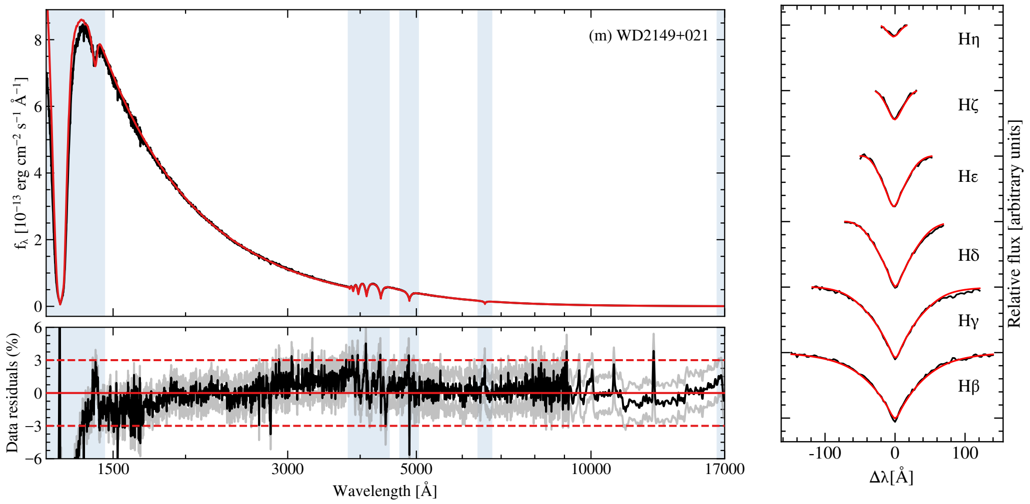
(m) WD2149+021
f$_\lambda$ [10^{-13} erg cm^{-2} s^{-1} Å^{-1}]
Data residuals (%)
Wavelength [Å]
1500
3000
5000
10000
17000
Hη
Hζ
Hε
Hδ
Hγ
Hβ
Relative flux [arbitrary units]
Δλ[Å]
-100
0
100

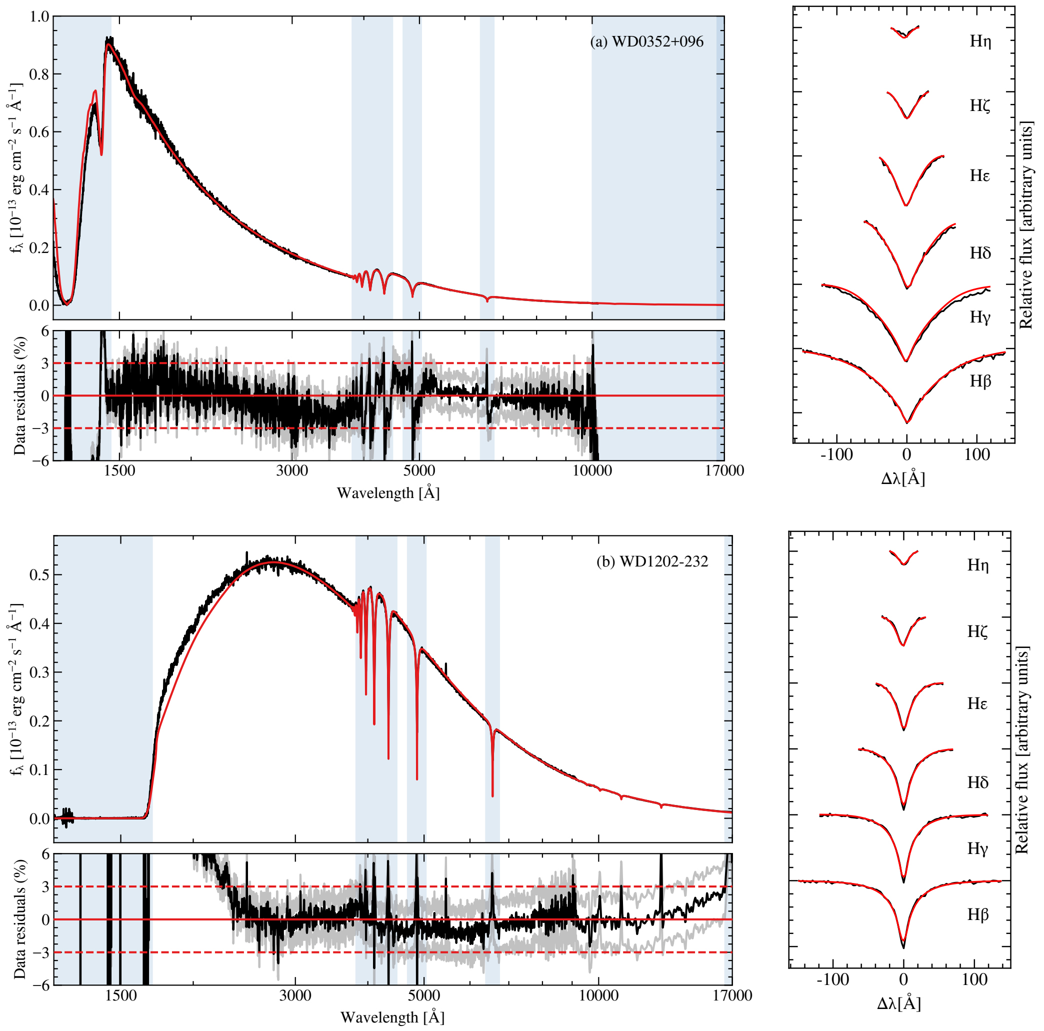

Figure 5.3: Similar to Figure 5.2 but for STIS and WFC3 spectrophotometry of the four extra white dwarfs proposed as flux standard candidates. (a) WD 0352+096 does not have WFC3 spectrophotometry.

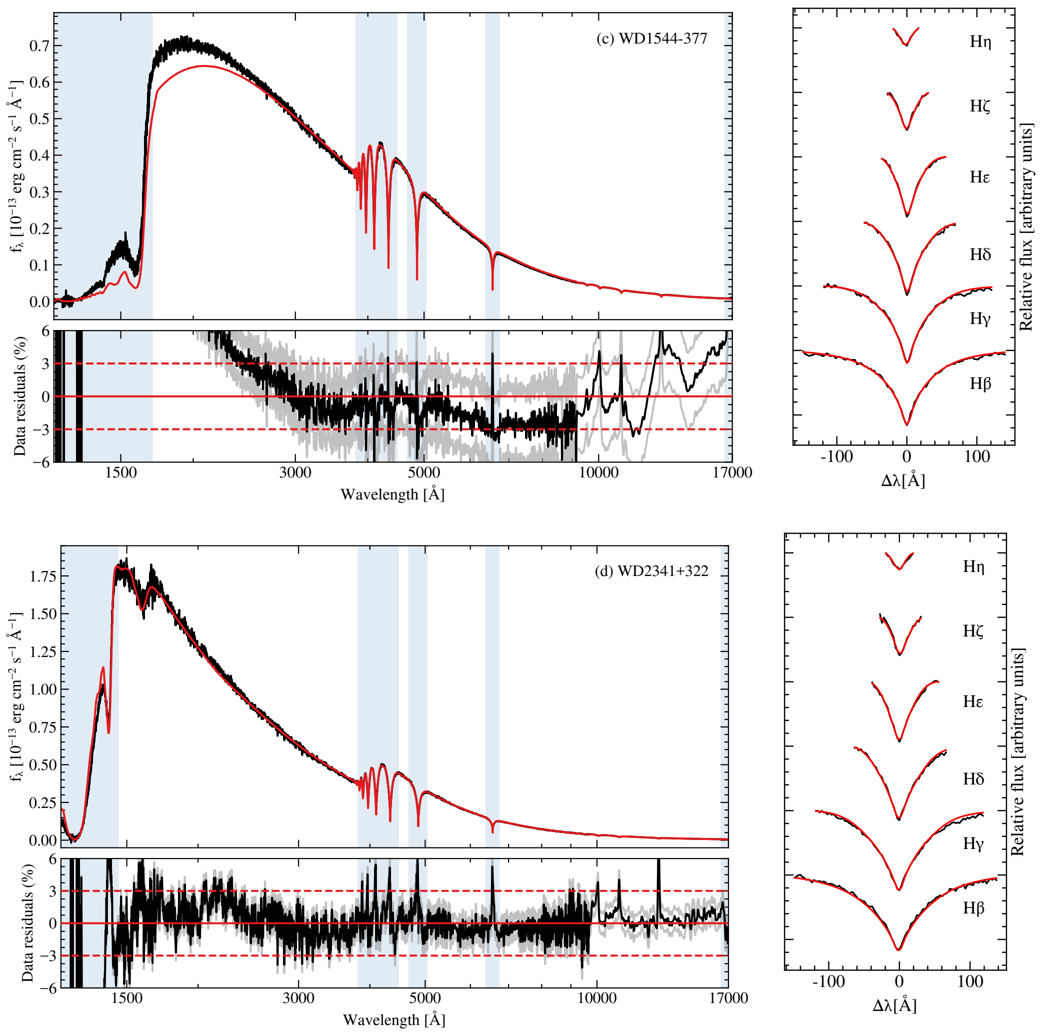
(c) WD1544-377
f_λ [10^{-13} erg cm^{-2} s^{-1} Å^{-1}]
0.0
0.1
0.2
0.3
0.4
0.5
0.6
0.7
Data residuals (%)
6
3
0
−3
−6
1500
3000
5000
10000
17000
Wavelength [Å]
Hη
Hζ
Hε
Hδ
Hγ
Hβ
Relative flux [arbitrary units]
-100
0
100
Δλ[Å]
(d) WD2341+322
0.00
0.25
0.50
0.75
1.00
1.25
1.50
1.75

Table 5.4: The standard deviation flux residual across three different wavelength ranges of the SED fit: the entire wavelength range of each SED fit (1450 − 16 000 Å); the UV region (1450 − 3065 Å); the optical+NIR region (3065 − 16 000 Å). The wavelength ranges for the extra flux standard candidates may differ - see text for details. Quantities are given as a percentage.

Object	Entire wavelength range %	UV %	optical+NIR %
Hot primary standards			
GD 153	0.36	0.31	0.36
GD 71	0.33	0.30	0.35
Warm flux standard candidates			
WD 0148+467	1.24	1.30	1.04
WD 0227+050	1.12	1.17	0.99
WD 0809+177	1.43	1.58	1.26
WD 1105−340	2.58	2.68	1.59
WD 1105−048	1.31	1.50	1.12
WD 1327−083	1.49	1.43	1.19
WD 1713+695	1.41	1.56	1.21
WD 1911+536	1.31	1.35	1.18
WD 1919+145	1.38	1.63	1.10
WD 2039−682	1.33	1.47	1.15
WD 2117+539	1.49	1.33	0.91
WD 2126+734	1.23	1.30	0.98
WD 2149+021	1.34	1.23	1.01
Extra flux standard candidates			
WD 0352+096	2.08	2.22	1.52
WD 1202−232	4.61	2.34	0.96
WD 1544−377	4.42	1.27	2.44
WD 2341+322	1.89	2.19	1.28

the G750L grating. In our analysis we opt to exclude Hα allowing us to use only the G430L tables with no need to splice together models at different resolutions. The Rel Pixel column shows the exact relative spacing of the grating in pixels. This is multiplied by the appropriate grating pixel dispersion in order to obtain the spacing in Angstroms. The G430L grating is split between 3200 Å and 5500 Å LSF tables therefore we averaged them to give a full coverage overview.

Convolving our models directly with the LSF proved computationally expensive and not feasible for use on large numbers of stars. Furthermore, severe edge effects arise at the end points of the LSF grid resulting in warping of the model spectra. We instead decided to fit the LSF tabulated data and create a function which closely reproduces the relative pixel spacing values of the grating. We used the sum of three Gaussian profiles and produced a function which matches the actual LSF data to within 1 %. This custom LSF function was then used in the convolution to degrade our models to the resolution of the STIS G430L grating.

The Balmer line best-fitting model to the observed spectrophotometry for the 13 warm and four extra flux standard candidates are shown in the right panels of Figures 5.2(a)-(m) and 5.3(a)-(d), respectively. The best-fitting T_{eff} and $\log g$ are displayed in Table 5.3. The uncertainties of the fit parameters are dependent on one another and are computed from the covariance matrix of the model atmosphere fit scaled by reduced χ^2 to account for the goodness of fit, therefore they are statistical in nature and do not account for systematic uncertainty.

5.3.2 Synthetic magnitudes and photometric fitting

Synthetic magnitudes were computed for the *Gaia* DR3 G, G_{BP} and G_{RP} bands, 2MASS J, H and K_S bands, and WISE $W1$ and $W2$ bands using our best-fitting STIS and WFC3 T_{eff} and $\log g$ parameters for the 17 flux standard candidates, in addition to GD 153 and GD 71 (Table 5.3). Synthetic apparent magnitudes, m, for *Gaia* DR3 photometry were computed by integrating under the model curves for each filter bandpass using

$$m = -2.5 \log \left(\frac{\int T(\lambda) f_\lambda(\lambda, T_{\mathrm{eff}}, \log g) \lambda d\lambda}{\int T(\lambda) \lambda d\lambda} \right) + c, \tag{5.6}$$

where λ is the wavelength, $T(\lambda)$ is the filter transmission function for any *Gaia* DR3 filter, obtained from the Spanish Virtual Observatory (SVO) Filter Profile Service (Rodrigo et al., 2012), $f_\lambda(\lambda, T_{\mathrm{eff}}, \log g)$ is the model flux at the distance of the white dwarf from Equation 5.1, and c is the zeropoint magnitude for the given filter.

For 2MASS and WISE, synthetic magnitudes were computed using

$$m = -2.5 \log \left(\frac{\int T(\lambda) f_\lambda(\lambda, T_{\rm eff}, \log g) d\lambda}{\int T(\lambda) d\lambda} \right) + c, \tag{5.7}$$

where filter transmission functions were also obtained from SVO.

All synthetic and observed magnitudes are in the Vega magnitude system and are displayed in Table 5.5. The Vega SEDs from CALSPEC used for synthetic magnitudes were a modified version of alpha_lyr_mod_002.fits[6] in the UV and optical range (to $\approx 1\,\mu$m, i.e. *Gaia* filters; Busso et al., 2022) and alpha_lyr_stis_011.fits beyond $1\,\mu$m (i.e. 2MASS and WISE filters).

We corrected the synthetic magnitudes for reddening by evaluating the extinction A_λ using the G23 model (Gordon et al., 2023) at the effective wavelengths of each filter obtained from SVO. We used $R(V) = 3.1$ and the best-fitting $E(B-V)$ values from our SED fits in Section 5.3.1 given in Table 5.3.

In the NASA/IPAC (Infrared Processing and Analysis Center) Infrared Science Archive, WD 2117+539 has no observed WISE data and WD 1544−377 has no observed 2MASS nor WISE data. WD 1919+145 has no observed 2MASS J magnitude error, meaning the reported J magnitude is not a detection but a 95% confidence upper limit. This source has a ph_qual flag of "U" and an rd_flg value of 6 in the J band, both of which denote a non-detection based on profile-fitting photometry. Consequently, we exclude the J-band magnitude of WD 1919+145 from our analysis.

The magnitude difference between observed and synthetic photometry for our network are shown in each band for *Gaia*, 2MASS and WISE in Figures 5.4, 5.5 and 5.6, respectively, for those stars with observed photometry. WD 1327−083, WD 1919+145 and WD 2126+734 are not included in Figure 5.6 because their observed and synthetic photometries are $> 3\sigma$ discrepant (see Section 5.4.3). The error bars in Figures 5.4 - 5.6 represent the combined observed and synthetic magnitude errors, where synthetic errors were calculated from the minimum statistical $T_{\rm eff}$ and $\log g$ errors on our STIS and WFC3 SED fits (Table 5.3).

Finally, we photometrically fit the observed *Gaia* DR3 G, $G_{\rm BP}$ and $G_{\rm RP}$ band photometry for our network and the two hot standards using Equation 5.6 and the same DA model grids as in our SED and Balmer line fitting to obtain *Gaia* atmospheric parameters. Table 5.6 displays the best-fitting $T_{\rm eff}$ and $\log g$ parameters obtained from our photometric fits. The differences between *Gaia* photometric fit

---

[6] https://gea.esac.esa.int/archive/documentation/GDR3/Data_processing/chap_cu5pho/cu5pho_sec_photProc/cu5pho_ssec_photCal.html#SSS3.P2

Table 5.5: Observed and synthetic photometry in the *Gaia* G, G_{BP} and G_{RP} bands, 2MASS J, H and K_S bands, and WISE $W1$ and $W2$ bands. The first row for each object is the observed photometry and error, then the second row is the synthetic magnitude computed from our best-fitting STIS and WFC3 T_{eff} and $\log g$ parameters. Values in parentheses are 1σ errors in mmag. WD 2117+539 has no WISE data, WD 1544−377 has no 2MASS nor WISE data, and WD 1919+145 only has an upper limit for the 2MASS J magnitude, so those fields are filled with dashes.

Object		*Gaia*			2MASS			WISE
	G [mag]	G_{BP} [mag]	G_{RP} [mag]	J [mag]	H [mag]	K_S [mag]	$W1$ [mag]	$W2$ [mag]
Hot primary standards								
GD 153	13.311(3)	13.151(3)	13.632(4)	14.012(25)	14.209(37)	14.308(62)	14.374(27)	14.506(52)
	13.288	13.118	13.616	14.048	14.162	14.271	14.353	14.393
GD 71	13.000(3)	12.853(3)	13.305(4)	13.728(25)	13.901(35)	14.115(65)	14.012(29)	14.103(51)
	12.979	12.820	13.287	13.701	13.810	13.921	14.005	14.052
Warm flux standard candidates								
WD 0148+467	12.496(3)	12.469(3)	12.588(4)	12.768(24)	12.826(32)	12.846(30)	12.906(24)	12.952(27)
	12.499	12.456	12.588	12.771	12.801	12.864	12.893	12.904
WD 0227+050	12.821(3)	12.745(3)	12.996(4)	13.282(26)	13.367(33)	13.425(36)	13.435(24)	13.468(33)
	12.827	12.737	13.003	13.276	13.336	13.416	13.466	13.485
WD 0809+177	13.429(3)	13.376(3)	13.552(4)	13.762(25)	13.841(36)	13.941(51)	13.970(26)	14.069(47)
	13.425	13.361	13.553	13.778	13.822	13.892	13.930	13.944
WD 1105−340	13.700(3)	13.686(3)	13.771(4)	13.954(28)	13.982(39)	14.054(66)	13.951(25)	13.898(37)
	13.661	13.624	13.739	13.913	13.939	14.001	14.029	14.040
WD 1105−048	13.091(3)	13.045(3)	13.214(4)	13.405(26)	13.445(30)	13.544(56)	13.570(25)	13.574(36)
	13.096	13.037	13.217	13.429	13.471	13.537	13.573	13.585
WD 1327−083	12.355(3)	12.323(3)	12.458(4)	12.621(37)	12.677(41)	12.736(48)	13.328(27)	13.165(29)
	12.351	12.303	12.452	12.644	12.679	12.743	12.774	12.785
WD 1713+695	13.328(3)	13.282(3)	13.450(4)	13.618(23)	13.720(29)	13.739(55)	13.811(24)	13.843(27)
	13.317	13.257	13.441	13.659	13.701	13.770	13.806	13.820

Object		*Gaia*			2MASS			WISE
	G	$G_{\rm BP}$	$G_{\rm RP}$	J	H	K_S	$W1$	$W2$
	[mag]	[mag]	[mag]	[mag]	[mag]	[mag]	[mag]	[mag]
WD 1911+536	13.247(3)	13.189(3)	13.391(4)	13.616(29)	13.734(46)	13.824(47)	13.795(24)	13.885(29)
	13.251	13.179	13.395	13.642	13.690	13.766	13.810	13.826
WD 1919+145	13.019(3)	12.980(3)	13.126(4)	-	13.452(55)	13.546(66)	12.412(47)	12.546(80)
	13.016	12.964	13.122	13.326	13.362	13.429	13.463	13.476
WD 2039−682	13.339(3)	13.288(3)	13.469(4)	13.729(26)	13.806(39)	13.800(50)	13.879(26)	13.934(38)
	13.330	13.265	13.463	13.703	13.746	13.822	13.864	13.880
WD 2117+539	12.393(3)	12.355(3)	12.496(4)	12.681(21)	12.785(23)	12.85(38)	-	-
	12.361	12.306	12.475	12.680	12.719	12.785	12.819	12.831
WD 2126+734	12.887(3)	12.836(3)	12.989(5)	13.096(31)	13.164(38)	13.166(44)	13.075(23)	13.110(25)
	12.879	12.819	13.001	13.214	13.256	13.323	13.359	13.372
WD 2149+021	12.777(3)	12.713(3)	12.930(4)	13.203(24)	13.286(37)	13.397(37)	13.385(25)	13.379(32)
	12.783	12.706	12.936	13.185	13.238	13.313	13.357	13.373
Extra flux standard candidates								
WD 0352+096	14.548(3)	14.520(3)	14.635(4)	14.831(41)	14.866(59)	15.061(99)	14.938(35)	15.116(81)
	14.544	14.500	14.634	14.827	14.856	14.923	14.956	14.969
WD 1202−232	12.738(3)	12.843(3)	12.548(4)	12.402(24)	12.301(27)	12.342(26)	12.318(25)	12.343(24)
	12.725	12.814	12.542	12.435	12.331	12.357	12.366	12.368
WD 1544−377	13.001(3)	13.036(3)	12.931(4)	-	-	-	-	-
	12.993	13.028	12.917	12.944	12.907	12.951	12.965	12.973
WD 2341+322	12.967(3)	12.964(3)	13.007(4)	13.171(29)	13.195(37)	13.179(28)	13.243(25)	13.291(29)
	12.951	12.929	12.996	13.142	13.159	13.218	13.242	13.254

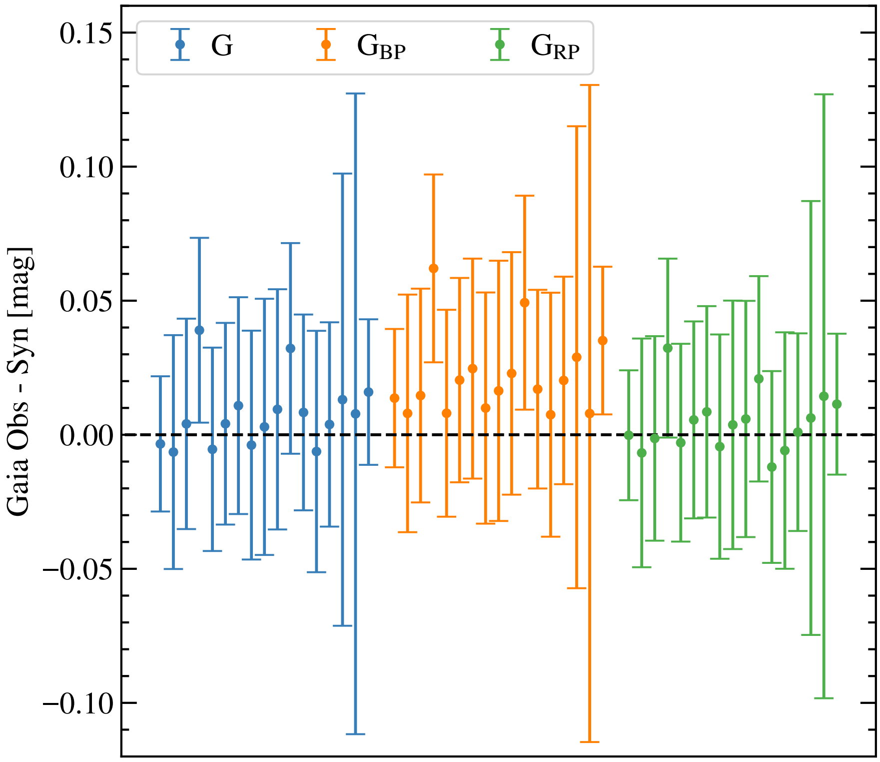

Figure 5.4: Observed minus synthetic photometry in the *Gaia* G, $G_{\rm BP}$ and $G_{\rm RP}$ bands. The x-axis coordinates within each band are uniformly spaced, ordered by RA with the warm flux standard candidates first, followed by the extra flux standard candidates. Observed (with errors) and synthetic magnitudes are given in Table 5.5. Error bars represent combined 1σ observed *Gaia* errors and synthetic magnitude errors, where synthetic errors are calculated from the $T_{\rm eff}$ and $\log g$ errors on our STIS and WFC3 SED fits (Table 5.3). The black dashed line indicates zero difference. Plot is based off fig. 10 in Axelrod et al. (2023).

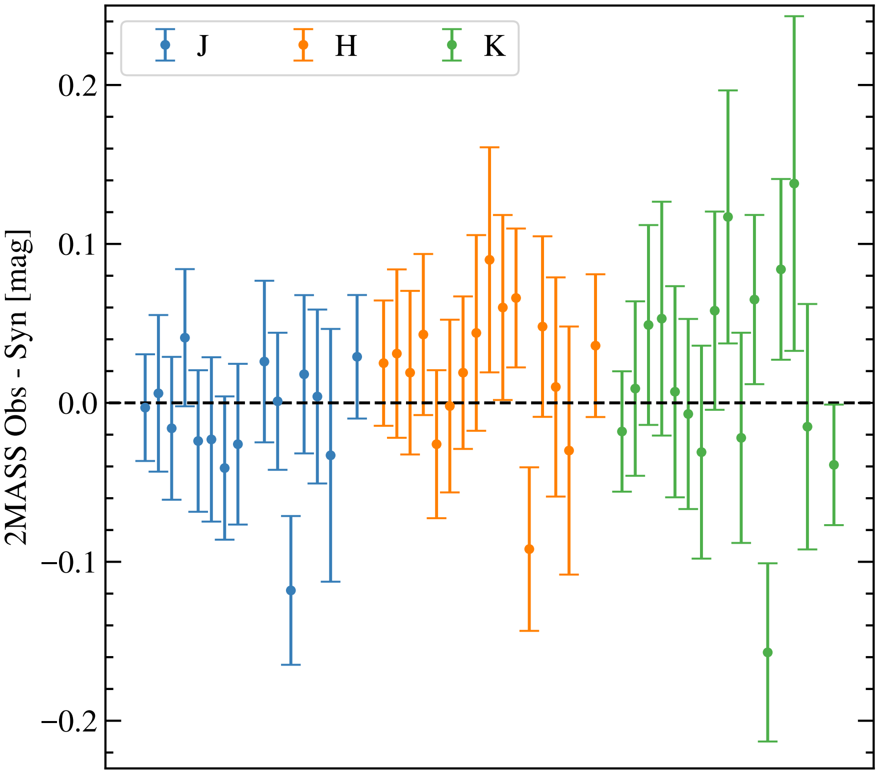

Figure 5.5: Same as Figure 5.4 but for 2MASS J, H and K_S bands. WD 1919+145 only has a J magnitude upper limit and WD 1544−377 has no observed 2MASS data so both white dwarfs are not included in this plot.

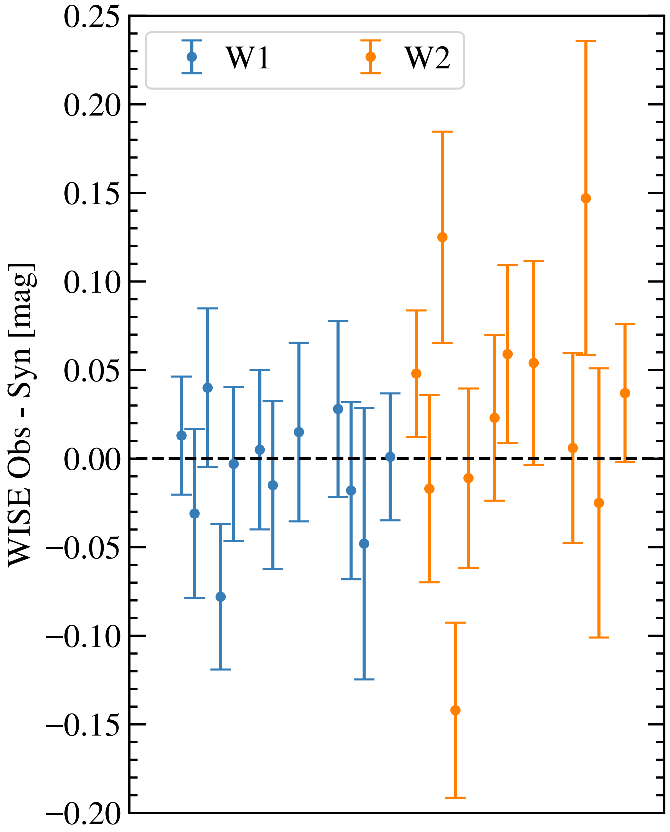

Figure 5.6: Same as Figure 5.4 but for WISE $W1$ and $W2$ bands. WD 2117+539 and WD 1544−377 have no observed WISE data so are not included in this plot. WD 1327−083, WD 1919+145 and WD 2126+734 are not included in this plot either because their observed and synthetic photometries are $> 3\sigma$ discrepant.

parameters and those obtained from our *HST* STIS and WFC3 SED fits are shown in Table 5.6 as $\sigma_{T_{\rm eff}}$ and $\sigma_{\log g}$.

5.4 Discussion

As the objective of this work is to fit the *HST* STIS and WFC3 spectrophotometry of 17 white dwarf flux standard candidates as accurately as possible, we tested different options in our fits to determine their implications.

For our Balmer line fits, we chose to fit from Hβ to Hη. The decision to omit Hα was motivated from the fact that Hα and the higher order Balmer lines are observed separately with two distinct STIS grating configurations. The G750L grating covers the range $5249 - 10\,270$ Å with a dispersion of 4.92 Å/pix, thus observes Hα, whereas the higher order Balmer lines are all observed using the G430L grating which covers the range $2900 - 5700$ Å with a dispersion of 2.73 Å/pix. The difference in dispersions shows the STIS sampling for Hα is coarser than the other Balmer lines, with a lower resolution by a factor of ≈ 2. Therefore including Hα in the same fit as the higher order Balmer lines requires a well understood instrumental response, and uncertainties on that response may outweigh any additional constraints the extra Balmer line gives on the stellar parameters.

To obtain the most accurate results from Balmer line fits, models have to be convolved to the resolution of the instrument, i.e. the LSF, as this gives a true account of the light distribution along the primary dispersion axis. Convolving with a Gaussian to a static resolution or full width half maximum (FWHM) is a valid approximation but using the instrumental resolution is the more accurate approach. STIS has four gratings which have slightly different instrumental profiles over their wavelength coverage. We selected the G430L grating LSF as that covered Hβ to Hη (see Section 5.3.1 for details). The LSF function we created is accurate within $< 1\,\%$ to the actual LSF however this small uncertainty will have propagated into the best-fitting Balmer line parameters shown in Table 5.3.

When using the DA M-R relation from Bédard et al. (2020) we used thick hydrogen layers with $q_{\rm H} = M_{\rm H}/M_{\rm WD} = 10^{-4}$ as this is the standard procedure for DA white dwarfs based on theories of post-asymptotic-giant-branch (post-AGB) evolution and the maximum hydrogen mass for residual nuclear burning (Iben and Tutukov, 1984; Althaus et al., 2010b). The other option is to use thin hydrogen layers with $q_{\rm H} = 10^{-10}$, which is normally employed for helium-dominated atmosphere white dwarfs (DB, DC, DQ, DZ). However, using thick or thin H-layers for white dwarfs of certain spectral types is not a strict rule - studies have shown evidence

Table 5.6: Atmospheric parameters of the 17 DA white dwarfs proposed as flux standards from a photometric fit of the *Gaia* G, G_{BP} and G_{RP} bands. $\sigma_{T_{\mathrm{eff}}}$ and $\sigma_{\log g}$ correspond to how many σ apart the best-fitting T_{eff} and $\log g$ parameters are from the *HST* STIS and WFC3 SED fit (Table 5.3) and *Gaia* photometric fit.

Object	T_{eff} [K]	$\log g$ [dex]	$\sigma_{T_{\mathrm{eff}}}$ [K]	$\sigma_{\log g}$ [dex]
Hot primary standards				
GD 153	35870 ± 1119	7.723 ± 0.031	3.531	2.553
GD 71	31526 ± 1092	7.760 ± 0.048	1.609	1.216
Warm flux standard candidates				
WD 0148+467	14110 ± 417	7.995 ± 0.037	0.834	0.760
WD 0227+050	18520 ± 583	7.858 ± 0.040	1.080	1.034
WD 0809+177	15790 ± 214	8.038 ± 0.017	2.071	1.761
WD 1105−340	13326 ± 420	8.079 ± 0.035	1.726	0.617
WD 1105−048	15469 ± 448	7.911 ± 0.036	0.743	0.741
WD 1327−083	15664 ± 444	7.919 ± 0.036	1.189	2.260
WD 1713+695	15495 ± 408	7.992 ±0.032	1.277	0.961
WD 1911+536	16923 ± 468	8.283 ± 0.031	0.991	0.948
WD 1919+145	14979 ± 345	8.149 ± 0.025	1.002	0.791
WD 2039−682	16453 ± 390	8.467 ± 0.024	1.437	1.052
WD 2117+539	14679 ± 293	7.898 ± 0.026	2.656	1.690
WD 2126+734	15076 ± 83	7.893 ± 0.007	4.976	4.454
WD 2149+021	17187 ± 457	7.971 ± 0.034	1.015	0.994
Extra flux standard candidates				
WD 0352+096	14308 ± 355	8.291 ± 0.028	1.282	1.019
WD 1202−232	8655 ± 87	7.981 ± 0.025	1.505	1.256
WD 1544−377	10377 ± 33	8.021 ± 0.007	0.591	0.654
WD 2341+322	12358 ± 293	7.996 ± 0.031	1.517	0.927

for thin H-layers in DA white dwarfs (Fontaine and Wesemael, 1987, 1997; Miller Bertolami et al., 2017; Bond et al., 2017; Cunningham et al., 2020). For the 17 white dwarfs in this study, using thin H-layers altered the $T_{\rm eff}$ best-fitting parameters by $< 50\,$K and $< 0.03\,$dex, resulting in the SED and Balmer line results being slightly more discrepant. Therefore, we conclude that thick H-layers is the more accurate assumption for this white dwarf network.

5.4.1 Observed vs model fluxes

Our 3D DA LTE models successfully predict the observed *HST* STIS and WFC3 spectrophotometry fluxes within 3 % over most of the range 1450 – 16 000 Å (Figures 5.2 and 5.3). The standard deviation of the flux residuals from the entire SED fit, in addition to the fits of only the UV and combined optical+NIR regions, are shown in Table 5.4. The median standard deviation flux residual of the entire fit wavelength range is 1.34 % for the warm flux standard candidates, 3.25 % for the extra candidates, and 1.41 % for all 17 candidates.

The two coolest white dwarfs, WD 1202−232 and WD 1544−377, have slight discrepancies between the observed and model fluxes between $\approx$ 1700 – 2700 Å, causing their residuals to be $\approx 4.5\,\%$. There are known modelling uncertainties for cool white dwarfs ($T_{\rm eff} \lesssim 10\,000\,$K) in the near-UV, as the total opacity is affected by the far red wing of the Lyman-α line where H and H_2 collisions significantly broaden the absorption line profile at those densities (Kowalski and Saumon, 2006; Saumon et al., 2022). While potential issues with this opacity have been discussed in the context of UV and optical data of white dwarfs cooler than $\approx 6000\,$K (Saumon et al., 2014; Caron et al., 2023; O'Brien et al., 2024), we speculate that our precise STIS UV data may have uncovered a related, milder issue at warmer temperatures. If we fit the SEDs of the two coolest white dwarfs in the network starting at 2300 Å then the flux residuals reduce to 1.26 % for WD 1202−232 and 2.88 % for WD 1544−377. The observed WFC3 data for WD 1544−377 is slightly irregular (Figure 5.3(c)), with the issues likely caused by its wide binary companion (Section 5.4.4) contaminating the detected IR flux.

Fitting the UV and combined optical+NIR regions of the spectra separately yield median standard deviation flux residuals for the warm candidates of 1.43 % and 1.12 %, respectively, showing better agreement over the redder wavelengths. The same trend is seen when fitting only the four extra candidates (UV = 2.21 % and optical+NIR = 1.40 %), and all 17 candidates together (UV = 1.47 % and optical+NIR = 1.15 %). The proposed network of white dwarfs with $T_{\rm eff} < 20\,000\,$K can therefore accurately reproduce the CALSPEC flux scale in the optical+NIR regime to within 1.5 %.

We also fit the *HST* STIS and WFC3 spectrophotometry of the current hot standards GD 153 and GD 71, with our models successfully predicting the observed fluxes within 0.5 % over most of the range 1450 − 16 000 Å. The standard deviation flux residuals are given in the first two rows of Table 5.4.

Our *HST* spectrophotometry consists of six separate observations from the four STIS gratings and two WFC3 gratings, which have been merged together. Small glitches in the SED can occur at the grating merge points (edges) causing residuals between observed and model fluxes to be $> 3\,\%$. Users of this white dwarf network as flux calibrators can remove these glitches if desired, but they have not been removed in this work.

Although we do not fit STIS spectra in the wavelength range 1140 − 1450 Å, discrepancies between model and observed SEDs can be found from a visual inspection of Figure 5.2. We note that the STIS flux calibration from the three primary hot white dwarf standards is uncertain at the $\approx 3\,\%$ level in this wavelength regime (see fig. 4 of Bohlin et al., 2020), a significant contrast to the sub-percent precision at longer wavelengths. This is largely attributed to differences in the predicted spectra from the TLUSTY and TMAP model atmosphere codes, and to a lesser degree on uncertainties in $T_{\rm eff}$ and $\log g$ determinations which propagate to model flux uncertainties. We note that Sahu et al. (2023) found a similar optical vs Lyman-α parameter discrepancy using *HST* Cosmic Origins Spectrograph (COS) observations of warm DA white dwarfs using instead the model atmospheres of Koester (2010). Therefore these results could be an indication that *HST* primary flux calibration needs to be revisited in the UV. In the present work, additional uncertainties in this wavelength range may be related to missing physics in Lyman-α H_2^+ satellite opacities, in particular the treatment of electron broadening and N-body collisions (Allard and Kielkopf, 2009; Gomez et al., 2024).

5.4.2 Atmospheric parameters

Independent $T_{\rm eff}$ and $\log g$ best-fitting parameters are obtained from fitting the *HST* STIS and WFC3 spectrophotometry SEDs and Balmer lines of the flux standard candidates. Statistical errors for both fitting routines are computed from the covariance matrix of the model atmosphere fit scaled by reduced χ^2. However, using statistical errors alone do not account for all uncertainties in the fits thus are underestimates. We calculated the systematic error on $T_{\rm eff}$ and $\log g$ on SED fits as 1.1 % and 0.01 dex, respectively (Section 5.3.1), which gives more realistic uncertainties (Table 5.3).

It is more challenging to define a systematic uncertainty on Balmer line fits, with sensible options being to compare fits of the same star using different models or fit multiple observations or different lines from the same star with the same model. However, there is only one publicly available model for Stark line broadening (Tremblay and Bergeron, 2009) and a limited number of Balmer lines to perform fitting. Reducing the number of lines in the fit drastically reduces precision and can introduce degeneracies between $T_{\rm eff}$ and $\log g$ (Tremblay and Bergeron, 2009). Therefore we arbitrarily assign a scale factor of $\times 3$ on all Balmer line fit statistical errors, as this brings the Balmer line best-fitting $T_{\rm eff}$ to within 3σ of the SED best-fitting $T_{\rm eff}$ for 16/17 of the flux standard candidates (13/17 within 2σ and 8/17 within 1σ). This is a reasonable scale factor to account for uncertainties on Stark broadening profiles and non-ideal gas effects (Cho et al., 2022). The best-fitting $\log g$ parameters agree within 1σ for 16/17 flux candidates - applying the $\times 3$ scale factor to the $\log g$ uncertainties does not change this result. In this work we only quote the purely statistical uncertainties from Balmer line fitting and not the scaled-up values. However for the purpose of comparing results we suggest users multiply by three the values provided in Table 5.3. Overall the independent $T_{\rm eff}$ and $\log g$ best-fitting parameters from our SED and Balmer line fits have a very tight linear correlation with no systematic deviations, and agree within 2.7 % in $T_{\rm eff}$ and 0.013 dex in $\log g$ as a median for the 17 flux standard candidates.

The SED and Balmer line best-fitting $T_{\rm eff}$ and $\log g$ parameters for the two hot primary standards, GD 153 and GD 71, agree within $\approx 1\sigma$ (Table 5.3). Compared to the parameters for these two standards in Table 1 of Bohlin et al. (2020), our SED parameters are within 1σ for GD 153 and within 1σ and 2σ for $T_{\rm eff}$ and $\log g$, respectively, for GD 71. Similarly, compared to the parameters in Table 2 of Narayan et al. (2019) our SED parameters are within 1σ and 2σ for $T_{\rm eff}$ and $\log g$, respectively, for GD 153, and within 1σ for GD 71. The strong agreement between best-fitting parameters in this work and the literature demonstrates the predictive power of the models adopted for our white dwarf flux candidate network.

5.4.3 Photometric analysis

The 17 white dwarfs proposed as flux standards in this work have optical photometry from *Gaia* G, $G_{\rm BP}$ and $G_{\rm RP}$ bands, in addition to IR photometry from 2MASS J, H and K_S bands and WISE $W1$ and $W2$ bands, with some exceptions. WD 2117+539 has no reported WISE data, potentially because it is near a bright star Gaia DR3 2176116584362421504 which could have contaminated the IR flux. WD 1544−377 has no 2MASS nor WISE data because it was likely not possible to accurately observe it due to its wide and bright binary companion (Section 5.4.4).

Our photometric analysis methods are detailed in Section 5.3.2 and the synthetic magnitudes computed are shown in Table 5.5, alongside observed magnitudes and uncertainties. The difference between observed and synthetic magnitudes for *Gaia*, 2MASS and WISE photometry are plotted in Figures 5.4 - 5.6 which illustrate the broad agreement across surveys and individual bands. For the *Gaia* photometric bands, there is 1σ agreement between observed and synthetic photometry for 16 of the white dwarfs in the G band, 14 white dwarfs in the $G_{\rm BP}$ band and all 17 white dwarfs in the $G_{\rm RP}$ band. All 17 white dwarfs agree within 2σ for the G and $G_{\rm BP}$ bands. The 16 white dwarfs with NIR 2MASS data all agree within 3σ across all bands, with 1σ agreement evident for 14, 12 and 10 white dwarfs across the J, H and K_S bands, respectively. 15 white dwarfs in the network have IR WISE photometric data, of which 12 agree within 3σ with our synthetic magnitudes across both bands, 11 agree within 1σ in the $W1$ band and 7 agree within 1σ in the $W2$ band.

The WISE observed and synthetic photometries for WD 1327−083, WD 1919+145 and WD 2126+734 are between $6 - 16\sigma$ discrepant. The reason for this discrepancy is likely due to contamination of the observed photometry. WD 1327−083 is in close proximity to a star; WD 2126+734 is in a crowded field and is in a WD+WD binary system (Section 5.4.4); and WD 1919+145 is in the Galactic plane with many nearby bright sources in the IR. Nevertheless, these stars are still suitable flux calibrators for spaced-based instruments or at moderate spatial resolution. The relatively high proper motions of our standards means their positions will vary with time and any of them could become temporarily blended with another star in the future.

Holberg and Bergeron (2006) made a similar residual comparison between observed and synthetic 2MASS J, H and K_S band photometries to that made in Figure 5.5, but for a larger sample of DA white dwarfs and without an upper $T_{\rm eff}$ constraint. The residual dispersions of $\lesssim 0.2$ mag across the bands measured in Holberg and Bergeron (2006) is similar to that calculated in this work.

In addition to synthetic photometry, we computed best-fitting atmospheric parameters from photometric fits of the *Gaia* G, $G_{\rm BP}$ and $G_{\rm RP}$ observed photometry and parallaxes with our 3D LTE models (Section 5.3.2) which are displayed in Table 5.6. There is good agreement between our best-fitting photometric $T_{\rm eff}$ and $\log g$ parameters and SED parameters with 16 white dwarfs being within 3σ, 14 being within 2σ for $T_{\rm eff}$ and 15 being within 2σ for $\log g$. The photometric and SED parameters for WD 2126+734 are just over 3σ discrepant. We compared our photometric *Gaia* atmospheric parameters with those computed in Gentile Fusillo et al. (2021) and found all 17 objects from our network agree within 3σ.

The same photometric analysis on the hot standards GD 153 and GD 71 was performed, with the results shown in Tables 5.5 and 5.6. The observed and synthetic magnitudes for GD 153 agree within 1σ for all three bands in *Gaia* and 2MASS and the WISE $W1$ band, whereas there is a 2σ agreement for $W2$. For GD 71, the observed and synthetic magnitudes agree within 1σ for all three bands in *Gaia*, two bands in WISE and the 2MASS J band, whereas the 2MASS H and K_S bands agree within 2σ and 3σ, respectively. The best-fitting atmospheric parameters obtained from *Gaia* DR3 photometric fits agree with our STIS and WFC3 SED best-fitting parameters (Table 5.3) within 4σ and 3σ for T_{eff} and $\log g$, respectively, for GD 153, and within 2σ for GD 71.

A small systematic offset is apparent between observed and predicted *Gaia* G_{BP} magnitudes in Fig. 5.4, which suggests that *Gaia* and *HST* are not on the same relative or absolute flux scales (Maíz Apellániz and Weiler, 2018). The offset is similar to that found in previous studies that have compared secondary *HST* flux standards with *Gaia* photometry (Narayan et al., 2019; Axelrod et al., 2023). Furthermore, the offset is consistent with a systematic difference in T_{eff} and mass found between Balmer line and photometric *Gaia* parameters for DA white dwarfs (Tremblay et al., 2019b; Bergeron et al., 2019; Cukanovaite et al., 2021).

5.4.4 Flags on individual white dwarfs in our network

We searched the literature for our network of 17 white dwarfs to find any instances of metal detections/limits, variability, magnetic field detections/limits or binarity. The *TESS* (Ricker et al., 2014) Input Catalog (TIC) numbers are given for each white dwarf, so readers can check current *TESS* Sectors for variability when they are choosing calibrators.

Some white dwarfs are flagged with small metal abundances/limits or magnetic fields $\lesssim 150\,\text{kG}$, but these would typically have a negligible effect on SEDs so are not removed from our network. One exception is the indirect effect of atmospheric metal pollution from planetary debris on the IR SED; while none of the white dwarfs in our network show a clear *WISE* excess attributable to a debris disk, metal polluted white dwarf calibrators are at greater risk of having so far undetected IR excess from debris. The white dwarfs in the El-Badry et al. (2021) *Gaia* eDR3 catalog of spatially resolved binary stars are flagged, with the projected separation in AU from their companion and the chance alignment ratio, which approximately represents the probability that a binary candidate is in a chance alignment. We present our findings below.

WD 0148+467 is not observed to vary in *TESS* (TIC 415880209).

WD 0227+050 is not observed to vary in *TESS* (TIC 422888592).

WD 0809+177 is not observed to vary in *TESS* (TIC 27634101).

WD 1105−340 has potentially contaminated *TESS* data (TIC 23226265). Landstreet and Bagnulo (2019) detected a probable dipolar magnetic field on the order of 150 kG and O'Brien et al. (2024) classified this star as DAH. Since it has $T_{\text{eff}} \approx 14\,000$ K and negligible convective energy transfer, the small magnetic field is not expected to significantly impact the atmospheric structure and predicted SED (Tremblay et al., 2015b). We also note that the continuum and Balmer line fits are in good agreement despite possible Zeeman line splitting.

WD 1105−048 is not observed to vary in *TESS* (TIC 53211451). Valyavin et al. (2006) stated this star has a rotation period longer than 3 h. Aznar Cuadrado et al. (2004) discovered an average magnetic field of −2.1 kG with polarimetry data from the FOcal Reducer and low dispersion Spectrograph (FORS1; Appenzeller et al., 1998), where different field values from two observations were obtained, potentially indicating stellar rotation. Valyavin et al. (2006) found a variable longitudinal magnetic field from $\approx 0 - 8$ kG. Koester et al. (2009) found no detectable magnetic field nor peculiarities in UVES/VLT (Ultraviolet and Visual Echelle Spectrograph/Very Large Telescope) spectra obtained for the ESO SNe Ia Progenitor Survey (SPY). However, this star was flagged as a magnetic white dwarf in Bagnulo and Landstreet (2018) with FORS2 and ISIS/WHT, with a suspected variable weak field between $< B_z > \approx 0 - 2.1$ kG and unknown period. This star has the spectral type DAH+dM in Bagnulo and Landstreet (2022) and DAH in O'Brien et al. (2024). At $T_{\text{eff}} \approx 15\,800$ K, it is too warm for magnetic fields to have an effect on atmospheric structure and predicted SED. WD 1105−048 is in a resolved WD+MS binary system with an M dwarf companion LP 672-2 (Gaia DR3 3788190605663811840) at a projected separation of 6944 AU and chance alignment of 1.08E-04 (Oswalt et al., 1988; Aznar Cuadrado et al., 2004; Holberg et al., 2016; Toonen et al., 2017; El-Badry et al., 2021).

WD 1327−083 has no *TESS* data (TIC 422888592). Bagnulo and Landstreet (2018) observed this star once with ISIS and once with FORS2, measuring $< B_z > = -0.9 \pm 0.4$ kG and $< B_z > = -0.3 \pm 0.2$ kG, respectively. Given the non-significant detection, this white dwarf has the spectral type DA (Bagnulo and Landstreet, 2021, 2022). This star is in a resolved WD+MS binary system with an M dwarf companion LHS 353 (Gaia DR3 3630015546177181952) at a projected separation of 8085 AU and chance alignment of 8.66E-09 (Perryman et al., 1997; Farihi et al., 2005; Holberg et al., 2016; Toonen et al., 2017; El-Badry et al., 2021).

WD 1713+695 is not observed to vary in *TESS* (TIC 219863212).

WD 1911+536 is not observed to vary in *TESS* (TIC 298900716).

WD 1919+145 has potentially contaminated *TESS* data (TIC 338305380) due to it being in the Galactic plane. Zuckerman et al. (2003) state this star has log (Ca/H) < -8.838 according to HIRES echelle spectra from the Keck telescope.

WD 2039−682 is not observed to vary in *TESS* (TIC 372109346). Koester et al. (1998) identified a broadened Hα core in this white dwarf, which could be explained by rotation or a magnetic field of ≈ 50 kG, although a distinction was not possible without circular polarization measurements. No magnetic field has been confirmed in the literature.

WD 2117+539 is not observed to vary in *TESS* (TIC 314771701).

WD 2126+734 is not observed to vary in *TESS* (TIC 323139945). This star is in a WD+WD binary system with WD 2126+734B (Gaia DR3 2274076301516712704) at a projected separation of 42 AU and chance alignment of 6.59E-08 (Zuckerman et al., 1997; Farihi et al., 2005; Holberg et al., 2016; El-Badry et al., 2021; Heintz et al., 2024; O'Brien et al., 2024). Despite WD 2126+734 and its companion being physically close together, they have an angular separation of 1.74" because this is a very nearby white dwarf (22.2 pc; Table 5.2) so they are easily resolved by *HST*, *JWST* and *Gaia*. The observations made by 2MASS and WISE are likely blended due to these telescopes having resolutions $\gtrsim 2$" and $\gtrsim 4$", respectively.

WD 2149+021 is not observed to vary in *TESS* (TIC 405122007). A log (Ca/H) abundance between -8.0 and -7.6 has been measured in this white dwarf leading to it being classified as a DAZ in some literature (Koester et al., 2005; Koester and Wilken, 2006; Berger et al., 2005; Kilic et al., 2006; Farihi et al., 2009; Kawka et al., 2011; O'Brien et al., 2024). While this small amount of metal pollution is not expected to impact the predicted SED which is dominated by hydrogen opacities at all continuum wavelengths according to our models, it has more risk of having a so far unseen debris disk.

WD 0352+096 is not observed to vary in *TESS* (TIC 415339071).

WD 1202−232 is not observed to vary in *TESS* (TIC 398243520). A log (Ca/H) abundance between -9.8 and -9.7 and log (Fe/H) abundance between -8.0 and -7.85 has been measured in this white dwarf leading to it being classified as a DAZ in some literature (Zuckerman et al., 2003; Koester et al., 2005; Koester and Wilken, 2006; Farihi et al., 2009; Kawka et al., 2011; Kawka and Vennes, 2012; Subasavage et al., 2017; Caron et al., 2023; O'Brien et al., 2024).

WD 1544−377 is not in *TESS*. Zuckerman et al. (2003) state this star has

$\log(\mathrm{Ca/H}) < -10.282$ according to HIRES echelle spectra from the Keck telescope. This white dwarf is in a WD+MS binary system with the high proper motion star HD 140901 (Gaia DR3 6009538585839374336) at a projected separation of 220 AU and angular separation of 14.6", with a chance alignment of 1.2E-05 (Zuckerman et al., 2003; Holberg et al., 2016; El-Badry et al., 2021; O'Brien et al., 2024). The *Gaia* DR3 G magnitude of the companion is 5.834 mag. Note that the binary companion is incorrectly listed in Holberg et al. (2008).

WD 2341+322 is not observed to vary in *TESS* (TIC 288144896). Zuckerman et al. (2003) state this star has $\log(\mathrm{Ca/H}) < -9.531$ according to HIRES echelle spectra from the Keck telescope. This white dwarf is not in the El-Badry et al. (2021) wide binary catalog nor is there any evidence of binarity in *Gaia*, but it is listed as a common proper motion companion in a non-interacting binary system in previous literature (McCook and Sion, 1999b; Zuckerman et al., 2003; Holberg et al., 2016).

5.4.5 White dwarfs as IR calibrators

White dwarfs are widely used for flux calibration in UV and optical regimes, along with A- and G-stars. The current three primary white dwarf standards achieve an accuracy better than 1 % at optical wavelengths and provide modelled SEDs which extend calibration from the UV to NIR (Bohlin et al., 2019, 2020). Using predicted SEDs from different model atmosphere codes, Bohlin et al. (2020) suggest that white dwarf flux calibration precision may be as good as 1 % up to 10 μm. Bohlin et al. (2011) and Gentile Fusillo et al. (2020) initially explored the accuracy of extending white dwarf flux calibration into the NIR and found modelled SEDs to be consistent with the *HST* flux scale within a few per cent. Recent work advancing *HST* primary calibration show promising agreement between the Sirius spectrum through the Spitzer Space Telescope Infrared Array Camera (IRAC) bands to $\approx 5\,\mu$m (Bohlin et al., 2022; Rieke et al., 2023).

This work expands upon previous studies and proposes 17 white dwarfs with $T_{\mathrm{eff}} < 20\,000$ K as IR calibrators. This network of white dwarfs is well-suited to provide an independent estimate for uniform calibration to the MIR as they have relatively featureless SEDs and lack variability. Also, IR opacities consists in well understood hydrogen free-free, bound-free and bound-bound transitions (Saumon et al., 2022), as shown by Figure 5.7 which is based on the same model atmospheres and spectra (Tremblay et al., 2013) as those used to fit our observed white dwarf network and predict their full SEDs. Considering this, and since the SEDs of these white dwarfs peak at UV, optical and NIR wavelengths, we predict that these white dwarfs can be reliably used as flux standards for IR observations. This needs to be tested with *JWST* spectrophotometric observations, since *WISE* observations are limited in wavelength coverage and precision ($\approx 5\,\%$ level). Such observations would also determine if any of our calibrators are inappropriate for the IR, such as from having debris disks or planets (Mullally et al., 2024).

The *JWST* absolute flux calibration programme is designed on *HST* absolute calibration therefore our network can provide another estimate for *JWST* calibration, set limits on the precision and provide legacy for its IR instruments (Gordon et al., 2022). We have shown that cool white dwarf stars are valuable NIR and potentially MIR calibrator additions and a composite approach to calibration with white dwarfs, A- and G-stars should be used to obtain the best possible results.

5.5 Conclusions

We have analysed *HST* STIS and WFC3 spectrophotometry of 17 DA white dwarfs with $T_{\rm eff} < 20\,000\,\rm K$ to investigate their reliability as flux calibrators, specifically in the IR regime. The stars in our network have significantly lower $T_{\rm eff}$ values than current hot DA primary standards (Bohlin et al., 2020), in addition to recent networks of hot but faint DA stars (Narayan et al., 2016, 2019; Axelrod et al., 2023), which has multiple advantages: their SEDs peak closer to the optical/NIR regime; have a larger sky density; NLTE effects and UV metal line blanketing have a negligible effect on continuum fluxes. Convection in cooler white dwarfs is not a significant issue either as our state-of-the-art 3D DA LTE model atmospheres account for convective effects without free parameters.

The results from this study show our model atmospheres successfully predict the observed fluxes of all 17 white dwarfs within $3\,\%$ over most of the wavelength range $1450 - 16\,000\,\text{Å}$. The median standard deviation flux residual for all 17 candidates over the entire fit wavelength range is $1.41\,\%$, with the coolest white dwarf residuals being $\approx 3\,\%$. The residuals when fitting the UV and optical+NIR regions separately for the 17 candidates are $1.47\,\%$ and $1.15\,\%$, respectively. Therefore, this network of white dwarfs cooler than current primary standards are fully consistent with the *HST*/CALSPEC flux scale over the UV, optical and NIR regimes.

Spectrophotometric fits of the observed *HST* STIS and WFC3 SEDs and Balmer lines of the 17 flux standard candidates yield independent atmospheric parameters. The best-fitting $T_{\rm eff}$ for 16 stars agree within 3σ and the best-fitting $\log g$ for all 17 stars agree within 2σ. Photometric fits of the observed *Gaia* DR3 G, $G_{\rm BP}$ and $G_{\rm RP}$ photometry results in 3σ agreement for all 17 stars with the best-fitting

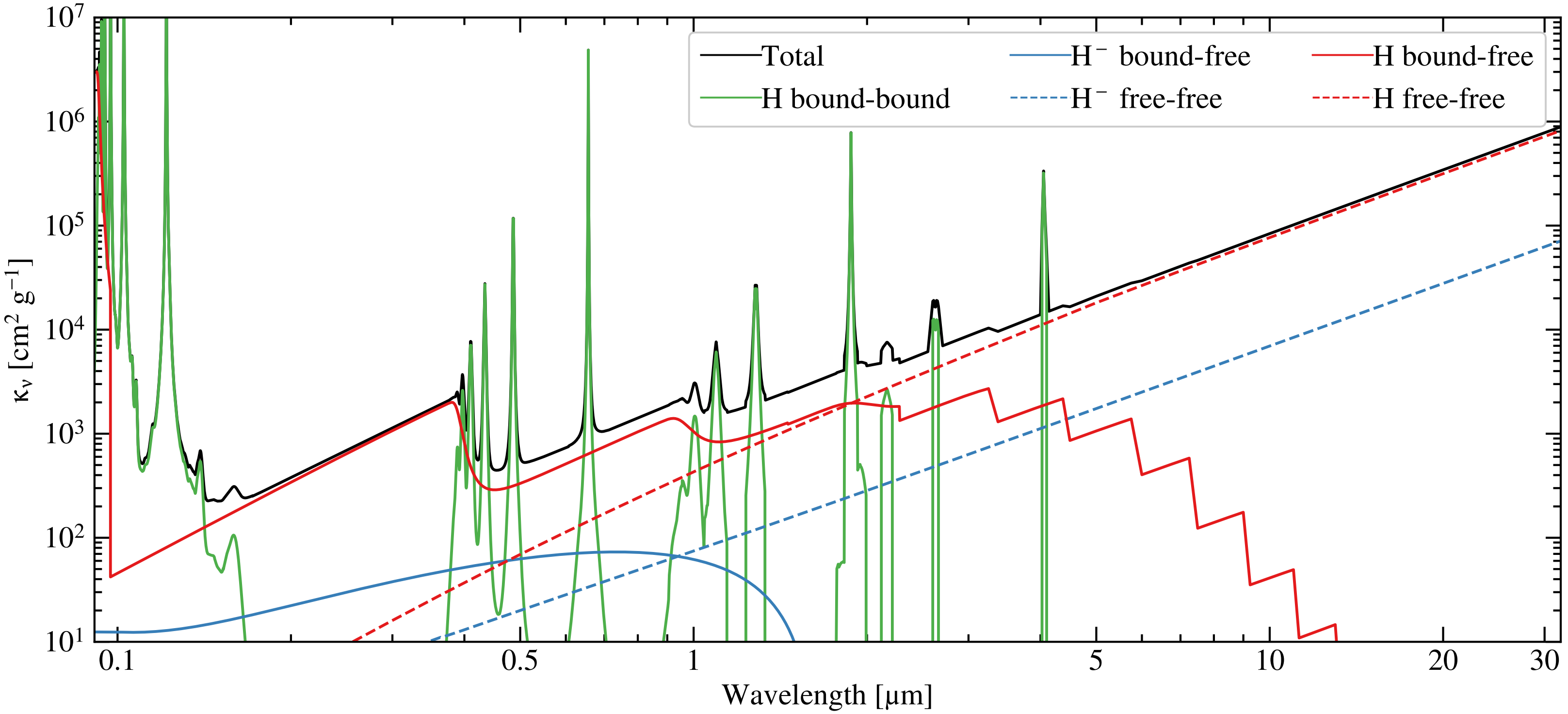

Figure 5.7: Dominant contributions to the radiative opacity of DA white dwarfs as a function of wavelength. The opacities shown are for a $T_{\mathrm{eff}} = 12\,000\,\mathrm{K}$ white dwarf. A $\log g$ of 8.0 dex is assumed and the opacities are evaluated for the conditions at the photosphere. Based off the bottom panel of Fig. 17 in Saumon et al. (2022).

SED T_{eff} and $\log g$ parameters. Therefore we find excellent agreement between independent atmospheric parameters for our network.

We also computed synthetic magnitudes for *Gaia* G, G_{BP} and G_{RP} bands, 2MASS J, H and K_S bands and WISE $W1$ and $W2$ bands so we could compare them with observed photometry. All 17 white dwarfs in our network agree within 2σ for the three optical *Gaia* photometric bands. For the IR photometric bands in 2MASS and WISE, all the white dwarfs in our network with 2MASS data agree within 3σ and 12/15 with WISE data agree within 3σ.

To conclude, our network of 17 DA white dwarfs with $T_{\mathrm{eff}} < 20\,000\,\mathrm{K}$ represents a valuable addition to available flux standards. These stars provide reliable independent estimates for secondary IR SEDs and the legacy for current and future IR instruments onboard spacecraft such as *JWST*, *Euclid* and *Roman*, in addition to ground based observatories such as the ELT (e.g. MICADO). The synthetic spectra of our network are available with the electronic distribution of Elms et al. (2024) and on CALSPEC[7]. Observers can select the most suitable flux standards for calibrating their observations based on specific wavelength coverage and target requirements.

---

[7] The models for WD 1202−232 and WD 1544−377 are not included in CALSPEC due to potential modelling issues and/or contamination in the IR.

Chapter 6

Conclusions and future research

6.1 Conclusions

The research in this thesis utilises the extraordinarily precise data from the spacecraft *Gaia*, combined with spectroscopy and photometry from ground- and space-based telescopes, to characterise special white dwarfs. The results presented here will advance multiple areas of white dwarf astrophysics, of which the major implications are outlined below.

In Chapter 3, I analysed new spectroscopic observations of the white dwarfs WD J2147−4035 and WD J1922+0233. Both white dwarfs are metal-polluted, faint and have ultra-cool T_{eff} - in fact they are the coolest DZ white dwarfs known to date. WD J2147−4035 has very red photometry as it has a depleted atmospheric H content. On the other hand, WD J1922+0233 has a larger atmospheric H content so it suffers from strong atmospheric CIA. As a result, the flux in the red optical and IR of WD J1922+0233 is suppressed, therefore it exhibits unusually blue colours relative to its absolute magnitude. Despite best efforts, the physics of CIA remains a challenge to model in white dwarf atmospheric codes, and combined with the immense densities of ultra-cool white dwarf atmospheres we rely mainly on assumptions. The total age of WD J1922+0233 could not be reliably computed, however we found WD J2147−4035 is over 10 Gyr old, making it the oldest DZ white dwarf known to date.

We detected Na and K in WD J2147−4035 and WD J1922+0233, in addition to Li and C in WD J2147−4035 and Ca in WD J1922+0233. The relative abundances of log (K/Na) and log (Li/Na) in WD J2147−4035 are extremely enhanced compared to solar system benchmarks like bulk Earth, Earth's continental crust, solar and CI chondrites. Tracing back the abundance evolution history did not provide any satisfactory combinations of abundances which resembled solar system benchmarks therefore we could not determine what type of object accreted onto this white dwarf. WD J1922+0233 has a far less exotic atmospheric chemical composition than WD J2147−4035, with a depleted current log (Ca/Na) abundance compared to solar system benchmarks but past relative abundances closer to known objects. For this reason, we assumed accretion has ceased so we could utilise diffusion timescales. If accretion ceased $\approx 4 - 15$ Myr ago, the parent body which accreted onto WD J1922+0233 was compositionally similar to planetary crust, with a minimum parent body mass corresponding to an extremely small fraction of the continental crust of an Earth-like planet.

Analysis of the *TESS* light curves for WD J2147−4035 revealed it is photometrically variable with a period of $\simeq 13$ h. The Li absorption lines in this white dwarf are Zeeman split into three components indicating the white dwarf has a magnetic field. We measured the magnetic field strength to be relatively weak at $\approx 0.5\,\mathrm{MG}$. We assigned the spectral type DZQH to WD J2147−4035.

In Chapter 4, we performed spectroscopic, photometric and time-series analysis on the latest data of DAe white dwarfs WD J0412+7549 and WD J1653−1001. WD J0412+7549 had previously been identified as a DAe by Tremblay et al. (2020) and WD J1653−1001 was tentatively identified as a DAe in O'Brien et al. (2023), but confirmed in this work. To date, only these two white dwarfs belong to the DAe spectral class. DAe stars have characteristics similar to DAHe stars, such as Hα and Hβ line emission, H-dominated atmospheres, photometric and spectroscopic variability, and they all cluster in a relatively small area on the *Gaia* HRD. The only known difference is DAHe stars have a detectable magnetic field whereas DAe stars do not.

We measured the upper limits on magnetic field strength for both DAe stars to be $B < 0.05\,\mathrm{MG}$. The period of WD J0412+7549 is $\approx 2.3\,\mathrm{h}$ and WD J1653−1001 is possibly $\approx 80.5\,\mathrm{h}$, although this needs to be verified using data with a larger phase coverage at a later date (see Section 6.2.2). Also, we determined that WD J0412+7549 has an anti-phase relationship between photometric (flux) and spectroscopic (emission) variability - the same phase relationship found in DAHe stars. There was not enough spectroscopic data of WD J1653−1001 to determine its spectroscopic variability.

The physical mechanism(s) causing Balmer line emission in DA(H)e stars is still unknown, although it is likely an intrinsic mechanism as all of the DA(H)e stars are single and independent. The close clustering on the *Gaia* HRD could suggest these stars may be experiencing a short evolutionary phase where magnetic fields with vastly different strengths trigger Balmer line emission. Each DA(H)e could have a photospheric dark spot/region with a temperature-inverted and optically thin chromospheric emission region. DAe stars could be on the brink of magnetic emergence from a global dynamo created from core crystallisation and white dwarf rotation, which could explain their lack of a detectable magnetic field but similarities with DAHe stars. Finally, DAe stars could have two faces: a radiative (magnetic) face and a convective face. These different faces could have field strengths above and below the convective flux suppression threshold of $B \approx 10\,\mathrm{kG}$, which would explain the photometric flux variation in WD J0412+7549.

To conclusively determine the physical mechanism(s) causing Balmer line emission in DA(H)e stars, more data is required. Ideally we require multi-epoch spectroscopy of WD J1653−1001 over the majority of its period, in addition to spectropolarimetry of one or both of the DAe stars to determine better limits on the magnetic field strengths (see Section 6.2.2). The research area of DA(H)e stars is still relatively new, with only 26 DAHe and 2 DAe white dwarfs discovered to date. With upcoming DESI data releases and more follow-up research on these stars, we will hopefully get more answers on their intrinsic phenomena in the near future.

Finally, in Chapter 5, we analysed *HST* STIS and WFC3 spectrophotometry of 17 DA white dwarfs with $T_{\text{eff}} < 20\,000\,\text{K}$ to test their reliability as accurate flux calibrators, specifically in the IR regime. In the modern era of astronomy, high-resolution IR instruments onboard spacecraft such as *JWST*, *Euclid* and *Roman*, in addition to ground-based observatories such as the ELT (e.g. MICADO), provide or will provide exceptional astrophysical and cosmological data. It is imperative that the scientific community has access to accurate flux calibrators in the IR so that these data are reduced as accurately as possible.

The network of flux calibrator white dwarfs in this thesis have lower T_{eff} values than current hot DA primary standards, in addition to the recent network of hot but faint DA stars. White dwarfs with cooler T_{eff} have the advantage of: negligible NLTE effects and UV metal line blanketing on continuum fluxes; SEDs which peak closer to the optical/NIR; and a larger sky density so closer targets with negligible reddening and more accurate *Gaia* parameters can be chosen.

Our model atmospheres successfully predicted the observed fluxes of all 17 white dwarfs within 3 % over most of the STIS+WFC3 wavelength range $1450 - 16\,000\,\text{Å}$. The median standard deviation flux residual when fitting the UV and optical+NIR regions separately were 1.47 % and 1.15 %, respectively. Thus, our network is fully consistent with the *HST*/CALSPEC flux scale over the UV, optical and NIR. The independent best-fitting atmospheric parameters of the SEDs and Balmer lines agreed within 3σ for 16 stars in T_{eff} and 2σ for all 17 stars in $\log g$. Additionally, best-fitting atmospheric parameters from photometric fits of the *Gaia* G, G_{BP} and G_{RP} observed photometry and parallaxes had 3σ agreement with the SED parameters for 16 of the white dwarfs. The synthetic magnitudes computed for the three optical *Gaia* bands were within 2σ for all 17 white dwarfs, and for the IR 2MASS and WISE bands within 3σ for most of the network.

The network of cooler flux calibrators presented in this thesis is a valuable addition to the current secondary standards and their spectra are publicly available on CALSPEC. Scientists now have a larger network of calibrator stars to choose from so they can select the most appropriate for their observations based on specific wavelength coverage and target requirements. That will in turn reduce the uncertainty in results obtained with observations, leading to more accurate scientific conclusions in astrophysics and cosmology.

6.2 Future research

The research presented in this thesis has advanced our understanding of ultra-cool white dwarfs, evolved planetary debris, Balmer emission in non-magnetic (or extremely weakly magnetic) white dwarfs, and cool white dwarfs as flux calibrators. However, there is still potential for further scientific advancement through follow-up studies. I will highlight below the follow-up studies that can and should be explored.

6.2.1 First highly variable DZ

Myself and collaborators organised new spectroscopic observations to be taken of the ultra-cool DZ white dwarf WD J2147−4035 with the MagE spectrograph on the 6.5-m Magellan Baade Telescope at Las Campanas Observatory, Chile (Marshall et al., 2008), in an attempt to confirm the metal abundances measured in the original 2021 X-Shooter spectrum. Twelve 1200 s consecutive exposures were taken with MagE on 2024 July 10, and another twelve taken on 2024 September 24. In total, 24 spectra were taken of WD J2147−4035 over two epochs. These spectra show spectroscopic line variability over the spin period in the Na and Li spectral lines. With these new observations, we have confirmed WD J2147−4035 is the third spectroscopically variable DZ (and the first photometrically variable) white dwarf discovered to date. The first and second variable DZ stars were reported in Bagnulo et al. (2024a) and Bagnulo et al. (2024b), which showed W_λ variations of a factor of $1.2 - 2.0$ over the rotation period. The new MagE observations of WD J2147−4035 show W_λ changes by more than a factor of five over the rotation period, making it the first highly variable DZ white dwarf.

Analysis of these new MagE observations will hopefully advance our understanding of spectroscopic variability in white dwarfs, such as changes in absolute/relative abundances of metals, C and the H/He ratio over the period. Specifically for WD J2147−4035, we hope to understand whether its variability is related to its unusual Li and K abundances and if its magnetic field strength changes over the period. These results could help determine the cause of the spectroscopic variability, whether it is a purely magnetic effect where all atmospheric material varies independently of the accretion event or if there is a physical spot on the surface in which metals have not been fully mixed post-accretion by the atmosphere (Bagnulo et al., 2024a,b).

6.2.2 Spectropolarimetry and spectroscopy of WD J1653−1001

Since the release of Elms et al. (2023), we have secured spectropolarimetric and additional spectroscopic observations of the DAe white dwarf WD J1653−1001. I had a successful ESO proposal for WD J1653−1001 to be observed with FORS2 on the VLT, which resulted in six 1 hr exposures from May to July 2024. Figure 6.1 shows the six spectra taken with FORS2 around the Hα region and emission is clearly evidenced in some phases. Six nights of spectroscopic observations were also taken over 2023 and 2024 on KAST, MagE, MIKE and INT. Archival FORS2 data from two nights in 2022 were also discovered, although only Hβ was observed. Table 6.1 details all the time-domain spectroscopic observations for WD J1653−1001 we currently have, including the two spectroscopic observations with KAST published in Elms et al. (2023).

Since the publication of Elms et al. (2023) which used DR15, ZTF has collected an additional 2 years worth of data in the g- and r-bands between 2018 March 17 and 2024 October 31. For WD J1653−1001, this equates to a data increase of 23 per cent in the red filter and 28 per cent in the green filter. I have computed Lomb-Scargle periodograms (Lomb, 1976; Scargle, 1982) using the `python` package `astropy.timeseries` (Astropy Collaboration et al., 2013, 2018, 2022) for the individual g-band and r-band light curves, in addition to the combined g- and r-band light curve, and show the results in Figure 6.2. Out of the strongest 200 unique signals (separated by at least 0.1 d) at periods less than 100 d, the periodic signal at $\simeq$ 80.30 h is the strongest in all three datasets and is detected above a FAP of one per cent. Table 6.2 displays the strongest signal measured in all three power spectra and the mean period. I phased the FORS2 2024 observations to the mean period and measured the W_λ of the Hα lines at each of the six phases, then plotted the data in Figure 6.3. The W_λ seems to have a sinusoidal pattern over one phase and the black fitted sine curve has a period of 80.30 h. I plan to do the same W_λ analysis for all observations in Table 6.1, to determine how the W_λ of the Balmer lines change with phase. Also, I will analyse the FORS2 spectropolarimetry to determine the mean longitudinal field, i.e. magnetic field strength, of the white dwarf.

The ZTF DR23 power spectra analysis of WD J1653−1001 confirms the period found in Elms et al. (2023), which at the time was most likely $\approx$ 80.31 h. The DR23 periodogram is $\approx$ 1/3 less noisy than the periodogram produced in Elms et al. (2023) from ZTF DR15, thus the data has improved in quality over the past couple of years but retained the same strongest signal. The data quality likely improved because the contaminant MS star, Gaia DR3 4334641562479650816, had an angular separation of 0.832” from WD J1653−1001 at the end of DR15 but increased to

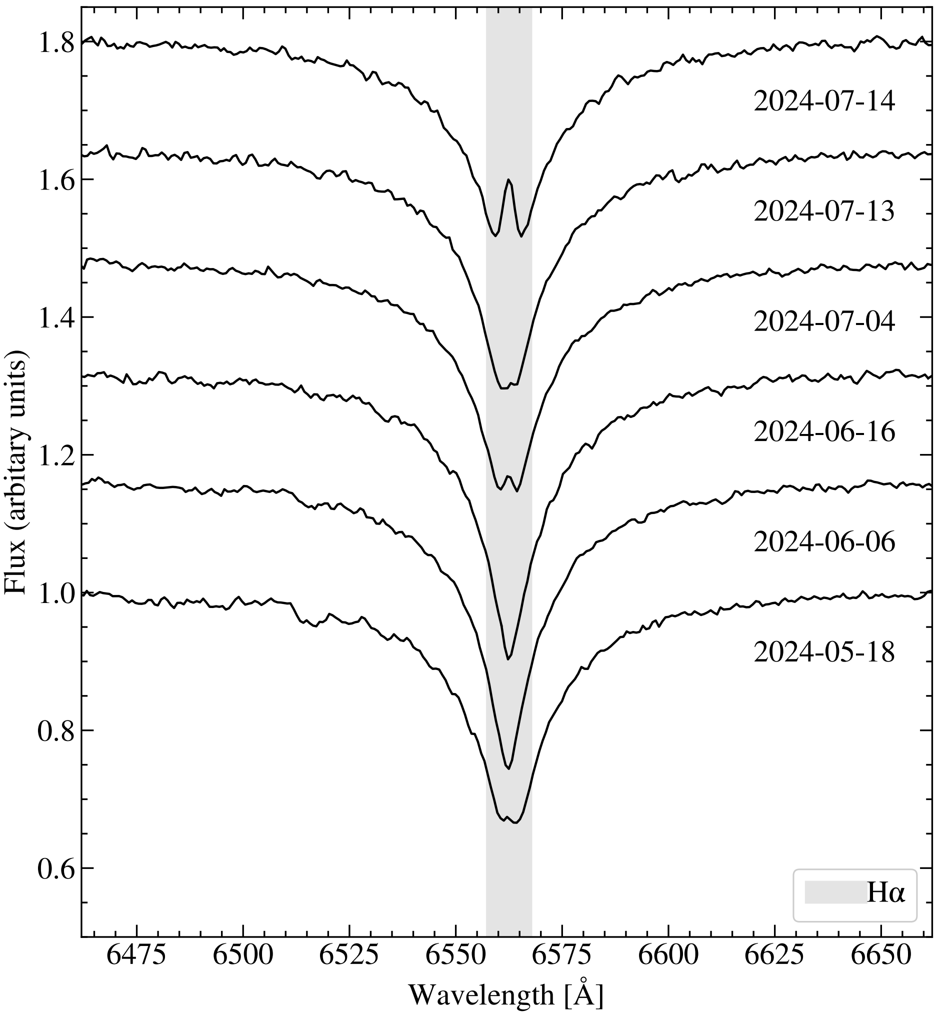

Figure 6.1: Spectra of WD J1653−1001 taken with the FORS2 spectrograph from May to July 2024 around the Hα Balmer line region. The observation UT dates are shown on the right of the plot. Spectra are convolved with a Gaussian with a FWHM of 1 Å and offset vertically for clarity.

Table 6.1: Time-domain spectroscopic observations for WD J1653−1001 obtained from ground-based telescopes, detailing the exposure time (t_{exp}), number of exposures (n_{exp}) for each observing run and the duration of the observing run. Numbers separated by a colon represent exposures taken in the blue:red arms. Observations are in ascending date order, with the date and time given at mid-exposure.

Date (yyyy-mm-dd)	Time at mid-exposure hh:mm:ss	Telescope/Instrument	t_{exp} (s)	n_{exp}	Duration (h)
2018-May-22	08:43:45	Shane/Kast	3000:1000	1:3	0.83
2022-May-15	03:38:06	VLT/FORS2	800	4	0.89
2022-Jun-01	02:28:58	VLT/FORS2	800	4	0.89
2023-May-15	09:56:59	Shane/Kast	2000:1000	2:4	1.11
2023-May-28	04:16:21	Magellan/MIKE	1200	1	0.33
2023-Jun-20	00:23:21	INT/IDS	1200	12	4.00
2023-Jun-25	05:57:27 : 05:52:26	Shane/Kast	2800:1100	1:3	0.78:0.93
2023-Jul-19	00:32:48	INT/IDS	1200	8	2.67
2024-May-18	03:21:44	VLT/FORS2	3600	1	1.00
2024-Jun-06	00:54:27	VLT/FORS2	3600	1	1.00
2024-Jun-16	00:55:09	VLT/FORS2	3600	1	1.00
2024-Jul-04	02:20:48	VLT/FORS2	3600	1	1.00
2024-Jul-11	01:56:24	Magellan/MagE	1200	3	1.00
2024-Jul-13	23:56:28	VLT/FORS2	3600	1	1.00
2024-Jul-14	23:58:11	VLT/FORS2	3600	1	1.00

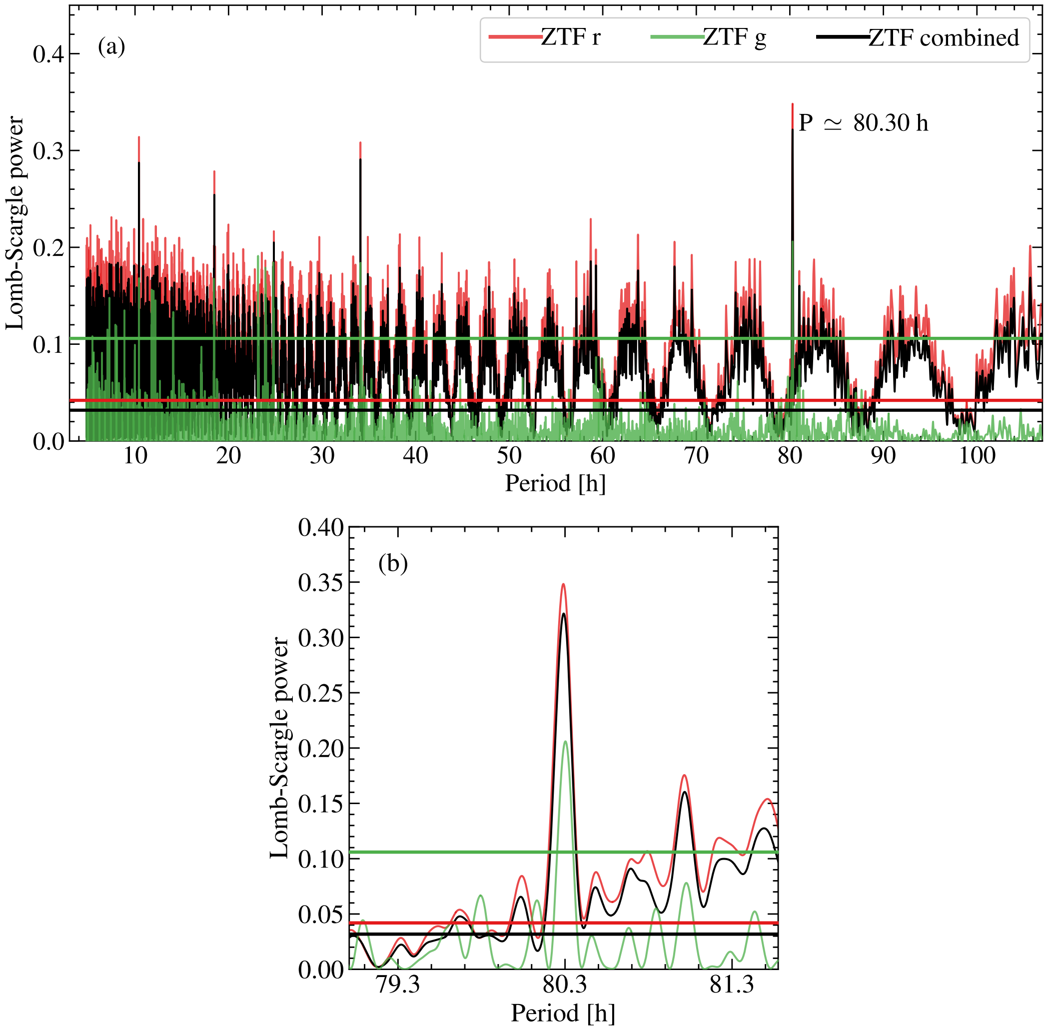

Figure 6.2: Power spectra computed from the r-band (red), g-band (green) and combined g- and r-band (black) DR23 ZTF data of WD J1653−1001. The strongest signal common to all power spectra corresponds to a period of $\simeq 80.30$ h, which is detected above a FAP of one per cent (green, red and black solid lines). Panel (b) shows the power spectra zoomed in on the periodic signal at $\simeq 80.30$ h. The legend applies to both panels.

Table 6.2: Measured period values for WD J1653−1001 from ZTF DR23 r-band, g-band and combined data using two techniques: identification of the strongest signal in the power spectra and fitting a sine wave on the phase-folded light curves.

Period measurement technique	r-band (h)	g-band (h)	Combined (h)	Mean (h)
Power spectra	80.2894	80.3025	80.2951	80.2957 ± 0.0054
Fit sine curve	80.1055 ± 0.8665	80.3852 ± 2.3204	79.4296 ± 1.0585	79.8767 ± 0.6441

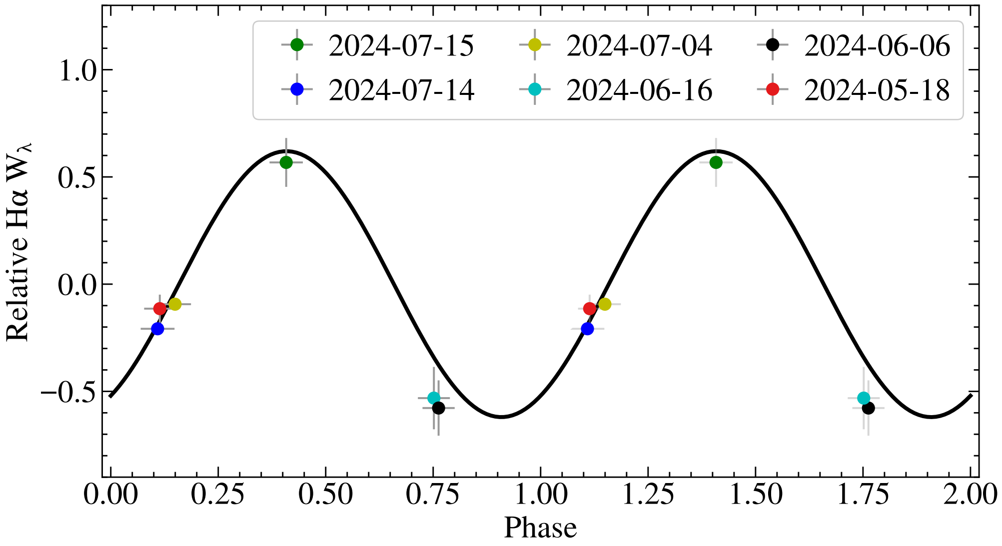

Figure 6.3: The phase of WD J1653−1001 as a function of the relative W_λ of its spectroscopically observed Hα Balmer lines in the six 1 h FORS2 observations. The data are fitted with a sine wave (black overlay) and repeated over two phases for illustrative purposes. Weakest emission corresponds to the smallest W_λ, which occurs at $\phi = 0$ (i.e. photometric maximum). Error bars are correspond to 3σ uncertainties.

1.214" at the end of DR23, thus the two stars moved further away from each other.

I created phase-folded light curves on the strongest signal period from the ZTF r-band, g-band and combined g- and r-band power spectra, which are shown in Figure 6.4. To determine the spin period of WD J1653−1001 from each phase-folded light curve, I fitted a sinusoidal function of the form

$$\Delta\text{flux} = A\text{sin}(2\pi t/P - \phi) + c, \tag{6.1}$$

where A is the amplitude, t is the observation time of each measurement, P is the period, ϕ is the phase-shift and c is a flux offset. The fitting was performed using the non-linear least-squares trust region reflective (**`trf`**; Byrd et al., 1987) algorithm implemented in `scipy optimize` to determine the best-fitting A, P, ϕ and c. No parameter bounds were imposed, ensuring an unrestricted exploration of the parameter space. The best-fitting periods for each light curve are reported in Table 6.2. The weighted mean period derived from the sinusoidal fits of the r-band, g-band and combined data light curves is 79.88 ± 0.64 h.

The periods measured from the ZTF DR23 power spectra and phase-folded light curves are 0.65σ apart, suggesting a strong consistency between the measurements. This makes us confident that WD J1653−1001 is photometrically variable with a dominant periodic signal of ≈ 80 h.

6.2.3 Additional observations for cooler flux calibrators

The goal of follow-up research for the network of 17 cooler flux calibrators in this thesis is to obtain higher resolution spectroscopic data than STIS to test the accuracy of the best-fitting SED and Balmer line atmospheric parameters. I have plans to secure ground-based telescope time on X-Shooter for this goal. Also, it would be beneficial to have long-term monitoring of the network for variability as standard stars should not be significantly photometrically variable (< 0.25 %) or rapidly rotating. To achieve this goal, time on the Multiple Mirror Telescope (MMT), Southern Astrophysical Research (SOAR) Telescope, Gemini, or the Las Cumbres Observatory (LCO) network of telescopes would be suitable for both northern and southern hemisphere white dwarfs. Long-term variability monitoring with *TESS* is also desirable. The more information obtained on flux calibrator stars the better, as then scientists can make an informed decision on the calibrator they use to then yield the most accurate scientific results possible.

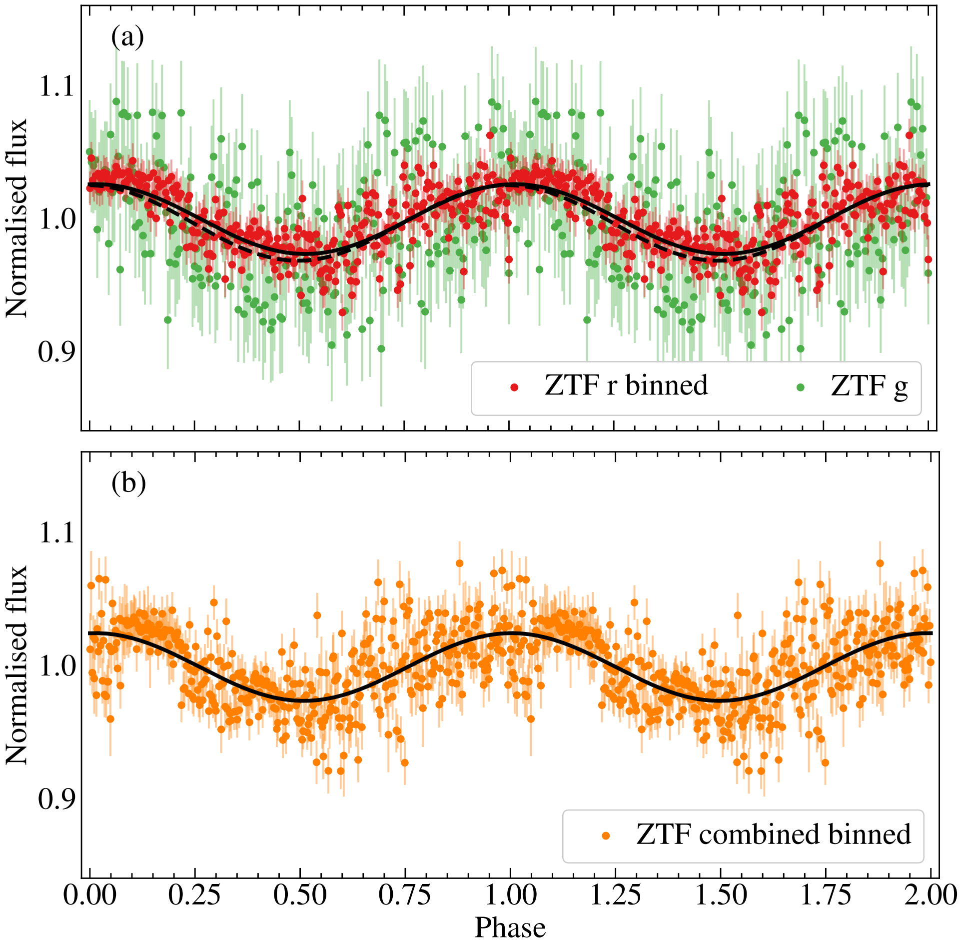

Figure 6.4: ZTF DR23 light curves of WD J1653−1001 phase-folded onto a period of 80.30 h. (a) r- (red) and g- (green) band light curves, where the r-band data are binned into 400 data points whereas the g-band raw 242 data points are shown. Sine waves are fitted on the r- and g-band light curves, shown by the black solid and dashed curves, respectively. Phase = 0 corresponds to the photometric maximum at $T_{\mathrm{BMJD}-50\,000} = 8992.67$ d for the r-band light curve and $T_{\mathrm{BMJD}-50\,000} = 8991.83$ d for the g-band light curve. (b) combined r- and g-band light curve binned into 400 data points, with a fitted sine wave shown by the solid black curve. Phase = 0 corresponds to the photometric maximum at $T_{\mathrm{BMJD}-50\,000} = 8992.40$ d for the combined light curve. In both panels, data are repeated over two phases for illustrative purposes and error bars represent the 1σ scatter in each measurement/bin.

Bibliography

Abbott T.M.C. et al., 2018. ApJS, 239(2):18.

Abel M. et al., 2011. *Journal of Physical Chemistry A*, 115(25):6805–6812.

Abel M. et al., 2012. J. Chem. Phys., 136(4):044319–044319.

Abohalima A. and Frebel A., 2018. ApJS, 238(2):36.

Adams W.S., 1914. PASP, 26(155):198.

Allard N.F. and Kielkopf J.F., 2009. A&A, 493(3):1155–1160.

Althaus L.G. et al., 2010a. A&A Rev., 18(4):471–566.

Althaus L.G. et al., 2010b. ApJ, 717(2):897–907.

Angel J.R.P., Borra E.F., and Landstreet J.D., 1981. ApJS, 45:457–474.

Angel J.R.P. et al., 1974. ApJ, 194:L47.

Appenzeller I. et al., 1998. *The Messenger*, 94:1–6.

Apps K., Smart R.L., and Silvotti R., 2021. *Research Notes of the American Astronomical Society*, 5(10):229.

Astropy Collaboration et al., 2013. A&A, 558:A33.

Astropy Collaboration et al., 2018. AJ, 156(3):123.

Astropy Collaboration et al., 2022. ApJ, 935(2):167.

Audouze J. and Silk J., 1995. ApJ, 451:L49.

Axelrod T. et al., 2023. ApJ, 951(1):78.

Aznar Cuadrado R. et al., 2004. A&A, 423:1081–1094.

Bagnulo S. and Landstreet J.D., 2018. A&A, 618:A113.

Bagnulo S. and Landstreet J.D., 2021. MNRAS, 507(4):5902–5951.

Bagnulo S. and Landstreet J.D., 2022. ApJ, 935(1):L12.

Bagnulo S. et al., 2024a. ApJ, 963(1):L22.

Bagnulo S. et al., 2024b. A&A, 688:L14.

Baranger M., 1962. *edited by DR Bates, Academic Press, New York*.

Barstow M.A., Hubeny I., and Holberg J.B., 1999. MNRAS, 307(4):884–894.

Bauer E.B., 2023. ApJ, 950(2):115.

Bauer E.B. et al., 2020. ApJ, 902(2):93.

Becklin E.E. et al., 2005. ApJ, 632(2):L119–L122.

Bédard A., Bergeron P., and Fontaine G., 2017. ApJ, 848(1):11.

Bédard A. et al., 2020. ApJ, 901(2):93.

Bédard A. et al., 2022. ApJ, 927(1):128.

Beers T.C. and Christlieb N., 2005. ARA&A, 43(1):531–580.

Bellm E.C. et al., 2019. PASP, 131(995):018002.

Belloni D. and Schreiber M.R., 2020. MNRAS, 492(1):1523–1529.

Berger L. et al., 2005. A&A, 444(2):565–571.

Bergeron P. and Leggett S.K., 2002. ApJ, 580(2):1070–1076.

Bergeron P., Ruiz M.T., and Leggett S.K., 1997. ApJS, 108(1):339–387.

Bergeron P. et al., 1994. ApJ, 423:456.

Bergeron P. et al., 2019. ApJ, 876(1):67.

Bergeron P. et al., 2022. ApJ, 934(1):36.

Bessel F.W., 1844. MNRAS, 6:136–141.

Blackman J.W. et al., 2021. Nature, 598(7880):272–275.

Blouin S. and Daligault J., 2021. Phys. Rev. E, 103(4):043204.

Blouin S., Daligault J., and Saumon D., 2021. ApJ, 911(1):L5.

Blouin S., Dufour P., and Allard N.F., 2018a. ApJ, 863(2):184.

Blouin S., Kowalski P.M., and Dufour P., 2017. ApJ, 848(1):36.

Blouin S. et al., 2018b. ApJ, 867(2):161.

Blouin S. et al., 2019a. ApJ, 872(2):188.

Blouin S. et al., 2019b. ApJ, 878(1):63.

Blouin S. et al., 2019c. ApJ, 875(2):137.

Blouin S. et al., 2020a. ApJ, 899(1):46.

Blouin S. et al., 2020b. A&A, 640:L11.

Bohlin R.C., 2014. AJ, 147(6):127.

Bohlin R.C., Deustua S.E., and de Rosa G., 2019. AJ, 158(5):211.

Bohlin R.C., Gordon K.D., and Tremblay P.E., 2014. PASP, 126(942):711.

Bohlin R.C., Hubeny I., and Rauch T., 2020. AJ, 160(1):21.

Bohlin R.C. et al., 2011. AJ, 141(5):173.

Bohlin R.C. et al., 2022. AJ, 164(1):10.

Bohlin R.C. et al., 2025. AJ, 169(1):40.

Bond H.E., Bergeron P., and Bédard A., 2017. ApJ, 848(1):16.

Borysow A., Jorgensen U.G., and Fu Y., 2001. J. Quant. Spec. Radiat. Transf., 68:235–255.

Braithwaite J. and Spruit H.C., 2004. Nature, 431(7010):819–821.

Briggs G.P. et al., 2018. MNRAS, 478(1):899–905.

Brinkworth C.S. et al., 2004. MNRAS, 348(3):L33–L37.

Brinkworth C.S. et al., 2013. ApJ, 773(1):47.

Brout D. et al., 2022. ApJ, 938(2):111.

Burleigh M.R., Clarke F.J., and Hodgkin S.T., 2002. MNRAS, 331(4):L41–L45.

Busso G. et al., 2022. Gaia DR3 documentation Chapter 5: Photometric data. Gaia DR3 documentation, European Space Agency; Gaia Data Processing and Analysis Consortium.

Byrd R.H., Schnabel R.B., and Shultz G.A., 1987. *SIAM Journal on Numerical Analysis*, 24(5):1152–1170.

Calamida A. et al., 2022. ApJ, 940(1):19.

Cantiello M., Fuller J., and Bildsten L., 2016. ApJ, 824(1):14.

Caron A. et al., 2023. MNRAS, 519(3):4529–4549.

Carroll B.W. and Ostlie D.A., 2006. *An introduction to modern astrophysics and cosmology*. Cambridge University Press.

Cassisi S. et al., 2007. ApJ, 661(2):1094–1104.

Cayrel R. et al., 2004. A&A, 416:1117–1138.

Cepa J. et al., 2000. In M. Iye and A.F. Moorwood, editors, *Optical and IR Telescope Instrumentation and Detectors*, volume 4008 of *Society of Photo-Optical Instrumentation Engineers (SPIE) Conference Series*, 623–631.

Cepa J. et al., 2003. In M. Iye and A.F.M. Moorwood, editors, *Instrument Design and Performance for Optical/Infrared Ground-based Telescopes*, volume 4841 of *Society of Photo-Optical Instrumentation Engineers (SPIE) Conference Series*, 1739–1749.

Chabrier G. and Potekhin A.Y., 1998. Phys. Rev. E, 58(4):4941–4949.

Chambers K.C. et al., 2016. *arXiv e-prints*, arXiv:1612.05560.

Chandrasekhar S., 1935. MNRAS, 95:207–225.

Chen Y.Q. et al., 2000. A&AS, 141:491–506.

Cho P.B. et al., 2022. ApJ, 927(1):70.

Cukanovaite E. et al., 2021. MNRAS, 501(4):5274–5293.

Cummings J.D. et al., 2018. ApJ, 866(1):21.

Cunningham T. et al., 2019. MNRAS, 488(2):2503–2522.

Cunningham T. et al., 2020. MNRAS, 492(3):3540–3552.

Cunningham T. et al., 2021. MNRAS, 503(2):1646–1667.

Cunningham T. et al., 2022. Nature, 602(7896):219–222.

Dályа G. et al., 2018. MNRAS, 479(2):2374–2381.

Dark Energy Survey Collaboration et al., 2016. MNRAS, 460(2):1270–1299.

De Gerónimo F.C. et al., 2019. A&A, 630:A100.

DESI Collaboration et al., 2016a. *arXiv e-prints*, arXiv:1611.00036.

DESI Collaboration et al., 2016b. *arXiv e-prints*, arXiv:1611.00037.

DESI Collaboration et al., 2024a. AJ, 168(2):58.

DESI Collaboration et al., 2024b. AJ, 167(2):62.

Dickinson N.J. et al., 2012. MNRAS, 423(2):1397–1410.

Dufour P. et al., 2017. In P.E. Tremblay, B. Gaensicke, and T. Marsh, editors, *20th European White Dwarf Workshop*, volume 509 of *Astronomical Society of the Pacific Conference Series*, 3.

Eisenstein D.J. et al., 2006. ApJS, 167(1):40–58.

El-Badry K., Rix H.W., and Heintz T.M., 2021. MNRAS, 506(2):2269–2295.

Elms A.K. et al., 2022. MNRAS, 517(3):4557–4574.

Elms A.K. et al., 2023. MNRAS, 524(4):4996–5015.

Elms A.K. et al., 2024. MNRAS, 534(3):2758–2782.

Eyer L. et al., 2017. *arXiv e-prints*, arXiv:1702.03295.

Eyer L. et al., 2022. *arXiv e-prints*, arXiv:2206.06416.

Fantin N.J., Côté P., and McConnachie A.W., 2020. ApJ, 900(2):139.

Fantin N.J. et al., 2019. ApJ, 887(2):148.

Farihi J., 2016. New A Rev., 71:9–34.

Farihi J., Becklin E.E., and Zuckerman B., 2005. ApJS, 161(2):394–428.

Farihi J., Jura M., and Zuckerman B., 2009. ApJ, 694(2):805–819.

Farihi J., Parsons S.G., and Gänsicke B.T., 2017. *Nature Astronomy*, 1:0032.

Farihi J. et al., 2010. MNRAS, 404(4):2123–2135.

Ferrario L., de Martino D., and Gänsicke B.T., 2015. Space Sci. Rev., 191(1-4):111–169.

Ferrario L., Wickramasinghe D., and Kawka A., 2020. *Advances in Space Research*, 66(5):1025–1056.

Fitzpatrick E.L. and Massa D., 1999. ApJ, 525(2):1011–1023.

Flammarion C., 1877. *Astronomical register*, 15:186–189.

Flaugher B. et al., 2015. AJ, 150(5):150.

Flewelling H.A. et al., 2020. ApJS, 251(1):7.

Fontaine G., Brassard P., and Bergeron P., 2001. PASP, 113(782):409–435.

Fontaine G., Thomas J.H., and van Horn H.M., 1973. ApJ, 184:911–916.

Fontaine G. and Wesemael F., 1987. In A.G.D. Philip, D.S. Hayes, and J.W. Liebert, editors, *IAU Colloq. 95: Second Conference on Faint Blue Stars*, 319–326.

Fontaine G. and Wesemael F., 1997. In J. Isern, M. Hernanz, and E. Garcia-Berro, editors, *White dwarfs*, volume 214 of *Astrophysics and Space Science Library*, 173.

Fouesneau M. et al., 2019. ApJ, 870(1):9.

Fowler R.H., 1926. MNRAS, 87:114–122.

Freudling W. et al., 2013. A&A, 559:A96.

Frewen S.F.N. and Hansen B.M.S., 2014. MNRAS, 439(3):2442–2458.

Friedrich S., Oestreicher R., and Schweizer W., 1996. A&A, 309:227–234.

Frommhold L., 1994. *Collision-induced Absorption in Gases.* Cambridge University Press.

Fuentes J.R. et al., 2023. ApJ, 950(1):73.

Fuller J. and Mathis S., 2023. MNRAS, 520(4):5573–5585.

Gaia Collaboration et al., 2016. A&A, 595:A1.

Gaia Collaboration et al., 2021. A&A, 649:A1.

Gaia Collaboration et al., 2022. *arXiv e-prints*, arXiv:2206.05595.

Gaia Collaboration et al., 2023. A&A, 674:A1.

Gänsicke B.T. et al., 2012. MNRAS, 424(1):333–347.

Gänsicke B.T. et al., 2016. ApJ, 818(1):L7.

Gänsicke B.T. et al., 2019. Nature, 576(7785):61–64.

Gänsicke B.T. et al., 2020. MNRAS, 499(2):2564–2574.

García-Berro E. et al., 2007. ApJ, 661(2):L179–L182.

García-Berro E. et al., 2012. ApJ, 749(1):25.

Gentile Fusillo N.P. et al., 2018. MNRAS, 473(3):3693–3699.

Gentile Fusillo N.P. et al., 2019. MNRAS, 482(4):4570–4591.

Gentile Fusillo N.P. et al., 2020. MNRAS, 491(3):3613–3623.

Gentile Fusillo N.P. et al., 2021. MNRAS, 508(3):3877–3896.

Giammichele N., Charpinet S., and Brassard P., 2022. *Frontiers in Astronomy and Space Sciences*, 9:879045.

Giammichele N. et al., 2018. Nature, 554(7690):73–76.

Gianninas A., Bergeron P., and Ruiz M.T., 2011. ApJ, 743(2):138.

Gianninas A. et al., 2010. ApJ, 720(1):581–602.

Gianninas A. et al., 2015. MNRAS, 449(4):3966–3980.

Ginzburg S. et al., 2022. MNRAS, 514(3):4111–4119.

Goldreich P. and Lynden-Bell D., 1969. ApJ, 156:59–78.

Gomez T.A., Stambulchik E., and White J., 2024. Phys. Rev. A, 109(5):052804.

Gordon K.D. et al., 2022. AJ, 163(6):267.

Gordon K.D. et al., 2023. ApJ, 950(2):86.

Graham J.R. et al., 1990. ApJ, 357:216.

Gratton R.G. and Sneden C., 1987a. A&AS, 68:193–210.

Gratton R.G. and Sneden C., 1987b. A&A, 178:179–193.

Gray R.O., 2007. In C. Sterken, editor, *The Future of Photometric, Spectrophotometric and Polarimetric Standardization*, volume 364 of *Astronomical Society of the Pacific Conference Series*, 305.

Greenstein J.L. and McCarthy J.K., 1985. ApJ, 289:732–747.

Greenstein J.L. and Oke J.B., 1979. ApJ, 229:L141–L144.

Griem H.R., 1960. ApJ, 132:883.

Griem H.R., 1974. *Spectral line broadening by plasmas.* Academic Press.

Guidry J.A. et al., 2021. ApJ, 912(2):125.

Gustafsson M. and Frommhold L., 2001. ApJ, 546(2):1168–1170.

Gustafsson M. and Frommhold L., 2003. A&A, 400:1161–1162.

Hall P.B. and Maxwell A.J., 2008. ApJ, 678(2):1292–1297.

Hansen B.M.S., 1998. Nature, 394(6696):860–862.

Hardy F., Dufour P., and Jordan S., 2023. MNRAS, 520(4):6111–6134.

Heintz T.M. et al., 2024. ApJ, 969(1):68.

Herschel W., 1785. *Philosophical Transactions of the Royal Society of London Series I*, 75:40–126.

Hertzsprung E., 1915. ApJ, 42:111–119.

Holberg J.B. and Bergeron P., 2006. AJ, 132(3):1221–1233.

Holberg J.B. and Wesemael F., 2007. *Journal for the History of Astronomy*, 38:161–174.

Holberg J.B. et al., 1985. ApJ, 293:294–302.

Holberg J.B. et al., 2008. AJ, 135(4):1225–1238.

Holberg J.B. et al., 2016. MNRAS, 462(3):2295–2318.

Hollands M.A., Gänsicke B.T., and Koester D., 2018. MNRAS, 477(1):93–111.

Hollands M.A. et al., 2021. *Nature Astronomy*, 5:451–459.

Hook I.M. et al., 2004. PASP, 116(819):425–440.

Hou S.Q. et al., 2017. ApJ, 834(2):165.

Hounsell R. et al., 2018. ApJ, 867(1):23.

Hubeny I. and Lanz T., 1995. ApJ, 439:875.

Hummer D.G. and Mihalas D., 1988. ApJ, 331:794.

Hurley J.R., Pols O.R., and Tout C.A., 2000. MNRAS, 315(3):543–569.

Iben I. J. and Tutukov A.V., 1984. ApJS, 54:335–372.

Iliadis C. et al., 2016. ApJ, 818(1):98.

Isern J. et al., 2017. ApJ, 836(2):L28.

Izquierdo P. et al., 2021. MNRAS, 501(3):4276–4288.

Jacobson R.A. et al., 2008. AJ, 135(1):261–263.

Jeans J.H., 1902. *Philosophical Transactions of the Royal Society of London Series A*, 199:1–53.

Jiao Z. et al., 2019. In *Materials Science and Engineering Conference Series*, volume 611 of *Materials Science and Engineering Conference Series*, 012071. IOP.

Johnson D.R.H. and Soderblom D.R., 1987. AJ, 93:864.

Johnson H.L., 1965. ApJ, 141:923.

Johnson R.C., 1927. *Philosophical Transactions of the Royal Society of London Series A*, 226:157–230.

Jordan S. et al., 2007. A&A, 462(3):1097–1101.

Jørgensen U.G. et al., 2000. A&A, 361:283–292.

Joyce S.R.G. et al., 2018. MNRAS, 479(2):1612–1626.

Jura M., 2003. ApJ, 584(2):L91–L94.

Jura M. and Young E.D., 2014. *Annual Review of Earth and Planetary Sciences*, 42(1):45–67.

Kaiser B.C. et al., 2021. *Science*, 371(6525):168–172.

Kausch W. et al., 2015. A&A, 576:A78.

Kawka A. and Vennes S., 2012. MNRAS, 425(2):1394–1412.

Kawka A. et al., 2007. ApJ, 654(1):499–520.

Kawka A. et al., 2011. In S. Schuh, H. Drechsel, and U. Heber, editors, *Planetary Systems Beyond the Main Sequence*, volume 1331 of *American Institute of Physics Conference Series*, 238–245. AIP.

Kepler S.O. et al., 2007. MNRAS, 375(4):1315–1324.

Kepler S.O. et al., 2017. In P.E. Tremblay, B. Gaensicke, and T. Marsh, editors, *20th European White Dwarf Workshop*, volume 509 of *Astronomical Society of the Pacific Conference Series*, 421.

Kepler S.O. et al., 2021. MNRAS, 507(3):4646–4660.

Kilic M. et al., 2005. ApJ, 632(2):L115–L118.

Kilic M. et al., 2006. AJ, 131(1):582–599.

Kilic M. et al., 2010. ApJS, 190(1):77–99.

Kilic M. et al., 2017. ApJ, 837(2):162.

Kilic M. et al., 2019. MNRAS, 482(1):965–979.

Kilic M. et al., 2020. ApJ, 898(1):84.

Klein B. et al., 2010. ApJ, 709(2):950–962.

Kleinman S.J. et al., 2004. ApJ, 607(1):426–444.

Kleinman S.J. et al., 2013. ApJS, 204(1):5.

Koester D., 2009. A&A, 498(2):517–525.

Koester D., 2010. Mem. Soc. Astron. Italiana, 81:921–931.

Koester D., 2013. In T.D. Oswalt and M.A. Barstow, editors, *Planets, Stars and Stellar Systems. Volume 4: Stellar Structure and Evolution*, volume 4, 559. Springer, Dordrecht.

Koester D., Gänsicke B.T., and Farihi J., 2014. A&A, 566:A34.

Koester D., Kepler S.O., and Irwin A.W., 2020. A&A, 635:A103.

Koester D., Provencal J., and Shipman H.L., 1997. A&A, 320:L57–L59.

Koester D., Weidemann V., and Zeidler E.M., 1982. A&A, 116:147–157.

Koester D. and Wilken D., 2006. A&A, 453(3):1051–1057.

Koester D. et al., 1985. A&A, 142:L5–L8.

Koester D. et al., 1998. A&A, 338:612–622.

Koester D. et al., 2005. A&A, 432(3):1025–1032.

Koester D. et al., 2009. A&A, 505(1):441–462.

Kolb A.C. and Griem H., 1958. *Phys. Rev.*, 111:514–521.

Kowalski P.M., 2006. ApJ, 641(1):488–493.

Kowalski P.M., 2010. A&A, 519:L8.

Kowalski P.M., 2014. A&A, 566:L8.

Kowalski P.M. and Saumon D., 2004. ApJ, 607(2):970–981.

Kowalski P.M. and Saumon D., 2006. ApJ, 651(2):L137–L140.

Lam M.C. et al., 2020. MNRAS, 493(4):6001–6010.

Landstreet J.D., 1967. *Physical Review*, 153(5):1372–1377.

Landstreet J.D., 1987. MNRAS, 225:437–450.

Landstreet J.D. and Angel J.R.P., 1975. ApJ, 196:819–826.

Landstreet J.D. and Bagnulo S., 2019. A&A, 623:A46.

Lenzuni P., Chernoff D.F., and Salpeter E.E., 1991. ApJS, 76:759.

Li J., Ferrario L., and Wickramasinghe D., 1998. ApJ, 503(2):L151–L154.

Liebert J. et al., 1978. ApJ, 225:181–190.

Lindegren L. et al., 2021. A&A, 649:A2.

Lodders K., 2003. ApJ, 591(2):1220–1247.

Lomb N.R., 1976. Ap&SS, 39(2):447–462.

López-Sanjuan C. et al., 2022. A&A, 658:A79.

Luhman K.L., Burgasser A.J., and Bochanski J.J., 2011. ApJ, 730(1):L9.

Luyten W.J., 1922. PASP, 34(197):54.

Maíz Apellániz J. and Weiler M., 2018. A&A, 619:A180.

Manser C.J. et al., 2023. MNRAS, 521(4):4976–4994.

Manser C.J. et al., 2024. MNRAS, 535(1):254–289.

Marigo P. et al., 2020. *Nature Astronomy*, 4:1102–1110.

Marocco F. et al., 2021. ApJS, 253(1):8.

Marshall J.L. et al., 2008. In I.S. McLean and M.M. Casali, editors, *Ground-based and Airborne Instrumentation for Astronomy II*, volume 7014 of *Society of Photo-Optical Instrumentation Engineers (SPIE) Conference Series*, 701454.

Masci F.J. et al., 2019. PASP, 131(995):018003.

McCleery J. et al., 2020. MNRAS, 499(2):1890–1908.

McCook G.P. and Sion E.M., 1999a. ApJS, 121(1):1–130.

McCook G.P. and Sion E.M., 1999b. ApJS, 121(1):1–130.

McCord T.B. and Sotin C., 2005. *Journal of Geophysical Research: Planets*, 110(E5).

McDonough W., 2000. In E. Teisseyre R. & Majewski, editor, *Earthquake Thermodynamics and Phase Transformation in the Earth's Interior*, International Geophysics, chapter 1 - The Composition of the Earth, 5–24. Elsevier Science Academic Press, 1st edition.

McMahon R.G. et al., 2013. *The Messenger*, 154:35–37.

Megessier C., 1995. A&A, 296:771.

Melis C. and Dufour P., 2017. ApJ, 834(1):1.

Mestel L., 1952. MNRAS, 112:583.

Miller Bertolami M.M., Althaus L.G., and Córsico A.H., 2017. In P.E. Tremblay, B. Gaensicke, and T. Marsh, editors, *20th European White Dwarf Workshop*, volume 509 of *Astronomical Society of the Pacific Conference Series*, 435.

Mozer B. and Baranger M., 1960. *Phys. Rev.*, 118:626–631.

Mullally S.E. et al., 2024. ApJ, 962(2):L32.

Munday J. et al., 2023. MNRAS, 518(4):5123–5139.

Munday J. et al., 2024. MNRAS, 532(2):2534–2556.

Mustill A.J. and Villaver E., 2012. ApJ, 761(2):121.

Mustill A.J. et al., 2018. MNRAS, 476(3):3939–3955.

Napiwotzki R. et al., 2020. A&A, 638:A131.

Narayan G. et al., 2016. ApJ, 822(2):67.

Narayan G. et al., 2019. ApJS, 241(2):20.

Nelan E.P. and Wegner G., 1985. ApJ, 289:L31–L33.

Nur M. et al., 2015. In *Journal of Physics Conference Series*, volume 622 of *Journal of Physics Conference Series*, 012055.

O'Brien M.W. et al., 2023. MNRAS, 518(2):3055–3073.

O'Brien M.W. et al., 2024. MNRAS, 527(3):8687–8705.

Oke J.B., 1974. ApJS, 27:21.

Oppenheimer B.R. et al., 2001a. *Science*, 292(5517):698–702.

Oppenheimer B.R. et al., 2001b. ApJ, 550(1):448–456.

Oswalt T.D., Hintzen P.M., and Luyten W.J., 1988. ApJS, 66:391.

Paquette C. et al., 1986. ApJS, 61:197.

Paturel G. et al., 2003. A&A, 412:45–55.

Pauli W., 1925. *Zeitschrift fur Physik*, 31(1):765–783.

Pedregosa F. et al., 2011. *Journal of Machine Learning Research*, 12:2825–2830.

Pelletier C. et al., 1986. ApJ, 307:242.

Perryman M.A.C. et al., 1997. A&A, 323:L49–L52.

Phillips M.W. et al., 2020. A&A, 637:A38.

Pols O.R. et al., 1998. MNRAS, 298(2):525–536.

Potekhin A.Y. and Chabrier G., 2000. Phys. Rev. E, 62(6):8554–8563.

Press W.H., Flannery B.P., and Teukolsky S.A., 1986. *Numerical recipes. The art of scientific computing.* Cambridge University Press.

Preval S.P. et al., 2013. MNRAS, 436(1):659–674.

Raddi R. et al., 2015. MNRAS, 450(2):2083–2093.

Rao S. et al., 2018. A&A, 618:A18.

Rauch T. et al., 2013. A&A, 560:A106.

Rebassa-Mansergas A. et al., 2021. MNRAS, 505(3):3165–3176.

Reding J.S. et al., 2020. ApJ, 894(1):19.

Reding J.S. et al., 2023. MNRAS, 522(1):693–699.

Renedo I. et al., 2010. ApJ, 717(1):183–195.

Ricker G.R. et al., 2014. In J. Oschmann Jacobus M., M. Clampin, G.G. Fazio, and H.A. MacEwen, editors, *Space Telescopes and Instrumentation 2014: Optical, Infrared, and Millimeter Wave*, volume 9143 of *Society of Photo-Optical Instrumentation Engineers (SPIE) Conference Series*, 914320.

Rieke G.H. et al., 2023. AJ, 165(3):99.

Rodrigo C., Solano E., and Bayo A., 2012. SVO Filter Profile Service Version 1.0. IVOA Working Draft 15 October 2012.

Ronco M.P. et al., 2020. ApJ, 898(1):L23.

Rowell N., 2013. MNRAS, 434(2):1549–1564.

Rudnick R.L. and Gao S., 2003. *Treatise on Geochemistry*, 3:659.

Russell H.N., 1944. AJ, 51:13.

Sahu S. et al., 2023. MNRAS, 526(4):5800–5823.

Salaris M. et al., 2010. ApJ, 716(2):1241–1251.

Salaris M. et al., 2022. MNRAS, 509(4):5197–5208.

Salpeter E.E., 1961. ApJ, 134:669.

Saumon D., Blouin S., and Tremblay P.E., 2022. Phys. Rep., 988:1–63.

Saumon D., Chabrier G., and van Horn H.M., 1995. ApJS, 99:713.

Saumon D., Holberg J.B., and Kowalski P.M., 2014. ApJ, 790(1):50.

Scargle J.D., 1982. ApJ, 263:835–853.

Schaeberle J.M., 1896. AJ, 17:37–37.

Scharwächter J. et al., 2018. In C.J. Evans, L. Simard, and H. Takami, editors, *Ground-based and Airborne Instrumentation for Astronomy VII*, volume 10702 of *Society of Photo-Optical Instrumentation Engineers (SPIE) Conference Series*, 107022T.

Schmidt G.D., Bergeron P., and Fegley B., 1995. ApJ, 443:274.

Schmidt G.D. et al., 1999. ApJ, 512(2):916–919.

Schmidt G.D. et al., 2003. ApJ, 595(2):1101–1113.

Schramm L.S., Brownlee D.E., and Wheelock M.M., 1989. *Meteoritics*, 24(2):99.

Schreiber M.R. et al., 2021a. MNRAS, 506(1):L29–L34.

Schreiber M.R. et al., 2021b. *Nature Astronomy*, 5:648–654.

Schultz G.V. and Wiemer W., 1975. A&A, 43:133–139.

Scolnic D. et al., 2015. ApJ, 815(2):117.

Scolnic D. et al., 2022. ApJ, 938(2):113.

Sigurdsson S. et al., 2003. *Science*, 301(5630):193–196.

Silvestri N.M. et al., 2006. AJ, 131(3):1674–1686.

Silvestri N.M. et al., 2007. AJ, 134(2):741–748.

Sion E.M. et al., 1983. ApJ, 269:253–257.

Skrutskie M.F. et al., 2006. AJ, 131(2):1163–1183.

Smette A. et al., 2015. A&A, 576:A77.

Smith E.W., Cooper J., and Vidal C.R., 1969. *Physical Review*, 185(1):140–151.

Smith J.C. et al., 2012. PASP, 124(919):1000.

Straniero O. et al., 2003. ApJ, 583(2):878–884.

Stubbs C.W. and Brown Y.J., 2015. *Modern Physics Letters A*, 30(40):1530030.

Stumpe M.C. et al., 2012. PASP, 124(919):985.

Subasavage J.P. et al., 2017. AJ, 154(1):32.

Takeda Y. et al., 2002. PASJ, 54:275–284.

Takeda Y. et al., 2009. PASJ, 61:563.

Tayar J. et al., 2022. ApJ, 927(1):31.

Thorsett S.E., Arzoumanian Z., and Taylor J.H., 1993. ApJ, 412:L33.

Tominaga N., Umeda H., and Nomoto K., 2007. ApJ, 660(1):516–540.

Toonen S. et al., 2017. A&A, 602:A16.

Tout C.A., Wickramasinghe D.T., and Ferrario L., 2004. MNRAS, 355(3):L13–L16.

Tout C.A. et al., 2008. MNRAS, 387(2):897–901.

Tremblay P.E. and Bergeron P., 2009. ApJ, 696(2):1755–1770.

Tremblay P.E., Bergeron P., and Gianninas A., 2011. ApJ, 730(2):128.

Tremblay P.E. et al., 2013. A&A, 559:A104.

Tremblay P.E. et al., 2014. ApJ, 791(2):92.

Tremblay P.E. et al., 2015a. ApJ, 809(2):148.

Tremblay P.E. et al., 2015b. ApJ, 812(1):19.

Tremblay P.E. et al., 2016. MNRAS, 461(2):2100–2114.

Tremblay P.E. et al., 2017. MNRAS, 465(3):2849–2861.

Tremblay P.E. et al., 2019a. Nature, 565(7738):202–205.

Tremblay P.E. et al., 2019b. MNRAS, 482(4):5222–5232.

Tremblay P.E. et al., 2020. MNRAS, 497(1):130–145.

Valyavin G. et al., 2006. ApJ, 648(1):559–564.

van Horn H.M., 1968. ApJ, 151:227.

van Maanen A., 1917. PASP, 29(172):258.

van Maanen A., 1920. *Contributions from the Mount Wilson Observatory / Carnegie Institution of Washington*, 182:1–35.

Vanderburg A. et al., 2020. Nature, 585(7825):363–367.

Vauclair G., Vauclair S., and Greenstein J.L., 1979. A&A, 80:79–96.

Venner A. et al., 2023. MNRAS, 523(3):4624–4642.

Veras D., 2016. *Royal Society Open Science*, 3:150571.

Veras D. et al., 2014. MNRAS, 445(3):2244–2255.

Veras D. et al., 2017. MNRAS, 465(1):1008–1022.

Vernet J. et al., 2011. A&A, 536:A105.

Villaver E. and Livio M., 2007. ApJ, 661(2):1192–1201.

Vogt S.S. et al., 1994. In D.L. Crawford and E.R. Craine, editors, *Instrumentation in Astronomy VIII*, volume 2198 of *Society of Photo-Optical Instrumentation Engineers (SPIE) Conference Series*, 362.

Vornanen T., Berdyugina S.V., and Berdyugin A., 2013. A&A, 557:A38.

Voslamber D., 1969. *Zeitschrift für Naturforschung A*, 24(10):1458–1472.

Walters N. et al., 2021. MNRAS, 503(3):3743–3758.

Wegner G., 1982. ApJ, 261:L87–L89.

Weidemann V., 1960. ApJ, 131:638.

Werner K., 1996. ApJ, 457:L39.

Whittet D.C.B. and van Breda I.G., 1980. MNRAS, 192:467–480.

Wickramasinghe D.T. and Ferrario L., 2005. MNRAS, 356(4):1576–1582.

Wickramasinghe D.T. et al., 2010. MNRAS, 404(4):1984–1991.

Wilson R.F. et al., 2023. ApJS, 269(1):5.

Winget D.E. et al., 1987. ApJ, 315:L77.

Wright E.L. et al., 2010. AJ, 140(6):1868–1881.

Wyatt M.C. et al., 2014. MNRAS, 439(4):3371–3391.

Xu S. et al., 2013. ApJ, 766(2):L18.

York D.G. et al., 2000. AJ, 120(3):1579–1587.

Zuckerman B., 2015. In P. Dufour, P. Bergeron, and G. Fontaine, editors, *19th European Workshop on White Dwarfs*, volume 493 of *Astronomical Society of the Pacific Conference Series*, 291.

Zuckerman B. et al., 1997. AJ, 113:764.

Zuckerman B. et al., 2003. ApJ, 596(1):477–495.

Zuckerman B. et al., 2007. ApJ, 671(1):872–877.

Zuckerman B. et al., 2010. ApJ, 722(1):725–736.